Montanuniversität Leoben – University of Leoben
Department Metallurgie – Department of Metallurgy
Simulation and Modeling of Metallurgical Processes

Characterization and optimization of the electrolyte flow in a conventional tankhouse cell

Dipl.-Ing. Andreas Kemminger

Dissertation zur Erlangung des akademischen Grades eines
Doktors der montanistischen Wissenschaften
an der Montanuniversität Leoben

Leoben, February 2015

Statutory Declaration

Ich erkläre an Eides statt, dass ich die vorliegende Arbeit selbstständig und ohne fremde Hilfe verfasst, andere als die angegebenen Quellen und Hilfsmittel nicht benutzt, wörtlich und inhaltlich entnommene Stellen als solche kenntlich gemacht habe.

I declare that I have authored this thesis independently, that I have not used other than the declared sources, and that I have explicitly marked all material which has been quoted either literally or by content from the used sources.

_____

Leoben, February 2015

Danksagung

Mein besonderer Dank Herrn Univ.-Prof. Dipl.-Phys. Dr.rer.nat Andreas Ludwig für sein grenzenloses Vertrauen in meine Arbeit und die wertvolle Unterstützung. Die Möglichkeiten, die du mir gegeben hast, um mich zu verwirklichen, rechne ich dir hoch an. Gleichzeitig danke ich Dr. Abdellah Kharicha und assoz.Prof. Dr-ing. Menghuai Wu, mit denen man nicht nur herzlich lachen, sondern auch hart arbeiten kann. Eure Diskussionsbereitschaft und eure offenen Türen haben maßgeblich beim Entstehen dieser Arbeit geholfen. Es war mir eine Ehre mit euch zusammen zu arbeiten.

Des Weiteren danke ich meinen Firmenpartnern: Aurubis Germany, Aurubis Belgium, Atlantic Copper, New Boliden, Kennecott, Montanwerke Brixlegg und Outotec, die diese Arbeit mit den nötigen finanziellen Mitteln unterstützt haben. Ein besonderer Dank gilt hierbei Dipl.-Ing. Peter Stantke für die fabelhafte Organisation der halbjährlichen Projekttreffen und seine Funktion als Ansprechpartner für die gesamte Projektgruppe.

Mein besonderer Dank gilt dem gesamten Lehrstuhl. Angefangen beim technischen Personal, welche stets dafür gesorgt haben das Computer Equipment in tadellosem Zustand zu halten. Des Weiteren möchte ich mich bei meinen administrativen Kolleginnen bedanken, die mich bei den organisatorischen Besonderheiten unserer Universität unterstützt haben. Ein herzlicher Dank gilt natürlich auch meinen Kollegen im wissenschaftlichen Personal, die stets ein offenes Ohr für mich hatten und mir erlaubten auch die verrücktesten Ideen zu besprechen.

Meiner Familie gilt der größte Dank. Für euren Rückhalt, eure Stärke und eure Geduld. Nur dank eurer Hilfe habe ich die vielen Jahre abseits der Heimat durchgehalten. Außerdem möchte ich mich bei meiner Lebensgefährtin Dipl.-Ing. Christina Sobotka bedanken. Für deine konstruktive Kritik, deine Hilfe und deinen Trost, wenn mal nicht alles geklappt hat, wie es soll.

Glück Auf!

Kurzfassung

In dieser Arbeit wird ein Verfahren zur CFD Simulation der Elektrolytströmung in einer Kupfer Raffinationselektrolyse vorgestellt. Die Elektrolytströmung wird dabei sowohl aufgrund von lokal auftretenden Massentransporten und Konzentrationsunterschiede als auch durch global wirkende Umwälzprozesse beeinflusst. Mit Hilfe einer Kopplung zwischen lokaler und globaler Simulation konnte das Strömungsverhalten erfolgreich simuliert werden. Zur Verifikation des Modells wurden Indikatorversuche an einer industriell eingesetzten Elektrolysezelle durchgeführt. Die Ergebnisse zeigen eine sehr gute Übereinstimmung mit der Simulation. Aufbauend auf diesem neuen Simulationsverfahren für Kupfer-Raffinationselektrolyse-Zellen erfolgte eine Optimierung verschiedener Zellparameter. Ziel war es, die Inhibitorenverteilung und -aktivität zu maximieren. Stellvertretend für die Summe aller Additive wurde das Verhalten von Leim simuliert. Durch die Variation verschiedener Parameter wie der Geometrie und Positionierung des Elektrolyt-Einlasses oder der Benutzung mehrerer Elektrolyt-Einlässe konnte der Einfluss auf die Elektrolytströmung und in weiterer Folge auf die Inhibitorenverteilung untersucht, sowie ein Optimum gefunden werden.

Abstract

In this work a method for a CFD simulation of the electrolyte flow in a copper electrorefining electrolysis cell is presented. The electrolyte flow is influenced by locally occurring mass transport and concentration differences as well as globally acting circulation processes. By coupling the results of the local and global simulation, the flow behavior could be successfully simulated. To verify the model indicator experiments were carried out at an electrolysis cell used in the industry. The results show a very good agreement with the simulation. Building on this new simulation method for copper refining electrolysis cells, an optimization of different cell parameters was carried out. The goal was to maximize the inhibitors distribution and activity. As a representation of all additives used in copper electrorefining electrolysis the behavior of glue was simulated. By varying different parameters such as the geometry and positioning of the electrolyte inlet or even using multiple electrolyte inlets the impact on the electrolyte flow and inhibitors distribution could be tested and finally an optimum could be found.

Table of Contents

1 Introduction

Today a lot of metallurgical processes can be described with the help of physical and mathematical models. Therefore it is possible to optimise process parameters and improve the product quality and output of metallurgical reactors before attempting any changes to them in situ. This work shows a computer fluid dynamics (CFD) simulation of the electrolyte flow in a full scale copper electrorefining cell. This is a process in which copper is refined by electrochemically dissolving into a $CuSO_4$-H_2SO_4-H_2O electrolyte at the anode and selectively electroplating from this electrolyte at the cathode without the anode impurities. The transport of the Cu^{2+} ions depends highly on the convective and diffusive electrolyte flow. Here the interaction between natural convection (caused by the density changes of the electrolyte due to different Cu^{2+} concentrations in front of the anode and cathode) and forced convection (caused by the circulation of electrolyte through the cell) of the electrolyte is investigated. Further the distribution of Cu^{2+} ions and inhibitors in the electrolyte is analysed. The results show non-uniform velocity and concentration profiles along the anode and cathode. This data can be used to detect areas with low Cu^{2+} or inhibitor concentrations which could otherwise lead to low quality cathodic copper. Additionally the influence of different cell geometries and operating conditions are shown in this work.

2 Copper Refining

2.1 Process Aim

The copper electrolysis process has been established to produce pure copper in industrial scale in large electrolysis cell groups (tankhouse cells). Pure copper is necessary in a large quantity of industrial applications i.e. electronic components where even small amounts of impurities reduce the conductivity. The process goals were nicely summarized by Davenport et al. [1] as:

The principal technical objective of the refinery is to produce high-purity cathode copper. Other important objectives are to produce this pure copper rapidly and with minimum consumption of energy and manpower.

This work aims to improve the product quality and increase the outcome of copper electrorefining cell groups by optimizing the process in the aspect of cell geometry and inlet design. Therefore a CFD tool for the simulation of large process plants has been implemented based on the Reynolds Average Navier Stokes method (RANS) used in the ANSYS Fluent Framework. This tool is based on the geometry of a Copper electrorefining plant in Pirdop Bulgaria but can be adapted to a wide range of geometries and process parameters. The CFD model has been validated against tracer experiments performed at the actual tankhouse cell in Pirdop with good agreement.

2.2 Copper extraction from ores

Depending on the type of copper ore, a pyrometallurgical or hydrometallurgical approach must be used to extract copper from the ore. Approximately 80 % of the global primary copper is extracted from low grade sulphide ores, which are treated by pyrometallurgical methods [2]. The typical sequence of processes is listed below:

- Concentration of Cu-Fe-S and Cu-S particles by froth flotation
- Optional partial roasting of concentrate
- Two stage pyrometallurgical extraction:
    - Smelting concentrates to Cu matte
    - Converting the molten matte to impure copper
- Refining the impure copper in two steps:
    - Pyrometallurgical refining in anode furnace
    - Electrorefining to high-purity copper

Additionally 20 % of the world's primary copper is produced by hydrometallurgical methods. This extraction process includes:

- Sulfuric acid leaching of Cu from broken or crushed ore to gain impure Cu aqueous solution
- Solvent extraction to transfer Cu from impure solution to pure high Cu bearing electrolyte
- Electrowinning high-purity cathode copper from this pure electrolyte

Figure 1 shows the flow diagram of a modern copper smelter from the copper ore to the finished copper cathode.

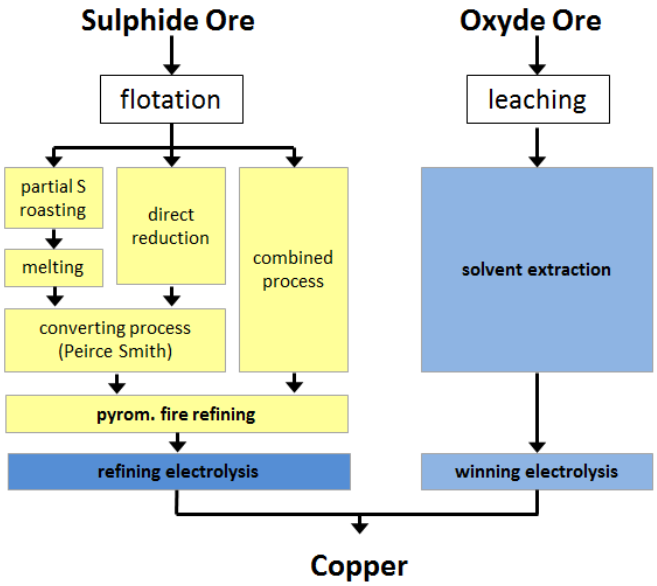

Figure 1: Copper production from ore concentrates [1]

The pyrometallurgical copper processes are mainly based on the principal of partial oxidation of the sulfide ore concentrates rather than the total oxidation of sulfide components. A total

oxidation followed by a reduction to the metal avoids of the formation of a Cu-rich matte and results in high fuel consumption, the formation of Cu-rich slags and high impurity levels in the crude copper and is therefore rarely used [1].
The method used in over 50 % of copper smelters is the direct reduction flash smelting or Outokumpu process. It combines the controlled oxidation of Fe and S and the smelting of Cu matte in one furnace.

Newer copper production processes aim to combine the two tasks of smelting and converting into one combined processes. The Direct-To-Copper Flash Smelting in theory has multiple advantages as minimizing of energy consumption and operation costs and would isolate the emissions into a single continuous gas stream but it introduces a couple of problems because 25 % of Cu entering the Direct-To-Copper Flash Smelter ends up dissolved in the slag. The cost of recovering the copper from the slag limits the industrial usage of this combined process [1].

The raw copper produced by smelting and converting is subsequently electro refined. Therefore it must be suitable for casting into thin, strong and smooth anodes for the usage in electrorefining cells. The copper must therefore be fire refined to remove most of its oxygen and sulfur. The molten blister copper from the converter contains 0.01 % S and 0.5 % O. These levels are high enough to allow the formation of SO_2 bubbles during solidification and would lead to weak and bumpy anodes. Fire refining removes sulfur and oxygen from the raw copper by:

- Air-oxidation removal of sulfur as SO_2 to 0.002 % S
- Hydrocarbon-removal of oxygen as CO and H_2O to 0.15 % O

2.3 Copper Electrorefining

Most of the copper produced in large scale quantities is treated electrolytically during production. It is either electro refined from impure copper anodes or electro won from solvent extraction electrolytes. The electrorefining process consists of:

- The electrochemical dissolution of impure copper anodes into $CuSO_4$-H_2SO_4-H_2O electrolyte
- The selective electroplating of pure copper from this electrolyte without the impurities

The half reactions occurring at the electrodes are shown in Table 1:

Table 1: Electrode half reactions [3]

Anode reactions	Cathode reactions	E_0 at 25 °C [V]
$Cu \Rightarrow Cu^{2+} + 2e^-$	$Cu^{2+} + 2\,e^- \Rightarrow Cu$	0.34
$Cu \Rightarrow Cu^{+} + e^-$	$Cu^{+} + e^- \Rightarrow Cu$	0.521
$Cu^{+} \Rightarrow Cu^{2+} + e^-$	$Cu^{2+} + e^- \Rightarrow Cu^{+}$	0.153

Table 2 shows additionally occurring secondary reactions in the electrolyte:

Table 2: Electrolytic reactions [3]

$2\,Cu^{+} \Rightarrow Cu^{2+} + Cu$	disproportionation
$2\,Cu^{+} + 2\,H^{+} + ½\,O_2 \Rightarrow 2\,Cu^{2+} + H_2O$	air oxidation
$Cu_2O + 2\,H^{+} \Rightarrow 2\,Cu^{+} + H_2O$	dissolution of Cu_2O
$Cu + H_2SO_4 + ½\,O_2 \Rightarrow CuSO_4 + H_2O$	corrosion of Cu

The disproportionation reaction of Cu^{+} ions leads to the accumulation of metallic copper powder in the anode slime. The corrosion of copper contributes to the enrichment of $CuSO_4$ and the depletion of H_2SO_4 in the electrolyte and can have a negative effect on the electrolyte conductivity.

One of the most important aspects in copper electrorefining is the power consumption and is mainly determined by the cell voltage and therefore the conductivity and electric resistance of the electrolyte. The specific resistance of the electrolyte is determined by the temperature and concentration of certain ions, namely H_2SO_4, Cu^{2+}, Ni^{2+}, Fe^{2+} and As^{3+} which continuously accumulates in the electrolyte and must be monitored and limited to certain boundaries. The specific resistance ρ can be estimated by equation 2-1 [2].

$$\rho[\Omega/\mathrm{cm}] = 1.1 \cdot \Big[1.0 - 7 \cdot 10^{-3} \cdot (T\,[°\mathrm{C}] - 55) - 3 \cdot 10^{-3}\left(H_2SO_4\left[\frac{\mathrm{g}}{\mathrm{l}}\right] - 200\right) + 6.6 \cdot 10^{-3}\left(Cu\left[\frac{\mathrm{g}}{\mathrm{l}}\right]\right) + 7.6 \cdot 10^{-3}\left(Ni\left[\frac{\mathrm{g}}{\mathrm{l}}\right]\right) + 8.2 \cdot 10^{-3}\left(Fe\left[\frac{\mathrm{g}}{\mathrm{l}}\right]\right) + 0.7 \cdot 10^{-3}\left(As\left[\frac{\mathrm{g}}{\mathrm{l}}\right]\right)\Big] \qquad \text{Eq. 2-1}$$

The overall bath resistance results from ρ times the distance between anode and cathode in cm. The distance cannot be chosen too small in order to keep anode cathode shorts to a minimum. Neither can the temperature be chosen too large because high temperatures lead to coarse grain growth of copper crystals at the cathodes. The concentration of H_2SO_4 is also limited due to the corrosion of Cu.

High Cu^{2+} contents in the electrolyte have a negative influence on the electric resistance. However, for electrochemical reason the Cu^{2+} concentration must be above 30-40 g/l. Otherwise a depletion of Copper can occur at the electrodes. For industrial applications the composition of the cell voltage can be found in Table 3.

Table 3: Cell voltage composition in industrial tankhouse cells [2]

Bath resistance	0.11 - 0.13 V
Overpotential caused by organic additives	0.04 - 0.08 V
Transition losses at anode cathode bus bar	0.03 - 0.06 V
Losses in conductor rail	0.01 - 0.02 V
Overall cell voltage	0.19 - 0.29 V

The most common impurities in copper anodes are Ag, As, Au, Bi, Co, Fe, Ni, Pb, S, Sb, Se and Te (see Table 4). They must be prevented from entering the cathode copper. The behavior of impurities is defined by their position in the electrochemical series.

Table 4: Average element concentrations [4]

Element	Anodes	Cathodes
Cu	98.4 - 99.8	99.99
O	0.1 - 0.25	Not determined
Ag	0.01 - 0.6	0.0004 - 0.0016
S	0.001 - 0.008	0.0002 - 0.001
Sb	0 - 0.3	0 - 0.001
Pb	0.001 - 0.35	0 - 0.0005
Ni	0.003 - 0.6	0 - 0.0003
Fe	0.001 - 0.03	0 - 0.0003

As	0 - 0.25	0 - 0.0001
Se	0.001 - 0.12	0 - 0.0001
Te	0.001 - 0.05	0 - 0.0001
Bi	0 - 0.05	0 - 0.0001
Au	0 - 0.02	traces

Au and Ag are insoluble under the given conditions and form the anode slime. This slime can adhere to the anode surface or fall down to the bottom of the electrolyte cell. Se and Te enter the slime and can build chemical compounds, e.g. Cu_2Se, Ag_2Se, Ag_2Te [5]. Pb and Sn both join the slime and form $PbSO_4$ and SnO_2.

The other elements dissolve in the electrolyte. To prevent an excessive buildup of these impurities the electrolyte is constantly replaced by a bleed stream and send to an electrolyte purification plant [2]. Copper has a standard potential of 0.34 V and is electroplated onto the cathode in favor of other inpurities with lower potentials.
The presence of the inpurities in cathode copper is explained by the accidental entrapment of electrolyte or anode slime. The impurities concentration in the cathode copper can be further reduced by:

- working on electrodepositing smooth copper plates on the cathodes
- washing the cathodes
- monitoring impurity levels and constantly exchange the electrolyte

2.3.1 Copper electrorefining cells

Industrial applied electrorefining cells are between 3 and 6 m long [6]. Width and depth are chosen to remain 0.1 to 0.2 m underneath anodes and cathodes. Each electrorefining cell consists of up to 30 - 60 anode cathodes pairs connected via an electrical bus bar in parallel. Large (1x1 m), thin (0.04 - 0.05 m) anodes and thin (0.001 - 0.003 m) cathodes are alternately submerged in the electrolyte about 0.05 m apart. All anodes in the cell are on the same potential, the cathodes are on a different, lower potential. For even distribution of current the anodes and cathodes are spaced evenly in the cell so that all anodes are dissolved uniformly. For this reason equal anode masses are also important.

Purified H_2SO_4 electrolyte continuously enters the electrorefining cell from one side at either the top or near the bottom, as shown in Figure 2. The electrolyte is transported through the cell and is loaded with dissolved impurities and small anode slime particles. It continuously leaves the cell at an electrolyte overflow transporting impurities to the electrolyte purification plant.

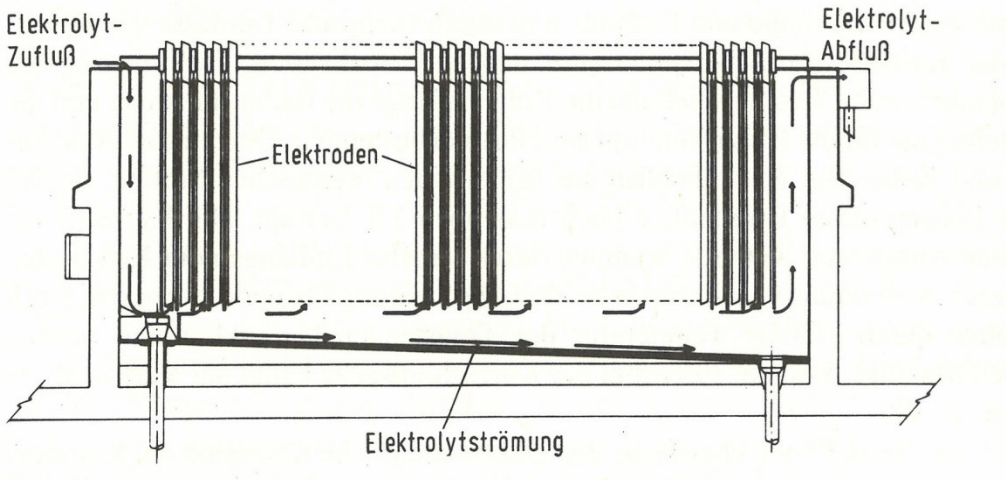

Figure 2: Industrial used copper electrorefining cells [2]

The impure anodes are cast in a cast wheel or a continuous anode cast process. They usually weight about 300 to 400 kg [4]. During the refining the anodes continuously thin as the copper dissolves into the electrolyte and have to be removed from the cell before they are in danger of breaking and falling. After being washed to remove the adhesive anode slime the used anodes are remelted and cast into new anodes. An industrial used anode and cathode design in shown in Figure 3.

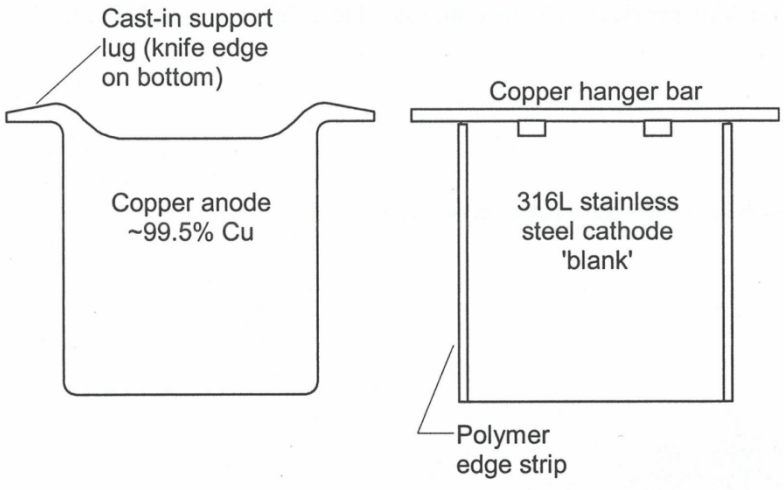

Figure 3: Anodes (left) and cathodes (right) used in electrorefining cells [1]

In new refineries stainless steel blanks welded to copper support bars are used for starter cathodes. The copper is electrodeposited onto these cathodes for 7 - 10 days, until each side holds 50 - 80 kg refined copper. The copper-loaded cathodes are then removed from the cell and washed in hot-water sprays. The deposited copper “plates” are machine-striped from the stainless steel and go to market or to melting and casting. The empty stainless blanks are carefully washed and returned to refining.

The cold- and bright-rolled stainless steel blanks are ~3 mm thick. Electrodeposited copper attaches quite firmly to this surface so it doesn´t accidentally detach during refining. Older refineries still use thin copper “starter sheets” cathodes, hung by copper support bars. Many European and North American refineries have switched from this older technology to stainless steel blanks [1].

To help the removal of the copper plates from the stainless steel cathodes the vertical edges of the blanks are covered with long, tight-fitting polymer edge strips. These strips prevent from copper depositing completely around the cathode. The bottoms of the stainless steel blanks are given a sharp-edge groove or are covered with wax to prevent copper deposition. This allows easy detachment of the plated copper from this region.

2.3.2 Electrolyte

Copper refining electrolytes usually contain 40 to 50 kg/m^3 Cu, 170 to 200 kg/m^3 H_2SO_4, 0.02 to 0.05 kg/m^3 Cl and impurities (mainly Ni, As and Fe) [4]. Additionally electrolytes hold 1 to 10 ppm organic leveling and grain refining agents. The electrolyte is steam heated to 60 - 65 °C; this heating is expensive but it beneficially:

- Increases $CuSO_4 \cdot 5H_2O$ solubility, preventing it from passivating the anode
- Lowers electrolyte density and viscosity and therefore reduces slimes movement
- Speeds up all electrochemical reactions

To avoid excessive evaporation and energy consumption, the temperature must not be too high. Electrolyte is circulated through each cell at ~0.02 m^3/min. This rate of flow replaces a cell´s electrolyte every few hours [1]. Steady electrolyte circulation is essential to:

- Replace warm, purified electrolyte in the cell
- Ensure uniform Cu^{2+} and leveling/grain-refining agent concentrations across all cathode surfaces
- Remove dissolving impurities from the cell

2.3.3 Electrical Arrangements

One main factor affecting cathode purity as well as economics is the current density. It is the rate at which electricity is passed through the electrodes in A/m^2. High current densities lead to rapid copper plating but can also cause the growth of overhanging copper crystals. This can cause entrapment of slimes on the cathodes and leads to lower cathode purity. Each refinery must therefore balance these competing economic factors [1].

Higher current densities lead to faster copper plating. However, excessive current densities can cause anodes to passivate. This can be obtained by producing Cu^{2+} ions at the anode surface faster than they can convect away. This results in a high concentration of Cu^{2+} at the anode surface and deposition of a dense $CuSO_4 \cdot 5H_2O$ layer on the anode.

The $CuSO_4 \cdot 5H_2O$ layer isolates the copper anode from the electrolyte and blocks further Cu^{2+} formation leading to a passivation of the anode. The problem is intensified by the impurities of the anode which also tend to form a coherent slime layer. By operating with current densities below 300 A/m^2 passivation can usually be avoided, depending on the impurities in the anode. Warm electrolyte (with a higher $CuSO_4 \cdot 5H_2O$ solubility) can also help. Another approach to avoid passivation is to periodically reverse the direction of the refining current, although this might decrease refining efficiency.

The technical obtainable cathode current efficiency in modern copper electro refineries is ~93 - 98 % [2]. The unused current is lost by:

- Anode cathode short-circuits ~3 %
- Stay current to ground ~1 %
- Reoxidation of cathode copper by O_2 and Fe^{3+} ~1 %

A short-circuit is obtained when cathodes and anodes touch. It can be avoided by precise, vertical electrode placement and accurate additions of levelling and grain-refining agents to the electrolyte. Its effect can be reduced by immediately locating and interrupting cathode-anode contacts whenever they occur.

Stray current loss is observed due to current flow to ground via spilled electrolyte. It can be minimized by good housekeeping around the refinery. Reoxidation of cathode is reduced by minimizing oxygen absorption into the electrolyte. A smooth and quiet electrolyte flow can help this cause

2.4 Limiting current density

In every electrolytic metal deposition the corresponding cations must be supplied from the inside of the solution to the cathode. This mass transport is generally accomplished by diffusion, convection and migration [7]. Newman [8] reports that the proportion of migration, ion motion due to the electric field, on the mass transfer is only 0.5 %.

In the small area directly in front of the electrode, charge transfer is coupled with a diffusion process. Without electric current the concentration c^0 is constant in the whole electrolyte. After switching on the current, the concentration is reduced at the electrode surface from c^0 to c^s. The forming concentration profile extends into the layers near the cathode with the thickness δ_N (Nernst diffusion layer). δ_N is defined by the intersection of the tangent of concentration profile with the horizontal line c^0 [9]. The concentration profile grows over time until steady state conditions are reached, as shown in Figure 4. The current density is defined after Fick Law, equation 2-2:

$$i = n \cdot F \cdot D \cdot \left(\frac{\partial c}{\partial x}\right)_{x=0} = n \cdot F \cdot D \cdot \frac{c^0 - c^s}{\delta_N} \qquad \text{Eq. 2-2}$$

When the surface concentration approaches zero (lim c^s => 0), the current density reaches a limiting value. This limit is called the limiting current density i_{limit}, equation 2-3.

$$i_{limit} = n \cdot F \cdot D \cdot \frac{c^0}{\delta_N} \qquad \text{Eq. 2-3}$$

The limiting current density increases linearly with increasing solution concentration c^0, with increasing diffusion constant D and decreasing diffusion layer thickness δ_N. Both the diffusion constant D and the solution concentration c^0 can be influenced only in a very narrow range, and thus the limiting current density can only be significantly increased by reducing the diffusion layer thickness δ_N.

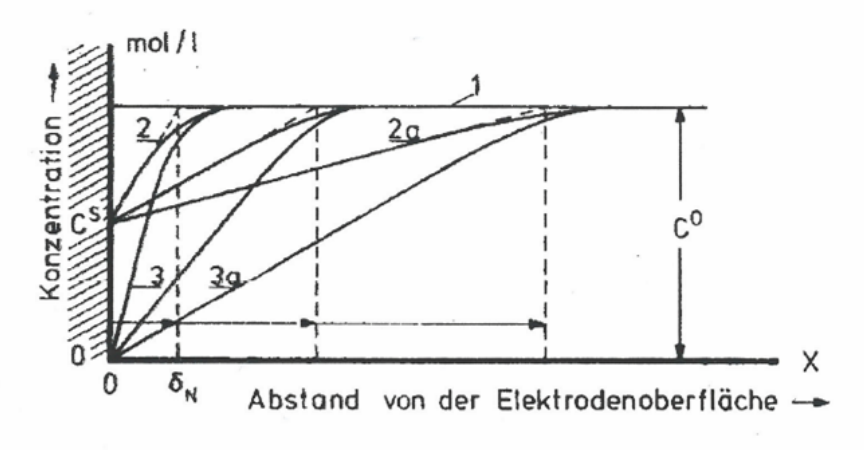

Figure 4: Development of the concentration boundary layer [9]

The thickness of the stationary diffusion layer is determined by the hydrodynamic conditions in front of the electrode surface, which can be between 0.5 mm and 10^{-4} mm wide. The hydrodynamic conditions are depend on the interaction of natural and forced convection, and may be laminar or turbulent.

Because of friction the electrolyte directly at the electrode surface is at rest. In front of the electrode surface a stationary velocity field builds up, which induces a stationary concentration profile and causes a certain thickness of the diffusion layer.

Figure 5 schematically shows the relationship between the velocity field and the concentration profile for a laminar and a turbulent electrolyte flow. It can be seen that the diffusion layer thickness δ_N becomes smaller in turbulent flow and therefore increasing the limiting current according to equation 2-3.

A general overview of the diffusion layer thickness and corresponding limiting current densities at different hydrodynamic conditions is given in Table 5.

Table 5: Limiting current densities at different convectional conditions [7]

	i_{limit} [A/m^2]	δ_N [mm]
Natural convection on vertical electrode	144	0.200
Natural convection on horizontal electrode	365	0.080
Lengthwise flow on electrode	300	0.100
Rotating cylinder	810	0.036

Gas developing electrode (13 cm^3 /cm^2 min)	7200	0.004
Gas developing electrode (1 cm^3 /cm^2 min)	1940	0.015
Inducing gas through frite (65 µm 0.1 l/min)	276	0.100
Inducing gas through frite (65 µm 0.17 l/min)	1320	0.020
Periodic destuction of diffusion layer with mesh	2280	0.013

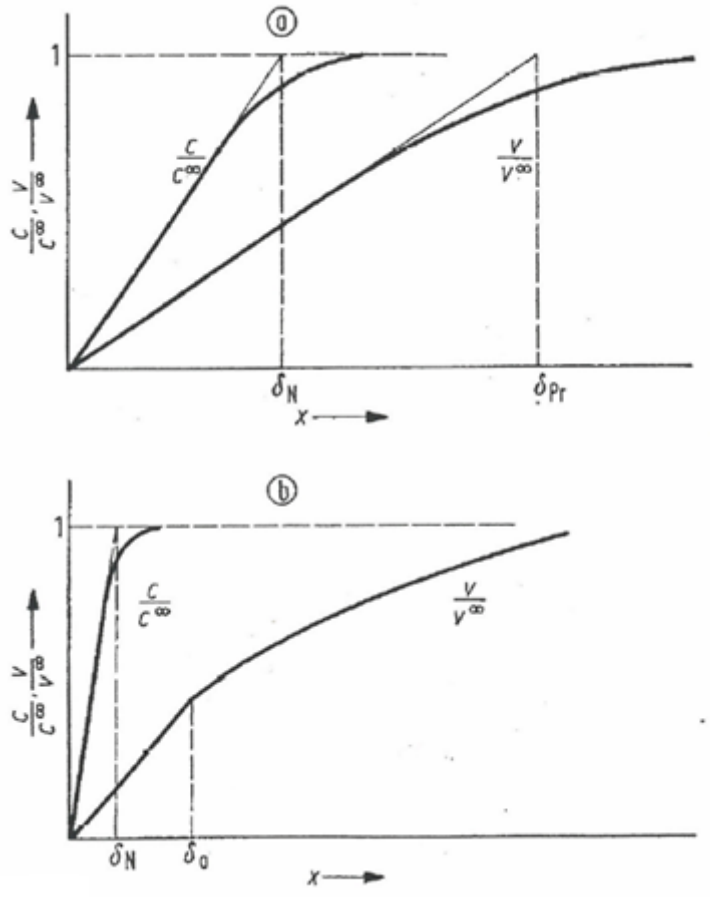

Figure 5: Velocity and concentration boundary layers for a laminar flow field (top) and a turbulent flow field (bottom) [6]

Table 5 shows that for strong forced convections the diffusion boundary layer is reduced and high current densities are possible. According to Rombach [10] the applied current density in industrial applications is limited to about 1/3 to 1/2 of the limiting current density. Applying current densities closer to the limiting current density leads to the formation of rough and partially non-compact copper deposits due to the increased dendrite formation on the cathode. High current densities can also lead to passivation effects at the anodes.

2.5 Natural and forced convection

Almost all copper electrorefining cells work by the principle of electrolyte circulation. A key task of the electrolyte circulation is to transport the necessary quantity of inhibitor additives to the cathode surface which cause a smooth and dense metal deposition. The circulation of electrolyte causes a forced convection in the electrolysis cell but its effect is relative small compared to the natural convection forming at the electrodes.

As described before the contribution of migration on the transport of Cu^{2+} from anode to cathode is insignificantly small. Additionally the electrolyte velocity at the cathode surface is reduced to zero by friction. Because of the dominance of diffusion near the electrode surface the formation of a Cu^{2+} concentration gradient occurs and thus leading to a change in electrolyte density. At the anode this concentration change is followed by an increase in electrolyte density causing a downward flow and at the cathode this flow is directed upwards for contrary reasons.

Figure 6 shows schematically the formation of the hydrodynamic boundary layer at the electrodes. The schematic concentration and velocity profiles clearly show the difference in thickness of the diffusion layer (0.15 - 0.2 mm) and the hydrodynamic boundary layer (1 - 4 mm) [7, 11]. The velocity and concentration profiles near the electrodes are dependent on the current density, electrode height, chemical electrolyte composition, viscosity and density as well as a variety of other factors.

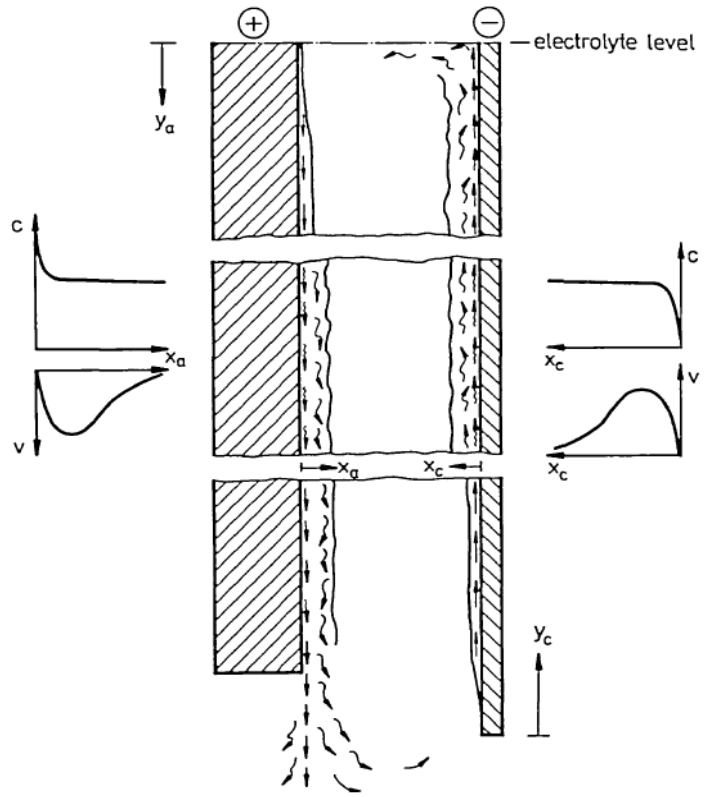

Figure 6: Concentration and velocity boundary layers inside an anode (left side) and cathode (right side) gap [11]

When considering the velocity profile over the electrode height, it can be seen that the maximum speed at the cathode is not constant but increases in flow direction. Figure 7 shows the measured velocity profiles for various electrode heights by Ibl [12] at 10 A/m^2. The results of Awakura [13] are in excellent accord. Both authors found the dependence of the maximum velocity $u_{\max}$ on the electrode height proportional to the 0.6th power, see equation 2-4.

$$u_{\max} \sim x^{0.6} \qquad \text{Eq. 2-4}$$

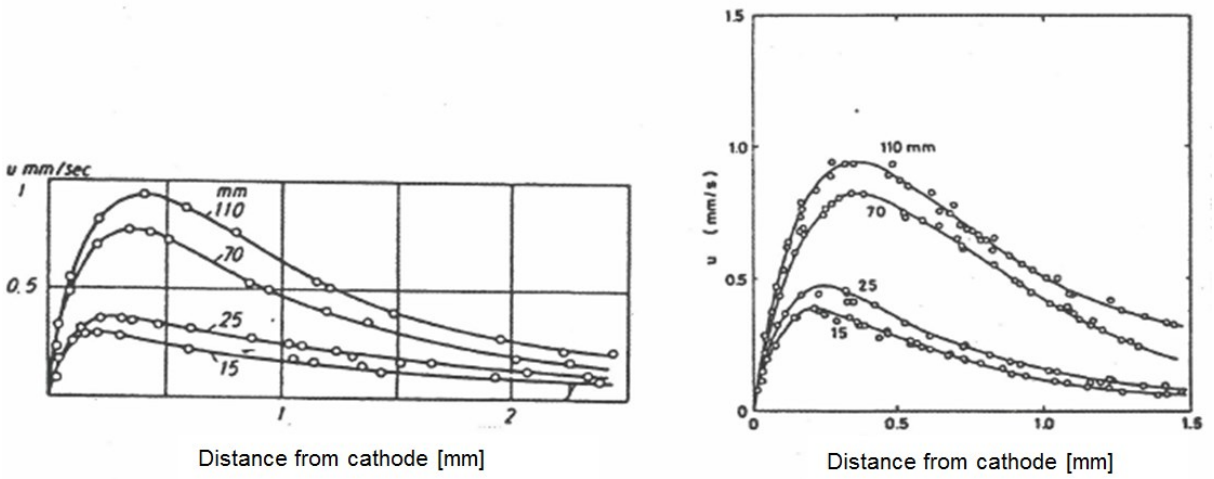

Figure 7: Velocity profiles as function of electrode height [13]

Figure 7 indicates a shift in the maximum speed with increasing altitude and speed in the direction of electrolyte flow. This dependence is given by equation 2-5. Here τ is the distance cathode surface – velocity maximum and x is the height measured from the cathode bottom.

$$\tau \sim x^{0.2} \qquad \text{Eq. 2-5}$$

The effect of current density on the velocity profile has been examined by Ibl [12] and Awakura [14]. However the investigated current densities are only up to 30 A/m^2. Therefore comparability, particular with industrial applications where ten times higher current densities are used, is limited. Figure 8 shows the experimental results of Awakura between 0.5 and 40 A/m^2 in a cathode height of 7 cm and a concentration of 38 g/l. Both authors found the dependence of the maximum velocity to the current density according to equation 2-6.

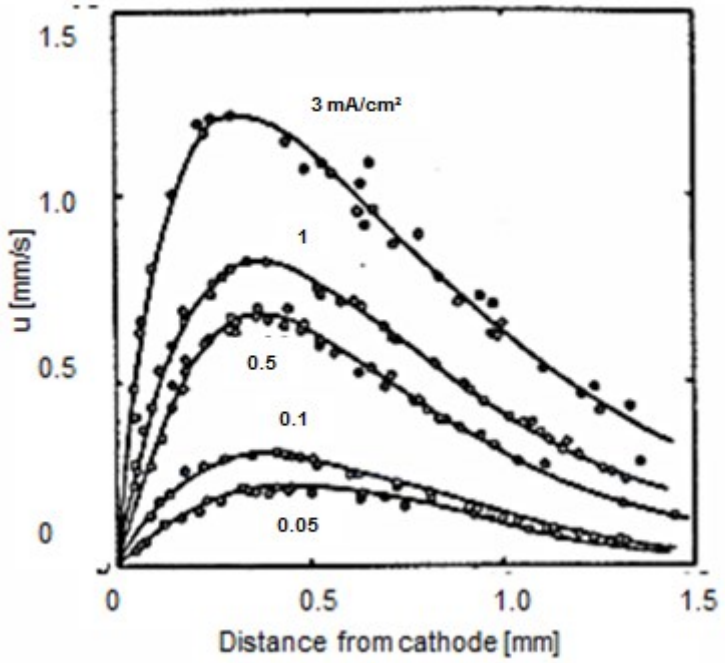

Figure 8: Velocity profiles as function of current density [13]

$$u_{\max} \sim i^{0.4} \qquad \text{Eq. 2-6}$$

The distance cathode surface – velocity maximum was found to be dependent on the current density as shown in equation 2-7.

$$\tau \sim i^{0.2} \qquad \text{Eq. 2-7}$$

2.6 Inhibitors

When copper ions are reduced they are incorporated into the metal lattice by electric crystallization. The electric crystallization of a metal in the electrolysis is determined by nucleation and crystal growth. In general electrodeposited metals have a polycrystalline structure and their shape is defined by a constant alternation between nucleation and crystal growth. Whether the metal deposition is fine-grained or coarse-grained depends on whether the rate of nucleation or crystal growth predominates during deposition [1].

The copper ions are transported to the phase boundary electrolyte/cathode primarily by convection and diffusion. After crossing the electrochemical double layer the ions are dehydrated and discharged. The atoms are then adsorbed on the cathode surface. The stacking of atoms leads to the formation of two-and three-dimensional nuclei which are only

stable after reaching a critical size [14]. Other mechanisms include surface diffusion of atoms towards a lattice space, ion passage through the double layer and two-dimensional nucleation, see Figure 9.

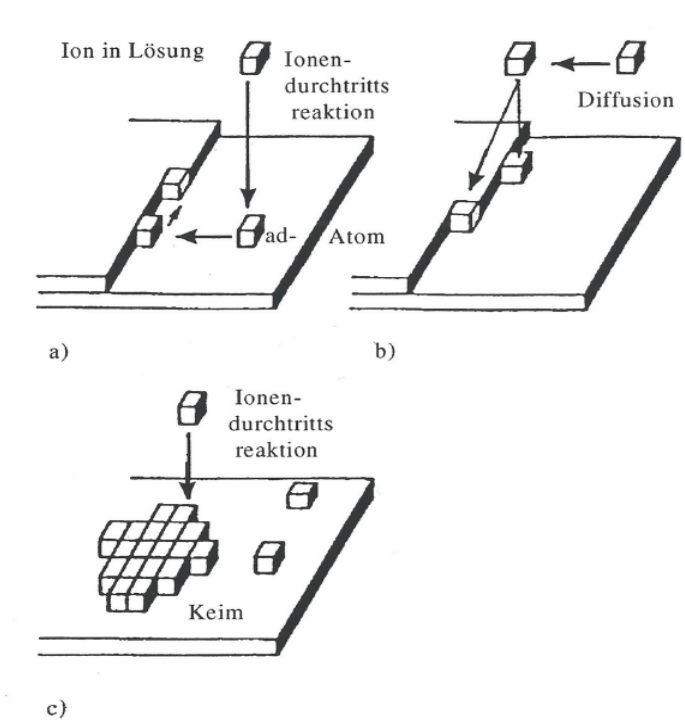

Figure 9: Different nucleation mechanisms at the electrode surface [15] a) ion passage through layer and surface diffusion b) direct ion passage to lattice space c) ion passage and 2-dimensional nucleation

The formation of a new crystal is energetically less likely than the growth of a crystal previously formed because the new nucleus requires additional energy. The only source of energy excess on the electrode surface is due overvoltage on electrodes released during the discharge of the ion. If the energy surplus is sufficiently large it can contribute to the formation of three-dimensional surface nuclei. The requirements for the formation of three-dimensional nuclei can be formulated as shown in equation 2-8:

$$\sigma \cdot S \leq z \cdot F \cdot \eta \qquad \text{Eq. 2-8}$$

σ is the surface tension metal-electrolyte, S is the surface of the forming nucleus, η is the overvoltage at the discharge of the metal ions, z is the electron number of the ion in the electrode process and F is the Faraday constant. The formation of new nuclei becomes more likely when $z \cdot F \cdot \eta$ is larger than $\sigma \cdot S$ [16].

The growth of a metal crystal occurs stepwise under the formation of microscopic thick growth layers [16]. After a three-dimensional nucleation many nuclei grow simultaneously. The crystal growth is blocked parallel to the surface, either because of the neighbor nucleus or because of the lack of local current density, so that the crystal can only continue to grow in the tangential direction [17].
There are 5 basic types of polycrystalline deposition [9] but there are also transitional forms between them:

- Field oriented isolated crystals FI
- Basis reproduction BR
- Twinning intermediate type Z
- Field-oriented texture type FT
- Unoriented dispersion type UD

1. The FI type consists of individual three-dimensional crystals growing in the direction of the current. Growth takes place predominantly at the crystals front face. At a critical current density the formation of fine, long crystal strands, so-called whisker is promoted. The FI type occurs especially at low addition of inhibitor or metals with low inhibitor sensitivity. The FI-type is undesirable because it leads to the formation of rough, pointy and needle-like surfaces.

2. If the addition of inhibitor or the current density is slightly increased, the FI-type will change to the BR-type. The BR-type represents a compact but coarse crystalline deposition. Unlike the FI- and FT-type and BR-type has a pronounced characteristic to grow perpendicular to the current.

3. In the transition phase between BR- and FT-type many twin structures (Z-type) can be noticed. The twin crystals are stacked on one another and thus form growth layers arranged diagonally against each other.

4. Further increasing the inhibitory activity or the current density in the electrolyte will cause the BR structure to change over for the FT-structure, which is characterized by strong growth parallel to the field lines with almost no perpendicular growth. In contrast to the FI-type a compact crystal growth is achieved. The FT-type occurs especially with strong inhibition.

5. With even greater inhibitor content and or increasing current density the UD-Structure can be found. At the beginning of the crystallization the crystals grow very quickly then they get

covered with inhibitors. This inhibitor layer prevents further crystal growth, forcing the formation of three-dimensional nuclei. The UD-type has a microstructure without visual grain boundaries but randomly oriented fine sub particles. The nucleation frequency is particularly large in the formation of this crystalline form [18].

The quality of copper deposit at the cathode is influenced by numerous factors as: metal ion concentration in the electrolyte, current density i, electrolyte circulation, temperature and pH value of the electrolyte, other cations and anions, addition of inhibitors, etc. [17].
The concentration of metal ions in the electrolyte has a considerable influence on the nucleation probability and the further growth of three-dimensional nuclei. Reducing the metal ion concentration in the solution leads to the depletion of copper ions at the phase boundary cathode/electrolyte and increases the value of $z \cdot F \cdot \eta$ and therefore the probability of nucleation [19]. A general rule is that a rising current density must be met with a rising copper ion concentration in the electrolyte [14, 20]. An increase in temperature causes a higher activity of the depositable metal ions is both in the interior of the electrolyte as well as the phase boundary layer. Simultaneously, the diffusion and convection are improved due to thermal motion of the electrolyte. This results in a higher concentration of the reducible metal ions in the phase boundary layer as well as decreasing the concentration dependent overpotential. With a lower $z \cdot F \cdot \eta$ the probability of nucleation decreases [14].

High current densities promote preferred growth directions of the crystal resulting in uneven, rough surfaces. To avoid such effects organic and or anorganic additives are used. The main task of the additives is to enable a fine-grained and dense surface structure. In order to ensure a high cathode quality the additives and their reaction products must not be deposited onto the metal surface. In industrial copper electrorefining plants the anorganic additive is always chlorine and the organic additives can be gelatin, glue or thiourea. In most cases the additives act as inhibitors. They are adsorbed on the cathode surface and then integrated into the copper deposit. Some additives prevent the growth of existing crystals and allow for the formation of new nuclei. The organic additives are predominantly adsorbed in areas of active growth and irregularities, allowing for a smooth, dense surface. Inhibitors can have a negative effect on the electrical conductivity of the electrolyte and the current efficiency. The optimum dosage also depends on system-specific factors and are different for every single copper electrorefining plant [21, 22, 23].

The correlation between current density/limit current density ratio and the inhibitors amount on the electro crystallization is shown in Figure 10. It can be seen that in the pure solvent, without inhibitors, the shape of the deposit is a function of $i/\, i_{limit}$. An increase of current

density i results in a decrease of inhibitors effectiveness. Low or no addition of inhibitors leads to the precipitation of Cu crystals in a BR- or FT-structure and with high current density the formation of FI-structures can be found. For an adequate addition of inhibitors and current densities smaller than 300 A/m^2 the formation of the FI- or FT-structures can be observed [17].

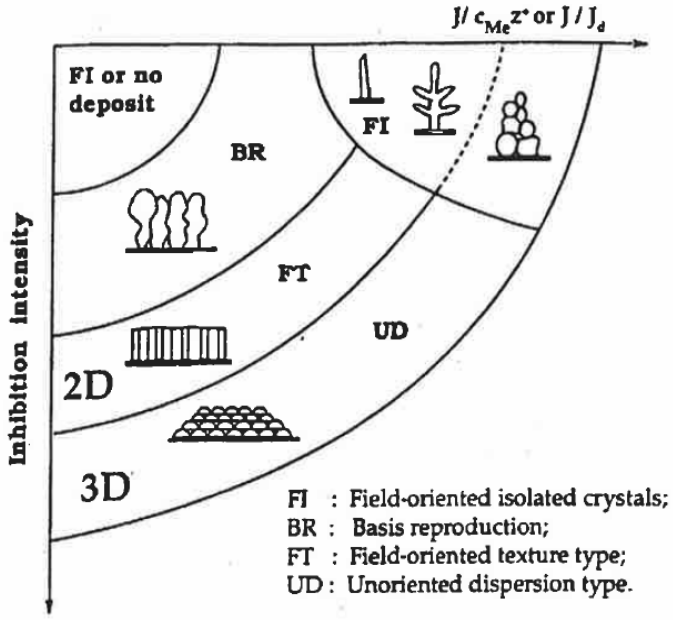

Figure 10: Basic types of polycrystalline deposition [17]

2.7 Summary of the literature review

The literature review shows that a number of important factors have to be considered in order to simulate the copper electrorefining process:

- The natural convection is caused by density changes created by the electrochemical reactions happening in the immediate vicinity of the electrodes.
- The main driving force for these electrochemical reactions can be found in the current density.
- The mass transport is accomplished mainly by diffusion and convection, a negligible small amount is caused by migration.
- The forced convection is caused by the recirculation of the electrolyte to keep the level of inpurities at bearable values.
- Leveling agents and inhibitors play a very important role on the quality of cathode copper. A main target should be to optimize the distribution of these inhibitors.

3 CFD Fundamentals

The common English term Computational Fluid Dynamics (CFD) is a collective term for numerical simulations of fluid mechanic problems by using a computer-based simulation. Since only for a few special cases the system of fluid mechanical balance equations can be solved analytically, the numerical approximation of fluid flow problems has a special significance in technical flow studies. Compared to costly experiments CFD resource demand is clearly favorable and also allows to provide every imaginable flow conditions.

The technical applications of computational fluid dynamics are almost unlimited – CFD calculations allow the investigation of physical phenomena of experimentally hardly accessible configurations (e.g. turbines, earth's atmosphere, micro-circuits, etc.). The RANS simulation is typically used in industrial applications and allows for an inexpensive and fast preliminary investigation, interpretation, optimization and validation of technical applications. The continuously increasing performance of computing systems in recent years allows not only for better flow forecast (e.g. higher mesh density), but also allows the increase in model detail (e.g. higher number of phases).

Any numerical flow simulation, whether performed with a commercial program including a graphical user interface or performed with an individual solver, includes at least three essential elements or steps: the preprocessor, the flow solver and the post-processor. While the preprocessing and processing steps are usually problem-specific, the actual numerical solution to the specific problem is general and only requires small modifications for adaptation to the question [24].

3.1 Spatial discretization

The absence of a general analytical solution for a system of partial differential equations requires the investigated flow configuration to be discretized by a numerical grid in a first step. The system of algebraic equations can then be converted, based on the discrete points in space and time. The main methods for the discretization of the continuous conservation equations are the finite difference method, the finite element method and the finite volume method.

Finite difference method: The finite difference method (FDM) is the oldest method for the numerical solution of partial differential equations and is associated to Leonhard Euler [25]. In the differential form of the conservation equations the necessary derivatives are replaced by difference quotients, based on the grid point values and their distances. The approximation and derivation of the difference quotients can be implemented using Taylor series expansion or polynomial methods. The resulting algebraic equations for each grid point contain the unknown field size in a number of neighboring grid points. A major drawback of FDM is the restriction to simple geometries because of the necessity of structured grids.

Finite Element Method: The finite element method (FEM) is based on the decomposition of the area into discrete, finite elements and the use of variational formulations for the unknown values. An important feature of the FEM is that the equations are multiplied by a weight function before they are integrated over the entire domain. In simple finite element methods the solution is approximated by a linear shape function within each element to guarantee continuity of the solution across element boundaries. The main advantage of the FEM is its basically unstructured system, allowing its application for arbitrary configurations. Since the matrices of the system of equations are also unstructured, it is difficult to find efficient solution methods [25].

Finite Volume Method: Due to the simple implementation and recognizable physical meaning of the individual terms, the finite volume method is the most used method in computational fluid dynamics. The process requires several approximation stages (interpolation, differentiation and integration) and is therefore more difficult for higher order methods as for example the FDM. However, when using the correct implementation a converging result and physically meaningful values can almost be guaranteed. For this reason the FVM was used in the present work.

In general consistency is common to all discretization methods, so that with decreasing grid spacing the discretization seeks towards the continuous equation. The stability of a method is ensured when errors cannot progressively increase during the simulation iterations and the solution doesn’t diverge. Other important criteria such as convergence, feasibility and accuracy are described in detail by Ferziger [25].

3.2 Generic transport equations

Based on the temporal change of an extensive quantity Φ, described by the intensive quantity ϕ in any volume V^*, a generic transport equation can be derived by using the Reynolds transport theorem and introducing a gradient diffusion approach [26]. This transport equation for ϕ describes the conservation properties of Φ and is representative of all conservation equations used in fluid mechanics. Equation 3-1 shows a generic transport equation in its typical form:

$$\frac{\partial \phi}{\partial t} + \frac{\partial (\phi u_j)}{\partial x_j} = \frac{1}{\rho} \frac{\partial}{\partial x_j} (J_\phi) + S_\phi \qquad \text{Eq. 3-1}$$

On the left side of the equation the terms of time change as well as convection are present, while on the right side the diffusive term and the source term of ϕ can be found. The non-uniformly representable terms in the conservation equations are summarized in this source term. By replacing ϕ by ρ, ρu_i or ρh and using corresponding diffusion coefficients Γ_ϕ and sources S_ϕ the fluid mechanical balance equations for mass, momentum and energy can be found. The differential form of the generic transport equation (equation 3-1) represents the starting point of the numerical discretization. Approaches, approximation techniques and derivations are applied directly to this differential equation and thus allow a uniform procedure for the numerical solution of various balance equations. Only the determination of the diffusion coefficient and the source term are different.

3.3 Finite-Volume-Method

As described above, in the finite volume method (FVM) the flow domain is discretized by a finite number of control volumes (CV). The resulting numerical grid represents the boundaries of the control volumes. The numerical grid can be distinguished into structured and unstructured grids as shown in Figure 11. Since the numerical results of this work have been created exclusively on structured numerical grids, the derivations of differential equations shown here are limited to structured grids.

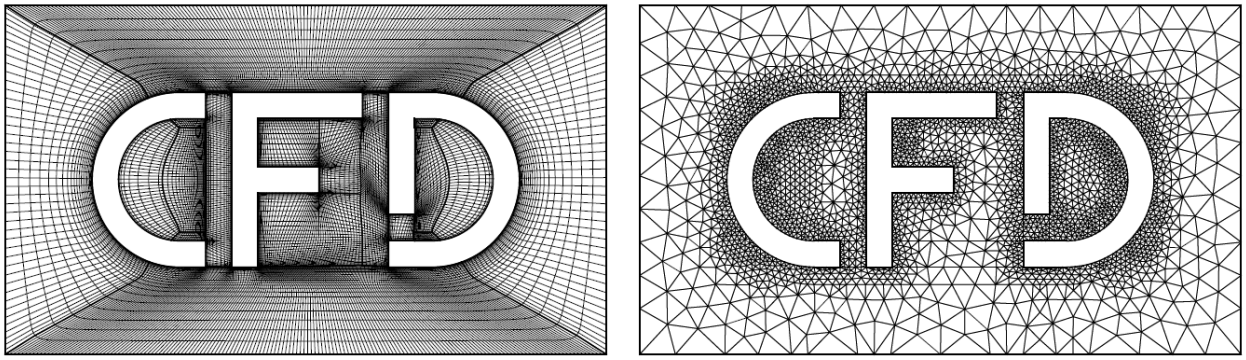

Figure 11: Structured (left) and unstructured (right) numerical grids [24]

For the deriving of the differential equations for each individual control volume typically the so-called compass notation is used. This means that the control volume centers adjacent to the central control volume center P are referred to as W, E, N, S, T, B and the individual faces of the control volumes are referred to as w, e, n, s, t, b, as shown in Figure 12. The figure also shows an example of an area vector of the control volume surface e denoted as A_i^e. During the discretization and simulation all values of the flow variables are stored in the geometric center P of the control volume [24].

The starting point of any discretization is to integrate the generic transport equation (equation 3-.1) over the control volume, so that there is an integral balance equation. In the course of the process the average value of each transport quantity ϕ in the respective control volume can be calculated with this integral balance equation. With the help of this integral form the various quantities of ϕ entering and leaving the control volume are balanced. Therefore it makes sense to convert individual terms in surface integrals using the Gauß integral form, equation 3-2:

$$\int \frac{\partial \phi}{\partial x_i} dV = \oint \phi \, dA_i \qquad \text{Eq. 3-2}$$

This transformation also allows an area-based treatment of the individual terms, so that the consistent determination of the flux at the interface between two control volumes is guaranteed. For the discretization mass-specific transport sizes are preferred, so that in addition to the intensive quantity ϕ, the density ρ is given [24].

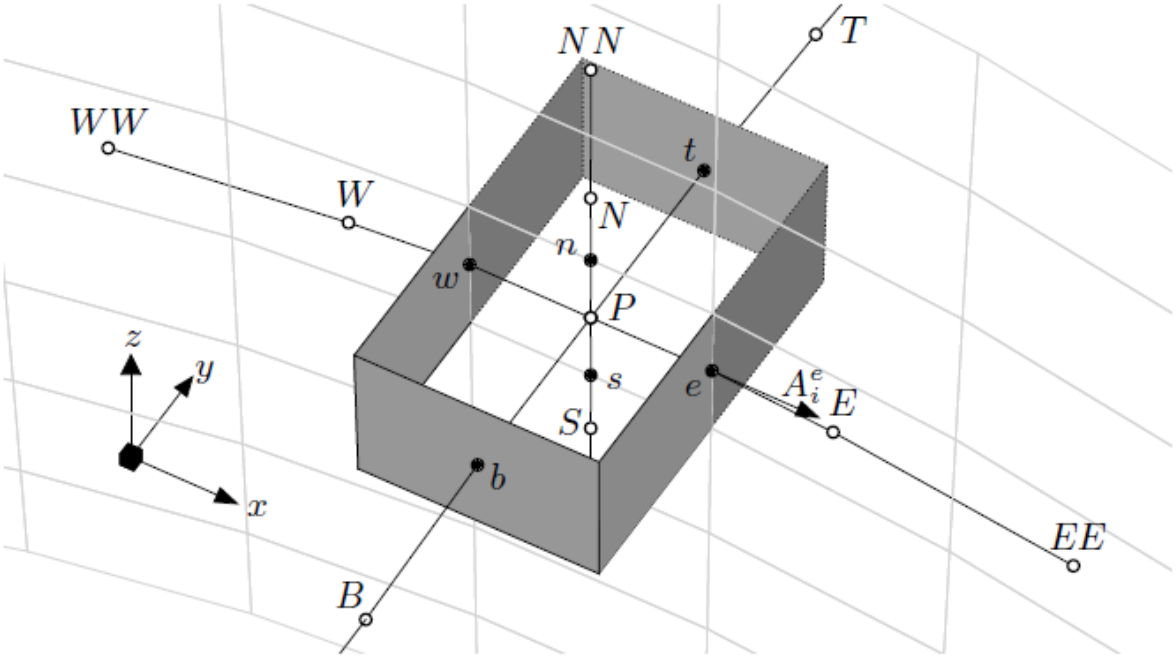

Figure 12: The compass notation used for an arbitrary control volume [24]

$$\int_V \frac{\partial \rho\phi}{\partial t} dV + \oint_A \rho\phi u_j dA_j = \oint_A \Gamma_\phi \frac{\partial \rho\phi}{\partial x_j} dA_j + \int_V S_\phi dV \qquad \text{Eq. 3-3}$$

3.4 Turbulent fluid flow

The turbulence of fluids combines a number of properties of the fluid moving above a critical Reynolds number. Three-dimensional turbulent flows are characterized by stochastically distributed and transient fluctuation of the fluid particles motion superimposed on the mean flow motion. Turbulence is caused by the laminar-turbulent transition where disturbances are introduced and can only be somewhat muted due to the flow state. The movement variations in the form of turbulence occur on almost all the time and speed scales of the flow, wherein the bandwidth is among other a function of the Reynolds number. Within this chaotic and turbulent fluid motion coherent structures of concentrated and phase-correlated vorticities can occur [27].

As a consequence of the fluctuation movements turbulent flows are characterized by a significantly higher diffusion compared to the molecular diffusion. Therefore high momentum, energy and mass transfers (mixing) are characteristic for turbulent flows. Additionally the viscosity of turbulent flows is apparently increased (turbulent viscosity). In technical applications of any kind turbulent flows are the rule, while laminar flow conditions, i.e. parent-

turbulent motions at low Reynolds numbers, are the exception. The properties of turbulent flows are responsible for increased flow resistance, energy losses, vibrations or noises. Due to the strong dependence of initial and boundary conditions, the turbulence structure is difficult to predict, even more so: it is not directly derivable from the initial and boundary conditions. Therefore general statistical variables must be used for the description of turbulence behavior.

3.4.1 Scales of turbulent motion

For any sort of calculation or quantification of turbulence, it is necessary to use as a starting point a conceptual model for turbulent flows. The foundation for the still valid description of turbulence structure and energy was laid down by Lewis Fry Richardson in the year 1922. His through observation and obtained correlations are referred to as turbulent energy cascade.

The energy cascade

Starting point of the considerations is a fully turbulent flow at a sufficiently high Reynolds number $Re = UL/\nu$ with the characteristic velocity U, the length scale L and the molecular viscosity ν of the fluid. As a first aspect it can be noted that the turbulence is composed of eddies of various size l with a characteristic velocity $u(l)$ and a time scale $\tau(l) = l/u(l)$. An eddy cannot be defined precisely but can be understood as a turbulent movement in a region of size l. The eddy is moderately coherent in its region, which can also include smaller eddies. The eddies with the largest dimensions are characterized by their length l_0 which is of the order of the length scale L, as well as their characteristic velocity $u_0 = u(l_0)$ which is in the order of magnitude of the root mean square (RMS) turbulence intensity $(2/3k)^{1/2}$ and comparable with the characteristic velocity U, with k being the turbulent kinetic energy quantified by the mean of the turbulence normal stresses, Equation 3-4.

$$k = \frac{1}{2}\left(\overline{(u_1')^2} + \overline{(u_2')^2} + \overline{(u_3')^2}\right) \qquad \text{Eq. 3-4}$$

Since the eddy Reynolds number $Re_0 = u_0 l_0/\nu$ is large (comparable to Re), viscous effects are negligible and the influence of internal friction is small compared to inertial forces [24].

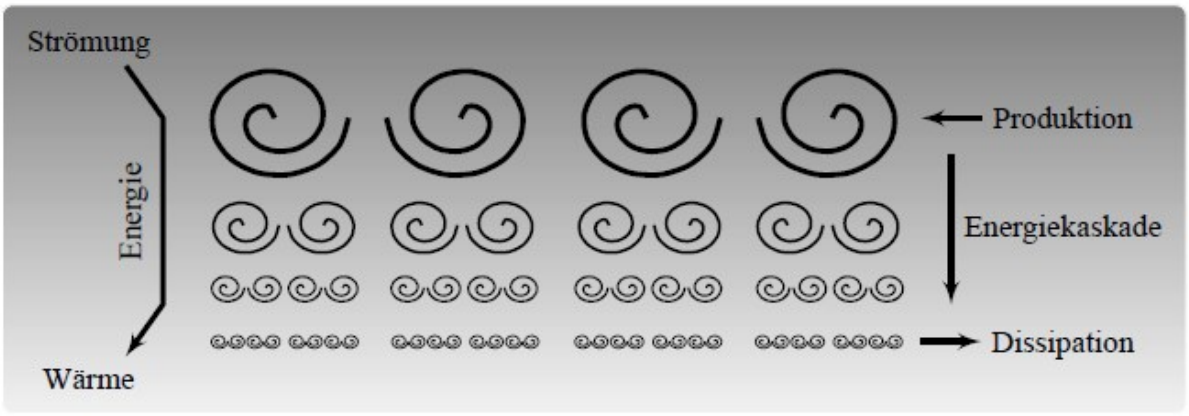

Figure 13: The energy cascade [24]

The second aspect in turbulent flows is the fact that large vortex structures (large eddies) are unstable and break up by transferring their energy to smaller and smaller eddies. These smaller eddies go through a similar process, and the energy transfer continuous to smaller and smaller scales. This energy cascade is continued until the eddie's Reynolds number $Re = UL/\nu$ is sufficiently small so that their movement is steady and energy is dissipated by molecular kinetic viscosity, as shown in Figure 13.

The most important conclusion from these considerations is that the dissipation can be found at the end of a series of energy-transfer processes. The rate of dissipation ε is therefore determined by the first process in the sequence, the transfer of energy from the largest scales. These scales or eddies have an energy level in the order of ${u_0}^2$ and a time scale $\tau_0 = l_0/u_0$ so the rate of energy transfer scales with ${u_0}^2/\tau_0 = {u_0}^3/l_0$. Observations in free shear flows confirm these considerations of energy cascade, and show that the dissipation rate ε scales independent from ν (for large Reynolds numbers) with ${u_0}^3/l$ [28].

3.4.2 Energy dissipation

The formulation of turbulent length, time and velocity measurements is not possible using the energy dissipation rate ε only. For an eddy with an initial size l the time and velocity scales can be formed by ε and the length scale l.

$$u(l) = \varepsilon^{\frac{1}{3}} l^{\frac{1}{3}} = u_\eta \left(\frac{l}{\eta}\right)^{\frac{1}{3}} \qquad \text{Eq. 3-5}$$

$$\tau(l) = \varepsilon^{-\frac{1}{3}} l^{\frac{2}{3}} = \tau_\eta \left(\frac{l}{\eta}\right)^{\frac{2}{3}} \quad \text{Eq. 3-6}$$

Whereby η is the uniform length, u_η the uniform velocity and τ_η the uniform time scale.

$$\eta = \varepsilon^{-\frac{1}{4}} \nu^{\frac{2}{3}} \qquad u_\eta = \varepsilon^{\frac{1}{4}} \nu^{\frac{1}{4}} \qquad \tau_\eta = \varepsilon^{\frac{1}{4}} \nu^{\frac{1}{4}} \quad \text{Eq. 3-7}$$

It is apparent that the characteristic velocity- and time scales are proportional with the initial eddie size l. The energy transfer rate from larger eddies to smaller eddies is according to the order of $u(l)/\tau(l)$. With the scale relations (equation 3-5 and equation 3-6) this scaling leads directly to the energy dissipation rate ε [28].

$$u(l)/\tau(l) = \varepsilon \quad \text{Eq. 3-8}$$

3.4.3 Energy transfer

In turbulent flows, vortex structures exist over a wide band of length and time scales. The global flow includes overlaying rotating coherent eddies of different size and durability. The extent of the largest eddies is limited by the geometry of the flow area. All of these structures result in fluctuations of the state variables. These large structures are driven and stretched, so inherently the main flow kinetic energy is extracted by the shear layers of the global flow. The large eddies decay by vortex filament-stretching into smaller vortices which pass on their energy to smaller and smaller eddies until the energy is dissipated by the action of viscous forces in the smallest eddies.

The vortex filament stretching is one of the most important mechanisms in turbulent flows because the transfer of turbulent kinetic energy is based on it. An important property of turbulent flows is the vorticity. It can be described by the rotation of the velocity field (equation 3-8).

$$\omega_i = \frac{\partial}{\partial x_j} \varepsilon_{ijk} u_k \quad \text{Eq. 3-9}$$

Here ε_{ijk} is the Levi-Civita symbol. By applying rotation on the incompressible momentum equation (equation 3-13) the laminar vorticity transport equation can be found. Its intensive magnitude is the vortex strength and it can be used for defining the vortex filament stretching.

$$\frac{D\omega_i}{Dt} := \frac{\partial \omega_i}{\partial t} + u_j \frac{\partial \omega_i}{\partial x_j} = \omega_j \frac{\partial u_i}{\partial x_j} + \nu \frac{\partial^2 \omega_i}{\partial x_k^2} \qquad \text{Eq. 3-10}$$

The two terms on the left-hand side of equation 3-9 represent the time evolution of the vorticity and transport with the main flow while the right side is divided into a vortex stretching term and the viscous dissipation [29].

If an existing shear or stretching flow is parallel and directed in the same direction as the vortex strength, the term $\omega_j \frac{\partial u_i}{\partial x_j}$ is positive and reinforces the vorticity $\frac{D\omega_i}{Dt}$. The vorticity increases and thus the viscous term is large enough to compensate for the gain [24]. However, since the viscosity ν with respect to the inertia is negligible, this leads to an ever-increasing vorticity or rotation speed. Due to conservation of angular momentum ωA = const. the cross-sectional area A of the vortex filament must therefore be reduced. This context is the basis of energy transfer from the large to the small scales by inviscid vortex stretching into the region of dissipation [30].

3.5 Mathematic description of turbulent flows

For the complete description of a single-phase flow field, the three cartesian velocity components u_i and the thermodynamic state variables pressure p and temperature T as a function of location x_i and time t must be known. The material parameters of the fluid: the dynamic viscosity μ and density ρ complete the description. The continuum mechanical balance equations of mass and momentum describe the relationship between the flow- and the material quantities. These equations are named after Claude Louis Marie Henri Navier and Georg Gabriel Stokes Navier-Stokes equations and are the basis for the calculation of flows.

Mass $$\frac{\partial}{\partial t}\rho + \frac{\partial}{\partial x_j}(\rho u_j) = 0 \qquad \text{Eq. 3-11}$$

Momentum $$\frac{\partial}{\partial t}(\rho u_j) + \frac{\partial}{\partial x_j}(\rho u_j u_i - \tau_{ij}) = \rho g_i + f_i \qquad \text{Eq. 3-12}$$

The additionally occurring, previously not designated quantities in equation 3-10 and equation 3-11 are: the stress tensor τ_{ij}, the gravitational vector g_i, and other body forces f_i (e.g. Buoyancy forces).

Due to the mathematical properties of this coupled system of equations (nonlinearity, coupling, heterogeneity, etc.) analytical solutions are available only for idealized special cases or simplifications, as shown in Figure 14. None of these simplifications are suitable for the complexity of a wall-bound turbulent flow.

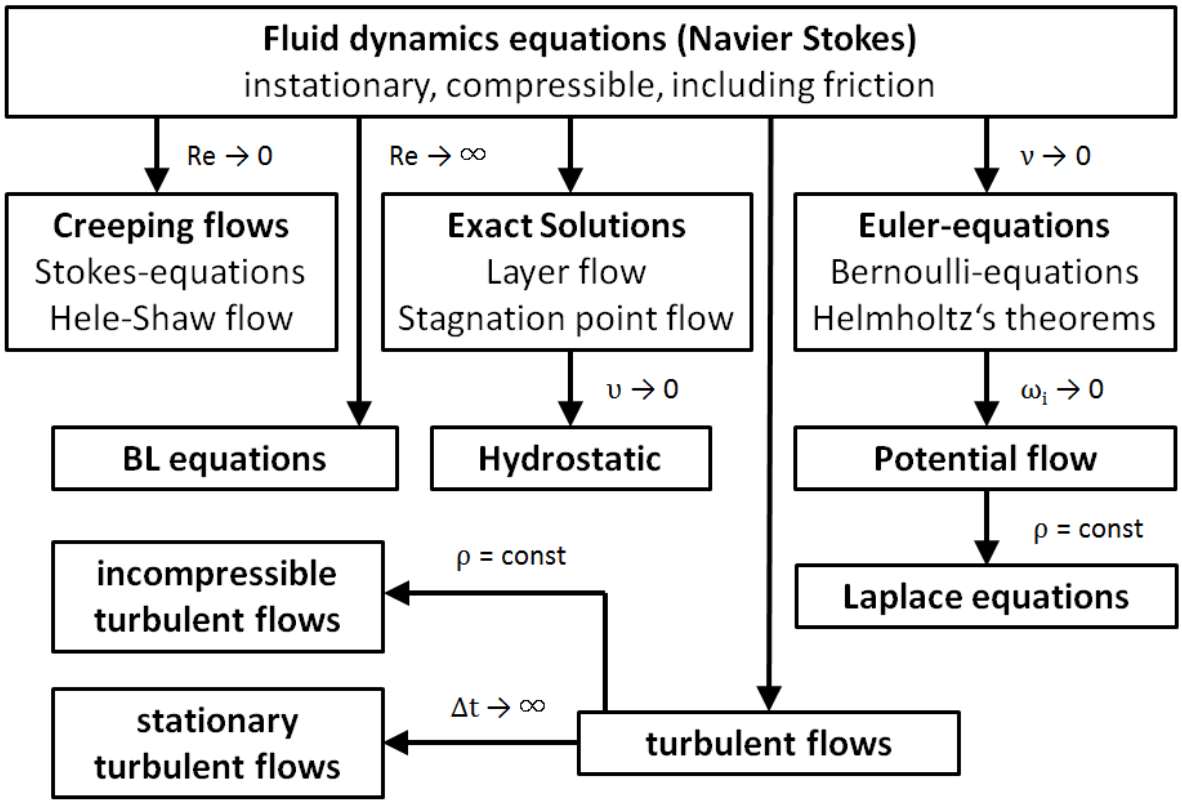

Figure 14: Cases of fluid flow and special cases [24]

A few influencing factors in equations 3-10 and 3-11 may be neglected depending on the investigated flow configuration. When calculating incompressible flows with small Mach numbers (Ma <0.3) and neglecting thermal effects, a new, reduced system of equations (equation 3-12 and equation 3-13) can be used.

Mass $$\frac{\partial}{\partial x_j} u_j = 0$$ Eq. 3-13

Momentum $$\frac{\partial}{\partial t} u_i + \frac{\partial}{\partial x_j}\left(u_j u_i - \frac{\tau_{ij}}{\rho}\right) = 0$$ Eq. 3-14

To complete the equations the unknown stress tensor τ_{ij} must be defined. This consists of the pressure component p as principal stress and the friction tensor for newtonic fluids. The derivation of the stress tensor is discussed in detail in [28].

$$\tau_{ij} = -p\delta_{ij} - \frac{2}{3}\mu S_{kk}\delta_{ij} + 2\mu S_{ij} = -p\delta_{ij} + 2\mu\left(S_{ij} - \frac{1}{3}S_{kk}\delta_{ij}\right) \quad \text{Eq. 3-15}$$

$$S_{ij} = \frac{1}{2}\left(\frac{\partial u_i}{\partial x_j} + \frac{\partial u_j}{\partial x_i}\right) \quad \text{Eq. 3-16}$$

$$\tau_{ij} = -\left(p + \frac{2}{3}\mu\frac{\partial u_k}{\partial x_k}\right)\delta_{ij} + \mu\left(\frac{\partial u_i}{\partial x_j} + \frac{\partial u_j}{\partial x_i}\right) \quad \text{Eq. 3-17}$$

The symmetric stress tensor can be split as in equation 3-14 can be seen in a spherical tensor and a symmetric deviator. In addition, an analog division into a shape-sustaining volume change (dilatation) and volume-maintaining shape change (distortion) is possible, equation 3-16. In the manner of understanding not only of the individual units also an analogue is strengthened, but created, which is taken up later in the turbulence modeling.
For the case of incompressible flows the stress tensor can be simplified due to the mass balance (equation 3-12), so that the incompressible momentum balance equations after inserting the stress tensor reveal their complete mathematical character, equation 3-17.

$$\frac{\partial}{\partial t}u_i + u_j\frac{\partial u_i}{\partial x_j} = -\frac{1}{\rho}\frac{\partial p}{\partial x_i} + \frac{\partial}{\partial x_j}\left[\nu\left(\frac{\partial u_i}{\partial x_j} + \frac{\partial u_j}{\partial x_i}\right)\right] \quad \text{Eq. 3-18}$$

Using the mass balance (equation 3-12) and the product rule, the convective term can be easily reformulated. In addition, for the case of location-independent viscosity ν the gradient in the diffusion term can be summarized by using the mass balance.

$$\frac{\partial}{\partial t}u_i + \frac{\partial u_i u_j}{\partial x_j} = -\frac{1}{\rho}\frac{\partial p}{\partial x_i} + \nu\frac{\partial^2 u_i}{\partial x^2{}_j} \quad \text{Eq. 3-19}$$

The simplifications for incompressible flows allow no general analytical solution of the coupled system of equations, so that must be avoided on numerical solution methods [24].

3.6 Reynolds averaged Navier Stokes

For the quantitative description of turbulent flows usually some kind statistics are used due to the stochastic character. This is particularly evident when considering turbulence quantities. In particular, for technical applications is often only the statistical average of a flow of interest instead of their full transient behavior. It therefore seems natural to use numerical method,

based on a statistical description of the flow field quantities.

The decomposition of the flow variables ϕ in an average $\overline{\phi}$ and a fluctuation component ϕ' goes back to Reynolds. For the incompressible case, this decomposition corresponds to the relations.

$\phi = \overline{\phi} + \phi'$ Incompressible: $u_i = \overline{u_i} + u_i'$ $p = \overline{p} + p'$

The average ϕ of a point x_i at time t is generally defined by an ensemble averaging over N instantaneous measurements [24].

$$\overline{\phi}(x_i, t) = \frac{1}{N}\sum_{i=1}^{N} \phi(x_i, t) \qquad \text{Eq. 3-20}$$

Inserting the size separation for the velocities u_i and the pressure p in the incompressible Navier-Stokes equations (3-12) and (3-18), followed by time averaging leads to the incompressible form of the so-called Reynolds-averaged-Navier-Stokes equations (RANS).

$$\frac{\partial \overline{u_j}}{\partial x_j} = 0 \qquad \text{Eq. 3-21}$$

$$\frac{\partial \overline{u_i}}{\partial t} + \frac{\partial \overline{u_i u_j}}{\partial x_j} = \frac{1}{\rho}\frac{\partial \overline{p}}{\partial x_i} + \nu \frac{\partial^2 \overline{u_i}}{\partial x^2{}_j} - \frac{\partial \overline{u'_i u'_j}}{\partial x_j} \qquad \text{Eq. 3-22}$$

The turbulence-induced additional term has a diffusive character and describes the turbulent momentum transport by the variation of movements analogous to the molecule-induced momentum transport in the diffusive term (spatial gradient of the stress tensor). The speed correlation $\overline{u'_i u'_j}$ multiplied with density is also known as Reynolds stress tensor ${\tau_{ij}}^{turb} = -\rho\overline{u'_i u'_j}$ [31]. In a fully turbulent flow the Reynolds stress tensor is far greater than the molecular stress tensor ${\tau_{ij}}^{turb} \gg \tau_{ij}$. This stress tensor is symmetric and leads (even if only as a spatial gradient) to six new unknowns in the momentum equations.

3.6.1 Closure problem

The non-linearity of the momentum equations leads to statistical moments of the second order in the form of the symmetrical Reynolds stress tensor. To describe the three unknown velocities, pressure, as well as the six new unknowns only the mass balance and three

momentum equations are available. To solve the flow problem additional equations must be provided or a turbulence model must be established. This is generally known as the closure problem in turbulent flows.

To close the entire system, the Reynolds stresses must be replaced in the momentum equations by a model. This usually happens with so-called eddy viscosity models or Reynolds-stress models. Another possibility is the determination of the statistical moments from the transport equations that are then to close again by a suitable model [24].

3.6.2 Eddy viscosity modeling

The task of a turbulence model for the Reynolds-averaged equation is to model the influence of the averaged turbulent fluctuating motions to the mean flow. The most common approach is based on the observation that turbulent flows are subject to increased diffusion or have a seemingly strong increase in viscosity. The introduction of a turbulent viscosity or eddy viscosity μ_t leads to the eddy viscosity modeling. In analogy to the molecular stresses according to equation 3-14, an approach is chosen that uses a shear proportional to turbulence by using the Boussinesq hypothesis [32].

$$-\rho\overline{u'_i u'_j} \sim \mu_t \frac{\partial u_i}{\partial x_j} \quad \text{or} \quad \overline{u'_i u'_j} \sim -\nu_t \frac{\partial u_i}{\partial x_j} \quad \text{for} \quad \nu_t = \mu_t/\rho \qquad \text{Eq. 3-23}$$

The fundamental properties of the Reynolds stress tensor is the symmetry of the tensor and the so-called contraction condition. This condition is based on the definition of the turbulent kinetic energy k according to $k = \frac{1}{2}\overline{\acute{u}_i^2}$.

$$\text{Contraction: } \overline{u'_i u'_j} = 2k \qquad \text{Symmetry: } \overline{u'_i u'_j} = \overline{u'_j u'_i} \qquad \text{Eq. 3-24}$$

In the general case, the eddy viscosity can be described as a tensor of fourth order for the description of anisotropic turbulence properties, but it is sufficient for most models to use a scalar and isotropic eddy viscosity. In particular the model of contraction and symmetry requires a scalar and isotropic eddy viscosity. Since the velocity gradient tensor $\frac{\partial u_i}{\partial x_j}$ is generally unbalanced the rotational flow components, due to the symmetry of the Reynolds stresses, limits the modeling to the stress tensor S_{ij}, representing only the symmetric part of the velocity gradient.

$$-\rho\overline{u'_i u'_j} \approx 2\mu_t S_{ij} \quad \text{or} \quad \overline{u'_i u'_j} \approx 2\nu_t S_{ij} \quad \text{with} \quad S_{ij} = \frac{1}{2}\left(\frac{\partial u_i}{\partial x_j} + \frac{\partial u_j}{\partial x_i}\right) \qquad \text{Eq. 3-25}$$

The contraction condition is eliminated from the stress tensor and treated separately. By splitting off this portion the stress tensor can now be separated in a spherically symmetric and deviatory part. The spherical portion is then modeled separately by means of the kinetic energy k, so that the turbulent intensity can be treated separately in the form of a turbulence energy and the turbulence structure, equation 3-25 [24].

$$\begin{aligned} -\rho\overline{u'_i u'_j} &= 2\mu_t\left(S_{ij} - \frac{1}{3}S_{kk}\delta_{ij} + \frac{1}{3}S_{kk}\delta_{ij}\right) \\ {\tau_{ij}}^{turb} &\cong -\frac{2}{3}k\rho\delta_{ij} + 2\mu_t\left(S_{ij} - \frac{1}{3}S_{kk}\delta_{ij}\right) \end{aligned} \qquad \text{Eq. 3-26}$$

The analogy between the eddy viscosity model for the Reynolds stress tensor (equation 3-25) and the molecular stress tensor of Newtonian fluids (equation 3-14) it is clear at this point. The isotropic part of the spherical tensor case has a similar effect as the pressure and is therefore treated numerically together with the pressure as: $\bar{P} = \overline{p} + 2/3\,k\rho$. For the case of incompressible flows the stress tensor is always traceless due to mass balance and the kinematic eddy viscosity is treated as $\nu_t = \mu_t/\rho$.
Inserting the linear eddy viscosity approach (equation 3-25) in the incompressible Reynolds-averaged equations (equation 3-21) shows the operation of this modeling.

$$\frac{\partial\overline{u_i}}{\partial t} + \frac{\partial\overline{u_i u_j}}{\partial x_j} = \frac{1}{\rho}\frac{\partial\overline{P}}{\partial x_i} + \frac{\partial}{\partial x_j}\left[(\nu + \nu_t)\frac{\partial\overline{u_i}}{\partial x_j}\right] \qquad \text{Eq. 3-27}$$

The closure problem of the RANS equations has now been shifted to the definition of the eddy viscosity. Depending on the type of closure approach these turbulence models are distinguished between algebraic models and transport equation models. The transport equation model can be further distinguished into one or two-equation models. With the help of dimensional analysis for eddy viscosity ν_t it can be determined that eddy viscosity can be described by the characteristic velocity U_c dimensions, the measures of length L_c or the time dimensions Γ_c.

$$\nu_t \sim U_c L_c \sim U_c^2 \Gamma_c \sim L_c^2/\Gamma_c \qquad \text{Eq. 3-28}$$

The definition of these characteristic properties of turbulence determines which parameters for the calculation of μ_t or ν_t are used and which model class is present. In the algebraic or

zero equation models an explicit calculation rule is used for μ_t or ν_t or the two characteristic values are defined algebraically [24]. The class of single equation is characterized by the fact that exactly one additional transport equation is to be solved and usually a more algebraic closure assumption is necessary. For example: a transport equation for the turbulence energy k can be formulated as U_c^2 together with algebraic calculation of L_c or Γ_c.

In the two-equation models the description of intensity and structure of the turbulence is each formulated by an additional transport equation. In general, the turbulent kinetic energy k is used for the intensity. The second parameter generally results from the modeling approach and the dimensional analysis and the different standard models. Among other approaches, particularly established are those models based on the dissipation rate ϵ or the specific dissipation rate ω, namely the $k-\epsilon$ model and the $k-\omega$ model. An overview of the mainly used models, the model constants and their calibration of reference test cases as well as the conversion of individual models into one another can be found in [33]. Table 6 shows the standard two-equation models.

Table 6: Standard two-equation turbulence models [33]

Model	U_c^2	Γ_c	$\nu_t = c_\mu U_c^2 \Gamma_c$	Reference
$k-\epsilon$	k	$\frac{k}{\epsilon}$	$c_\mu \frac{k^2}{\epsilon}$	Jones & Launder
$k-\omega$	k	$\frac{1}{c_\mu \omega}$	$\frac{k}{\omega}$	Wilcox
$k-\tau$	k	τ	$c_\mu k\, \tau$	Speziale et al
$k-l$	k	$\frac{l}{c_\mu \sqrt{k}}$	$\sqrt{kl}$	Rotta

The modeling of the additional transport equations is not shown here, since it is not relevant to the current work.

4 Electrolysis models

4.1 Electrolysis simulations

A number of papers can be found regarding the simulation of copper electrolysis cells. The simulation of copper winning electrolysis is a special topic since it involves the simulation of gas induced convection. The papers aimed at copper refining electrolysis can be classified into three groups: simulation of small scale 2D processes in the anode cathode gap, simulation of technical scale cells and the simulation of large scale industrial used cells.

In the literature, various methods have been introduced to experimentally determine the boundary layer thickness (hydrodynamic and concentration boundary layer) in copper electrolysis cells. For example with the aid of porous hollow electrodes [34], interferometric investigations [35, 36], investigations using optical recordings, auto radiographic studies with miniature probes, using temperature measurements [37], filming of dispersed particles [38] and using the LDA technique [39-45].

Numerical simulation methods have been introduces by a number of researchers, including [43, 44 and 46]:

Ziegler and Evans [43, 44] compared computational fluid dynamics calculations with their own experimentally measured values for cadmium electrolysis without forced convection. Lackner [45] developed a model for the numerical flow simulation using the copper refining electrolysis. They modelled the interaction of forced convection (caused by electrolyte circulation) and natural convection which occurs at the electrodes (caused by density differences). The influence of the design of the inlet and outlet of the electrolysis cell and other parameters (flow rate, influence of the turbulence) on the electrolyte flow patterns was also investigated. Finally the inhibitor distribution and behavior of the anode slime was calculated and discussed. Furthermore, a substantially improved calculation model was discussed and approaches to further developments were investigated.

The literature review of Lackner [46] showed that only Starzinsky [37, 47] and Simon [42] performed flow studies of industrial sized electrolysis cells with forced convection. In order to compare the results with data from the literature, Lackner performed his numerical calculations on the experimental cell used by Starzinsky (dimensions: 0.35 x 0.21 x 0.25 m, three anodes and four cathodes).

In almost all the electrolytic cells is the inflow of fresh electrolyte happens through an inlet at the bottom, while the spent, somewhat warmer, electrolyte is withdrawn at the bath surface. Advantages and disadvantages of the inlet and outlet height and its effect on the electrolyte are discussed by Starzinsky [47]. The main disadvantage when electrolyte is withdrawn at the cell bottom is the formation of different concentration layers in the cell. This should be avoided.

A detailed summary of the different concepts of various parallel flow cells can be found in [48]. Basically the different parallel electrolysis cells can be divided in the ones with group wise electrolyte supply (i.e. Balchás cells and its developments) and the ones with separate electrolyte supply (Andersen and Archipov cells [49]).

4.2 Simulation model by Ziegler

Ziegler [44] calculated the flow profile of a refining and electrowinning electrolysis cell (without forced convection) using the two-dimensional calculation program TEACH.
He used a, for today's standards, very coarse computational grid of 22 x 22 cells. The calculated electrolysis section was 80.5 cm by 4.25 cm, leading to a grid density of 1.4 cells/cm^2. By comparison, the present study uses a nonlinear grid with a maximum density near the electrodes of 100 cells/cm^2. In order to check the calculated results laser Doppler anemometry (LDA) measurements were carried out on a cadmium electrolysis at 100 A/m^2. The cadmium electrolysis was chosen because the used laser was too weak for a copper electrolyte. The experimental cell had a height of 94 cm, a depth of 12.5 cm and variable electrode spacing from 2.4 to 4.25 cm.

Due to numerical stability problems no stable and convergent solutions were obtained. The main focus of the work aimed on the mathematical description of the near-electrode processes and different turbulence models ($k-\epsilon$ turbulence model, algebraic turbulence model and a one-equation turbulence models). However, Ziegler received even when using the $k-l$ turbulence model - in his opinion the best option - only limited similarities between calculation and measurements. This can probably be explained by the outdated software.

4.3 Simulation model by Lackner

The model of a copper refining electrolysis used by Lackner [46] takes the change in density in the vicinity of the electrodes into account. Here, the density is reduced in the boundary layer in front of the cathode and increased in front of the anode (see Figure 15). The layer thickness and the density profile and concentration profile depend on the electrolysis conditions and will change over the electrode height. As a first step towards the simulation of the entire flow field in electrolysis cells a constant density was assumed in a bulk layer near the electrodes. Lackner made the assumption that the different densities in the vicinity of the cathode and anode by the same amount from the average density of the bath electrolyte. The change in density was calculated according to the measured concentration profiles by Schab [11, 50] and using the density concentration correlation by Jaskula [51] or Davenport [52].

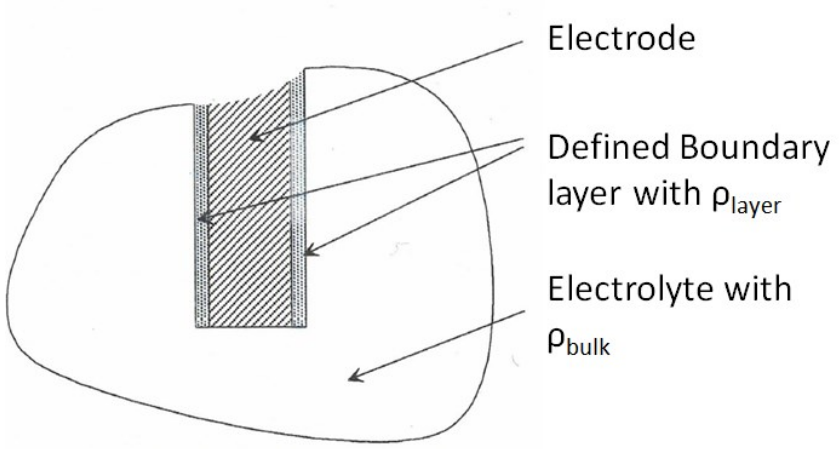

Figure 15: Electrolysis model by Lackner [46]

The layer thickness was varied in the range from 0.24 to 0.97 mm and the influence of the turbulence in the hydrodynamic boundary layer was investigated by using the $k-\epsilon$ turbulence model that assumes isotropic local turbulence. In the hydrodynamic boundary layer influential parameters such as diffusion coefficient, laminar viscosity and density over the electrode height were disregarded. The simulated cell geometries by Lackner are shown in Figure 16.

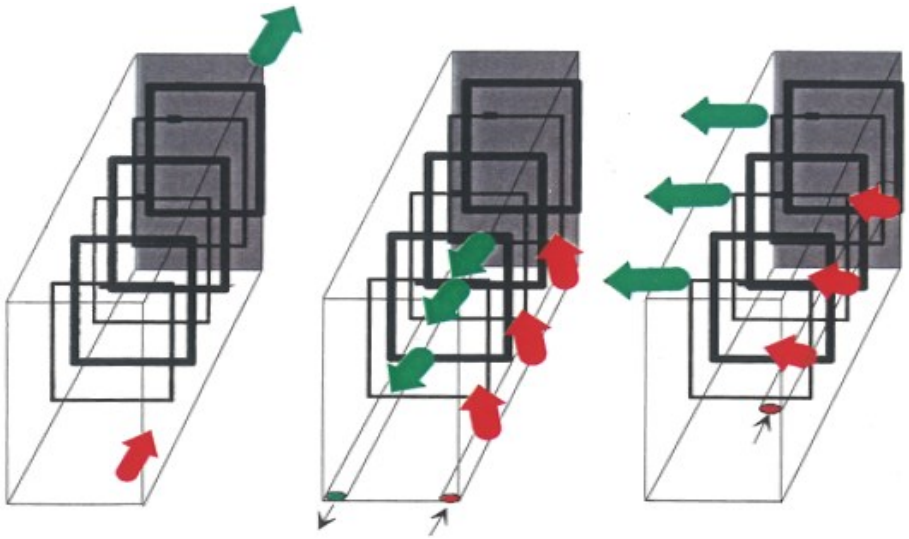

Figure 16: Schematic representations of different cell types simulated by Lackner [46]: conventional cell design (left); cell design by Andersen (center); modified Balchas cell design (right)

Figure 17 shows a vertical section through a conventional cross flow electrolysis cell with purely natural convection (without forced circulation of the electrolyte) caused by the density differences at the electrode surfaces. As can be seen in the figure the specific heavier electrolyte in the anodic boundary layer sinks to the bath floor and the specific lighter electrolyte in the cathodic boundary layer rises to the bath surface.

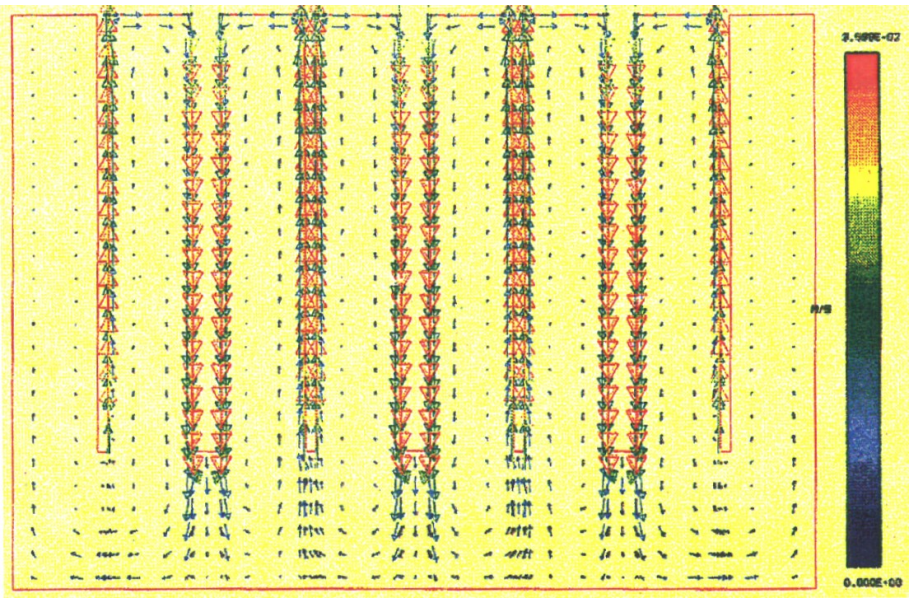

Figure 17: Vertical section through cross flow electrolysis cell; v_{max} = 3.5 cm/s; no forced convection [46]

Lackner found the maximum flow velocity in the hydrodynamic boundary layer at the electrodes to be 2 to 3.5 cm/s. At the electrodes the electrolyte moved more than ten times faster as in the rest of the cell. Lackner assumed the absolute velocity maxima as too large and declared the considered density differences were set too high in the boundary layers but points out that the quality of the overall electrolyte flow is in very good agreement with the literature data. Lackner also introduced an equation for the maximum speed as a function of the electrode height according to his calculated velocity profiles, as shown in Equation 4-1.

$$v_{max} = 2.36 - 0.08 \cdot h^{0,84} \qquad \text{Eq. 4-1}$$

Ibl [35] and Awakura [38] found a proportion of maximum speed v_{max} in the hydrodynamic boundary layer with the 0.6^{th} power proportional to the electrode height, as shown in chapter 2.5.

In the investigation of the influence of forced convection on the total flow Lackner found that even a thirty-fold bath change per hour (equivalent to a 100-fold increase in the conventional bath changes) results in no major improvement in the flow between the electrodes, however, at already three bath changes per hour a swirling of bottom layer was found. This swirling is extremely disturbing with respect to the anode slime. Lackner concludes, like Schab [48] and Ibl [7] that to increase the limiting current density by reducing the thickness of the diffusion boundary layer a modified electrolyte inlet and outlet construction or completely different cell geometry is required.

The investigation of the thickness of the near-electrode boundary layer with altered densities as well as the variation of densities in the near-electrode boundary layer showed a strong dependence of the absolute velocity values. The qualitative overall flow pattern however was hardly affected. This made sure that for a macroscopic observation of current in electrolysis cells the used simplifications allowed to compare different electrolyte inlet and outlet constructions. The same applies for the investigation of turbulence. The difference between a mathematical laminar simulation and a simulation performed with the aid of a turbulence model was only important in the vicinity of the electrodes of importance. Here, a 20 % lower speed was found when using a turbulence model, but only 4 mm away from the respective electrode, the difference in the absolute values drops to less than 3 %.

The above described studies were carried out on the cell model with a conventional crosswise flow principle. The comparison of the different cell geometries (see Figure 16) revealed that the first parallel flow cell (by Andersen et al [49]) causes no significant

advantage in terms of enhanced mass transfer. Better results could be achieved with the so-called modified Balachas cell type. In this version multiple electrolyte inlets are arranged in the middle of the bottom edge of the anode. The electrolyte outlet is positioned at the bath surface along the side walls. Therefore, the flow is intensified in the electrode space and there is an optimal inhibitors distribution over the entire cathode surface (see Figure 18 and Figure 19).

To study the different inhibitor distribution in the various electrolytic cells, Lackner [46, 53] added a transport equation for the mixture fraction, as a boundary condition the fraction was set to "100 %" or “1” at the electrolyte inlet. The transport equation was solved simultaneously with the other conservation equations for impulse, turbulent kinetic energy and dissipation rate. The result is the concentration distribution of the added inhibitor in the tankhouse cell and allows for an assessment of the resulting efficiency of the supplied inhibitor. Lackner points out that this method of calculation of the concentration distribution neglects the decomposition of the inhibitor, however when comparing the 3 cell types relatively short after addition of the inhibitors (eight and a half minutes) the decomposition can be neglected.

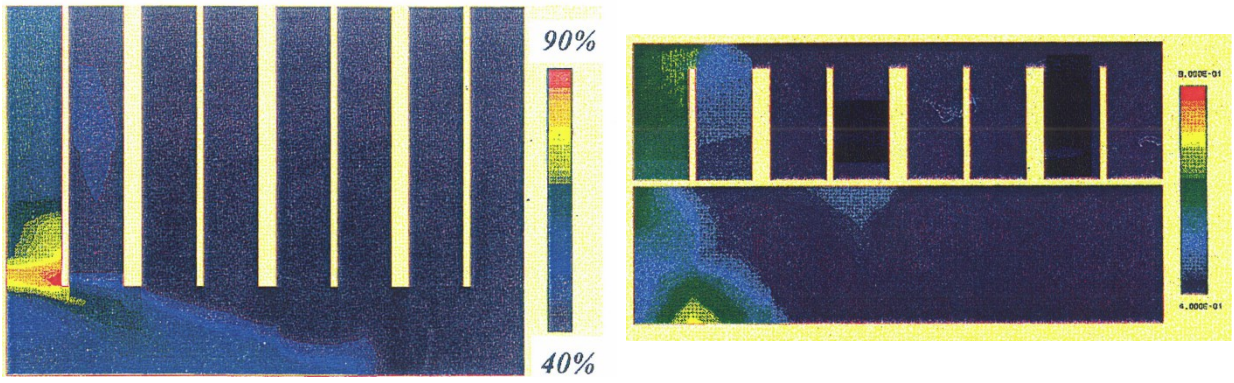

Figure 18: Inhibitor distribution in a conventional cross flow electrolysis cell: vertical cut (left), horizontal cut at bath level (right top) and underneath electrodes (right bottom) [46]

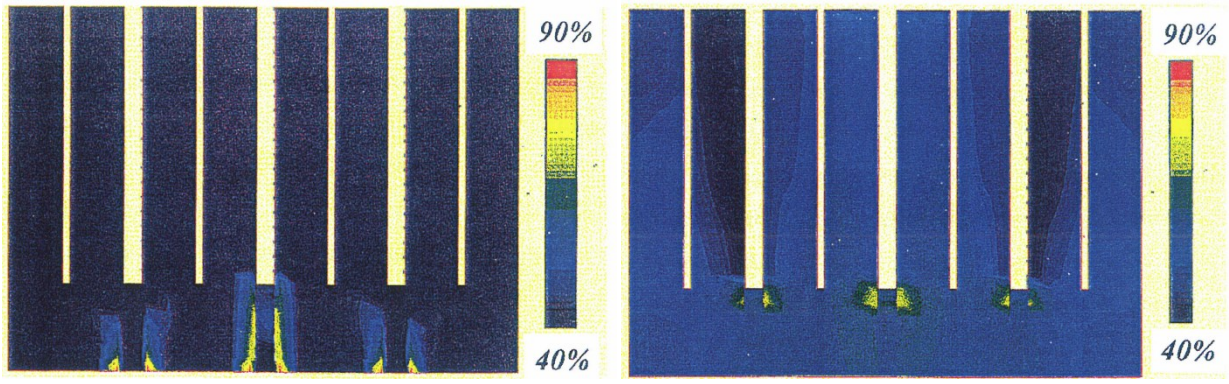

Figure 19: Inhibitor distribution in an Andersen cell type (left) and Balachas cell type (right) [46]

In addition to general observation of the flow and the distribution of inhibitors Lackner [46] also performed a calculation of the motion of the anode slime:

The chemical composition of the anodes and the chemical and electrochemical processes in the near-anode space determine the chemical composition and morphology of the resulting anode slime in the electrolysis cell. This can affect both the dissolution and passivation of the anodes and the desired refining effect. The dispersion of anode slime in the electrolyte can lead to heavy pollution of cathode copper by cataphoretic transition or mechanical installation in case of unfavorable flow conditions. Anode slime particle sizes and chemical compositions, which also determine the density, are responsible factors for the accumulation of anode slime in the electrolyte and the incorporation into the cathode. The anode slime typically consists of selenides and tellurides of copper, silver as well as sulfates, arsenates and complex oxide phases of other metals. Often traces of metallic silver and gold and metallic copper can also be found. The chemical composition and phase distribution of the anode slime depends largely on the quality of the anode material [46].

The flow field in the electrolysis cell determines the behavior of the formed anode slime during the electrolysis. A portion of the anode slime adheres to the anodes, while the main portion sinks to the bottom. Coarse particles and agglomerates > 5 - 10 µm tend to sink on the cell floor. Colloidal particles such as e.g. silver / silver compounds (< 1 µm) may well migrate to the cathode, where they are incorporated mechanically into the cathode copper. The collection of the anode slime at the bottom of the cell – the current industrial practice - on the one hand ensures a good output of precious metals and on the other hand prevents anode slime from polluting the cathode surface [54-57].

As a first estimation Lackner [46] calculated the trajectory of a massless anode slime particles by integrating over the three-dimensional velocity field calculated after $v_i=(dx_i/dt)$. This allows the estimation of the particular behavior of very small colloidal particles.

Figure 20 shows the particle tracks of anode slime particles released at half electrode height in a conventional cross flow electrolysis cell with 0.3 and 10 bath changes per hour. For the 0.3 bath changes per hour the particle tracks follow the anode flow downward until it reaches to lower electrode edge. The anode slime particles then move back into the electrode gap and end up at the opposite cathode side. Of course this estimation does not include the mass and therefore gravity acting on the anode slime, but it shows how easy the slime particles can reach the cathodes. At a higher bath changes per hour the flow in the region under the electrodes is greatly intensified. For a bath change number of 10, the anode slime

particles first follow the downward anode flow but as soon as they enter the area underneath the electrodes they are kicked up by the strong ground flow and move randomly through the entire cell.

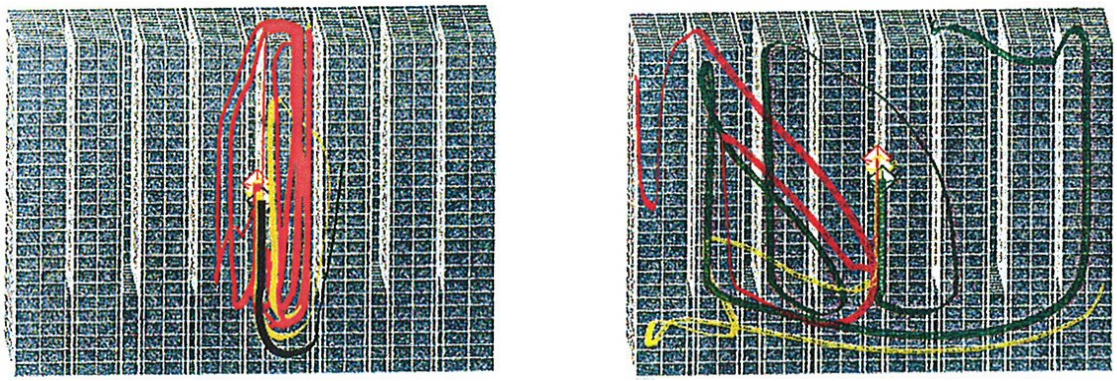

Figure 20: Distribution of anode slime particles released from a certain point at one anode surface, at 0.3 bath changes/hour (left) and 10 bath changes/hour (right) in a conventional cross flow electrolysis cell design [46]

5 Simulation strategy

The present work divers from the available literature as it uses a two way simulation strategy dividing the simulation effort into a local and global simulation domain. This approach becomes more understandable when looking at the electrodes' concentration and velocity boundary layers in an electrolysis cell (see Figure 21 and Figure 22)

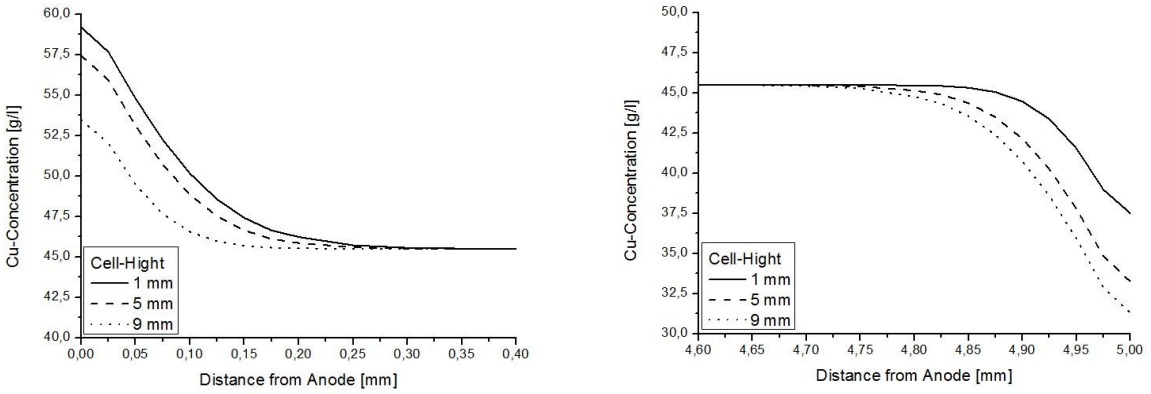

Figure 21: Concentration boundary layer at the electrodes for a copper refining electrolysis

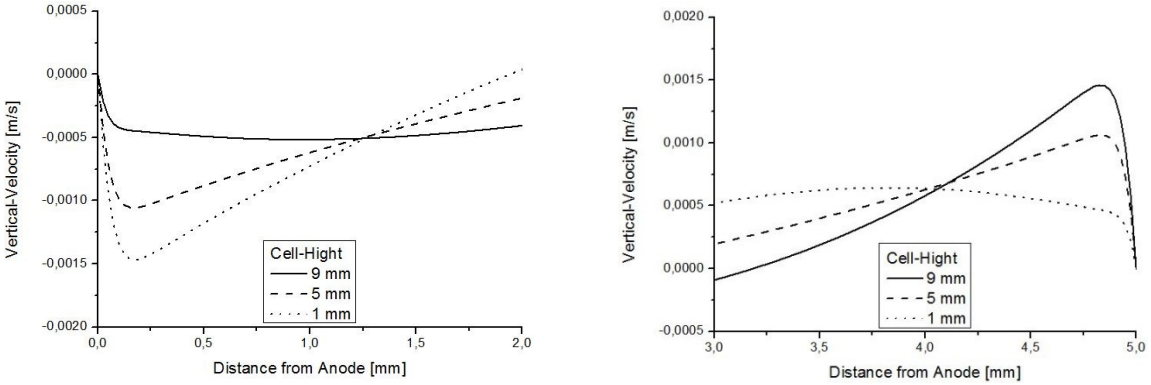

Figure 22: Velocity boundary layer at the electrodes for a copper refining electrolysis

As discussed in chapter 2.5 the concentration and velocity boundary layers both are a function of electrode height. Considering the thickness of the corresponding layers it is clearly visible that the concentration layer is far thinner than the velocity layer. Although the variation of copper concentration is restricted to a very small area directly in front of the electrodes the resulting velocity boundary layer can reach far into the electrolyte. This must be considered when constructing the simulation domain.

5.1 Geometry of the Pirdop electrolysis cell

The numeric simulation domain is based on the electrolysis cells used in Aurubis Pirdop, Bulgaria. Figure 23 shows the overall geometry of the used cell group.

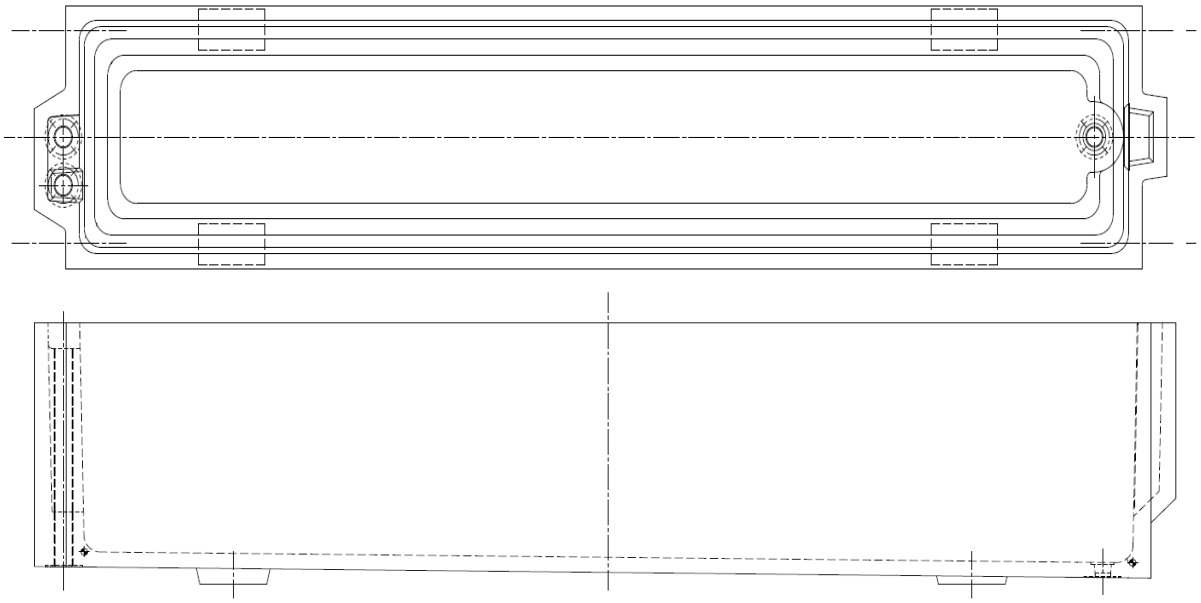

Figure 23: Geometry of electrolysis cells used in Aurubis, Pirdop

The cell has an overall length of about 6200 mm. It is 1400 mm high and 1300 mm wide. The electrolysis cell consists of 61 anodes and 60 cathodes to ensure that every single cathode is neighboring an anode on both sides. The dimensions of the electrodes are shown in Figure 24. The edge strips attached on both sides of the cathodes prevent copper from plating along the edges and allow for easy stripping operations. The anodes are produced by open mold casting and are therefore cone-shaped for an easier removal from the mold. At the bottom the corners are rounded off with a 60 mm radius. These features were simplified by a 45° angle and the cone shape was removed to save on volume elements during meshing.

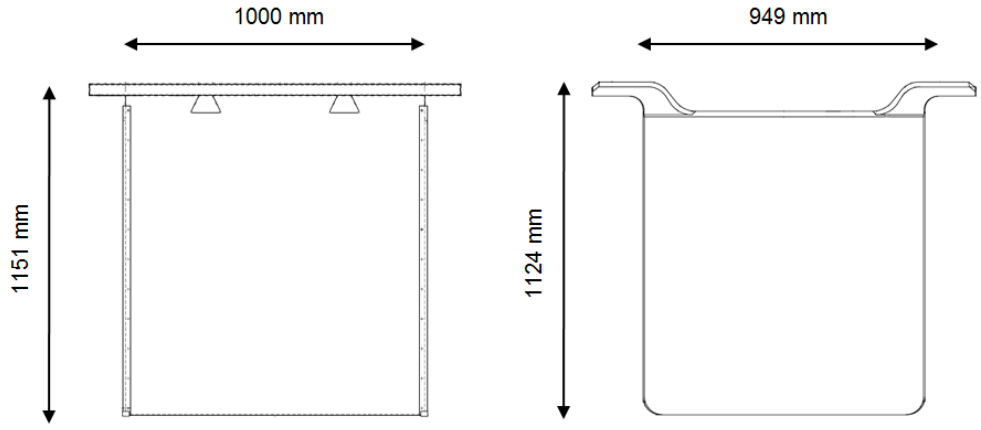

Figure 24: Geometry and dimensions of cathodes with edge strips attached (left) and anodes (right)

The electrodes are submerged alternatively into the electrolyte and the anode cathode spacing is set to 21 mm. Figure 25 shows the electrodes installed in the tankhouse cell. Only a narrow gap remains between the electrodes and the left and right cell walls. The bottom of the electrolysis cell itself is inclined to allow for an easy discharge of the used electrolyte and anode slime after the anode cycle. The height difference between the shallow and deep end is 65 mm, with the deep end being located at the inlet.

During the electrolysis process the dissolution and electroplating of copper and impurities cause a change of the electrodes geometry and spacing. Later crops are therefore calculated on a different simulation domain, see chapter 8.7.

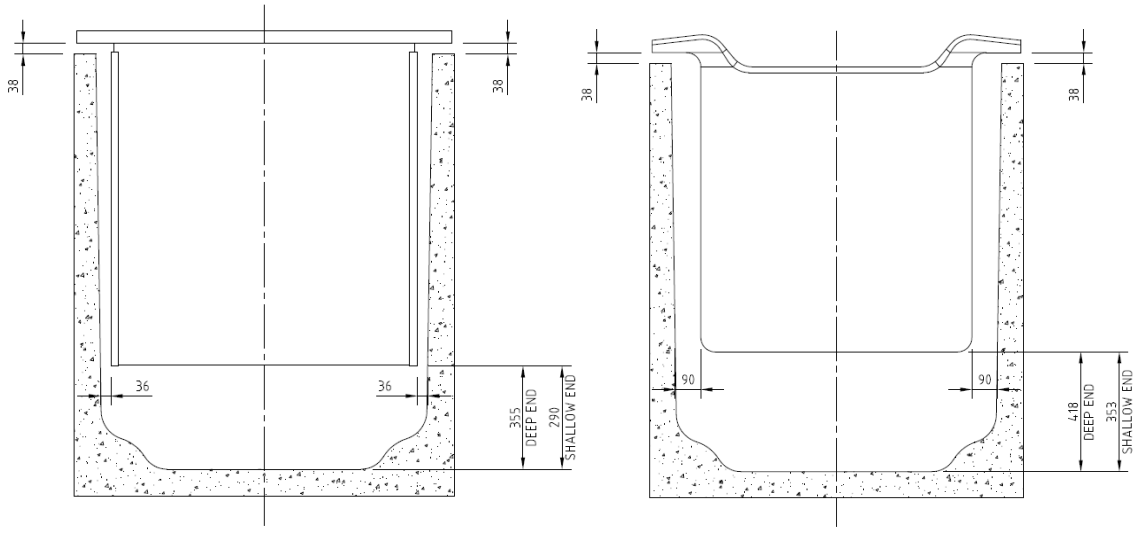

Figure 25: Anode and cathodes installed in tankhouse cell

Figure 26 shows the details of the tankhouse cell inlet. The electrolyte fed to the system at the top of the inlet “box” but the actual inlet is submerged 1100 mm underneath the electrolyte surface. At this point the electrolyte is entering the tankhouse cell under a 45° angle caused by the shape of the inlet “box”.

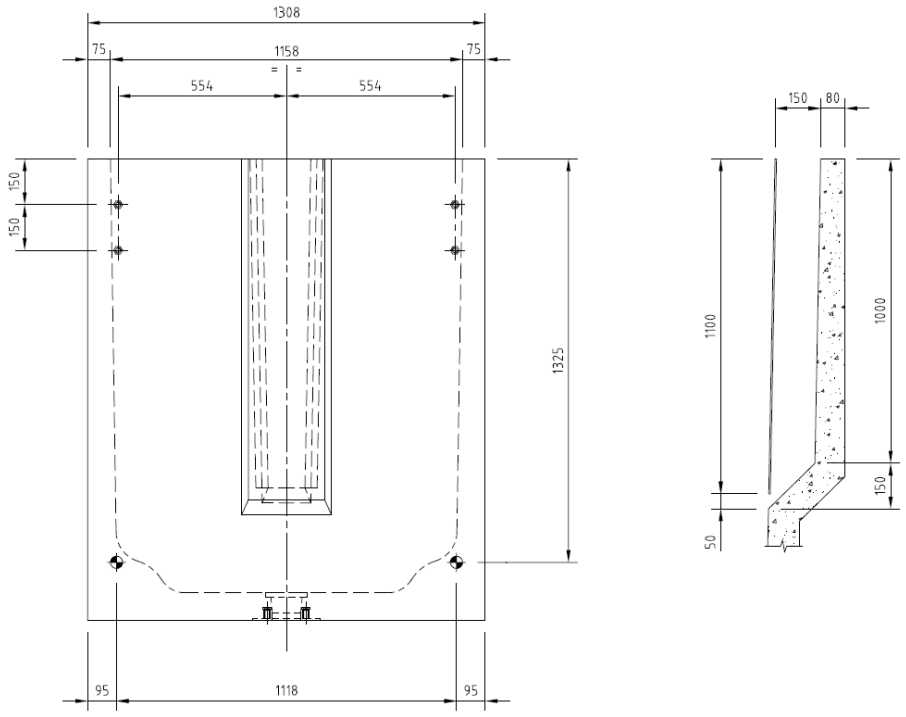

Figure 26: Detail inlet with inlet “box” on the right side

Since the natural convection is based on a concentration variation in the vicinity of the electrodes, the numerical grid must be very fine in these areas in order to achieve a sufficient accurate solution. On the other hand, the large size of an industrial electrolysis tankhouse cell (see Figure 23) would make more than a billion numerical volume elements necessary and thus, considering the today’s computer technology, a simultaneous calculation of natural and forced convection in a full-scale simulation domain is unpractical, if not impossible.

Therefore, the simulation had to be separated into two steps. First, the flow of the electrolyte caused by natural convection in a typical anode-cathode gap was simulated with a so-called “local” simulation. The simulation of the forced convection is then done as so-called “global” simulation, where the simulation domain consisted of the whole tankhouse cell including the gaps between anodes and cathodes. The concentration variation and momentum equations in these anode cathode gaps are however not calculated but the correspondent values are imported from the “local” simulation.

5.2 Local Simulation

In order to study the natural convection occurring along the electrodes a so-called local simulation of the Cu^{2+} concentration and the 3D velocity field between the electrodes has to be performed. The local simulation domain includes one anode and two cathodes (with the attached edge strips). The geometry for the detailed cathode-cathode simulation is shown in Figure 27. To achieve a better solution of the concentration and velocity boundary layers the size of the volume elements at the electrodes is set to 500 µm, see Figure 28. To decrease the total number of volume elements in the domain and therefore decrease the computation time, only half of the symmetric anode-cathode pair is simulated.

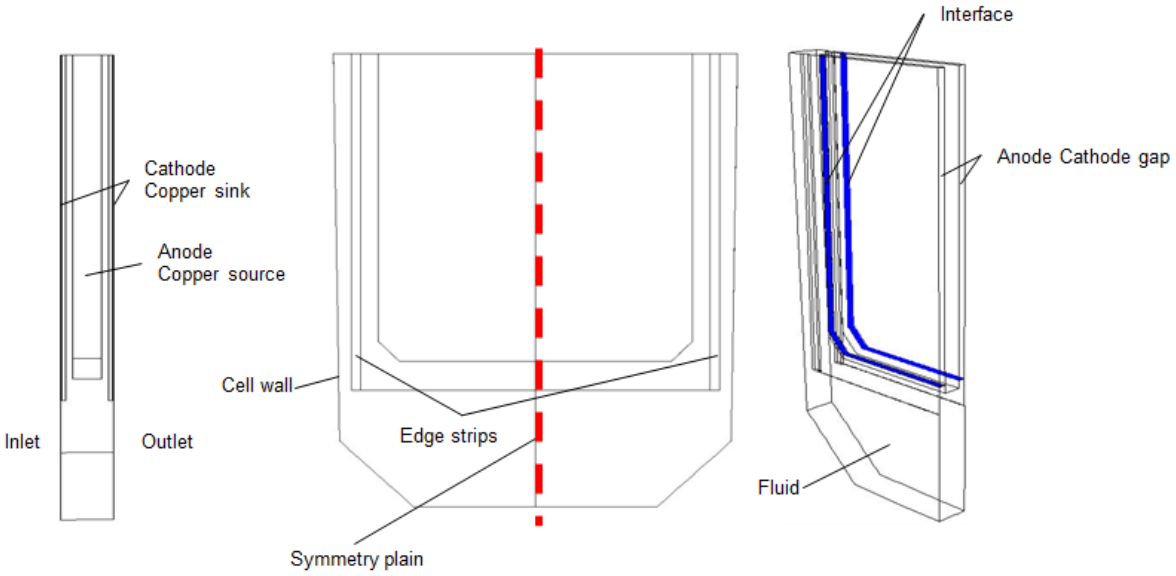

Figure 27: Local simulation domain for the electrolytic cell

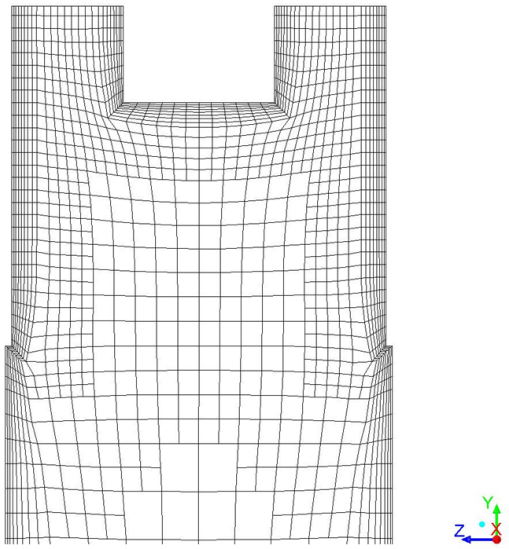

Figure 28: Local simulation; detailed mesh at electrodes

With the continuity equation (Equation 5-1) and the momentum conservation equation (Equation 5-2) the flow of the electrolyte and with the species conservation equation (Equation 5-3) the variation in Cu^{2+} cations concentration is calculated.

$$\frac{\partial \rho}{\partial t} + \nabla \cdot (\rho \vec{u}) = 0 \qquad \text{Eq. 5-1}$$

$$\frac{\partial}{\partial t}(\rho \vec{u}) + \nabla \cdot (\rho \vec{u}\vec{u}) = \nabla p + \nabla \cdot (\bar{\bar{\tau}}) + \rho \vec{g} + \vec{F} \qquad \text{Eq. 5-2}$$

$$\frac{\partial}{\partial t}(\rho c) + \nabla \cdot (\rho \vec{u} c) + \nabla \cdot (-D \nabla c) = \dot{Q}_c \qquad \text{Eq.5-3}$$

In the formula ρ is the density of the electrolyte, p the static pressure, $\bar{\bar{\tau}}$ the stress tensor and $\rho \vec{g}$ and $\vec{F}$ are the gravitational body force and external body forces that arise from dissolving and plating of copper as used by Leahy [58-60]. The external body force given by Equation 5-4 represents a boussinesq approximation [61-63]. By using this approach the density ρ can be considered constant in the conservation Equations 5-1 and 5-2. D is the diffusion coefficient. The quantity $\dot{Q}_c$ represents the rate of dissolution and plating of the Cu^{2+} cations. The dissolution happens at the anode where the copper cations enter the numerical domain. Cations are transported to the cathode by diffusion and convection where they are plated i.e. taken out of the numerical domain. Therefore, $\dot{Q}_c$ has a positive value on the anode and a negative value at the cathode. In the rest of the numerical domain it is set to zero. As shown in equation 4-5, $\dot{Q}_c$ is governed by the current density j.

$$\vec{F} = -\rho \cdot \vec{g} \cdot \beta \cdot (c - c_0)$$ Eq. 5-4

$$\dot{Q}_c = \begin{cases} \pm \frac{j \cdot m_{Cu}}{z \cdot F_a}, anode: (+) \quad cathode: (-) \\ 0, \ elsewhere \end{cases}$$ Eq. 5-5

The current density is calculated only at the surface of every cathode and anode by using the Butler-Volmer equation [64-68] ,as show in Equation 5-6.

$$j = j_a \cdot exp\left(\frac{\alpha_a \cdot z \cdot F_a \cdot \mu_a}{R \cdot T}\right) - j_c \cdot \left(\frac{c}{c_0}\right) \cdot exp\left(\frac{\alpha_c \cdot z \cdot F_a \cdot \mu_c}{R \cdot T}\right)$$ Eq. 5-6

The equations are closed with a set of model parameters, given in Table 7. The model was set up using an User Defined Subroutine (UDS) lister in Apendix 1.1 and Appendix 1.2.

Table 7: Model parameters for the copper refining electrolysis

	Parameter	Value	Unit	
ρ	density	1220	kg m^{-3}	[*]
c_0	initial copper concentration	45.5	kg m^{-3}	[*]
β	solutal expansion coefficient	$2.2 \cdot 10^{-3}$	m³ kg^{-1}	[58]
D	diffusion coefficient	$1.125 \cdot 10^{-6}$	kg m^{-1} s^{-1}	[69]
m_{Cu}	molar mass of Cu	0.064	kg mol^{-1}	[70]
z	Charge number (# e$^-$ per Cu^{2+} cation)	2	-	[71]
F_a	Faraday constant	96485	C mol^{-1}	[72]
α_a, α_c	anodic, cathodic transfer coefficient	0.6, 0.4	-	[69]
μ_a, μ_c	anodic; cathodic overpotential	0.01, 0.08	V	[69]
T	electrolyte temperature	338.15	K	[*]
j_a, j_c	anodic, cathodic exchange current	258	A m^{-2}	[69]

[*] provided by the industry partners. The boundary and cell zone conditions are shown in Table 8. At the walls no slip boundary conditions are applied while on the top a “no friction” boundary condition is applied to simulate a free surface.

Table 8: Local simulation boundary and cell conditions

Wall	No slip	No electrolyte movement at walls due to friction	BC
Top	No shear stress	Bath surface cannot take shear stress (free surface)	
Anode	No slip, scalar flux	Cu^{2+} cations enter the domain	
Cathode	No slip, scalar flux	Cu^{2+} cations leave the domain	
Inlet	Pressure Inlet	No gauge pressure, electrolyte can enter/leave domain	
	Turb. parameters	Turb. intensity: 5 % turb. Length scale: 0.3 m	
Outlet	Pressure Outlet	No gauge pressure, electrolyte can enter/leave domain	
	Turb. parameters	Turb. intensity: 5 % turb. Length scale: 0.3 m	
Symm.	Symmetry	All gradients are zero	
Fluid	Electrolyte	Initial Cu^{2+} concentration is 45.5 g/l; initial vel. = 0 m/s	IC

The simulation was performed on a SGI computer cluster issuing 12 CPUs and 64 GB in total memory. The simulation domain was initialized with no movement apart from an upwards directed velocity of 0.001 m/s to help with convergence and an initial Cu^{2+} concentration of 45.5 g/l. In order to archive a steady state result, the simulation must be separated into two steps.

1. First a steady state calculation must be performed with only a laminar flow formulation. In this simulation the convergence criteria for mass and momentum conservation would not reach the 10^{-3} convergence limit. The calculation was performed for 1000 iterations until the peaks in the residuals plot straighten out as shown in Figure 29.

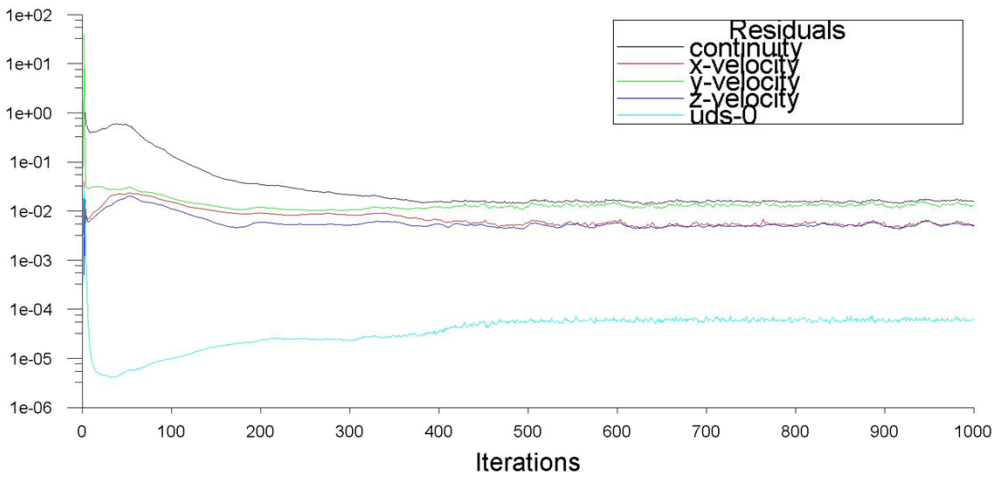

Figure 29: Residuals for the steady state laminar simulation

2. Secondly the time depending $k-\omega$ turbulence model was implemented into the simulation and a transient calculation was continued. The time step size was set to 0.01 s and a total of 50,000 time steps were calculated. The still occurring periodic fluctuations where then time averaged to achieve a steady state result.

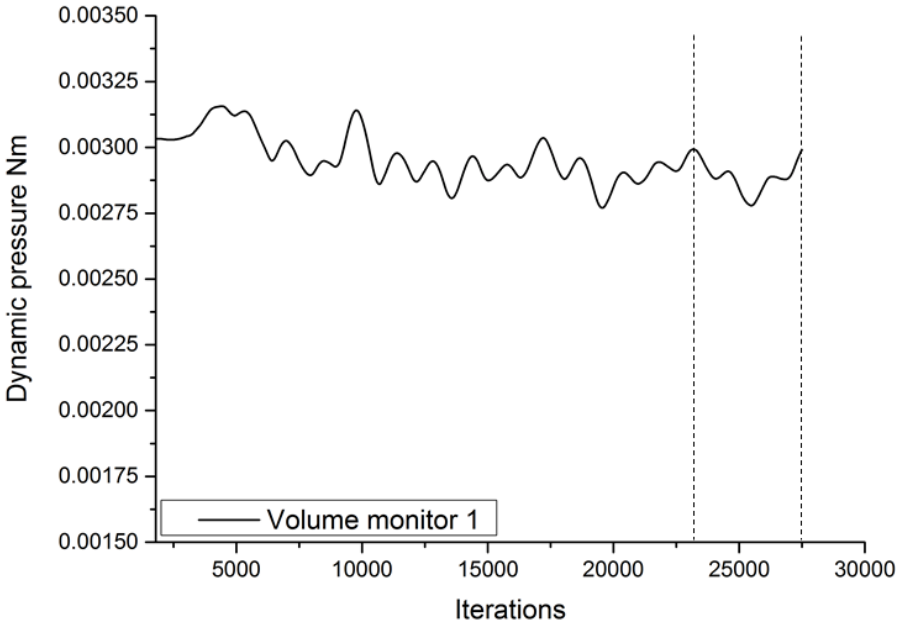

Figure 30: Progress of the dynamic pressure in the simulation domain. The fluctuating values were time averaged over 5000 time steps to achieve a steady state result.

5.2.1 Concentration field

The electrochemical reactions cause the dissolution of Cu^{2+} cations at the anode and their deposition at the cathode. Therefore, a gradient of concentration forms between the electrodes. Figure 31 shows a detailed view of the Cu^{2+} concentration in the anode-cathode gap at different heights.

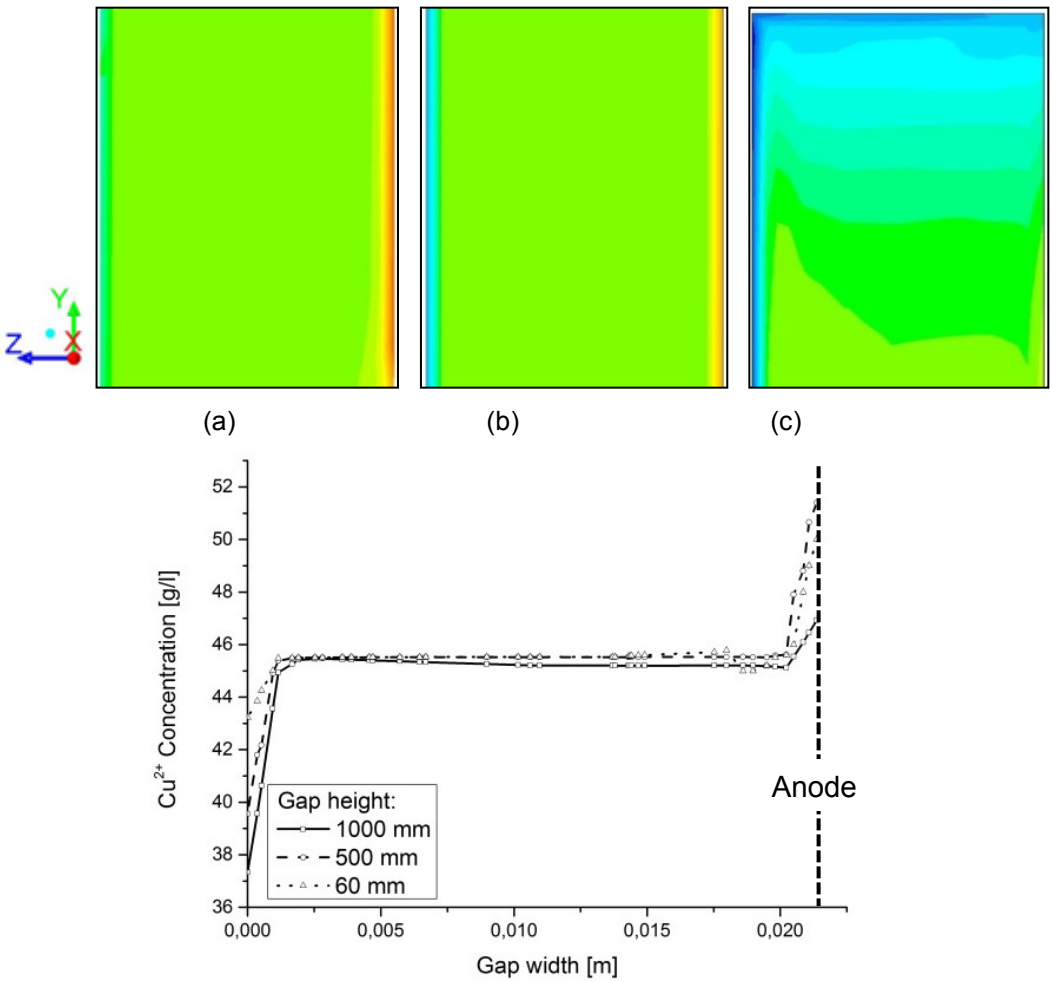

Figure 31: Concentration distribution in the gap between cathode (left) and anode (right) (a) 60 mm above the lower end of the anode, (b) 500 mm, (c) 1000 mm and diagram plot of Cu^{2+} concentration profile across the gap. Note that (a), (b) and (c) had to be scaled by a factor of 4 in z-direction to better visualize the concentration distribution.

Figure 32 shows the copper concentration directly in front of the anode and cathode. Clearly visible is the stacking of layers with different concentrations. The downward movement of electrolyte at the anode transports the cations to the lower part of the anode. While moving, more and more cations are loaded into the electrolyte resulting in a high concentration at the bottom part of the anode. The opposite can be seen at the cathode. While moving upward, more cations are removed from the electrolyte leading to a low concentration of Cu^{2+} at the top.

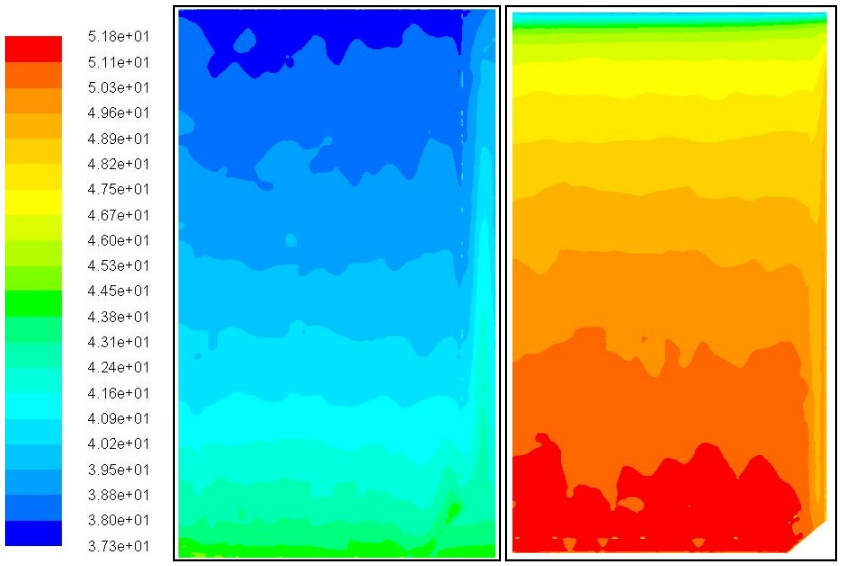

Figure 32: Cu^{2+} concentration in g/l adjacent to the cathode (a), adjacent to the anode (b)

Figure 33 shows a plot of the Cu^{2+} concentration adjacent to the electrodes over the cell height. At the cathode a difference in Cu^{2+} concentration of 10 g/l can be found between top and bottom of the electrode. The lower density causes the formation of a Cu^{2+} poor electrolyte layer at the top of the tankhouse cell. This layer also influences the concentration adjacent to the anode. The concentration gradient between the anode top and bottom is therefore larger with about 15 g/l.

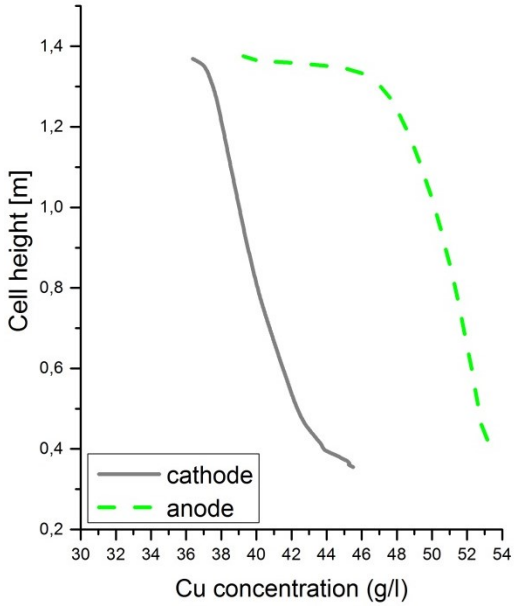

Figure 33: Concentration profile over cell height

Figure 34 shows the Cu^{2+} distribution half way between anode and cathode. For the most part the concentration equals the initial copper concentration of 45.5 g/l. Only the top shows

the low Cu^{2+} electrolyte layer described above. At the bottom the concentration is only slightly elevated with 45.7 g/l.

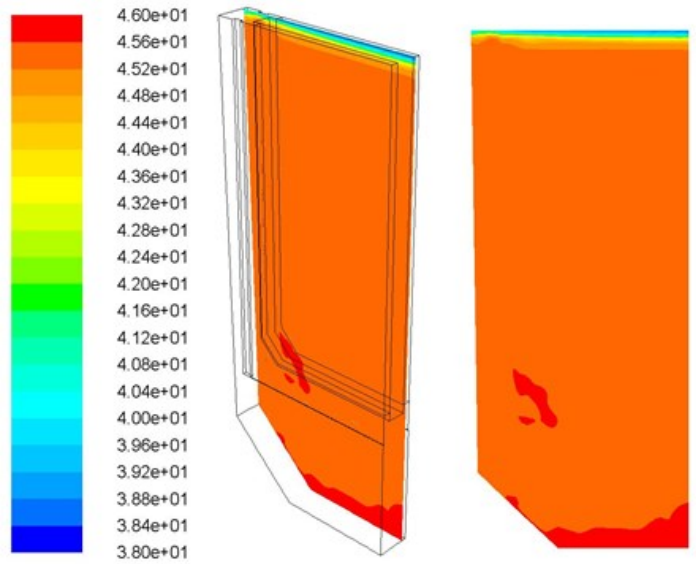

Figure 34: Cu^{2+} concentration half way between anode and cathode in g/l

The Cu^{2+} distribution underneath the anode can be seen in Figure 35. Here the downward flowing high Cu^{2+} electrolyte causes an increase in Cu^{2+} concentration. Again the elevated Cu^{2+} concentration of 45.9 g/l is only slightly above the initial Cu^{2+} concentration of 45.5 g/l. After leaving the anode surface the electrolyte quickly mixes with the incoming electrolyte flow and the high Cu^{2+} concentration dilutes.

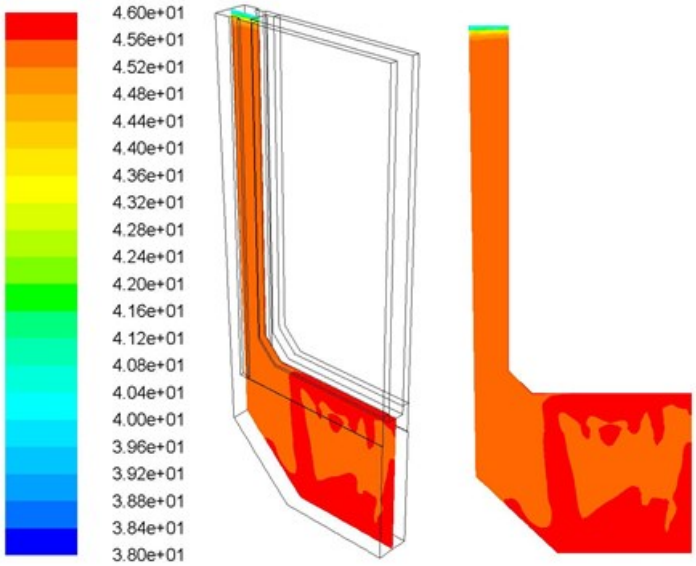

Figure 35: Cu^{2+} concentration below the anode in g/l

5.2.2 Velocity Field

This concentration gradient leads to a convective electrolyte flux as shown in Figure 36. The low density in front of the cathode causes an upward movement while the higher density at the anode leads to a downward movement of the electrolyte. The velocity of the electrolyte changes with height. At the top of the anode only a small amount of Cu^{2+} has been added to the electrolyte already and the downward movement is very slow. While moving downward along the anode more Cu^{2+} is added to the electrolyte causing a stronger buoyancy force and a faster movement. Therefore, the highest downward velocity can be found at the bottom of the anode where also the concentration of Cu^{2+} reaches its highest values. At the cathode the opposite mechanism happens.

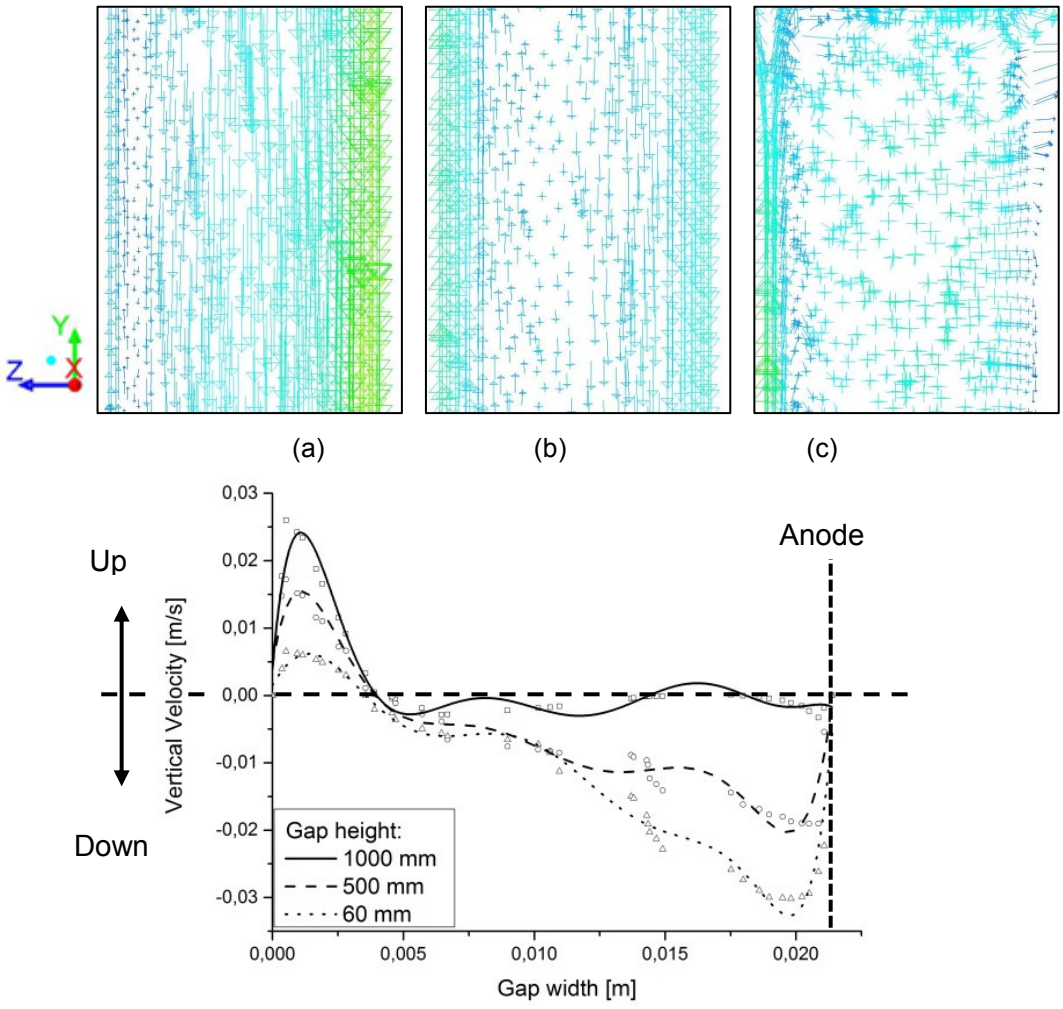

Figure 36: Velocity vectors in the gap (a) 60 mm above the lower end of the anode, (b) 500 mm, (c) 1000 mm and diagram plot of vertical velocity over the gap width. Note that (a), (b) and (c) had to be scaled by a factor of 4 in z-direction for better visualization of the results.

The thickness of the downward moving electrolyte layer increases towards the lower end of the electrode gaps. At the lower edge of the anode the high density, downward moving

electrolyte clearly dominates the flow, as shown in Figure 37. Only a small part of the electrolyte directly adjacent to the cathodes is forced to flow upwards.

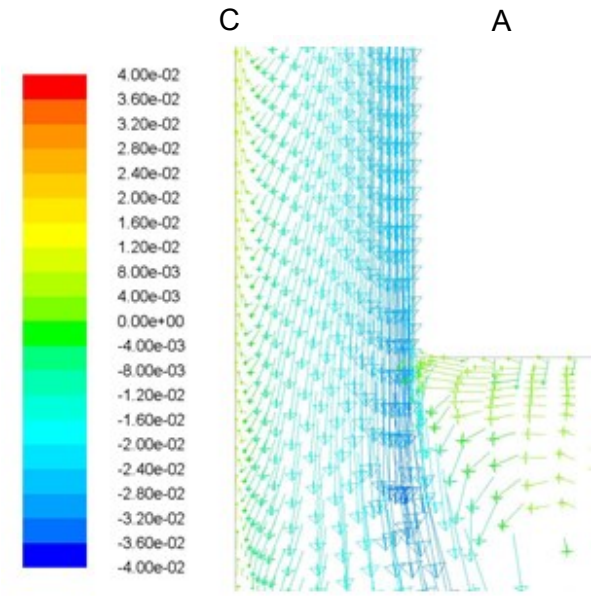

Figure 37: Vertical electrolyte velocity at lower anode edge in m/s

The area underneath the anode is characterized by a highly chaotic electrolyte flow pattern and is strongly influenced by the inlet boundary condition (the effects of forced convection), as shown in Figure 38.

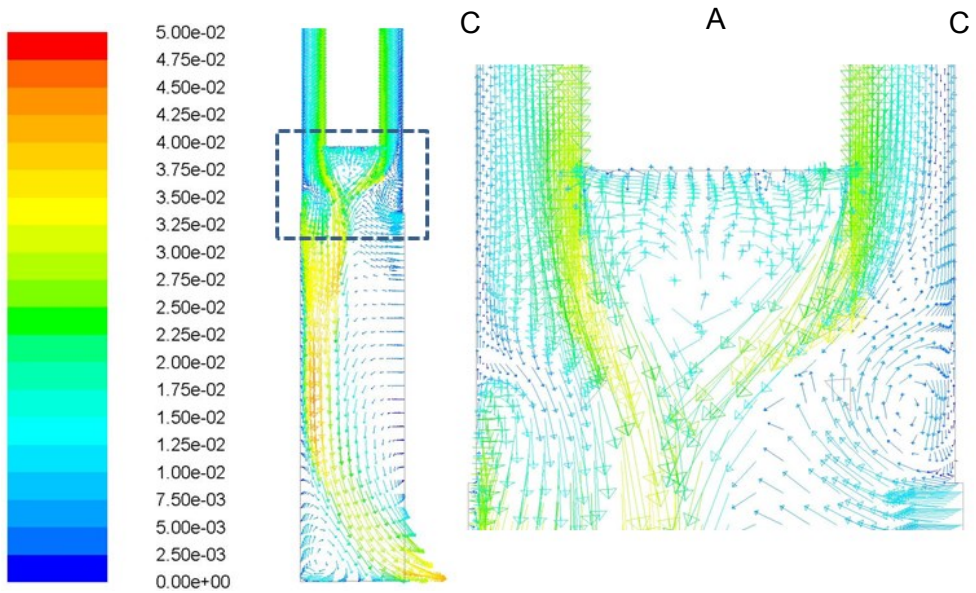

Figure 38: The flow pattern underneath the anode, outside the anode cathode gap shows a highly chaotic and boundary condition dependent behavior (dotted area)

The electrode gaps are confined by a so called interface, as shown in Figure 27. The interface separates the simulation domain into the two electrode gaps and the bulk. Along this interface the mass flow must be equal to zero in order to maintain mass conservation

inside the electrode gaps. Figure 39 shows the electrolyte flow along the interface. Since the mass flow at the lower end is primarily directed outwards, the electrolyte is forced to reenter the gaps at the side. At the top the lower density electrolyte layer forces the flow vector outwards.

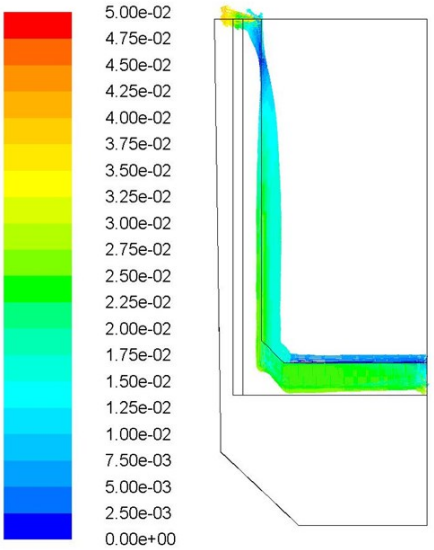

Figure 39: Electrolyte flow along the interface in m/s

The position of the interface in the local and global domain is equal; however it does not include the whole anode cathode gap. In order to produce a profile mostly independent of the boundary condition at the inlet, the interface must be indented 25 mm above the lower edge of the anode. This ensures the same electrolyte behavior in all anode cathode gaps in the tankhouse cell.

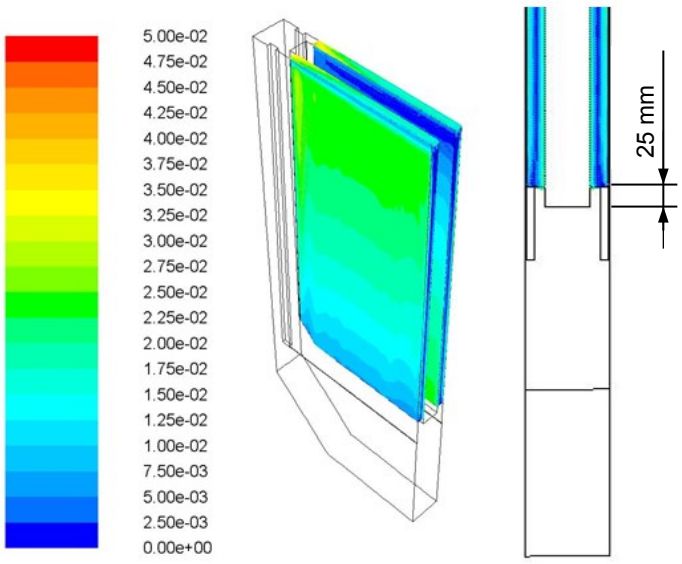

Figure 40: Velocity profiles inside the interfaces; the interface is indented 25 mm inside the anode

Figure 41 and Figure 42 shows the influence of the inlet boundary condition on the electrolyte velocity and Cu^{2+} concentration. Three different cases have been investigated: The standard case used in the local simulation (pressure inlet boundary condition with no additional mass flow rate) and two mass flow inlet boundary conditions with 0.3 and 0.5 bath changes per hour. All three cases were compared at the same y-position (50 mm above the anode bottom => position of the interface). The maximum difference in Cu^{2+} concentration for the 0.5 bath changes and the 0.0 bath changes is only 0.7 g/l or 1.36 %. The maximum difference in velocity is only 0.69 mm/s or 5.3 %. Further inside the electrode gaps the difference gets even smaller. It can therefore be assumed that the electrolyte flow inside the electrode gaps is primarily defined by natural convection.

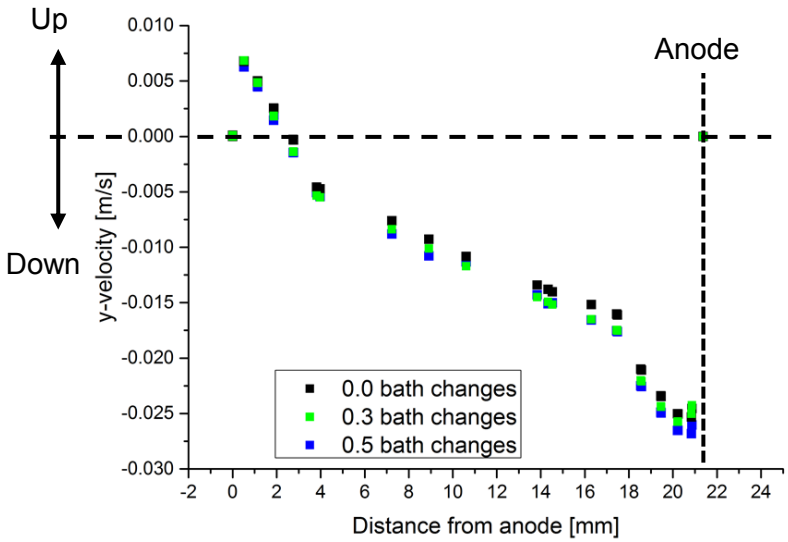

Figure 41: y-velocity in m/s for different inlet boundary conditions

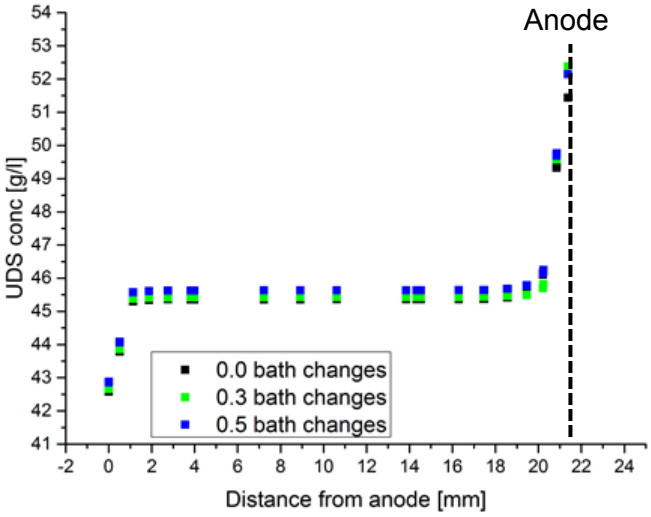

Figure 42: Cu^{2+} concentration in g/l (labeled UDS conc) for different inlet boundary conditions

The velocity vectors inside the interface describe the behavior of the electrolyte inside the electrolyte gaps. The data won by the local simulation can then be transported to the global simulation using a profile file format. The format of the profile files is very simple. Each profile consists of a header that specifies the profile name, profile type (point, line, mesh, radial, or axial), and number of defining points, and is followed by an arbitrary number of named "fields". Some of these fields contain the coordinate points and the rest contain velocity data. In this work a point file format is used meaning that for every point (volume element) in the simulation domain a set of coordinates, velocity data (x-velocity, y-velocity, z-velocity) and turbulence data (turbulent kinetic energy and specific dissipation rate) is defined. An example for this profile file is shown in Table 9.

Table 9: Example of the profile file format

((turb-prof point)				
(x	4.00000E+00	4.00000E+00	4.00000E+00	4.00000E+00)
(y	1.06443E-03	3.19854E-03	5.25478E-03	7.26589E-03)
(z	5.45784E+00	6.5987E+00	7.12568E+00	8.12568E+00)
(x-vel	1.25871E-02	1.35897E-02	1.00124E-02	1.19878E-02)
(y-vel	2.21457E-02	3.21457E-02	2.15478E-02	1.12478E-02)
(z-vel	1.12487E-02	1.24878E-02	3.21787E-02	4.24787E-02)
(k	5.47854E-07	1.32589E-08	1.98791E-07	1.23589E-07)
(ω	3.45877	4.54878	3.12548	2.15478))

5.3 Inlet Simulation

The electrolyte is entering the tankhouse cell via a submerged inlet nozzle. This inlet is shaped in a way so that a 45° angle of electrolyte flow is achieved. The flow pattern must be simulated in order to gain the correct values for the kinetic energy and the specific dissipation rate for the $k-\omega$ turbulence model. Figure 43 shows the inlet simulation domain with the inlet "box" on the left side. The electrolyte is fed into this inlet box, which is blocked off the tankhouse cell by a plate. Only a narrow gap at the bottom is left open for the electrolyte to enter the cell, see Figure 44.

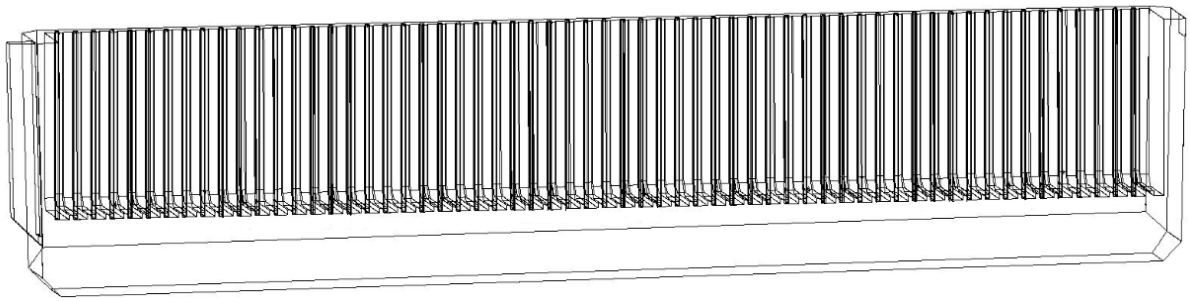

Figure 43: Inlet simulation domain, inlet "box" on left side.

The simulation domain consists of the whole tankhouse cell without the anode cathode gaps. It is assumed that the natural convection, caused by the density changes between the electrodes, does not influence the electrolyte flow at the inlet. The simulation domain uses a very fine mesh at the inlet "box" as shown in Figure 44.

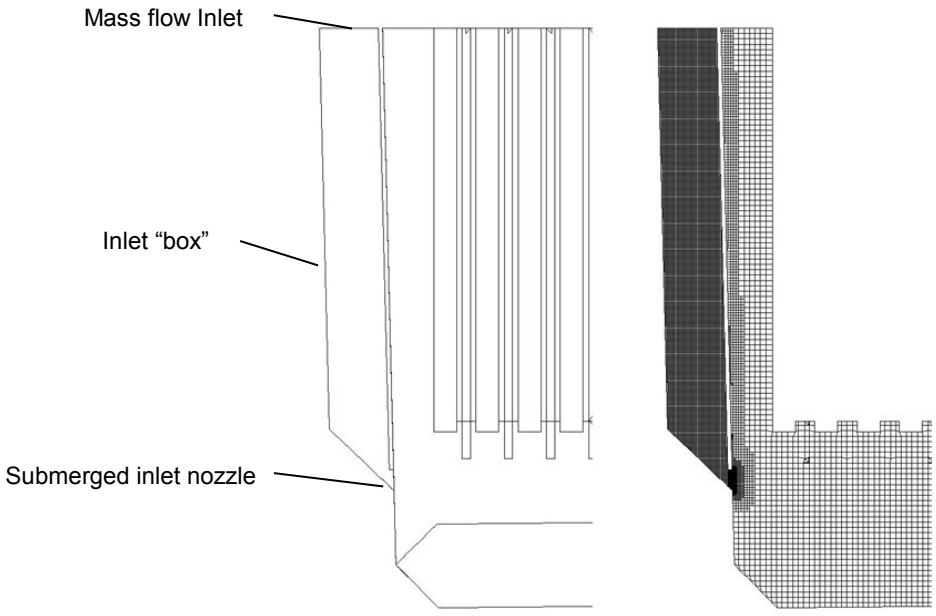

Figure 44: Inlet simulation domain detail, the inlet box is blocked off except for a narrow gap

The mass flow inlet at the top was set to 42 l/min and the same turbulent parameters as used in the local simulation. The simulation was performed on a transient solver and a time step size of 0.1 s until the results oscillated around a mean value. The steady state results were then obtained by time averaging. Figure 45 to Figure 47 show the results of the inlet simulation. The highest velocities can be found in the gap between inlet “box” and tankhouse cell.

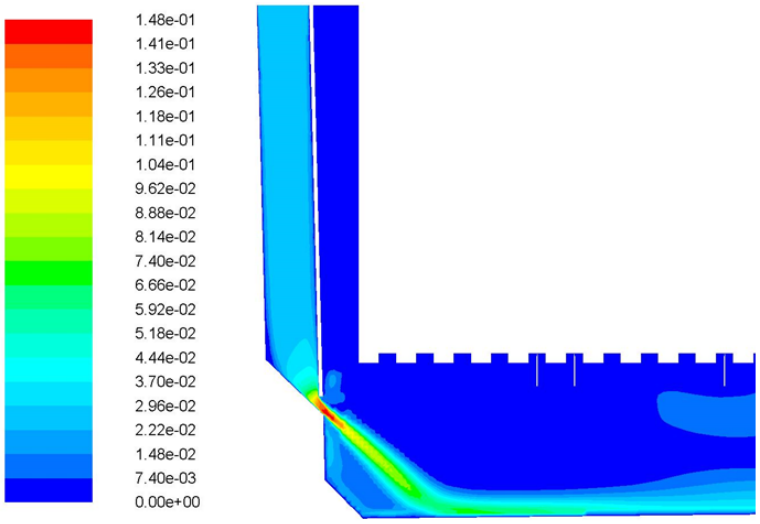

Figure 45: Contours of electrolyte velocity in m/s

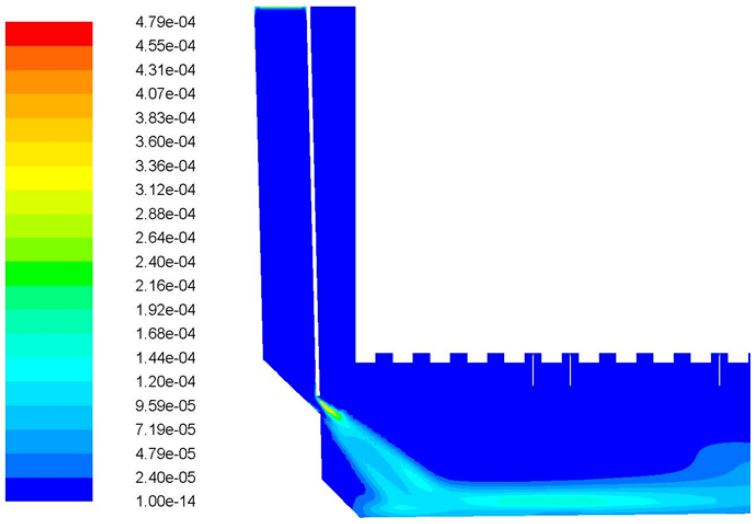

Figure 46: Contours of turbulent kinetic energy in m²/s²

With a given mass flow rate of 42 l/min and a known inlet area of 12500 mm², the velocity would calculate to 56 mm/s. The highest velocity in the simulation is found to be 148 mm/s. This is caused by a reversed flow in the inlet gap around the plate separating the inlet “box” from the tankhouse cell. The reversed flow reduces the effective area of inside flowing

electrolyte and causes higher velocities, therefore the inlet simulation must be performed to gain the correct inlet velocity profile for the global simulation.

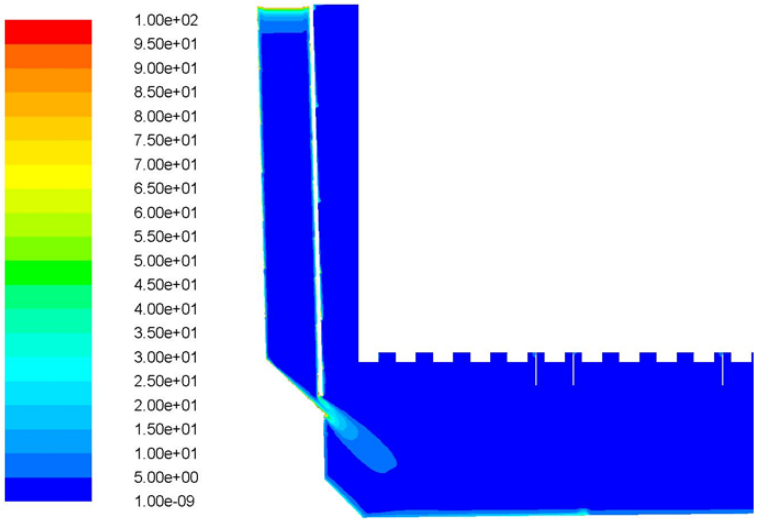

Figure 47: Contours of specific dissipation rate in 1/s

Figure 48 shows the reversed flow at the inlet. The sharp corners of the plate separating the inlet “box” from the tankhouse cell cause a disturbance in the electrolyte flow and leads to the formation of the shown flow pattern.

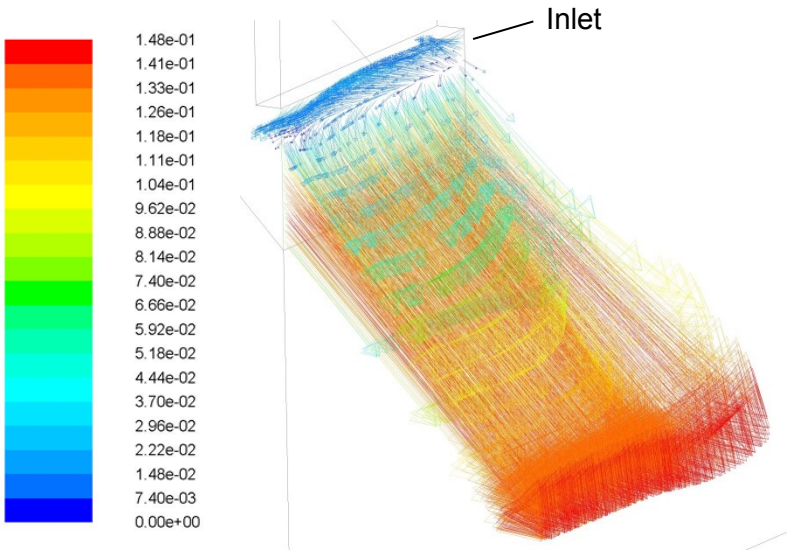

Figure 48: Inlet flow in m/s shows reversed flow in the inlet gap

As with the local simulation, the velocity vectors and turbulent parameters are saved in a point-type profile matrix and can be interpolated into the global simulation.

5.4 Global simulation

In the global simulation the natural convection between the electrodes interacts with the forced convection coming from the electrolyte flow at the inlet. Figure 49 shows the global simulation domain. In order to save on volume elements only half of the tankhouse cell is considered and a symmetric boundary condition is set up for the y-z plain. The boundary and cell zone conditions are listed in Table 10. The electrolyte enters the tankhouse cell at the left side via a submerged inlet nozzle. The velocity profiles were previously calculated by an inlet simulation and are implemented as boundary conditions. The electrolyte leaves the tankhouse cell via an outlet, located at the right side. The top is considered as a no shear stress boundary condition to simulate a free liquid surface. The walls bordering the tankhouse cell at the sides and the bottom have no slip boundary conditions attached as well as the electrode surfaces. The outside surfaces of the first and last anode are deactivated, meaning no copper dissolution effects are assumed. The geometry of the anode cathode gaps are set in a way to resemble the first production cycle of newly installed anodes. In later simulation trials the geometry was changed to equal different production cycles, as shown in chapter 8.7.

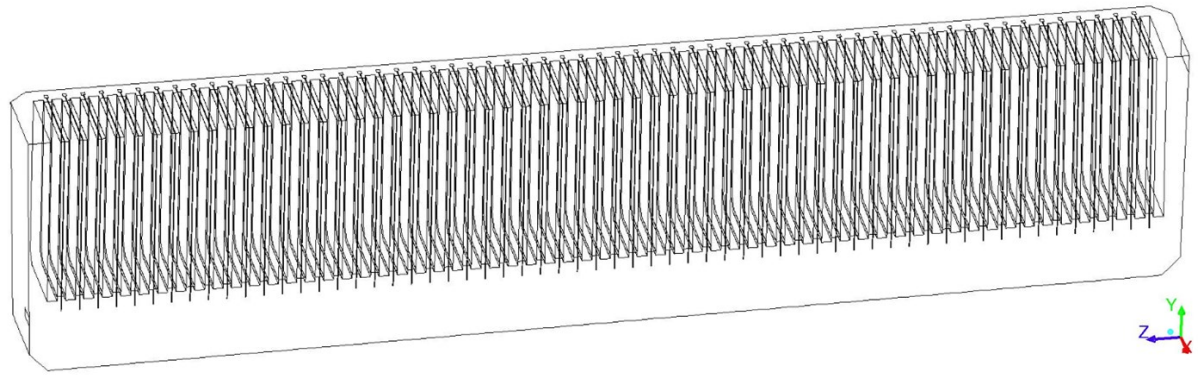

Figure 49: Global simulation domain for the electrolytic cell

Table 10: Global simulation boundary and cell conditions for copper refining electrolysis

Wall	No slip	No electrolyte movement at walls due to friction
Top	No shear stress	Bath surface cannot take shear stress (free surface)
Anodes	No slip	No electrolyte movement at walls due to friction
Cathodes	No slip	No electrolyte movement at walls due to friction
Inlet	Velocity Inlet	Velocity and turbulence profiles from inlet simulation
Outlet	Pressure Outlet	No gauge pressure, electrolyte can enter/leave domain
Symm. plane	Symmetry	All gradients are zero
Electrode gaps	Electrolyte	Velocity and turbulence profiles from local simulation

The local simulation domain resembles the volume between the first and second cathode from the inlet. In order to use the velocity profiles from the local simulation in all 120 electrode gaps the profiles must first be reoriented. Figure 50 shows the nomenclature of the electrode gaps, even numbers are located left, odd numbers are located right of the anodes. The gaps 2 and 3 can be imported without any reorienting, since the Cartesian coordinates are equal in the local and global domain. The gaps 1, 5, 7... are filled with the reoriented velocity and turbulent data from gap 3, while the gaps 4, 6, 8…are filled with the reoriented data from gap 2. The distance between one cathode centerline to the neighboring cathode centerline is exactly 100 mm. Therefore the distance between any individual volume element in gap 2 is exactly 100 mm to its corresponding volume element in gap 4 and 200 mm to its corresponding volume element in gap 6 and so on. The reorientation can therefore be done by simply subtracting (negative z-direction) 100 mm for every electrode gap from the z-coordinate of the initial velocity profile, see Table 11.

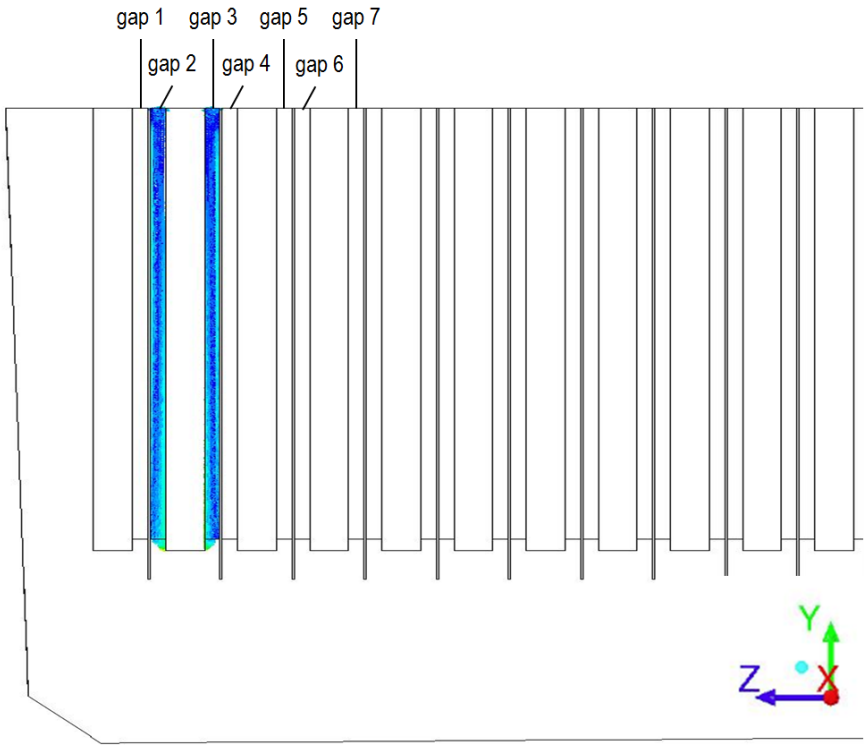

Figure 50: Nomenclature of the electrode gaps

Table 11: Profile orientation for the global simulation domain

Left side anode		Right side anode	
gap	z-coordinate	gap	z-coordinate
gap 01	+100 mm	gap 02	**0**
gap 03	**0**	gap 04	-100 mm
gap 05	-100 mm	gap 06	-200 mm
gap 07	-200 mm	gap 08	-300 mm
gap 09	-300 mm	gap 10	-400 mm
…		…	
gap 119	-5900 mm	gap 120	-5800 mm

The velocity profiles are imported using a least square interpolation method. This means that the values are assigned to the cell centers through a first-order interpolation method that tries to minimize the sum of the squares of the offset (residuals) between the profile points and the cell centers. The interpolation is important because of the difference in mesh size between the local and global simulation, as shown in Figure 51. The values for velocity and turbulence parameters from the fine local mesh are interpolated on the coarse global mesh. Since the copper concentration is no issue in the global simulation, this approach is acceptable.

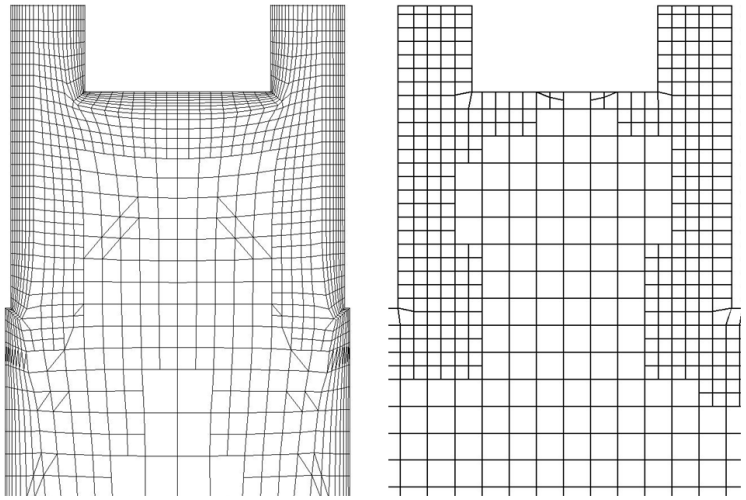

Figure 51: Comparison between the local (left) and global (right) mesh

The simulation was performed on a SGI computer cluster issuing 24 CPUs and 256 GB in total memory. The simulation domain was initialized with no movement apart from the electrolyte at the inlet and inside the electrode gaps. The time step size was set to 0.1 s and

the simulation was continued until the results were oscillating around a mean value. The steady state velocity profiles can then be found by time averaging over the typical oscillation frequency.

Figure 52 shows the results for the global simulation. Here the electrolyte flow inside the electrode gaps caused by natural convection interacts with the forced convection from the inlet.

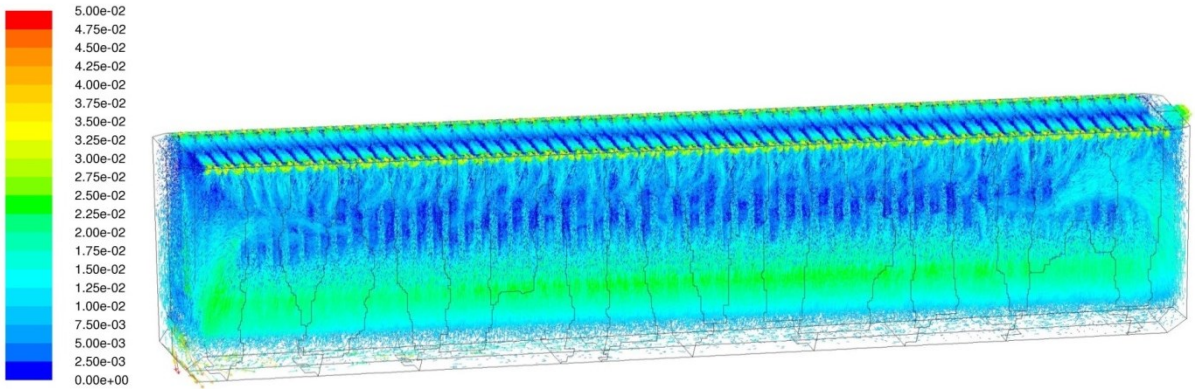

Figure 52: Velocity vectors in the global simulation in [m/s] for a copper refining electrolysis

The pathlines entering the tankhouse cell at the inlet are shown in Figure 53. The figure shows the incoming electrolyte (blue) forming a layer at the bottom, moving from the inlet towards the outlet. A small portion of the electrolyte reaches the outlet after only 800 s.

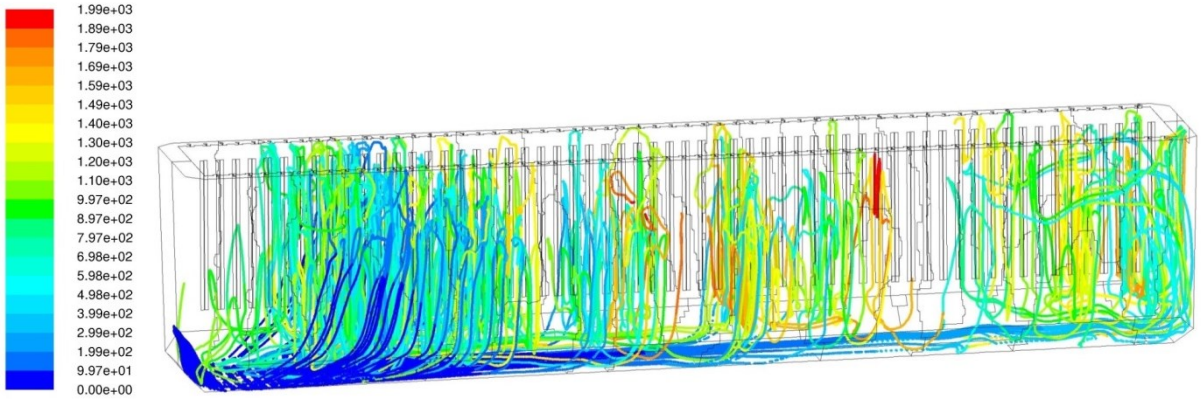

Figure 53: Pathlines in the global simulation colored by residence time in [s] for a copper refining electrolysis

From this bottom layer some of the electrolyte is pushed outwards and upwards along the walls of the tankhouse cell. From there the electrolyte enters the electrode gaps and is pushed upwards near the cathodes and downwards near the anodes. At the top of the electrode gap the natural convection forces the electrolyte outwards towards the wall, from

where the electrolyte is recirculated into the electrode gap. At the bottom of the electrode gap the electrolyte flows downward into the bottom layer. From there the electrolyte can either move with the bottom layer towards the outlet or is pushed outside again to reenter another electrode gap. This process is shown in detail in Figure 54 and Figure 55.

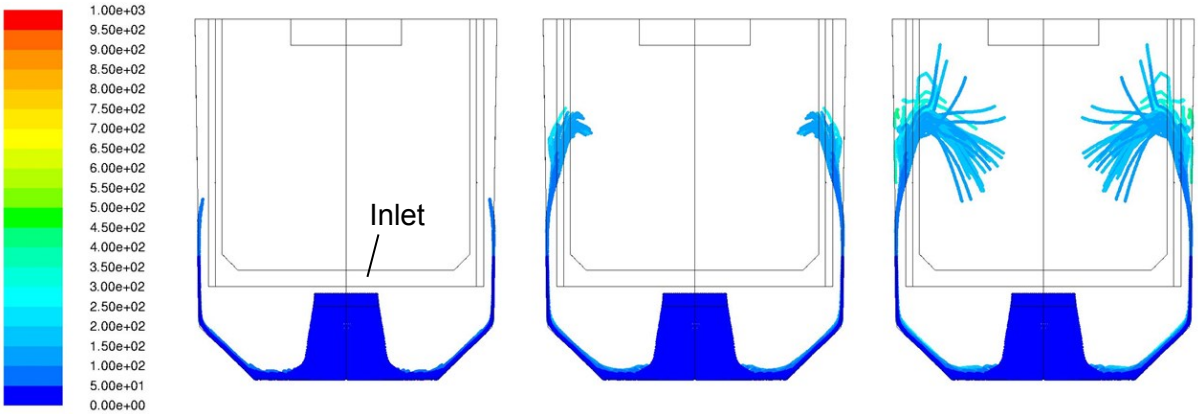

Figure 54: Electrolyte entering the electrode gaps

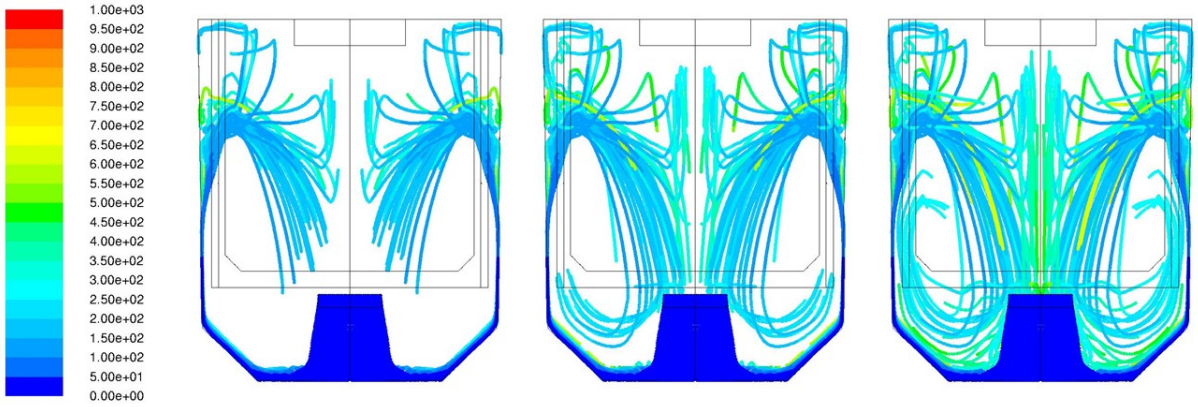

Figure 55: Electrode distributes inside the electrode gaps

The pathlines shown in Figure 53 to Figure 55 are calculated from the steady state velocity vectors in each volume element. The pathlines simply follow the vectors in a volume element until they reach the boarder of the neighboring volume element where they appropriate the new velocity vector. The pathlines therefore are based on the vector flow field alone and do not follow the laws of diffusion. The vector field is shown in detail in Figure 56 to Figure 58.
Near the cathode the upward directed flow is dominating with the exception of the area close to the bottom of the electrode. Here the downward directed flow from the anode causes the formation of a clockwise rotating swirl, see Figure 56.

Near the anode the downward directed flow is dominating with exception of the area close to the top of the electrode. Here the upward directed flow from the cathode causes the formation of a counter clockwise rotating swirl, see Figure 57.

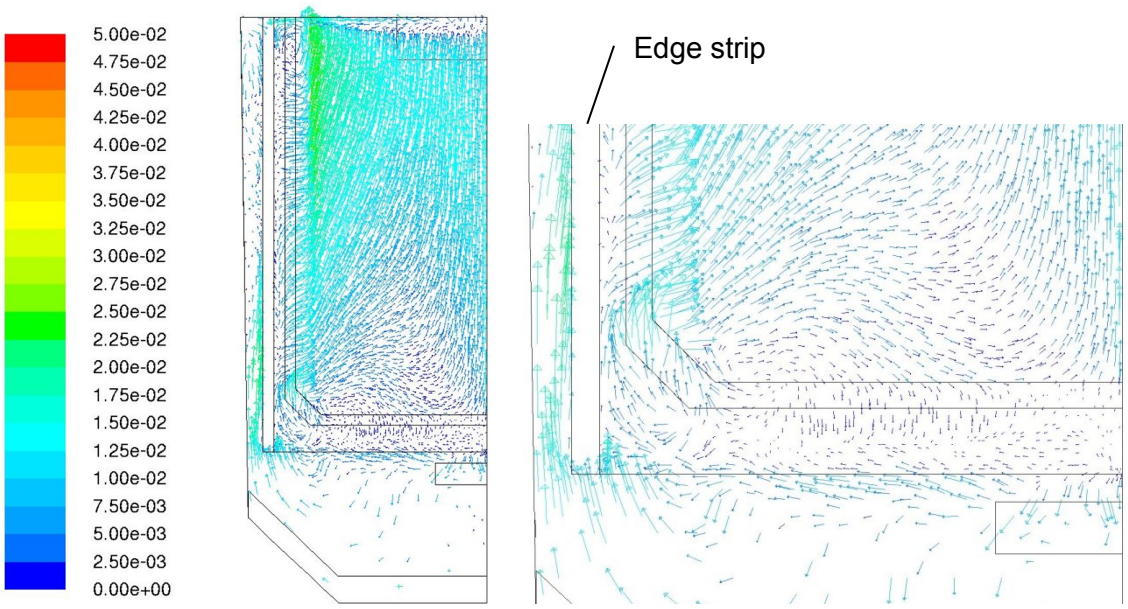

Figure 56: Electrolyte flow in front of the cathode (left); clockwise swirl (right)

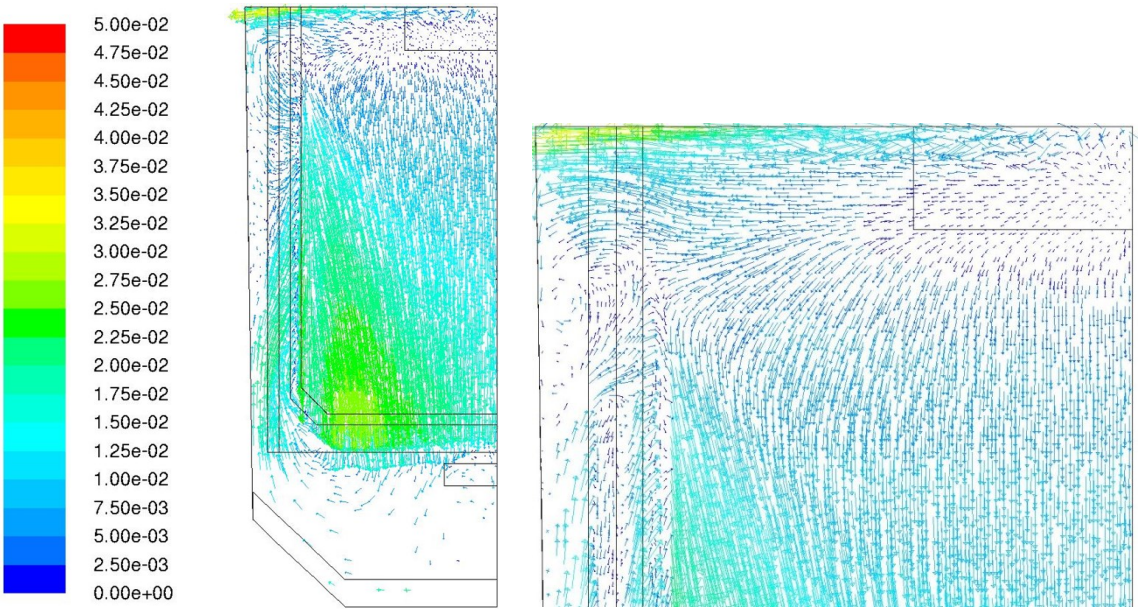

Figure 57: Electrolyte flow in front of the anode (left); counter clockwise swirl (right)

The electrolyte movement underneath the electrodes can best be studied in Figure 58. Here the outward pointing velocity vectors can clearly be seen. Also the upward directing velocity vectors in the gap between the wall and the electrodes are visible. The electrolyte enters the electrode gap on the lower half and leaves the gap at the top where it is pushed downwards and reenters the electrode gap.

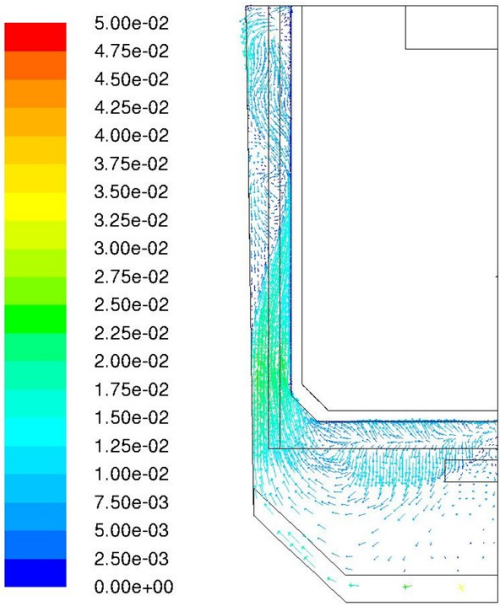

Figure 58: Electrolyte flow underneath the anode

The electrolyte flow in the tankhouse cell can be summarized by two fundamental mechanisms:

1) The electrolyte entering the tankhouse cell at the inlet forms a bottom layer moving from the inlet towards the outlet.
2) From this layer the electrolyte is pushed outwards and upwards along the walls of the tankhouse cell from where it is sucked into and distributed inside the electrode gaps.

Both mechanisms combined describe the distribution of electrolyte in the tankhouse cell. This knowledge is fundamental in order to study the behavior of additives, as discussed in chapter 7.

6 Validation of the simulation results

In order to prove the correctness of the simulation model, the simulation results were validated against real life experiments performed on the actual tankhouse cell in Pirdop.

6.1 Experimental Setup

A lithium based tracer element was added at the inlet and the distribution was monitored at a number of measurement points located throughout the cell. Figure 59 and Table 12 show the positioning of the measurement points in the tankhouse cell. The measurements were taken at the 1st, 5th, 16th, 30th, 44th, 56th and 61st anode at a depth of 50 cm and at different positions between the walls. The electrolyte was extracted from the measurement points via a 90 cm long steel tube and a hydraulic pump. While taking the samples the tube was in touch with the anodes, the removed electrolyte was therefore taken in direct vicinity of the anodes.

A typical result of one experimental run is shown in Table 13. At a certain time the continuous feeding of tracer solution was started. The solution was added to the electrolyte shortly before entering the tankhouse cell with a flow rate of 2.13 liters per hour. This flow rate was chosen to maintain a constant concentration of tracer at the measuring point at the inlet (Measurement point #1).

After the tracer solution flow was started the different measurement points were approached in succession and a sample was taken at every measuring point. After the last measurement point (#15, outlet) was reached the process was repeated beginning from the first point (#1, inlet). One experimental trial took between 3 and 4 hours in which each measurement point was sampled up to 4 times. The samples were later analyzed to obtain the lithium concentration.

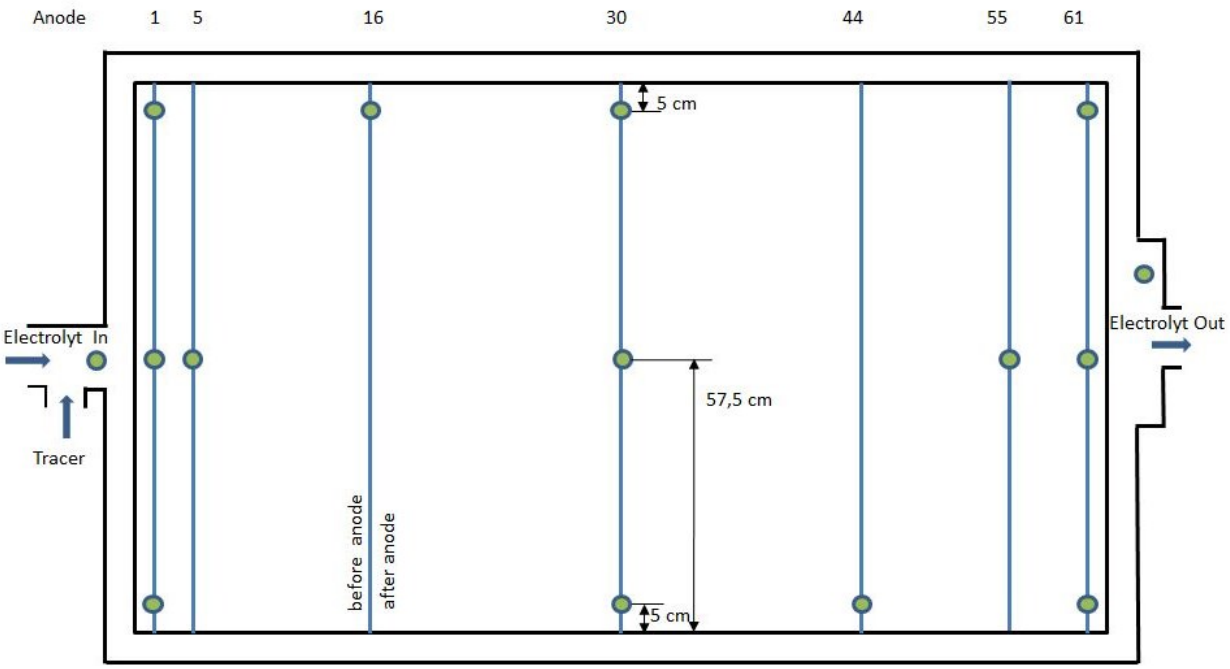

Figure 59: Map of the measurement points at the electrolytic cell in Pirdop

Table 12: Position of the measurement points at the electrolytic cell in Pirdop

Measure point #	Position	From center	From Anode side	Depth
1	Inlet			
2	before 1. anode	left	5 cm	50 cm
3	before 1. anode	middle	57.5 cm	50 cm
4	before 1. anode	right	5 cm	50 cm
5	before 5. anode	middle	57.5 cm	50 cm
6	before 16. anode	left	5 cm	50 cm
7	before 30. anode	left	5 cm	50 cm
8	before 30. anode	middle	57.5 cm	50 cm
9	before 30. anode	right	5 cm	50 cm
10	before 44. anode	right	5 cm	50 cm
11	before 55. anode	middle	57.5 cm	50 cm
12	before 61. anode	left	5 cm	50 cm
13	before 61. anode	middle	57.5 cm	50 cm
14	before 61. anode	right	57.5 cm	50 cm
15	Outlet			

Table 13: Example of an experimental trial for a copper refining electrolysis

Date	Time hh.mm	Measure point	Remark	Li, mg/l
1st run				
06.08.2013	14:19		tracer	5796
06.08.2013	14:10	0	outlet	0,031
06.08.2013	14:23	1	inlet	5,20
06.08.2013	14:27	2	1. anode left	2,04
06.08.2013	14:31	3	1. anode middle	2,08
06.08.2013	14:34	4	1. anode right	2,12
06.08.2013	14:37	5	5. anode middle	1,98
06.08.2013	14:42	6	16. anode left	1,91
06.08.2013	14:45	7	30. anode left	1,13
06.08.2013	14:47	8	30. anode middle	1,06
06.08.2013	14:51	9	30. anode right	1,22
06.08.2013	14:54	10	44. anode right	1,20
06.08.2013	14:58	11	56. anode middle	0,76
06.08.2013	15:02	12	61. anode left	0,43
06.08.2013	15:05	13	61. anode middle	0,54
06.08.2013	15:08	14	61. anode right	0,71
06.08.2013	15:14	15	outlet	1,16

6.2 Simulation Setup

The tracer experiments were simulated in the local simulation by adding a scalar transport equation (Eq. 6-1) to the solver. The diffusivity constant was provided by the industry partners and set to $\rho \cdot D = 1.125 \cdot 10^{-6}$ kg/m/s. The scalar has a passive behavior, it does not alter the physical properties of the electrolyte as density or viscosity nor does it change the flow behavior in any way. The scalar concentration was set to 1 at the inlet and no other sources and sinks (except for the outlet) are present. As initial conditions the steady state velocity field from the global simulation was used.

$$\frac{\partial}{\partial t}(\rho c) + \nabla \cdot (\rho \vec{u} c) + \nabla \cdot (-D \nabla c) = 0 \qquad \text{Eq. 6-1}$$

The simulation was saved every 1000 s to obtain the value of scalar concentration at the corresponding measurement points. As in the experimental trials the concentration was

inspected directly adjacent to the anodes at a depth of 50 cm underneath electrolyte level. An example is shown in Figure 60 the simulated tracer distribution at the first anode.

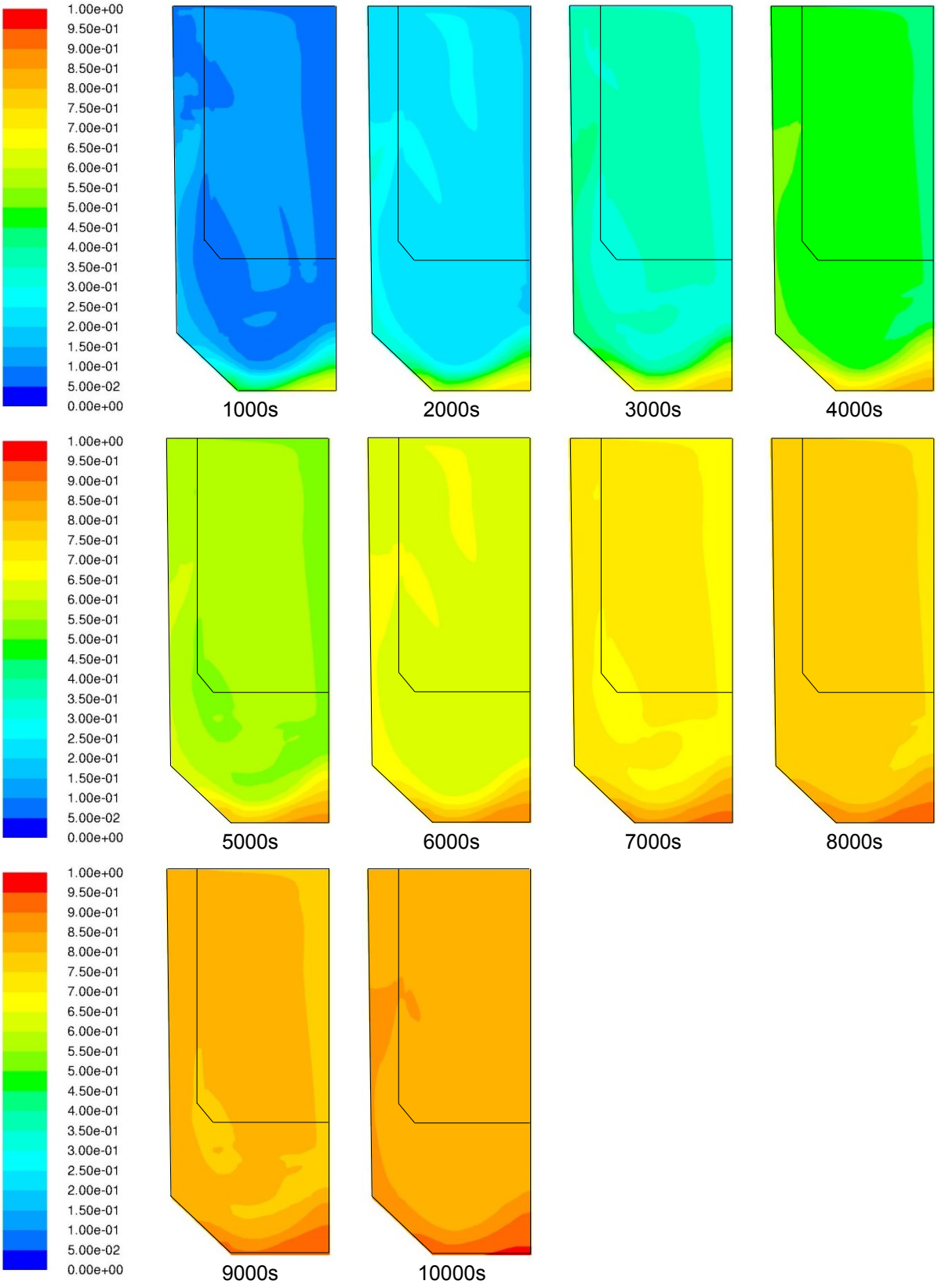

Figure 60: Tracer distribution at first anode

6.3 Comparison between simulation and experiments

The figures Figure 61 to Figure 63 show the comparison between the simulations (lines) und the experimental measurements (points).

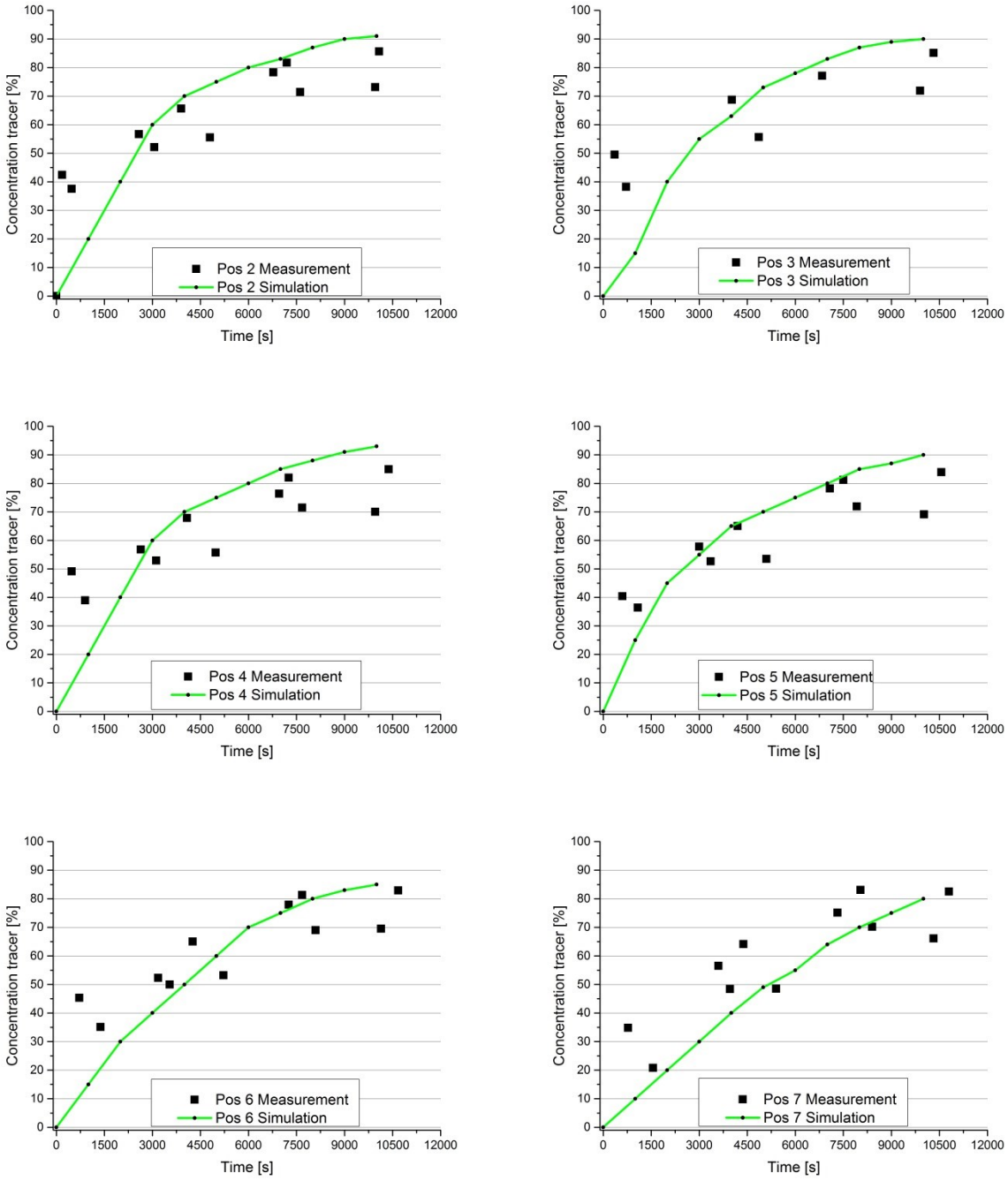

Figure 61: Comparison between Simulation and Experiments I

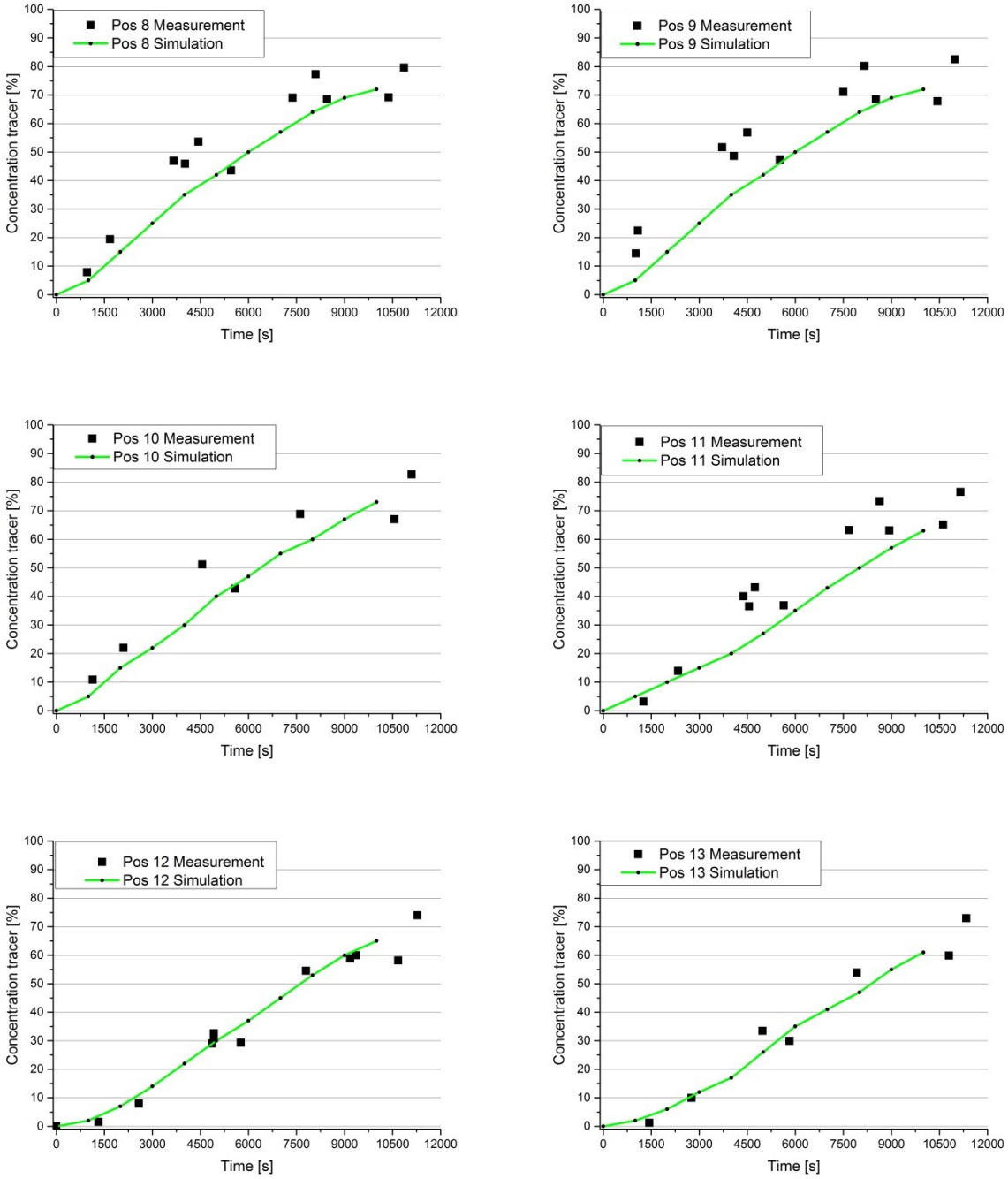

Figure 62: Comparison between Simulation and Experiments II

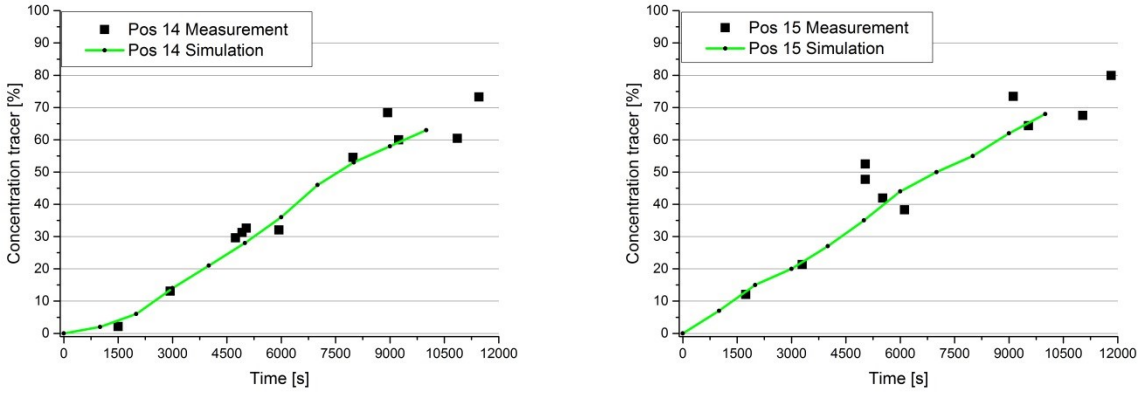

Figure 63: Comparison between Simulation and Experiments III

6.4 Summary and discussion of the validation

The simulation results are in good agreement with the experimental measurements. A small variation can be found only at the first three measurement point (#2, #3, and #4) before the first anode. Here the experiments suggest a concentration of 40 % after only 200 s. The simulation model however reaches these levels of concentration after 2000 s. After 3000 s the simulation results are in good agreement again.

The results also show a wide variation of measured concentrations especially in the first half of the tankhouse cell. Here a variation in concentration of up to 15 % can be found.

7 Behavior of Inhibitors

Inhibitors are added to the electrolyte to ensure a smooth, hard and dense cathode surface and hence prevent short circuiting of the electrical connections. Usually small amounts of 65 to 75 g/ton copper of glue and thiourea is added to the electrolyte before entering the tankhouse cell are enough to ensure a high quality copper cathode [73, 74]. The leveling mechanism of glue and the grain-fining mechanism of thiourea can be summarized as followed:

- The cathode leveling ability of glue is caused by its ability to electrodeposit large protein molecules at the tips of protruding, rapidly growing copper grains. This deposit creates an electrical barrier at the tips of the copper crystals preventing further growth. The net result is the formation of a dense and level growth without the formation of dendrites [75, 76].

- The grain-refining abilities of chlorine ions and thiourea are still subject to research. A possible explanation can be found in the formation of Cu-Cl-thiourea which electrodeposits on the cathode surface and might act as nucleation sites for new copper crystals [77, 78].

For the simulation of inhibitors the focus was set primarily on the activity of glue. In the tankhouse cell the glue is subject to two major mechanisms. Firstly the high temperatures and acid contents of the electrolyte lead to the decomposition of the glue via hydrolysis reaction and decrease the glue activity. Secondly the main task of glue is to deposit onto the copper grains on the cathodes, which further reduces the activity. The combination of these two mechanisms is responsible for the distribution of glue activity in the tankhouse cell. In industrial tankhouse cells a third mechanism can be observed: the absorption of glue in the anode slime layer. Since the formation of this slime layer however is not part of this simulation, this effect is not considered.

7.1 Decay of glue

Figure 64 shows the activity development when glue is added into fresh copper electrolyte that previously contained no glue. The activity will at first rise and after 10 to 15 minutes drop significantly. This is caused by very long chained but inactive molecules in the glue. When these chains break down and form smaller, but active molecules due to hydrolysis reactions, the overall activity in the electrolyte rises [79]. After this initial increase, the glue activity quickly decreases as the now formed shorter molecule chains have a less than optimal size [80].

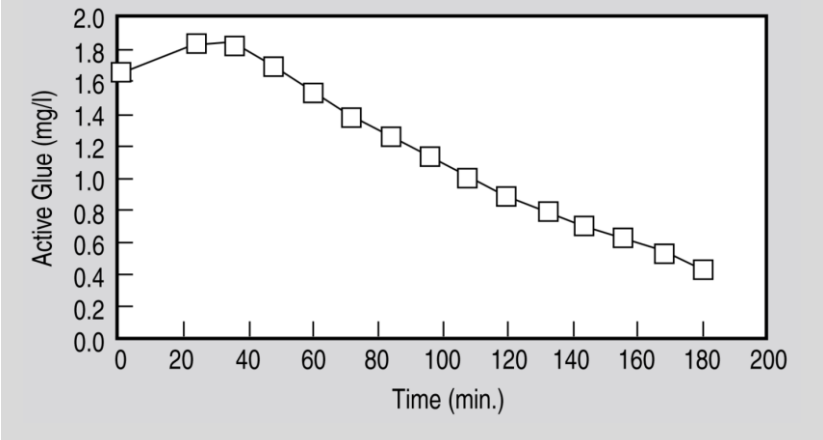

Figure 64: Glue decay in a tankhouse electrolyte [80]

The rate of decay can be measured in laboratory experiments and is dependent on multiple factors such as acid concentration and electrolyte temperature, as shown in Figure 65. An increase in acid concentration from 120 g/l to 240 g/l results in a reduction of half lifetime from 115 min to 30 min. Similarly an increase in temperature from 50 °C to 70 °C results in a decrease in half lifetime from 145 min to only 20 min.

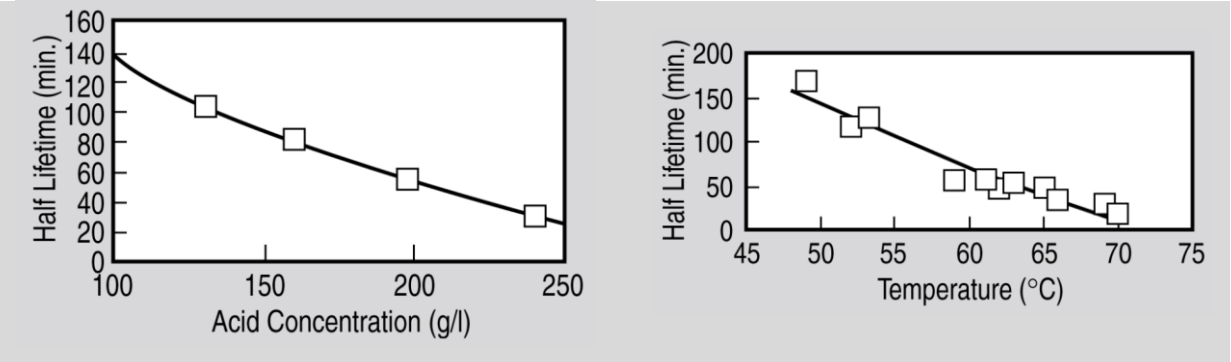

Figure 65: Glue half lifetime dependence on acid concentration (left) and temperature (right) [80]

For the simulation of the glue decay the knowledge of the exact decay rate is necessary. In agreement with the industrial partners, the half lifetime of the inhibitor (glue) was chosen to be 90 minutes. The decomposition of glue in electrolyte is a hydrolysis reaction which takes place according to the following reaction equation:

$$A + B = C + D \qquad \text{Eq. 7-1}$$

With A being the glue and B the water content in the electrolyte and C and D are the reaction products. The reaction rate can be written as followed:

$$-\frac{d[A]}{dt} = k_2 \cdot [A] \cdot [B] \qquad \text{Eq. 7-2}$$

Here $[A]$ and $[B]$ are concentrations for glue and water and k_2 is the reaction constant. Since the concentration of water $[B]$ is much larger than the concentration of glue it can be considered constant for the reaction. Therefore the equation can be simplified to:

$$k_2 \cdot [B] = k' \qquad \text{Eq. 7-3}$$

$$-\frac{d[A]}{dt} = k' \cdot [A] \qquad => \qquad \frac{1}{[A]} \cdot d[A] = -k' \cdot dt \qquad \text{Eq. 7-4}$$

Therefore the decay (hydrolysis) can be described as a reaction of pseudo first order for which the reaction rate and therefore the half lifetime is independent of the initial concentration [81]. By integration of equation 7-4 one obtains:

$$\int_{[A]_0}^{[A]} \frac{1}{[A]} \cdot d[A] = -k' \cdot \int_0^t dt \qquad \text{Eq. 7-5}$$

$$\ln\left(\frac{[A]}{[A]_0}\right) = -k' \cdot t \qquad => \qquad [A] = [A]_0 \cdot e^{-k' \cdot t} \qquad \text{Eq. 7-6}$$

With the known half lifetime of $t_{1/2}$ = 90 min the reaction rate can be calculated to:

$$\frac{[A]_{t=90\,\mathrm{min}(5400s)}}{[A]_0} = 0.5 \qquad => \qquad k' = \frac{\ln(0.5)}{t_{1/2}} \qquad \text{Eq. 7-7}$$

$$k' = 1.28361 \cdot 10^{-4}$$ Eq. 7-8

With the reaction rate the activity of glue due to decay can be calculated in the simulation. The source term for the glue decay can be obtained by multiplying the reaction rate with electrolyte density and local glue activity. The UDS source code for the glue decay is shown in Appendix 1.4. Since the decay occurs in the whole tankhouse cell, a source term has the unit [kg/m³s].

7.2 Consumption of glue

The mechanics behind the consumption of glue at the cathodes are not entirely researched but it is safe to assume that the electrodeposition is dependent on the current density at the cathode surface. Rather than researching a new consumption mechanism without the possibility to validate the results, it was decided together with the industry partners to choose an empiric approach.

The empirical know how provided by the industry partners suggests a ration of Decay/Consumption of 3/1. The effect of decay, due to high temperature and acid concentration, on the glue activity is three times larger than the effect of consumption at the cathodes. The consumption occurs only at the cathodes and can be set up as a boundary condition with the unit [kg/m²s]. The UDS source code is listed in Appendix 1.3.

Since the decay itself is a function of glue activity the overall decay rate at steady state is not known a priori and must be simulated. This first simulation was set up without consumption and achieves only a start value for further calculations. Based on this start value the initial consumption constant could be obtained by adjusting the consumption constant until the 3/1 ration was met. The consumption constant was set as a boundary condition at the cathodes for the next simulation until a new steady state result was obtained. Naturally the overall glue activity decreased due to the additional boundary condition and as a result the activity dependent decay rate changes, resulting in a new consumption constant. This iterative simulation scheme had to be continued until a conclusive consumption constant of $1.2166 \cdot 10^{-3}$ was found. This final consumption constant was used in all following glue activity simulations.

7.3 Simulation of glue activity distribution

Since the copper electrorefining electrolysis process lasts several weeks, the best representation of reality can be achieved by calculating the glue activity in a steady state configuration. The simulation on glue activity distribution is set up on the steady state electrolyte flow result obtained by the global simulation. As described in chapter 5.4 the steady state result can be obtained by time averaging over the velocity results oscillating around a mean value. FLUENT can only display this time averaged results for post processing applications but cannot use time averaged values for further calculations. Therefore a UDS was created to overwrite the velocity values stored in the cells with the time averaged velocity values. The UDS source code for the UDS Define_velocity is listed in Appendix 1.5. After simulating for one time step the averaged values are written in the cells but the fluxes between cells are not changes. To correct this wrong fluxes and smooth the velocity field a number of iterations must be simulated using a very small time step size. The finally obtained velocity field can now be used to simulate the glue activity. The simulation approach is listed in Table 14.

Table 14: Simulation approach for the inhibitor activity calculation

1:	Simulation of the transient velocity field until result is oscillating around a mean value
2:	Time averaging the oscillating velocity field (typically 60-80s)
3:	Overwrite cell values with mean values by compiling UDS Define_Velocity
4:	Simulate one time step (Δt=0.1 s) to overwrite cell values
5:	Unload Define_Velocity and remove the mean cell values
6:	Simulate 10 time steps (Δt=0.001 s) to obtain correct fluxes and a smooth velocity field
7:	Compile UDS_Define_Decay, UDS_:Define_Consumption and UDS_Define_Diffusivity
8:	Perform a steady state simulation for inhibitor activity

8 Parameter study

The goal of this work is to optimize the electrolyte flow in conventional cross flow electrorefining tankhouse cells. The results shown up to this point were taken from a simulation of the actual tankhouse cell used in the Pirdop refinery. These results are therefore the standard against which all other simulation results are measured against.

The following parameters have been investigated in the simulation trials:

- Variation of the inlet angle
- Variation of the vertical inlet position
- Variation of the horizontal inlet position
- Variation of the inlet shape
- Variation of the mass flow
- Variation of the inlet number
- Study on the effects of different crops

Especially interesting are the effects on the electrolyte velocity profile in the bulk and the distribution of inhibitors in the whole electrolysis cell. All simulation results were compared against the standard case of a 45° inlet angle.

8.1 Electrolyte flow conditions

Figure 66 shows the pathlines, colored by vacancy time, for this standard case. For better visibility the results are mirrored along the symmetry centerline of the simulation domain. The direction of the pathlines is given by the velocity vectors in each volume element and shows the path a small amount of electrolyte would take through the tankhouse cell entering at the inlet.

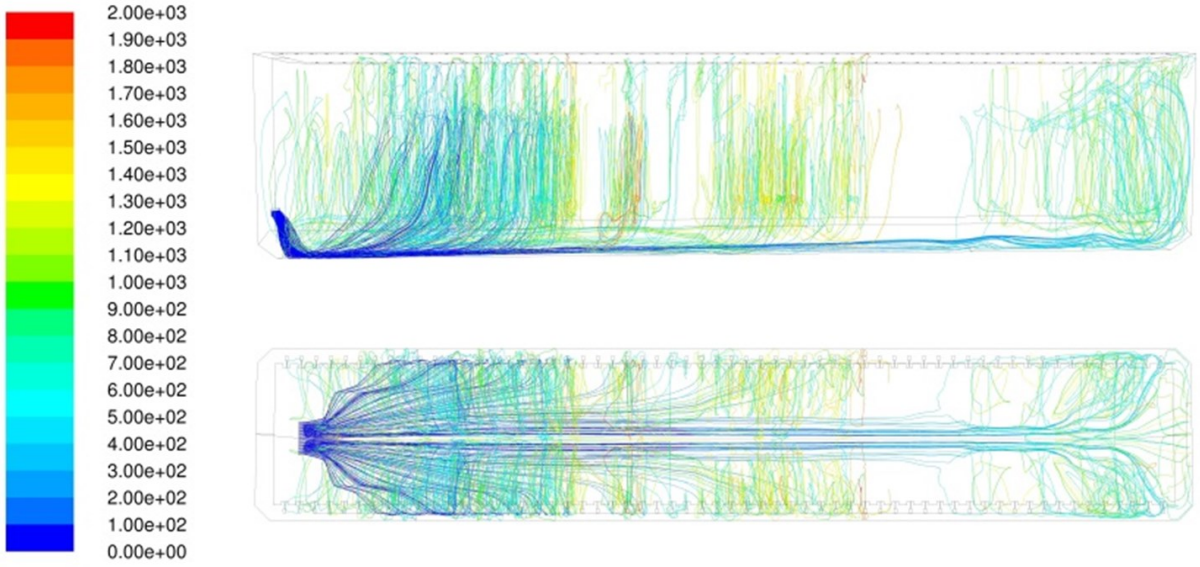

Figure 66: Pathlines colored by residence time for a 45° inlet angle

Figure 67 shows the electrolyte flow conditions in the bulk underneath and to the sides of the first electrode. In the figure the electrolyte velocity in z-direction (direction from the outlet to the inlet, see Figure 49) can be seen. Negative velocities (blue) are directed from the inlet towards the outlet, while positive values (red) are flowing in the opposite direction. At the first cathode, near the inlet the electrolyte velocity reaches values of up to 5 cm/s. Further away from the inlet, the maximum velocity drops to 1-2 cm/s.

When analyzing the flow direction it can be seen that in the first third of the tankhouse cell the electrolyte flow at the bottom is directed towards the outlet, but a significant part of electrolyte flow directly underneath the electrodes is directed towards the inlet. At the sides the flow direction is directed towards the outlet, except for the area just underneath the bath surface, here the electrolyte is again flowing back towards the inlet.

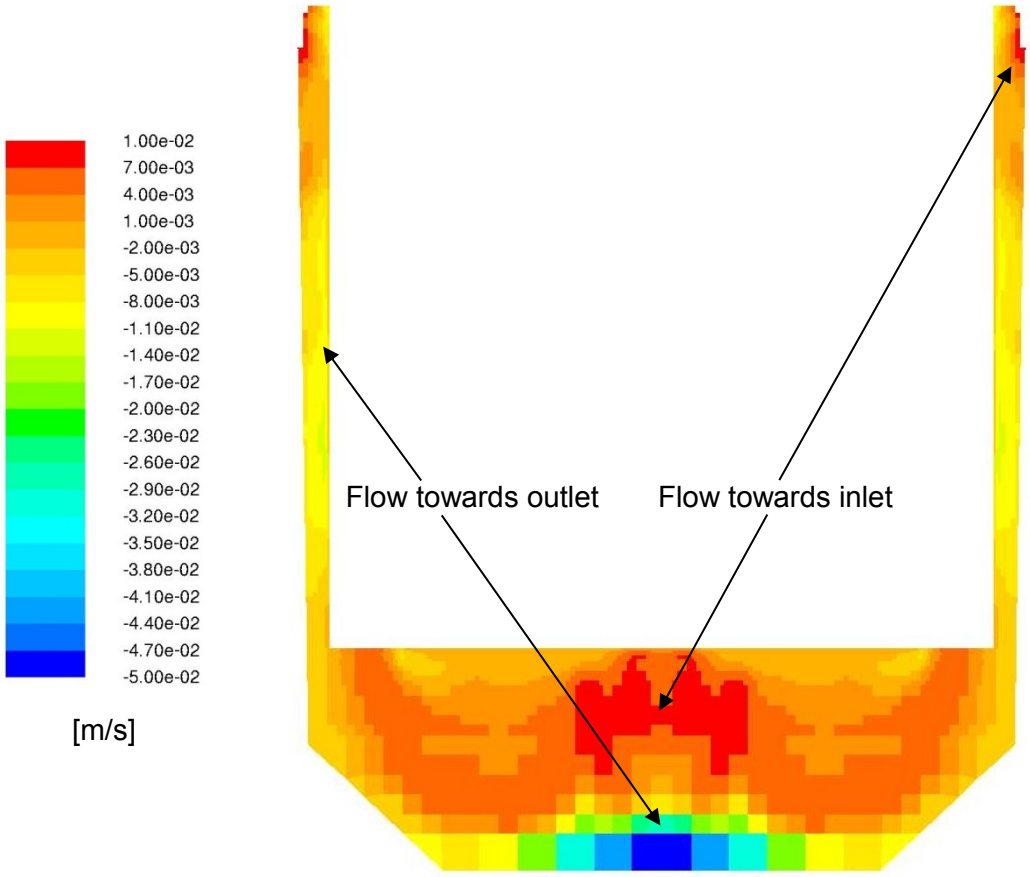

Figure 67: Vertical cut at centerline of the first cathode showing the velocity and direction of electrolyte flow; negative values (blue-orange) are moving towards the outlet; positive values (orange-red) are moving towards the inlet

Figure 68 shows the course of electrolyte flow at different positions in the electrolysis cell. It can be seen that close to the outlet, the electrolyte underneath the electrodes is now flowing only towards the outlet. The electrolyte flow at the sides also changes: the electrolyte is now directed towards the inlet.

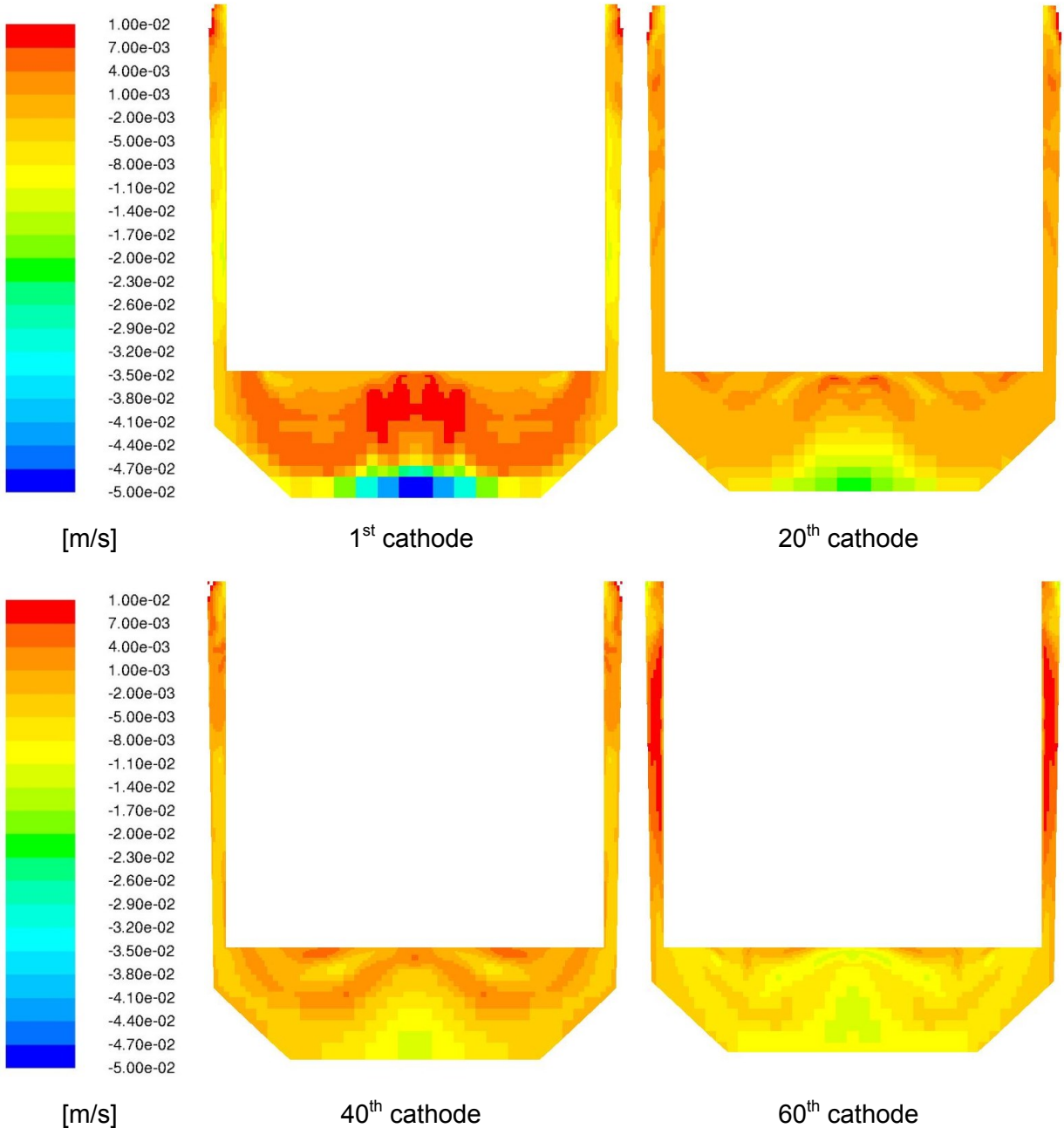

Figure 68: Vertical cut at center line of 1st, 20th, 40th and 60th cathode; velocity and direction of the electrolyte

This transition of flow patter can also be seen in Figure 69 and Figure 70. Close to the inlet the electrolyte forms a bottom layer flowing towards the outlet and an intermediate layer directed towards the inlet. This reverse directed electrolyte flow, together with the highly chaotic flow patterns underneath the electrodes, lead to a high mixing of the incoming electrolyte close to the inlet and to a homogeneous distribution of inhibitors especially in the first third of the tankhouse cell.

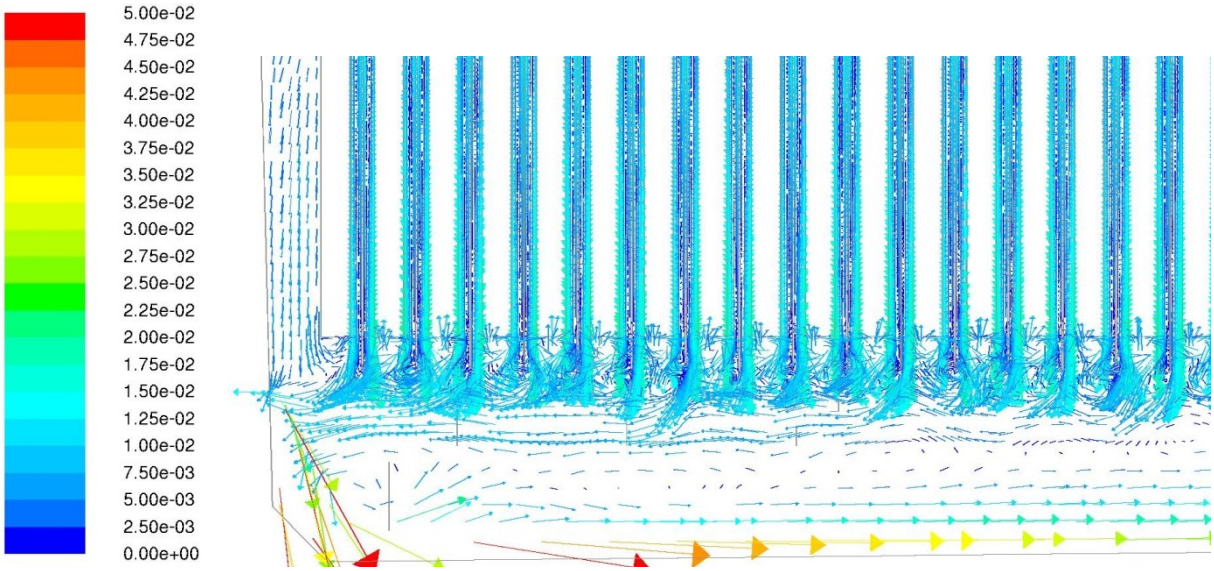

Figure 69: Vertical cut at symmetry centerline showing the electrolyte flow close to the inlet; visible is the formation of a bottom layer directed towards the outlet, an intermediate layer directed towards the inlet and the top layer of highly chaotic velocity vectors

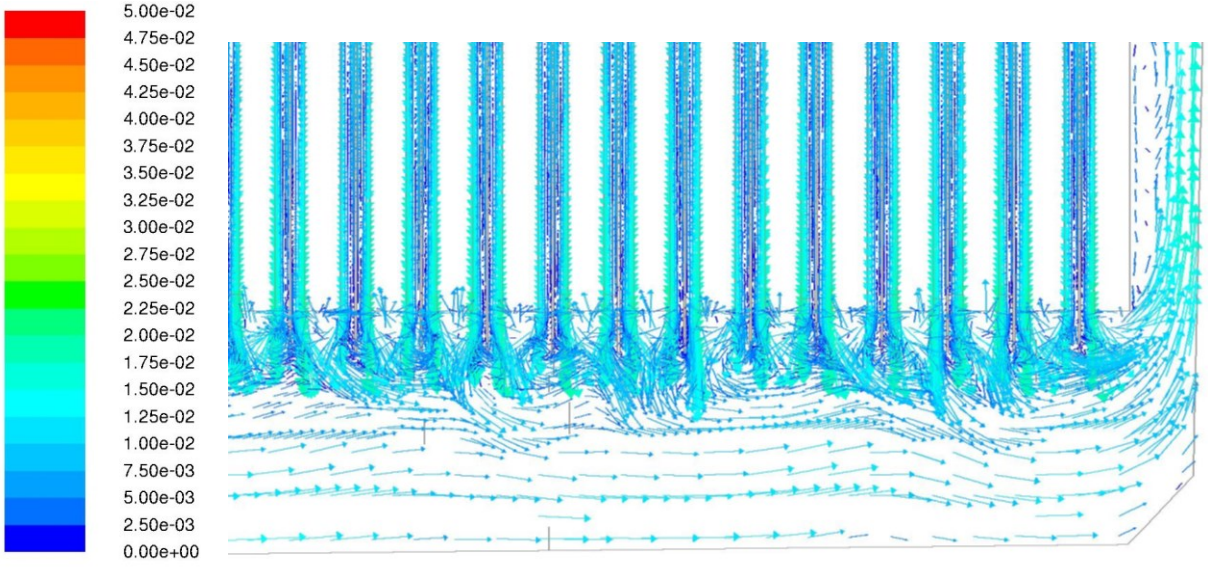

Figure 70: Vertical cut at symmetry centerline showing the electrolyte flow close to the outlet; underneath the chaotic top layer the electrolyte flow is directed exclusively towards the outlet

8.2 Inhibitor distribution

The inhibitor distribution in the tankhouse cell is shown in Figure 71. In first third of the tankhouse cell an activity in the electrode gaps of 70 - 75 % can be observed. This coincides with the reversed flow patterns found in this area. In the later parts of the tankhouse cell the inhibitor activity in the electrode gaps gradually decreases and reaches its minimum close to the outlet. This can be explained by the steady decomposition of the inhibitor and its consumption at the electrodes. The electrode gaps close to the inlet are supplied by electrolyte that had not yet had the time to decompose or get consumed.

At the bottom of the electrolysis cell a layer of high activity inhibitor can be found. This can be explained by the layer of high velocity electrolyte coming from the inlet and flowing towards the outlet. From this bottom layer the inhibitor is transported into the electrode gaps.

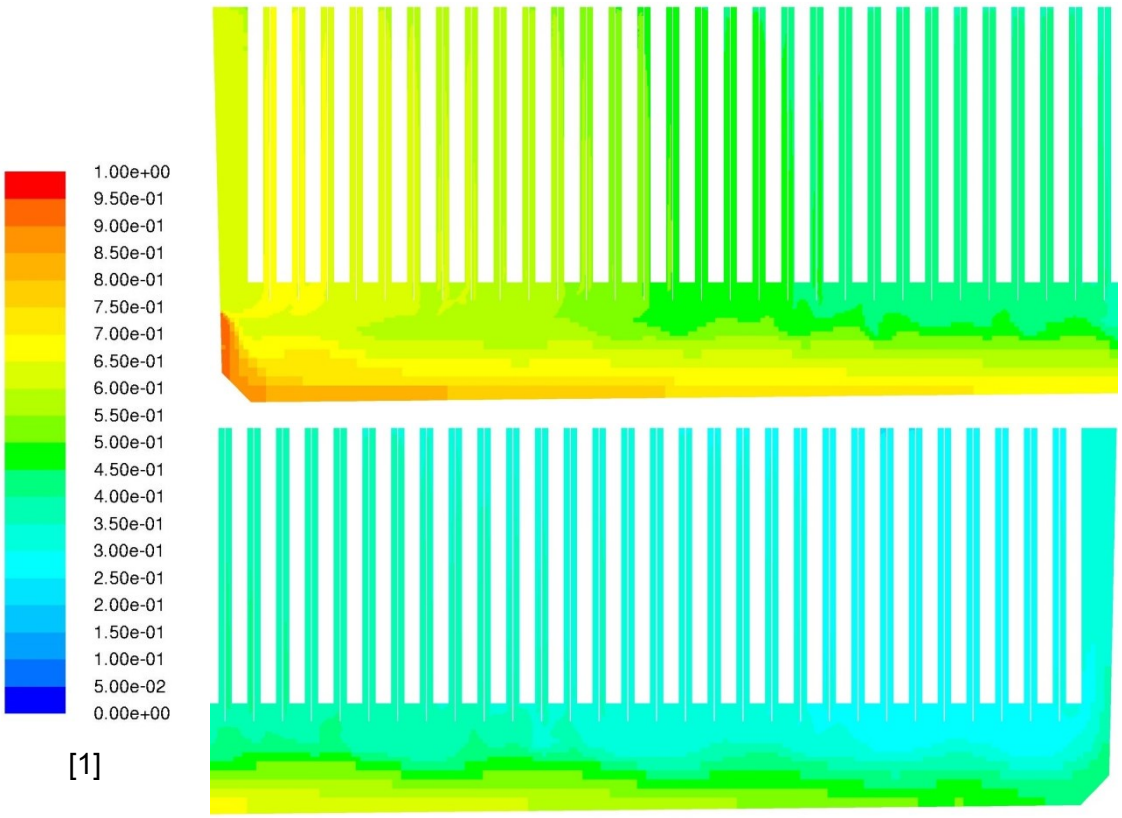

Figure 71: Vertical cut at symmetry centerline showing the inhibitor distribution in the tankhouse cell

The location of the minimum inhibitor activity and the overall activity distribution can be seen in Figure 72 to Figure 74. The absolute minimum in inhibitor activity is 23.6 % for the standard case. This value can be found just underneath the bath surface at the 54th anode near the symmetry centerline. Besides the minimum value, the distribution around this minimum is also of interest.

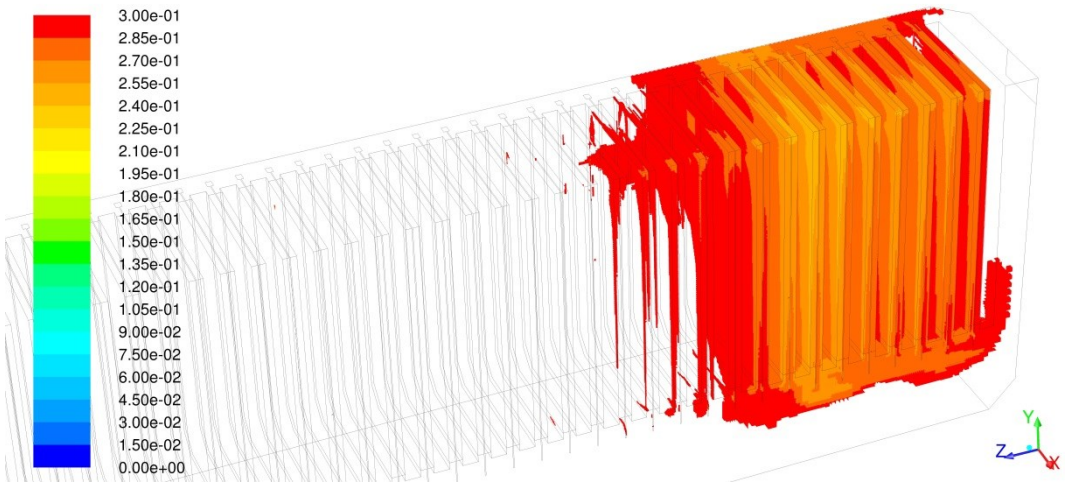

Figure 72: Inhibitor activity distribution (0 - 30 %) for the 45° inlet angle standard case

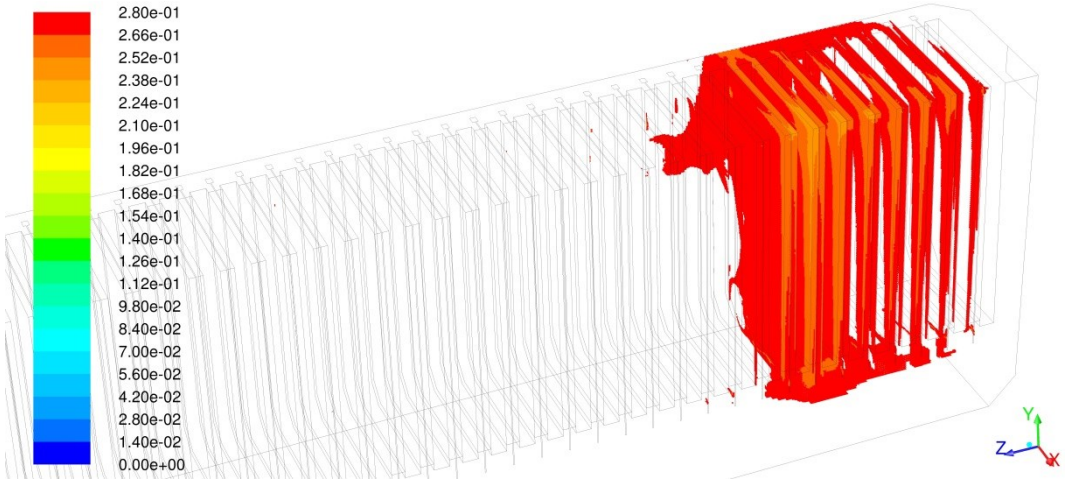

Figure 73: Inhibitor activity distribution (0 - 28 %) for the 45° inlet angle standard case

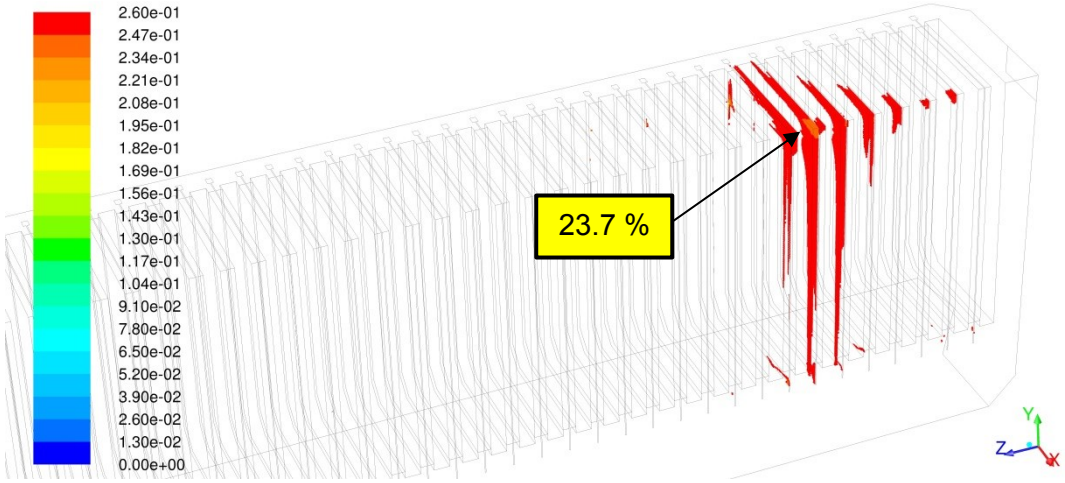

Figure 74: Minimum inhibitor activity for the 45° inlet angle standard case

8.3 Variation of the inlet angle

A fast and easy to implement way to change the electrolyte flow in the tankhouse cell is to adapt the inlet geometry. In the first optimization trials the angle of the inlet manifold was changed to observe the impact on the electrolyte flow patterns. Figure 75 shows the chosen geometries. The standard case (45 °) was compared to the simulation results using a shallow inlet (35° and 40°) and the results using a steeper inlet (50° and 55°).

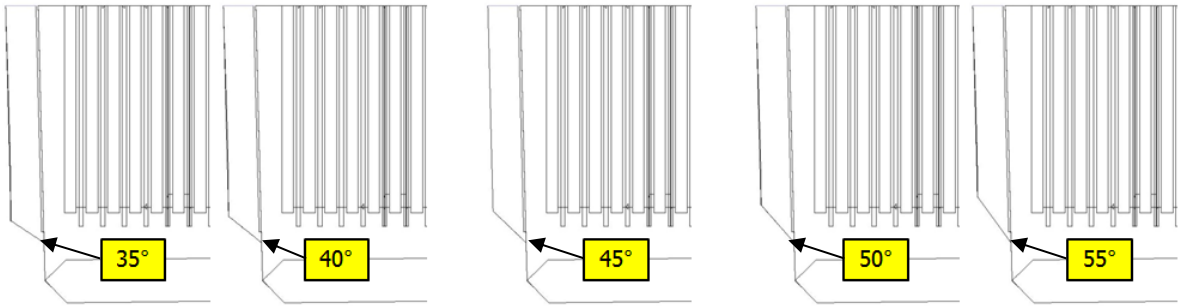

Figure 75: Inlet design with different angles, the 45° standard case was compared with the shallow cases (35° and 40°) and the steeper cases (50° and 55°)

Figure 76 and Figure 77 show the pathlines for the different inlet angles. The pathlines are colored by residence time [s]. In all four cases the electrolyte entering the tankhouse cell at the inlet forms a layer on the bottom. This layer travels along the tankhouse cell bottom towards the outlet and reaches the far side end after approximately 600 s. From this layer some of the electrolyte is transported upwards along the side walls into the electrode gaps.

When comparing the pathlines of the shallow and steep inlet angles, it can be seen that in the shallow cases the pathlines in the last third of the tankhouse cell (the position of the minimum inhibitor activity) are older, i.e. it takes more time for the electrolyte to reach this position. This means that the inhibitor is longer exposed to decomposition resulting in lower inhibitor activity. In the steeper cases the pathlines in the last third are younger, i.e. the electrolyte from the inlet reaches this position faster resulting in a higher remaining inhibitor activity.

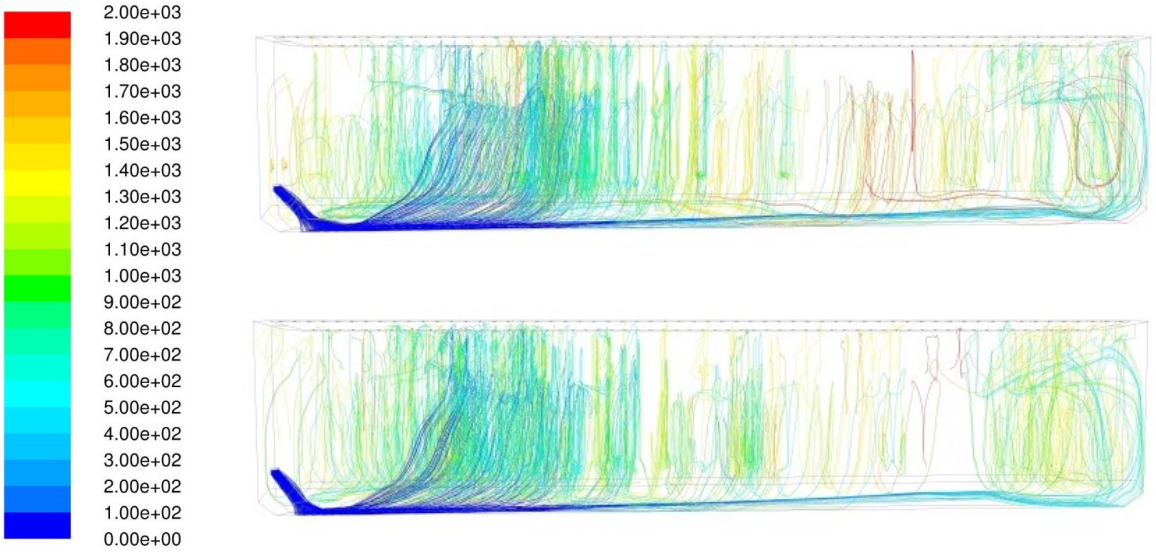

Figure 76: Pathlines colored by time [s]; shallow inlet angles: 35° (top) and 40° (bottom)

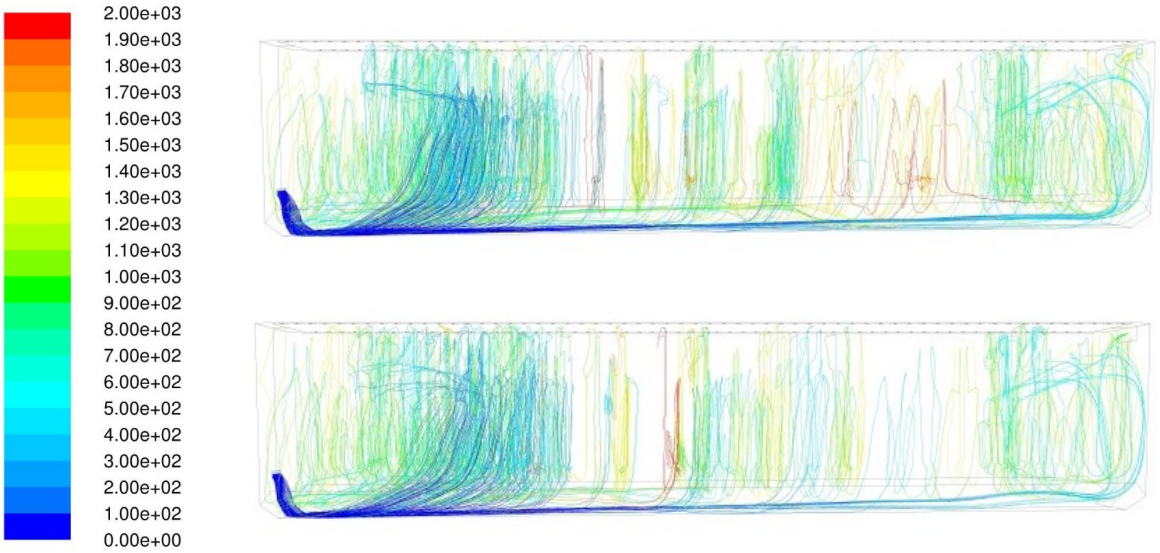

Figure 77: Pathlines colored by time [s]; steep inlet angles: 50° (top) and 55° (bottom)

Figure 78 and Figure 79 show the minimum and average inhibitor activity in the electrode gaps. In all four cases the changing of the inlet angle results in an increase of inhibitor activity in the first half of the tankhouse cell. The shallow inlet angles show higher inhibitor activities in the first half (until gap #50) of the tankhouse cell. Between gap #50 and gap #85 all four inlet angles perform very similar. In the last part (gap #85 to gap #120) the steep inlet angles show a higher inhibitor activity than the shallow angles and the standard 45° inlet angle. The average inhibitor activities show a very similar behavior.

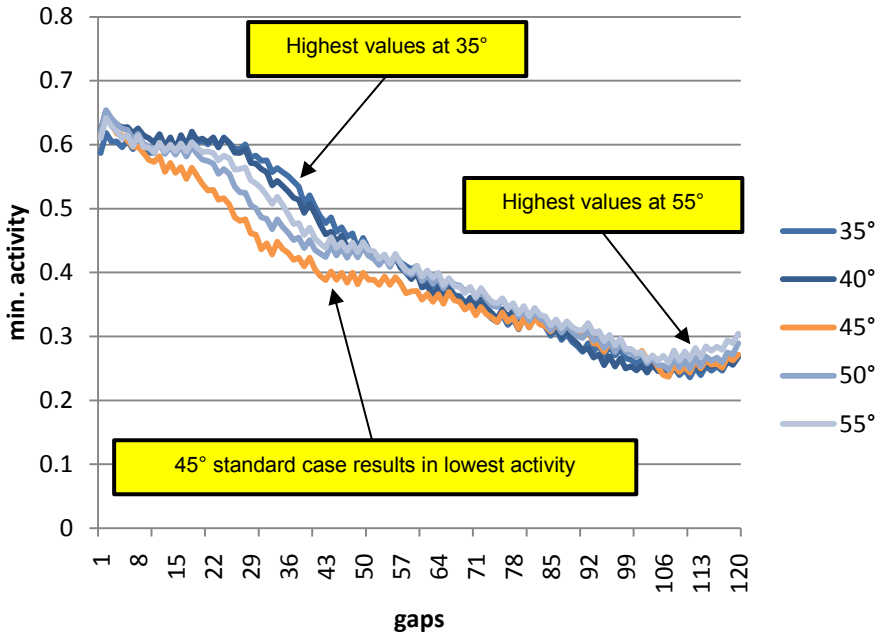

Figure 78: Minimum inhibitor activity at different inlet angles

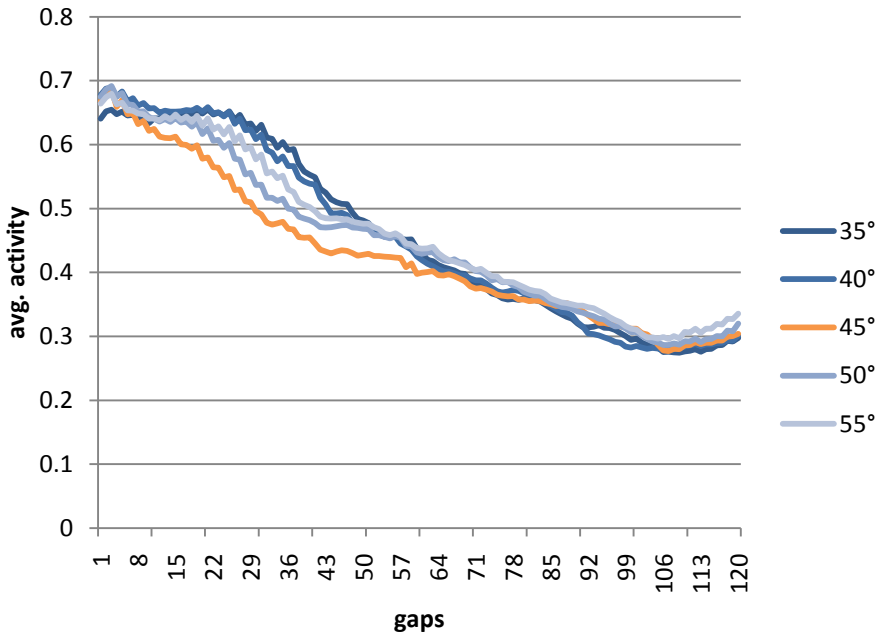

Figure 79: Average inhibitor activity at different inlet angles

Figure 80 shows the distribution of inhibitor activity and the minimum inhibitor activities for the four inlet angles. Since the minimum value is not the only important factor, the figure also shows the distribution of the inhibitor activity below 30 %. The arbitrary value was chosen to allow a comparison of the different inlet angles.

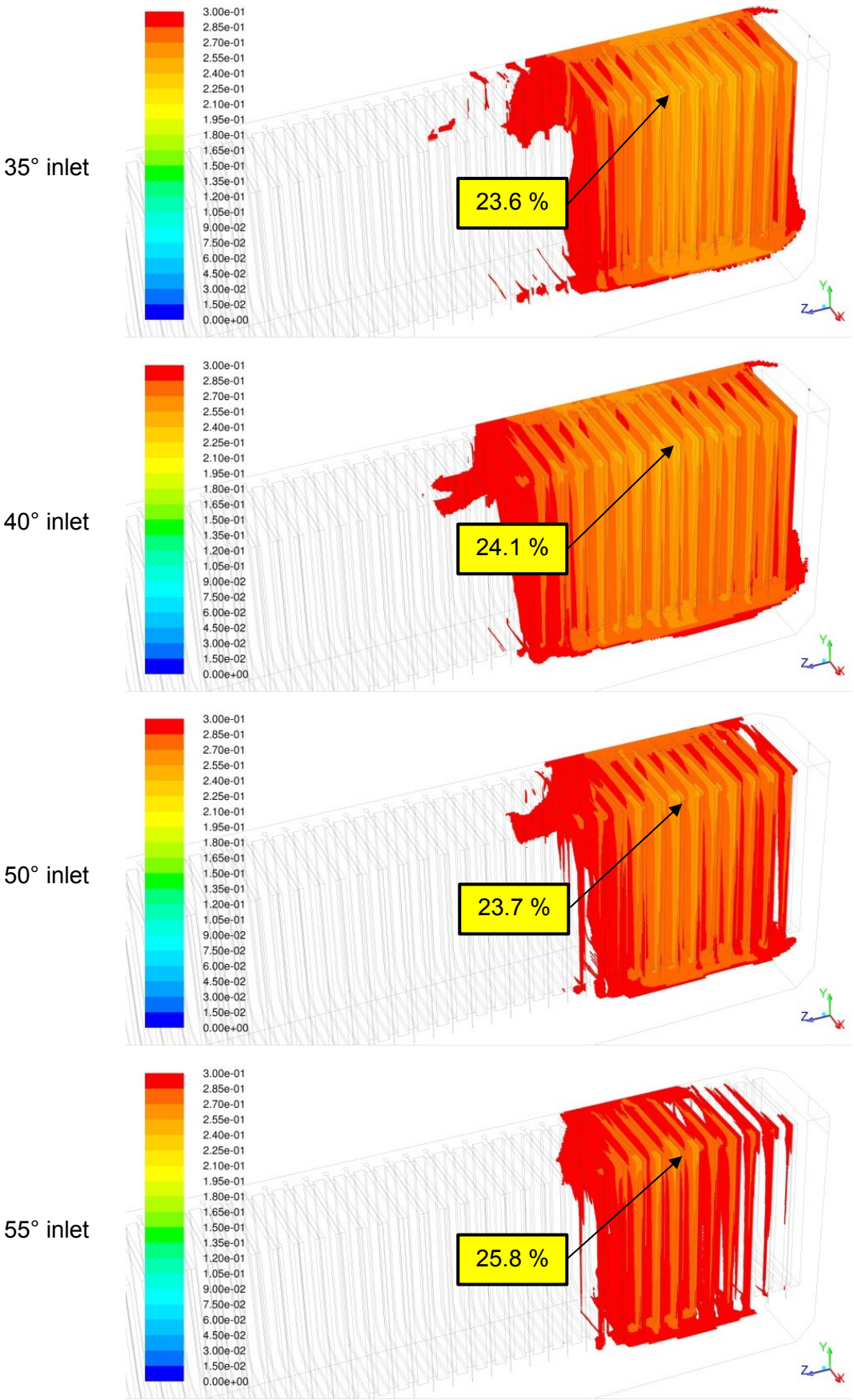

Figure 80: Distribution and minima of inhibitor activity for the different inlet angles

In the figure above the white areas have an inhibitor activity higher than 30 %. The optimum case does not only need to have a high minimum inhibitor activity but this minimum should also be localized in a small area. In this part of the parameter study the best results can be found with the 55° inlet case. It has the highest minimum value of 25.8 % and the smallest number of cathodes with inhibitor activities lower than 30 %. The results are shown in Table 15.

Table 15: Results of the inlet angle study

Case	# cathodes < 30 %	Lowest activity
35° inlet	11	23.6 %
40° inlet	15	24.1 %
Standard case	13	23.7 %
50° inlet	12	23.7 %
55° inlet	11	25.8 %

8.4 Variation of inlet elevation

The second parameter study included the variation of the inlet height. In the standard case the lower edge of the inlet nozzle is located 275 mm above the bottom. Figure 81 shows the different inlet designs used in this parameter study. For the high inlet cases the distance between inlet nozzle and tankhouse cell bottom was increased by 75 mm resulting in 350 mm for High 1 and 425 mm for High 2. For the lower inlet cases the distance was decreased by the same value resulting in 200 mm for Low 1 and 125 mm for Low 2, as shown in Table 16.

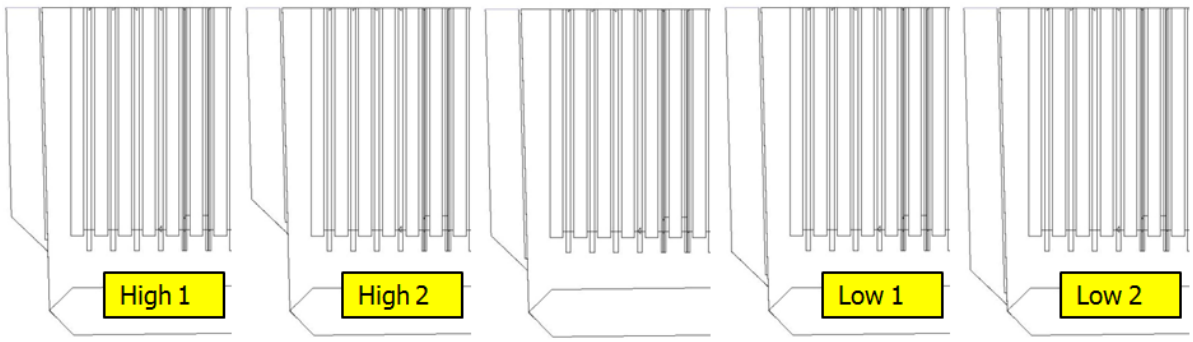

Figure 81: Inlet designs for the variation of inlet height studies: The standard case was compared to two low inlet cases (Low 1, Low 2) and two high inlet cases (High 1 and High 2)

Table 16: Variation of inlet elevation

Name	Short name	Distance bottom-inlet
Standard case		275 mm
High elevation 1	High 1	350 mm
High elevation 2	High 2	425 mm
Low elevation 1	Low 1	200 mm
Low elevation 2	Low 2	125 mm

Figure 82 und Figure 83 show the pathlines for the different inlet cases. Higher resolution figures are shown in the Appendix. The figures indicate that in all four cases the electrolyte entering at the inlet form a bottom layer from which the electrode gaps are fed. In the case of High 1 (350 mm above bottom) the bottom layer takes longest to reach the far side. Additionally there is a high concentration of pathlines directly above the inlet so a high mixture of the electrolyte can be expected in this area. In the High 2 case (425 mm above the bottom) reaches the far side much quicker and shows a better mixture in the last quarter of the tankhouse cell. Low 1 and Low 2 show a very similar behavior. In both cases the electrolyte reaches the outlet in a sufficiently short time, resulting in a higher remaining inhibitor activity. The pathlines in both cases also show a homogenous distribution in the tankhouse cell, while especially for the case of Low 2 a high concentration of pathlines can be found in the last quarter.

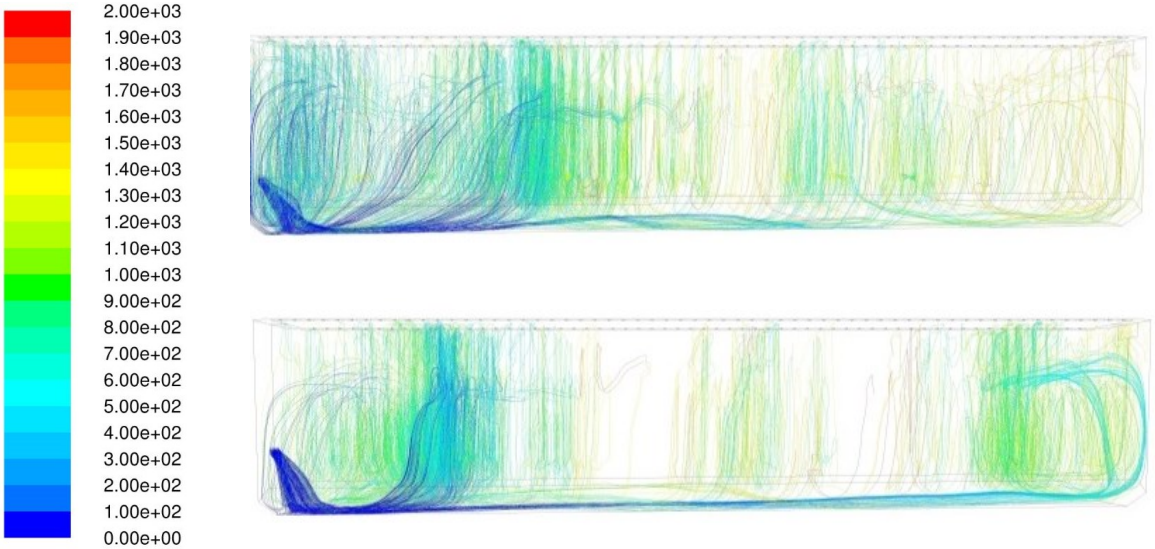

Figure 82: Pathlines colored by time [s]; High elevation cases: High 1 (top) and High 2 (bottom)

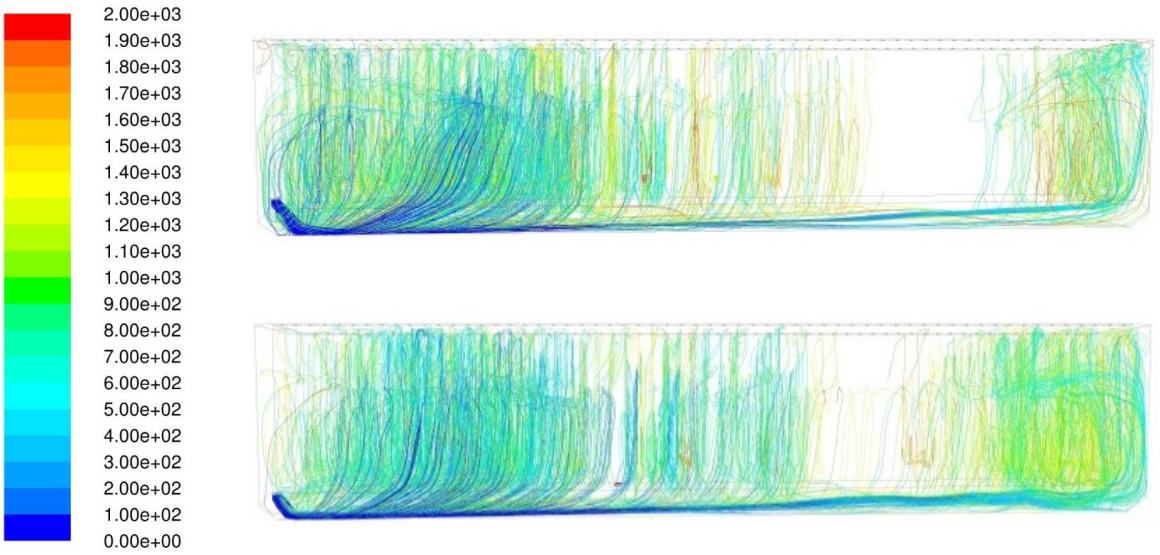

Figure 83: Pathlines colored by time [s]; Low elevation cases: Low 1 (top) and Low 2 (bottom)

Figure 84 and Figure 85 show the minimum and average inhibitor activity in the electrode gaps. As predicted by the pathlines, High 1 indicates very high activity levels in the first third of the tankhouse cell but quickly drops below Low 1 and Low 2 in the second half. In the middle part of the tankhouse cell Low 2 results in the highest minimum and average inhibitor activities, but only performs very badly in the very first part close to the inlet. Apparently the low inlets perform better in the later parts of the tankhouse cell but the electrolyte is partially directed away from the first few electrodes. In the electrode gaps close to the outlet the activity levels are very close together. However the highest minimum could be observed in the Low 2 case and the lowest activity was in High 1.

By comparing the minimum and average activity it can be observe that the distribution of inhibitor activity inside the electrode gaps is very homogenous. Inside an electrode gap the difference between minimum and average values is usually less than 5 %.

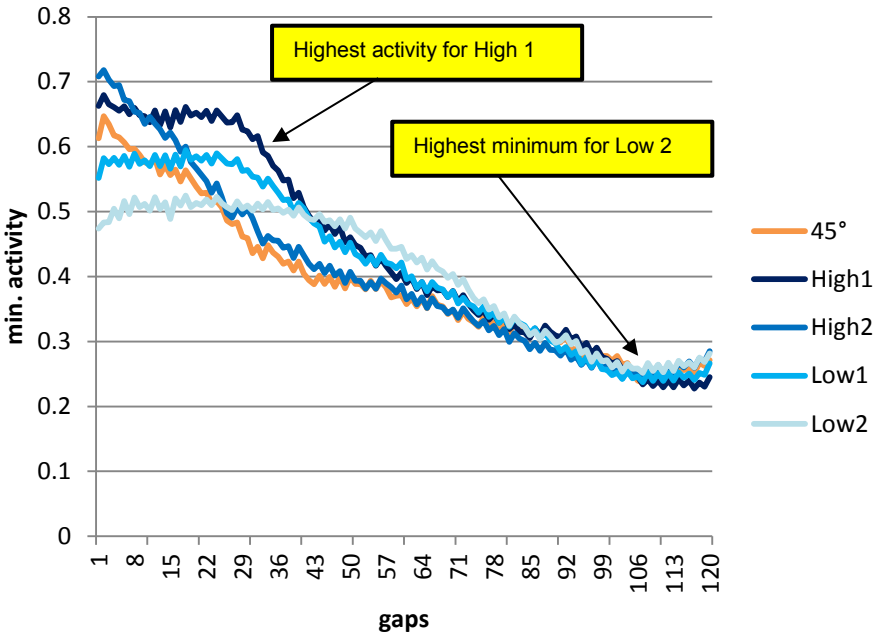

Figure 84: Minimum inhibitor activity at different inlet elevations

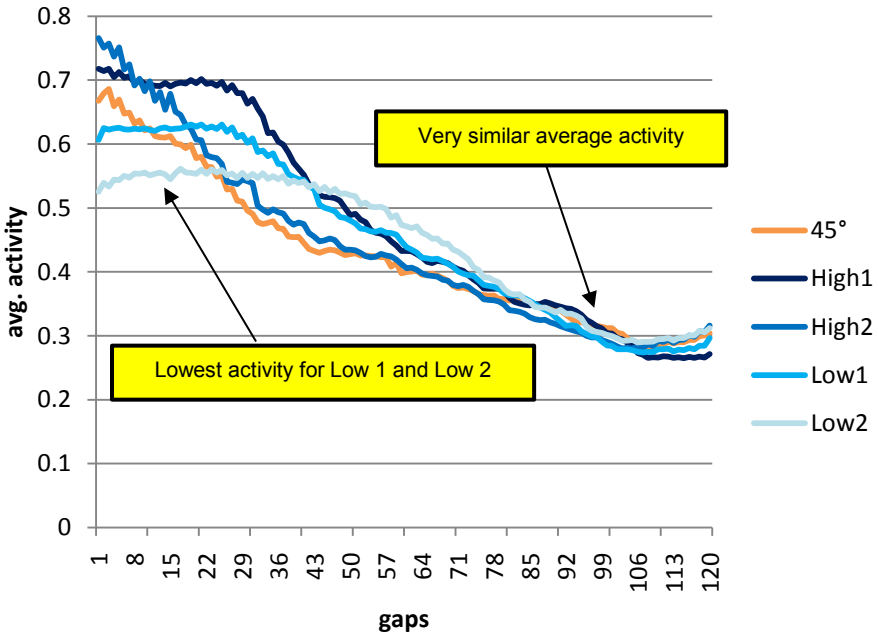

Figure 85: Average inhibitor activity at different inlet elevations

Figure 86 shows the inhibitor activity distribution and the minimum activity for the four inlet elevation cases. In terms of minimum activity the Low 2 case performs best even if the differences are very small (less than 1 % between High 2 and Low 2). The distribution of the inhibitor activity < 30 % shows very similar results. For the case High 1 the activity at the outlet drops below 30 % but the number of cathodes with activities < 30 % is smaller than in

the cases High 2 and Low 1. In the case Low 2 only 12 cathodes with low activity inhibitor can be found. The results are shown in Table 17.

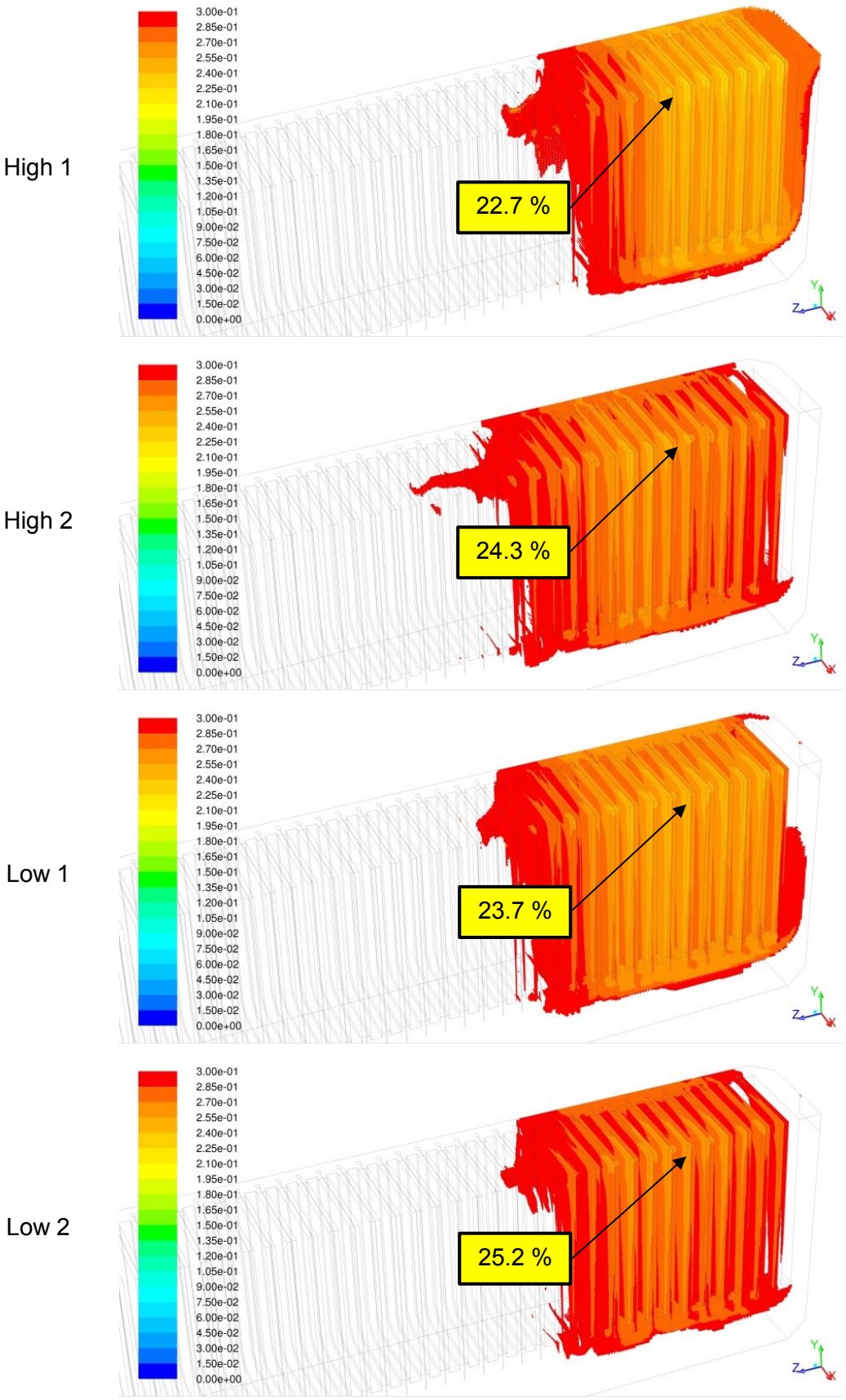

Figure 86: Distribution and minima of inhibitor activity for the different inlet elevations

Table 17: Results of the inlet elevation study

Case	# cathodes <30 %	Lowest activity
High 1	13	22.7 %
High 2	15	24.3 %
Standard case	13	23.7 %
Low 1	15	23.7 %
Low 2	12	25.2 %

8.5 Variation of the inlet shape

The variation of inlet shape was performed in a way to ensure a constant inlet nozzle area. This ensured a constant average velocity for the given mass flow rate of 42 l/min. The used inlet shapes are shown in Figure 87 and Table 18. For the cases Inlet 1 and Inlet 2 a wider but thinner shape was chosen, to channel the bottom electrolyte layer over a wider area. The cases Inlet 3 and Inlet 4 use a taller but narrower inlet shape. Here the motivation was to concentrate the bottom electrolyte layer in a narrow channel to decrease the transport time to the cathodes close to the outlet. Inlet shape 4 is special in the way that is has a square inlet nozzle shape.

Figure 87: Inlet designs for the variation of inlet shape studies: The standard case was compared to two wide inlet cases (Inlet 1, Inlet 2) and two narrow inlet cases (Inlet 3 and Inlet 4)

Table 18: Variation of inlet shape

Name	Short name	Width	Height	Area
Standard case		250 mm	50 mm	6250 mm²

Inlet different shape 1	Inlet 1	500 mm	25 mm	6250 mm²
Inlet different shape 2	Inlet 2	178.6 mm	35 mm	6250 mm²
Inlet different shape 3	Inlet 3	83.3 mm	75 mm	6250 mm²
Inlet different shape 4	Inlet 4	111.8 mm	111.8 mm	6250 mm²

Figure 88 and Figure 89 display the pathlines for the different inlet shapes. Higher resolution figures are shown in the Appendix. The differences in the inlet designs are clearly visible: Inlet 1 and Inlet 2 result in a bottom layer that is stretched out perpendicular to the flow direction, while bottom layer in Inlet 3 and Inlet 4 is much more focused. Especially Inlet 2 indicates promising results and the youngest pathlines at the electrodes near the outlet. The narrow inlets result a very high density of pathlines near the inlet. This is interesting, as the narrow inlet cases were set up specifically to increase the range of the boundary layer and to ensure a high activity of inhibitor near the outlet. The results however suggest a high mixing in the first part of the tankhouse cell and show very mature pathlines in the last part of the tankhouse cell, usually resulting in lower inhibitor activities.

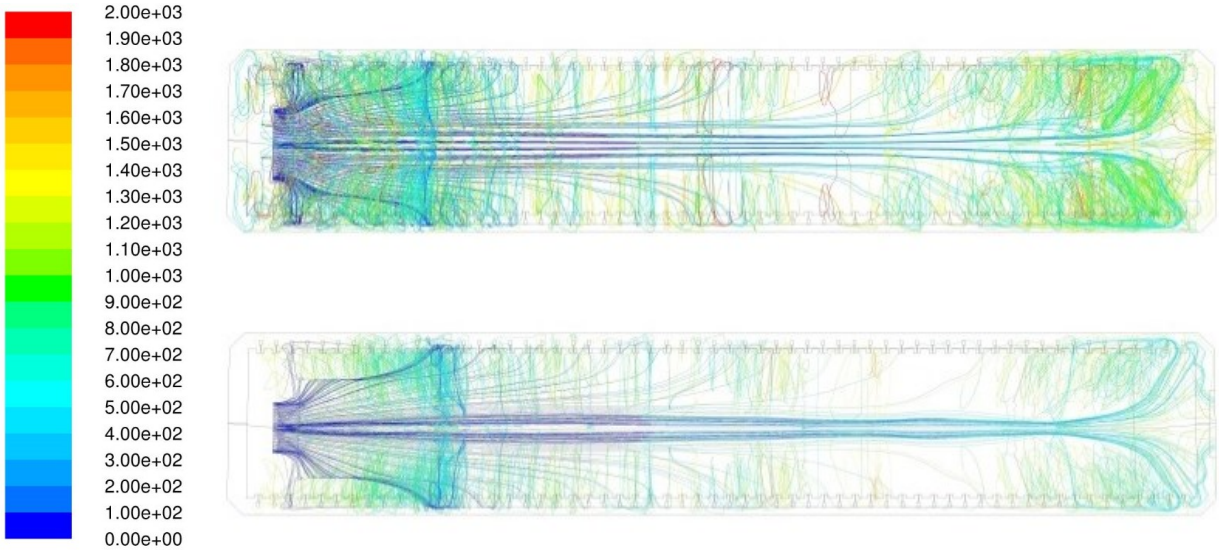

Figure 88: Pathlines colored by time [s]; wide inlets: Inlet 1 (top) and Inlet 2 (bottom)

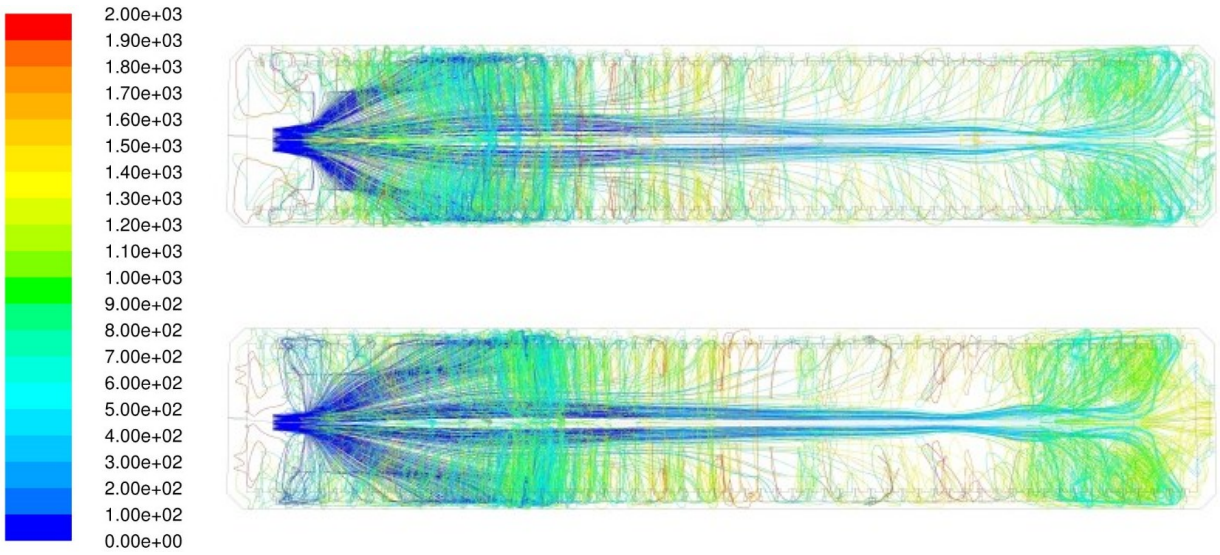

Figure 89: Pathlines colored by time [s]; narrow inlets: Inlet 3 (top) and Inlet 4 (bottom)

Figure 90 and Figure 91 show the minimum and average inhibitor activity in the electrode gaps. In the first part of the cell near the inlet, the highest activities can be obtained with the narrow inlet shapes (Inlet 3 and Inlet 4). This is in good agreement with the high density of pathlines near the inlet. The wide inlet designs (Inlet 1 and Inlet 2) result in the lowest activities in the first part, the values are even below the standard case. This behavior changes past the 40th electrode gap. Here the wide inlet designs, especially Inlet 2, show the highest minimum and average activities over large parts of the tankhouse cell. The inhibitor activity plots for the narrow inlets indicate an almost linear decline from the inlet to the outlet. In the last part of the tankhouse cell the largest minimum activity can be obtained with Inlet 1. However, since Inlet 2 performs better over large parts of the cell, the absolute minimum should not be the exclusive parameter.

Figure 92 shows the Inhibitor distribution and minimum inhibitor activities in the tankhouse cell. Even though the highest minimum activity can be achieved with Inlet 1, in terms of cathodes below 30 % activity Inlet 2 clearly performs better. The narrow inlet shapes (Inlet 3 and Inlet 4) perform worse, both in terms of minimum activity and number of cathodes below 30 %.

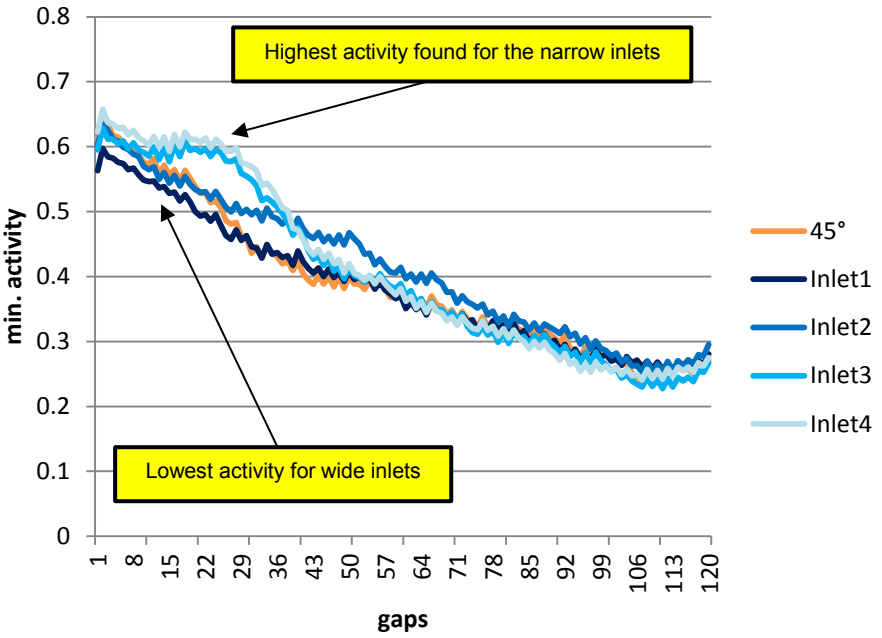

Figure 90: Minimum inhibitor activity at different inlet shapes

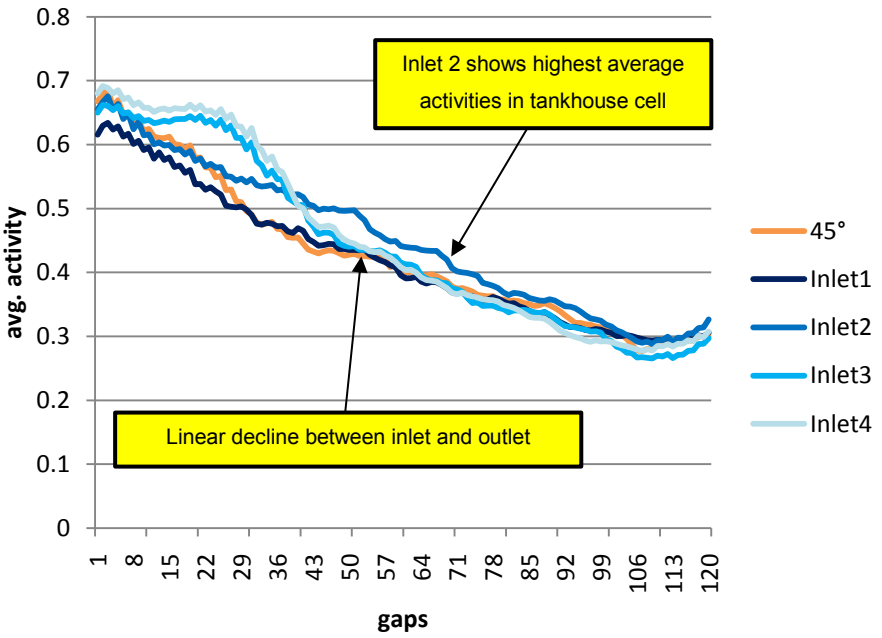

Figure 91: Average inhibitor activity at different inlet shapes

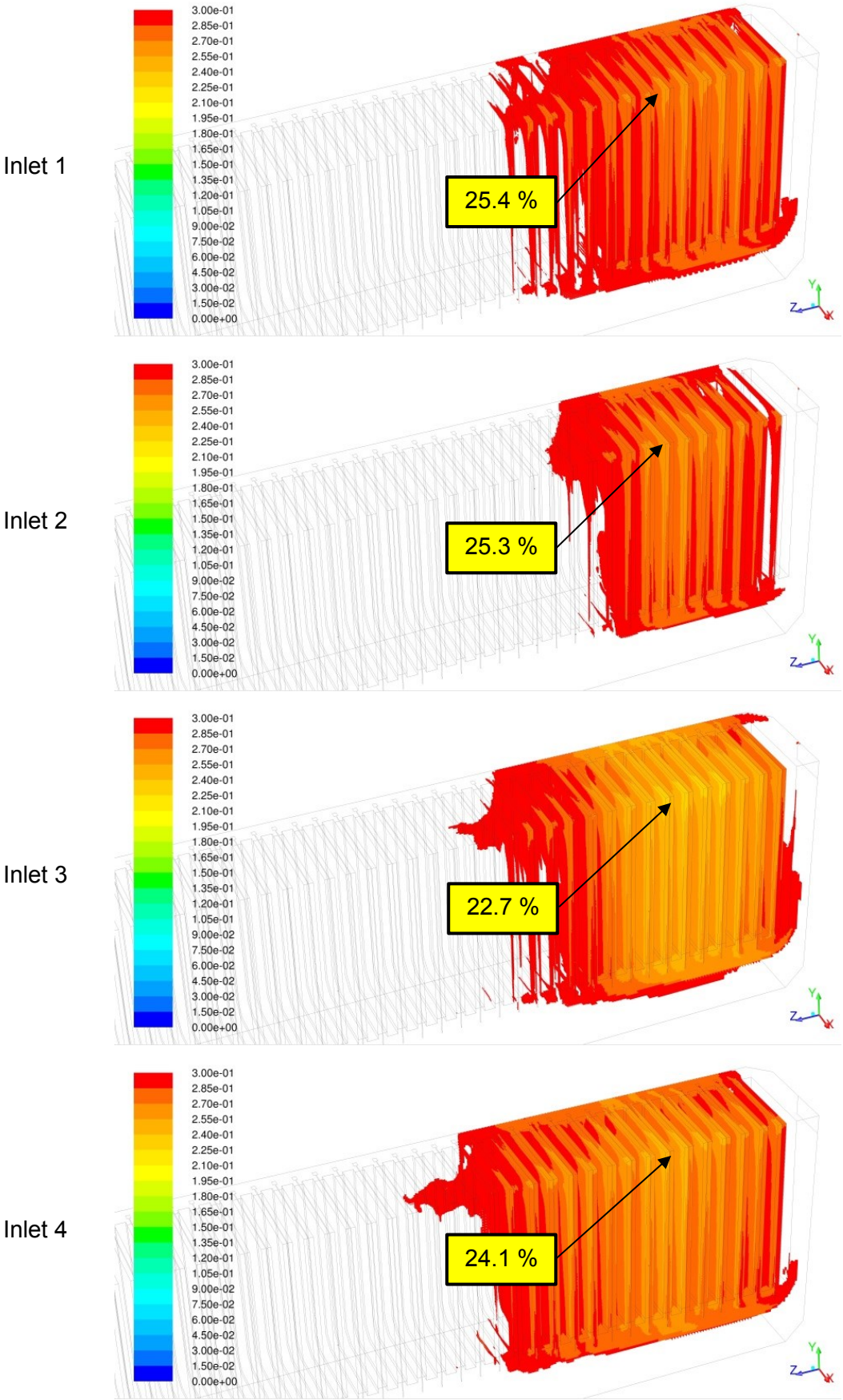

Figure 92: Distribution and minima of inhibitor activity for the different inlet shapes

Table 19 shows the results of the inlet shape parameter study. The wide inlets (Inlet 1 and Inlet 2) perform better in terms of absolute minimum values and number of cathodes below 30 % inhibitor activity. Even though the best absolute minimum can be obtained using Inlet 1, the best overall performance is achieved when using Inlet 2. This shape distributes the electrolyte over a wider area than the standard case but still has a certain inlet nozzle height which is apparently important to form a strong electrolyte bottom layer and to achieve a good overall inhibitor activity in the tankhouse cell.

Table 19: Results of the inlet shape study

Case	# cathodes <30 %	Lowest activity
Standard case	13	23.7 %
Inlet 1	14	25.4 %
Inlet 2	10	25.3 %
Inlet 3	14	22.7 %
Inlet 4	15	24.1 %

8.6 Multi inlet designs

The aim for the multi inlet designs parameter study was to increase the inhibitor distribution in the tankhouse cell by using two inlets instead of only one. For the simulation this means to simply include an offset to inlet from the symmetry boundary condition. Figure 93 shows the used designs. In case Two 1 the inlet is positioned 250 mm left of the centerline and in case Two 2 the offset was increased to 500 mm, see Table 20.

Figure 93: Inlet designs for the multi inlet design study: The standard case was compared to two cases with off center inlet positioning (Two 1 and Two 2)

Table 20: The multi inlet designs for the electrolytic cell

Name	Short name	Offset from centerline
Standard case		0 mm
Multi inlet design 1	Two 1	250 mm
Multi inlet design 2	Two 2	500 mm

Figure 94 shows the pathlines for the two different cases. The two inlets clearly change the electrolyte flow pattern in the tankhouse cell. In both cases the bottom layer that can usually be found flowing from the inlet to the outlet is getting highly disturbed. This is particularly true for the case Two 2. The large distance between the two inlets causes the bottom layer to slow down significantly. Case Two 2 also shows a very high pathlines density in the first part of the tankhouse cell. In generally the density of pathlines inside the electrode gaps appear larger than in the other parameter studies. The position of the inlet close to the side walls and the reduction of the bottom layer obviously lead to a higher electrolyte flow at the side walls of the tankhouse cell.

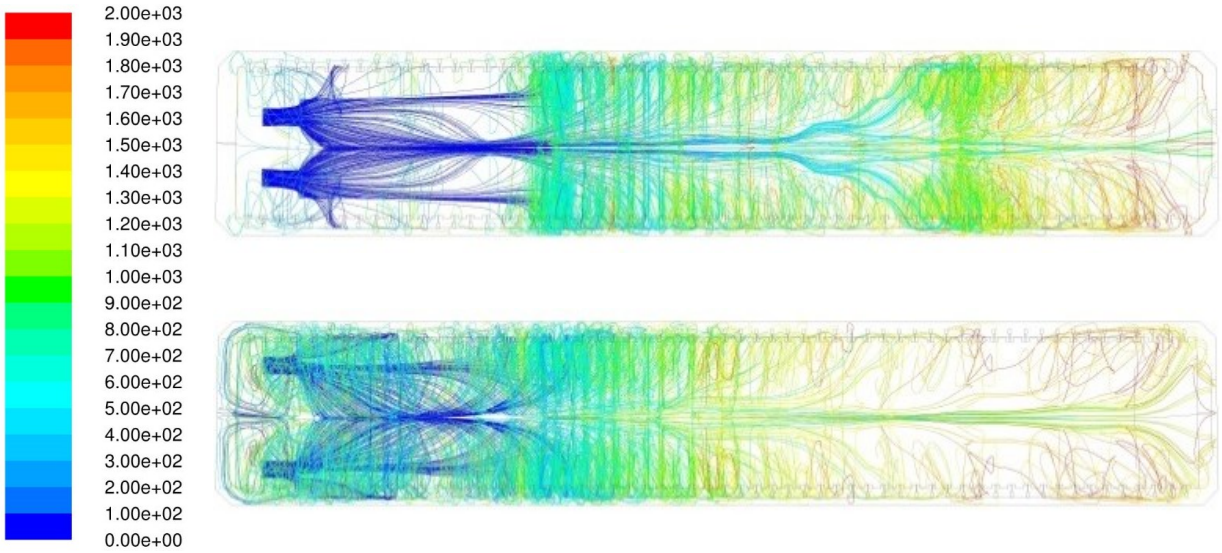

Figure 94: Pathlines colored by time [s]; Two 1 (top) and Two 2 (bottom)

Figure 95 and Figure 96 show the minimum and average inhibitor activity in the electrode gaps. In both cases the inhibitor activity in the first and middle part of the tankhouse cell is considerably higher than the standard case. This is especially true for case Two 2; here the obtained inhibitor activities are up to 20 % higher than in the standard cases. However, both cases fail to provide good results in the last part of the tankhouse cell. Here the standard case is clearly superior to the multi inlet design. The average inhibitor activity in case Two 2 was the lowest value found in the whole parameter study.

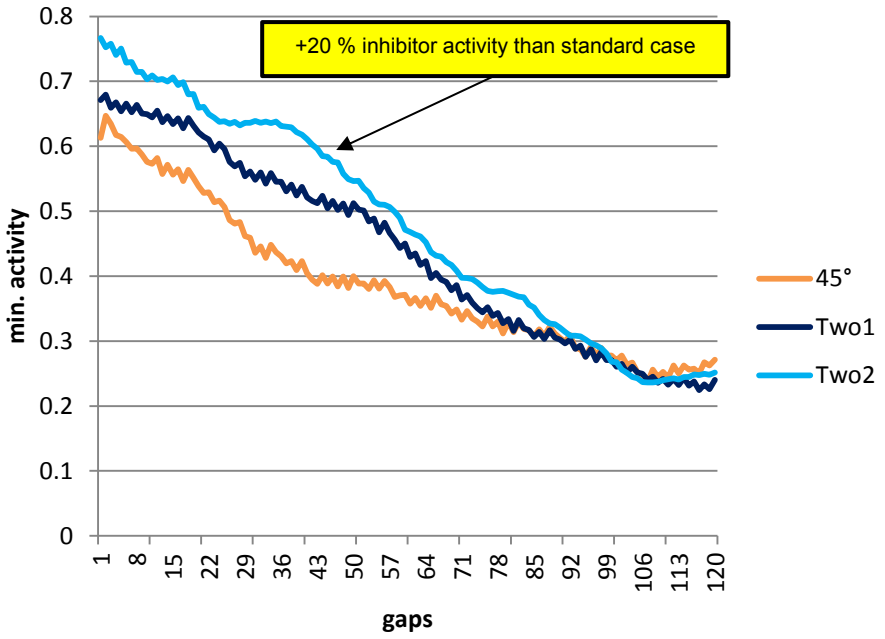

Figure 95: Minimum inhibitor activity for the multi inlet designs

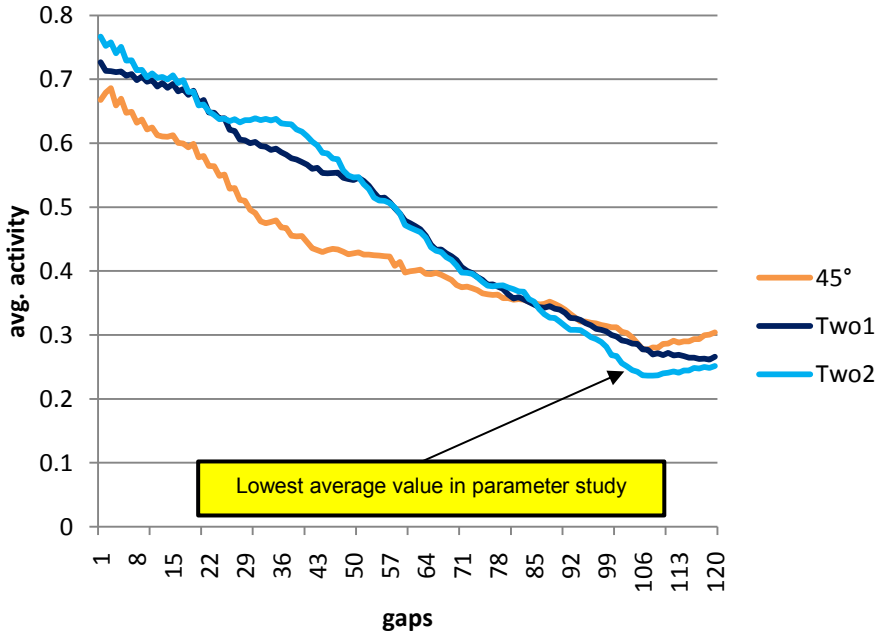

Figure 96: Average inhibitor activity for the multi inlet designs

Figure 97 shows the minimum inhibitor activity and the overall inhibitor distribution in the tankhouse cell for the multi inlet study. Both cases perform worse than compared to the standard case in terms of minimum value and number of cathodes below 30 %.

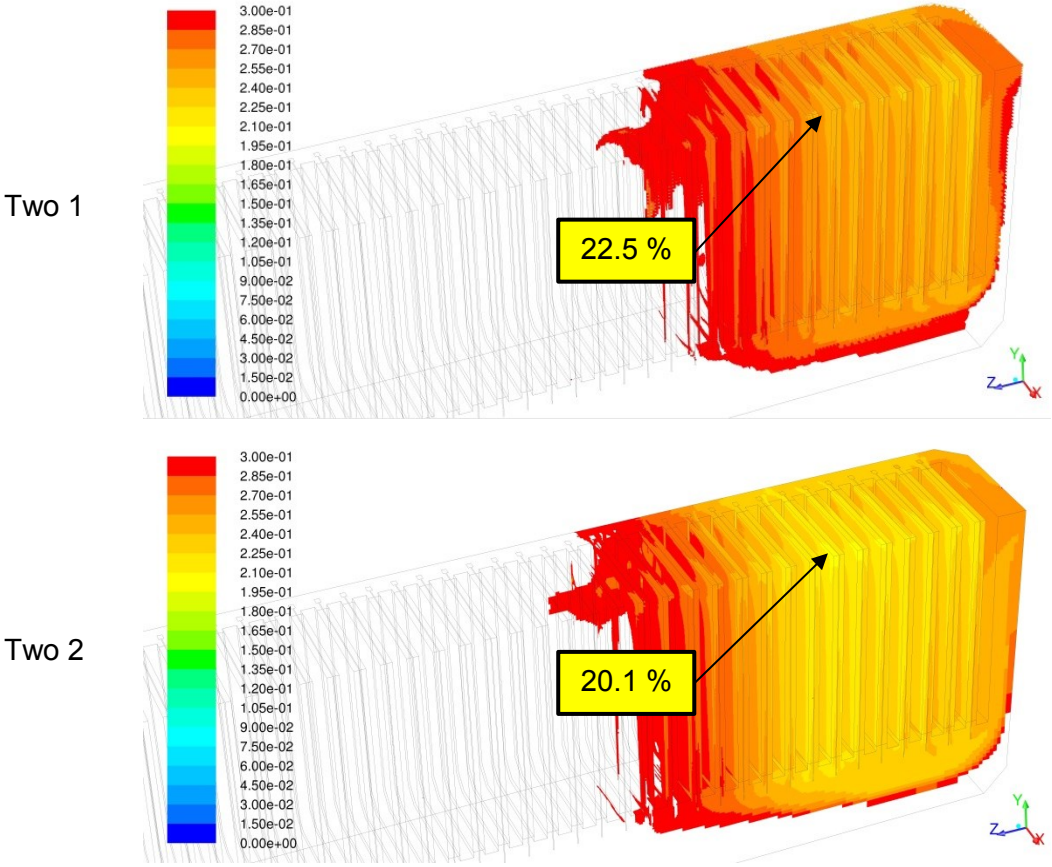

Figure 97: Distribution and minimum inhibitor activities for different multi inlet designs

The results of the multi inlet design study are shown in Table 21. Although the multi inlet designs strongly increase the inhibitor activity in the first part of the tankhouse cell, they fail to provide good results in the later parts of the tankhouse cells. This outlines the importance of the bottom electrolyte layer as a transport mechanism to the electrodes close to the outlet.

Table 21: Results of the multi inlet designs study

Case	# cathodes < 30 %	Lowest activity
Standard case	13	23.7 %
Two 1	13	22.5 %
Two 2	15	20.1 %

8.7 Different crops

In the copper electrorefining process, copper is dissoluted into the electrolyte and electroplated onto the cathodes. The cycle is complete when most of the anode mass has been refined into cathodic copper. A certain thickness of the anodes has to remain to

eliminate the threat of breaking off the anodes. Over the course an anode lifecycle the cathodes have to be replaced periodically. Typical values for cathodic and anodic lifecycles are 7 respectively 21 days. Besides the changes in anode and cathode geometry, the anode slime buildup on the tankhouse cell bottom causes a change in tankhouse geometry. This part of the parameter study is aimed to investigate the effects of different crops stages on the electrolyte flow and inhibitor activity distribution. Figure 98 shows the changes in tankhouse geometry. The cases Crops 2 and Crops 3s represent the tankhouse cell at the start of the corresponding cathodic cycle (empty cathodes) while Crops 3e represents the end of the third cathodic cycle (loaded cathodes).

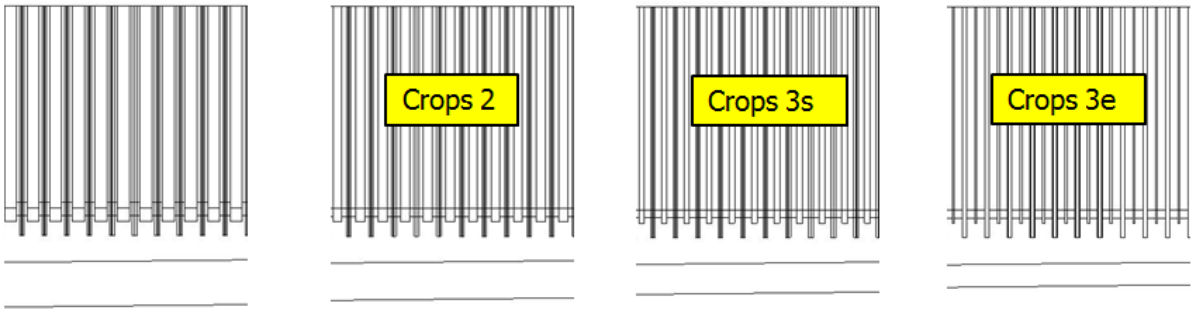

Figure 98: Geometries for the different crops study; the standard case (left) was compared to the start of the 2nd and 3rd crops (Crops 2 and Crops 3s) and the end of the 3rd crops (Crops 3e).

For the calculation of the anode thickness, it was assumed that the width and height of the anode do not change during the electrorefining process and only the thickness decreases. The anode mass is 404 kg and the remaining scrap is 11 %. With the known copper density of 8920 kg/m³ the anode thickness after the 1st, 2nd and 3rd cathode cycle can be calculated. The results are shown in Table 22. After an anode life cycle, an anode slime buildup of approximately 10 cm can be observed after emptying the tankhouse cell. For the simulation a uniform growth of the slime layer is assumed. For further simplifications the anode slime is assumed to grow evenly on the whole tankhouse cell bottom.

Table 22: Geometries for the different crops parameter study

Name	Short name	Anode thickness	Cathode thickness	Slime layer
Standard case		54.00 cm	0.33 cm	0 cm
Start 2nd crops	Crops 2	39.21 cm	0.33 cm	3.3 cm
Start 3rd crops	Crops 3s	24.41 cm	0.33 cm	6.6 cm
End 3rd crops	Crops 3e	0.96 cm	1.67 cm	10.0 cm

Figure 99 shows the pathlines for the three different cases, higher resolution figures are shown in the appendix. While Crops 2 still results in a distinctive bottom layer and a strong transport of electrolyte towards the outlet, this flow pattern is gradually reduced in Crops 3s and Crops 3e. The reduced distance between tankhouse cell floor and electrodes does not allow for a bottom layer and pushes the electrolyte towards the side and into the electrode gaps. As a result the transport of inhibitor towards the outlet is increasingly directed through the electrode gaps rather than underneath the electrodes for the cases Crops 3s and Crops 3e. Therefore it takes more time for the inhibitor to reach the later parts of the tankhouse cell and the inhibitor is longer exposed to decomposition.

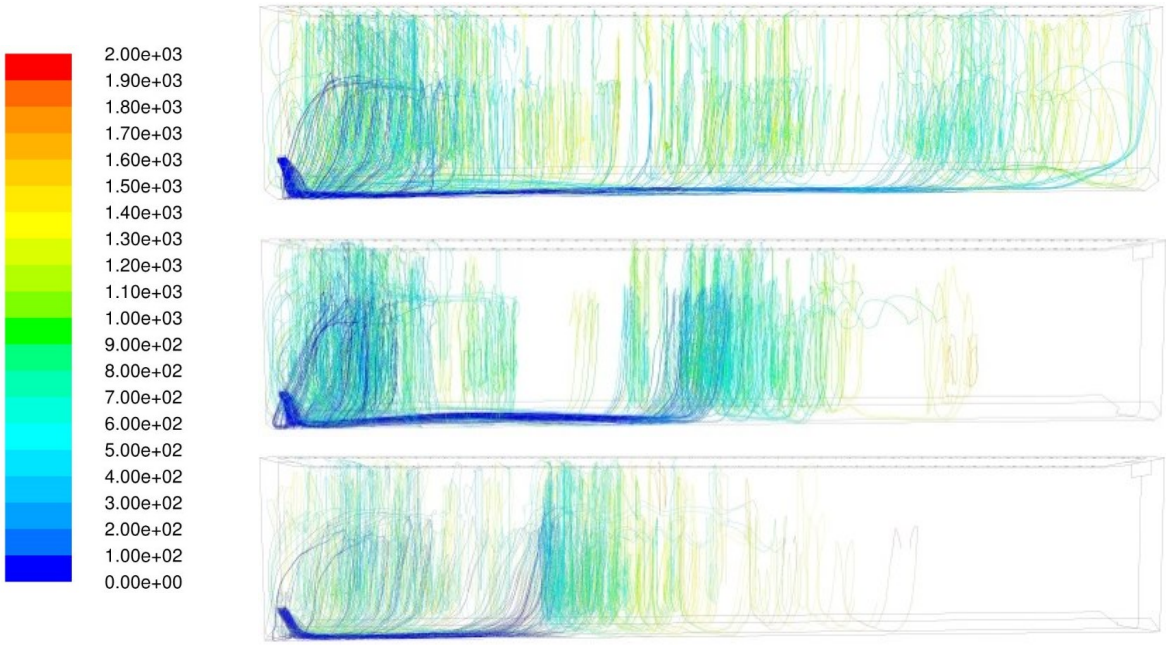

Figure 99: Pathlines for the different crops: Crops 2 (top), Crops 3s (middle) and Crops 3e (bottom)

Figure 100 and Figure 101 show the minimum and average inhibitor activity in the electrode gaps. As a result of the change in electrolyte flow, Crops 3s and Crops 3e achieve a very high inhibitor activity in the first part of the tankhouse cell but result in a decreased activity in the later parts.

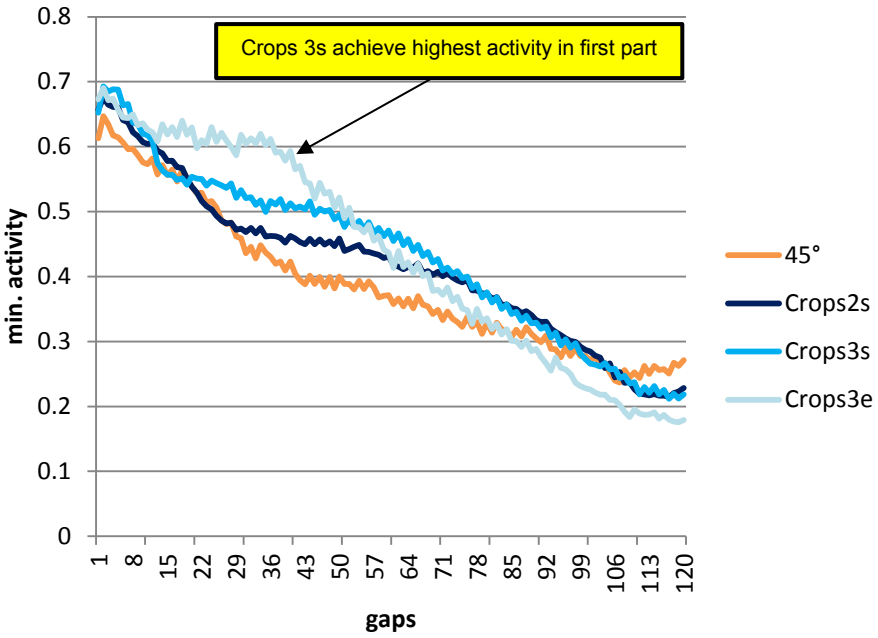

Figure 100: Minimum inhibitor activity at different crops

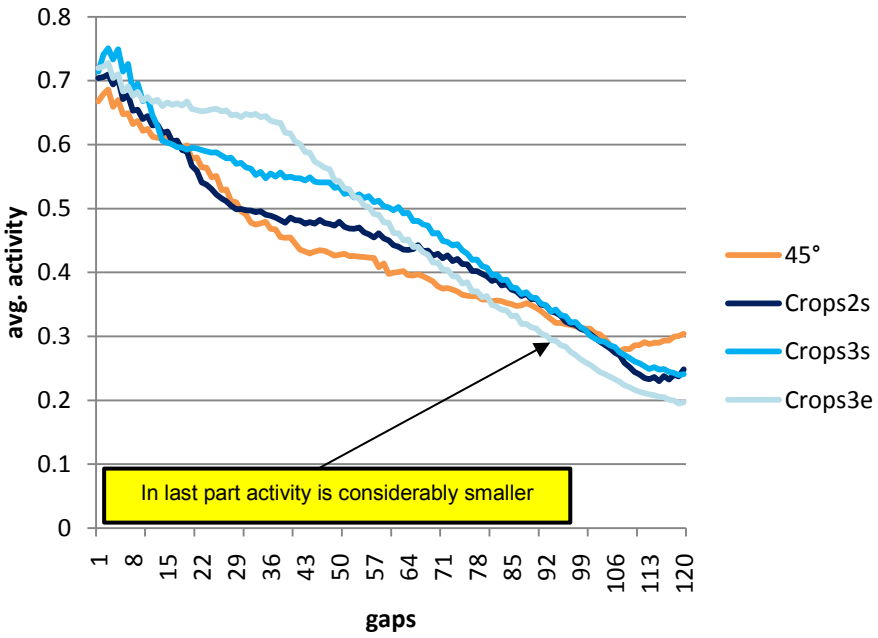

Figure 101: Average inhibitor activity at different crops

Figure 102 shows the minimum inhibitor activity and overall inhibitor distribution in the tankhouse cell. Due to the change in tankhouse cell geometry, the articulated slime layer and wider electrode gaps, all three cases perform noticeable worse than the standard case.

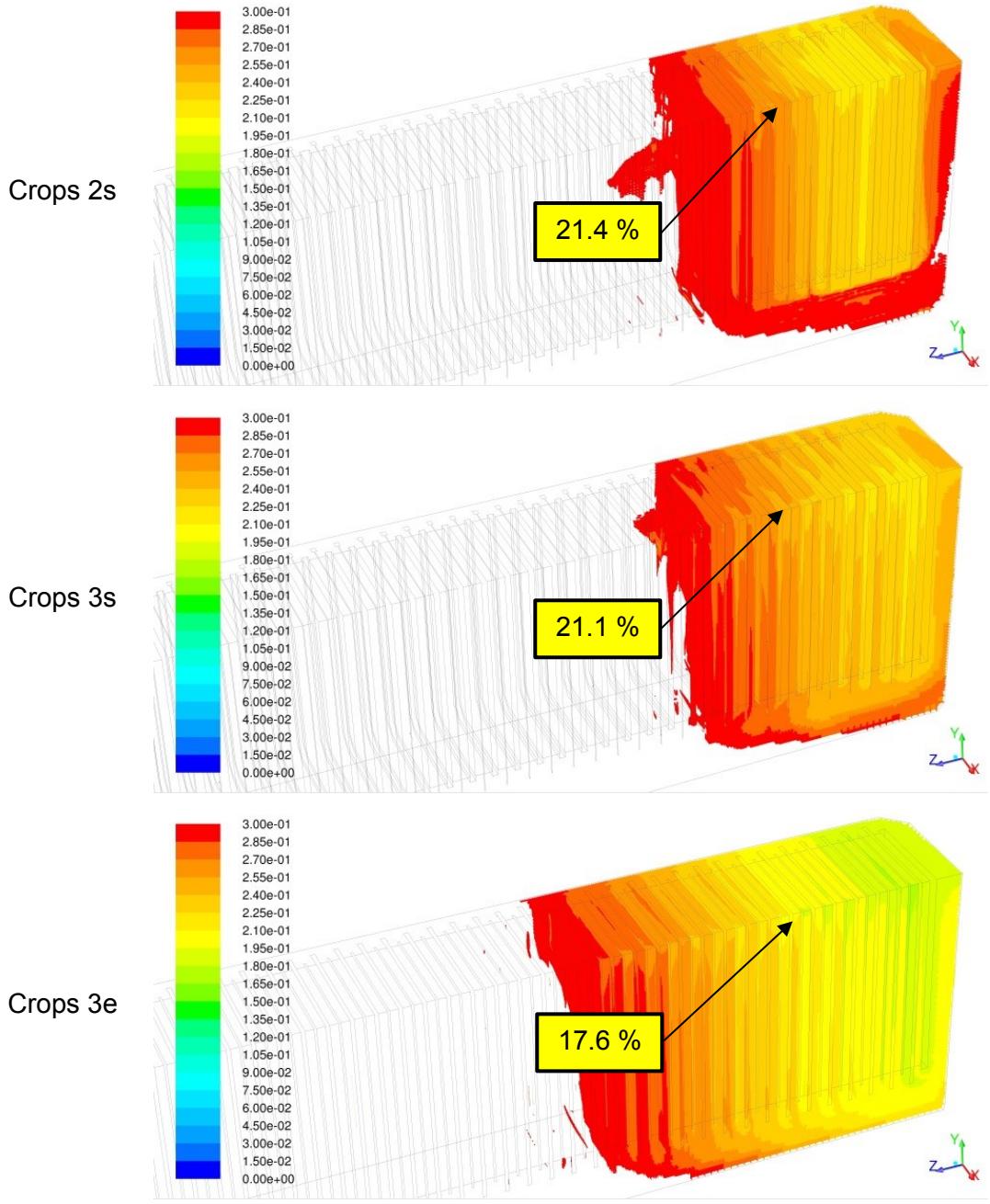

Figure 102: Distribution and minimum inhibitor activities for different crops

The results for the different crops study is shown in Table 23. The reduced inhibitor activity and distribution for the later crops is clearly observable. The difference is caused by change in electrode gaps geometry but also caused by buildup of anode slime. In the simulations this slime layer was regarded as a rigid body and no interaction (dispersion of slime layer) was considered. The decrease in space underneath the electrodes results in a breakdown of the bottom layer. This again shows the importance of this bottom layer as a transport mechanism for fresh electrolyte for the later parts of the tankhouse cell.

Table 23: Results for the different crops study

Case	# cathodes < 30 %	Lowest activity
Standard case	13	23.7 %
Crops 2	13	21.4 %
Crops 3s	13	21.1 %
Crops 3e	15	17.6 %

8.8 Different flow rate

The final parameter study includes the investigation of different flowrates at the inlet. For this study two separate cases with a 20 % increase and a 20 % decrease in mass flow rate have been chosen. Figure 103 shows the resulting velocities at the inlet. For the reduced flowrate the maximum velocity results in 0.13 m/s and for the increased flowrate the maximum velocity results in 0.2 m/s. The mass flow rates and bath changes are listed in Table 24.

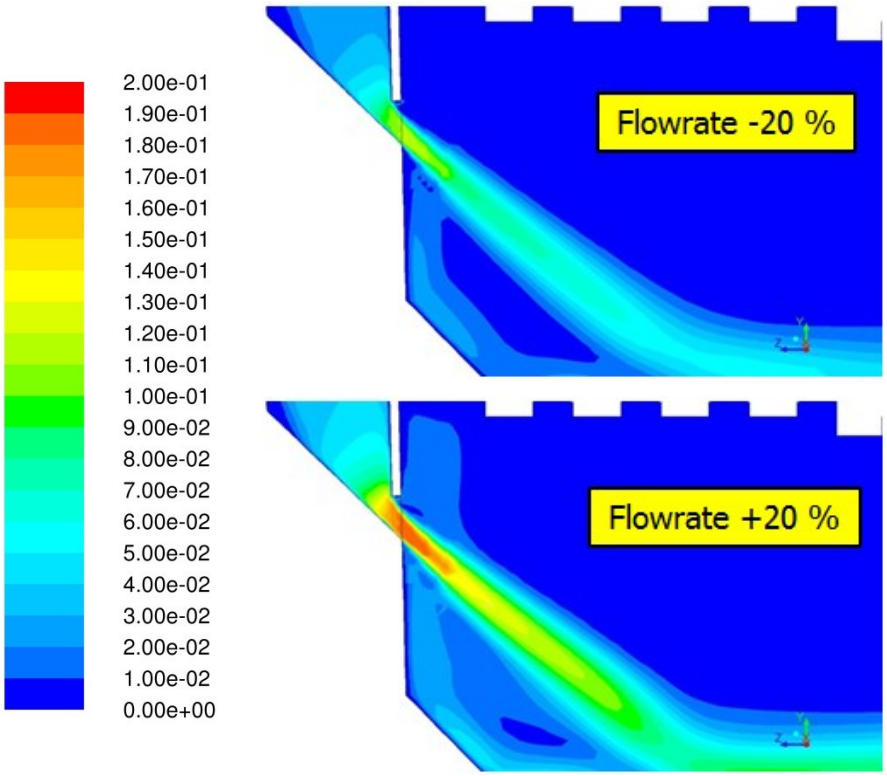

Figure 103: Contours of the electrolyte velocity in m/s for the different mass flow rates

Table 24: Flowrates for the parameter study

Name	Short name	Mass flow rate	Bath changes per hour
Standard case		0.854 kg/s	0.42
Flowrate -20 %	FR 1	0.683 kg/s	0.33
Flowrate +20%	FR 2	1.025 kg/s	0.50

Figure 104 shows the pathlines for the different mass flow rates. Since both cases use the same geometry, they indicate very similar electrolyte flow behavior. In case FR 1 the pathlines near the outlet are older than in FR 2. The lower mass flow rate at the inlet results in a lower velocity of the bottom layer. Therefore, it takes more time for the electrolyte to reach the electrodes near the outlet and the inhibitor is longer exposed to decomposition. In the first part of the tankhouse cell near the inlet both cases show a similar density in pathlines, although in case FR 2 the pathlines are tilted toward the outlet. This is caused by the higher velocities near the inlet. The electrolyte pushed in the gap between outer wall and electrodes has a higher momentum towards the outlet and causes this difference.

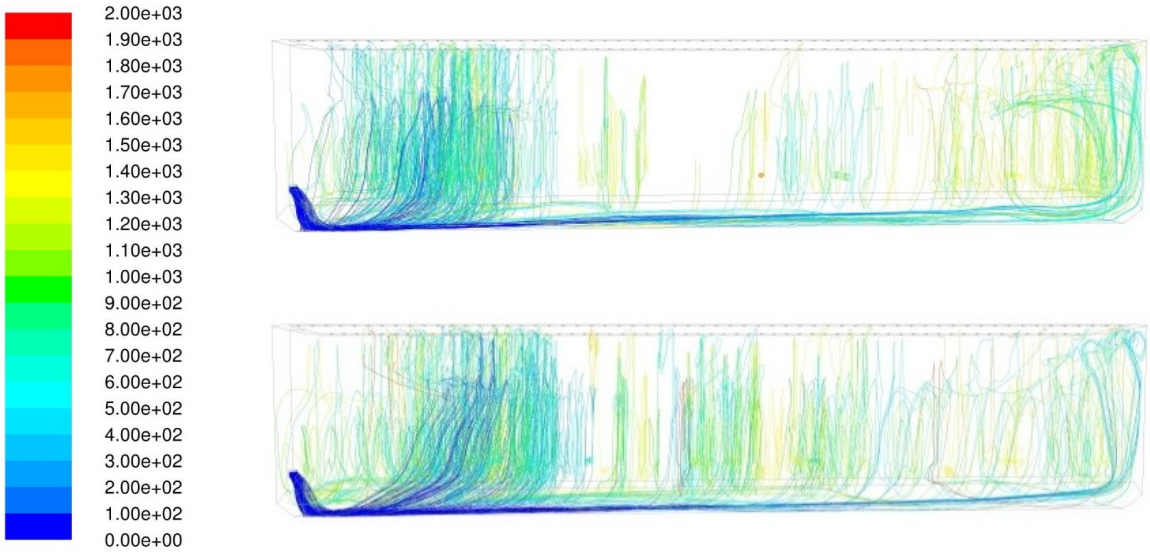

Figure 104: Pathlines for the different flow rates colored by time [s]; FR 1 (top) and FR 2 (bottom)

Figure 105 and Figure 106 show the minimum and average inhibitor activity in the electrode gaps. As predicted by the electrolyte flow, FR 1 results in a lower activity throughout the tankhouse cell and FR 2 a higher activity. It is important to comprehend that in both cases the absolute concentration of inhibitor [inhibitor/volume] is the same. Only the throughput of the inhibitor is smaller for FR 1 and higher for FR 2. Because of the very similar electrolyte flow pattern the plotted inhibitor activities are very alike. They show the same behavior in term of plateaus and position of minimum activity.

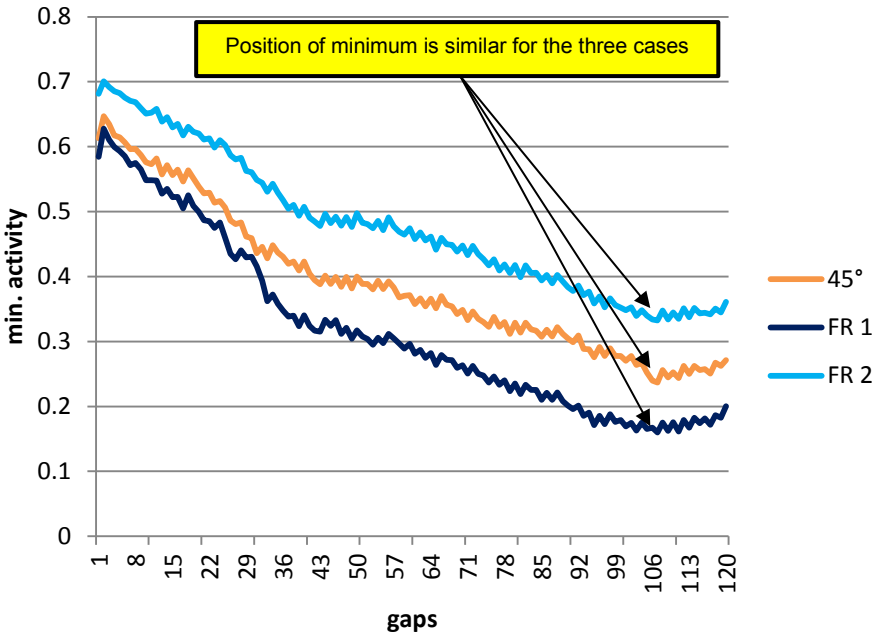

Figure 105: Minimum inhibitor activity at different flow rates

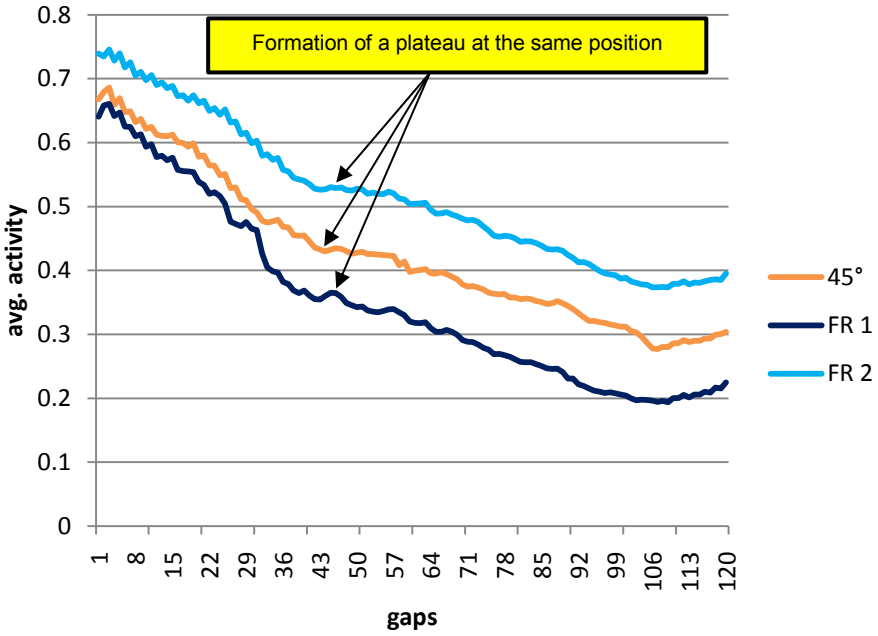

Figure 106: Average inhibitor activity at different flow rates

Figure 107 shows the minimum inhibitor activity and overall inhibitor distribution in the tankhouse cell. The color map for FR 2 had to be adapted to account for the high activities. FR 1 achieved the lowest measured inhibitor activity in the parameter study with a value of only 16 % of the initial activity.

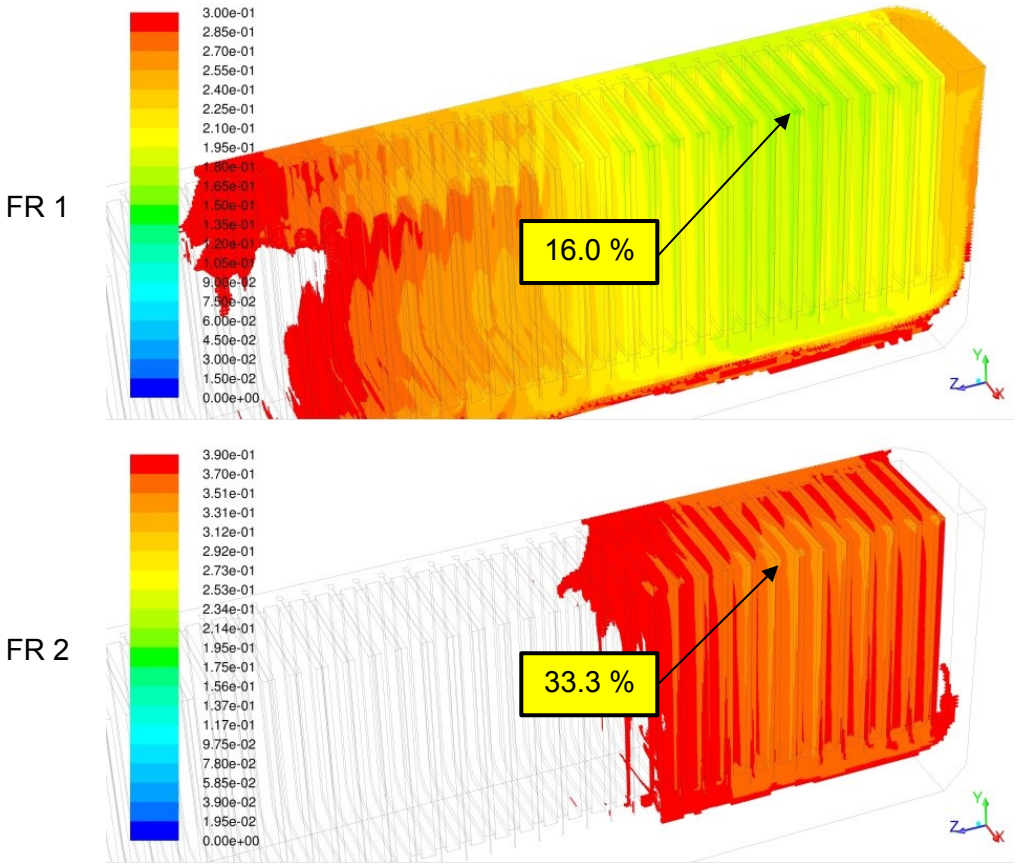

Figure 107: Minimum inhibitor activity and overall inhibitor distribution for the different flowrates

The results of the parameter study regarding the flow rate are listed in Table 25. By increasing the flow rate at the inlet the inhibitor activity in the whole tankhouse cell rises. However, this would also result in a higher dispersion of anode slimes in the electrode gaps and would certainly reduce the cathodic copper quality by the input of anode slime in the copper surface as shown by Lackner [46].

Table 25: Results for the different flow rate studies

Case	# cathodes < 30 %	Lowest activity
Standard case	13	23.7 %
FR 1	27	16.0 %
FR 2	0	33.3 %

8.9 Final thoughts on the parameter study

The parameter study reviled the importance of the bottom layer as a transport mechanism for the electrolyte. The strong electrolyte stream transports fresh inhibitor toward the electrode gaps close to the outlet in a matter of minutes. The parameter studies in which the bottom layer was influenced, resulting in an increased residence time, altogether showed a lower inhibitor activity in the critical areas close to the outlet. However, this also means that a large part of the inhibitor leaves the tankhouse cell via the outlet without being consumed at the cathodes. In order to optimize the electrolyte flow, this otherwise lost inhibitor should be utilized. Therefore a new tankhouse cell geometry was created. This geometry includes an obstacle in very last part of the electrolysis cell, close to the outlet. The idea behind the obstacle is that the fresh electrolyte with high inhibitor activity is forced to flow outwards and through the critical electrode gaps that normally show very low inhibitor activity. The geometry used in this simulation in shown in Figure 108.

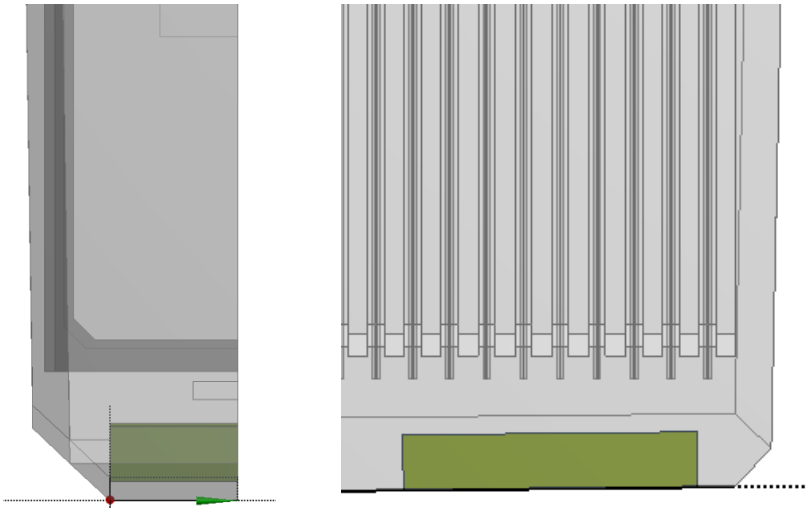

Figure 108: Geometry and position of the obstacle flow simulation

The geometric dimensions of the obstacle are listed in Table 26. The obstacle height is limited to 15 cm, to account for the anode slime buildup during the electrolysis. The overall length is 80 cm and the width 70 cm (35 cm inside symmetrical simulation domain). The obstacle is positioned 10 cm from the back slope.

Table 26: Dimensions of the obstacle flow simulation

Name	Height	Width	Length	Dist. from back slope
Obstacle	15 cm	35 cm (symmetry)	80 cm	10 cm

Figure 109 and Figure 110 show the pathlines for the obstacle simulation compared to the standard case (same inlet and cell design apart from the obstacle), higher resolution figures are listed in the Appendix. The obstacle flow simulation shows a high pathline density in the last part of the tankhouse cell. The electrolyte is restricted from flowing directly towards the outlet and must evade outwards to the cell walls. From there it is pulled into the electrode gaps. However the pathline density close to the inlet is somewhat lower than in the standard case.

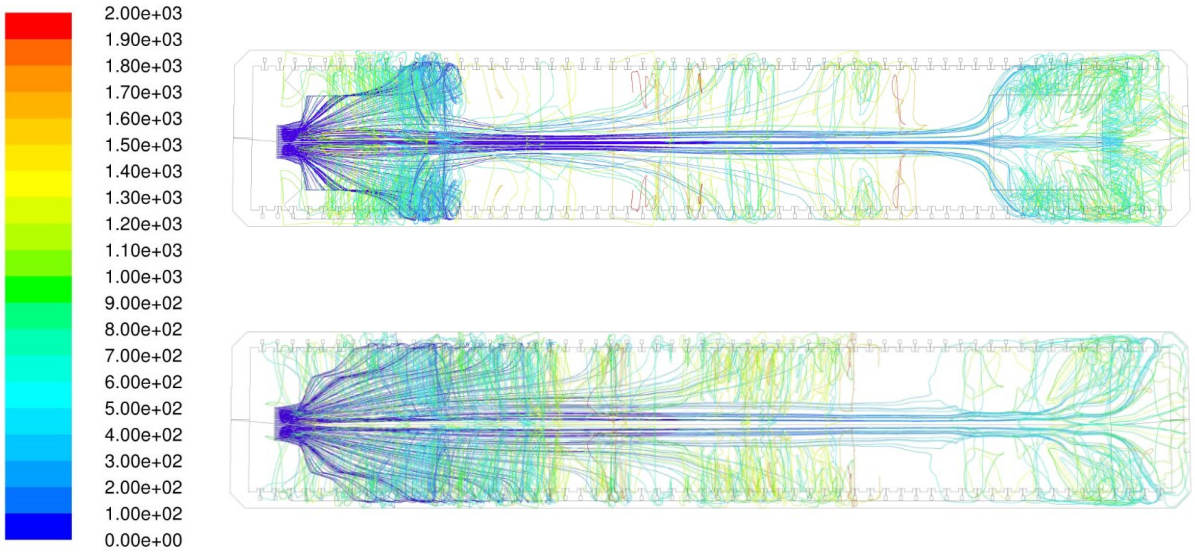

Figure 109: Pathlines for the obstacle flow simulation (top) compared to the standard case (bottom), top view

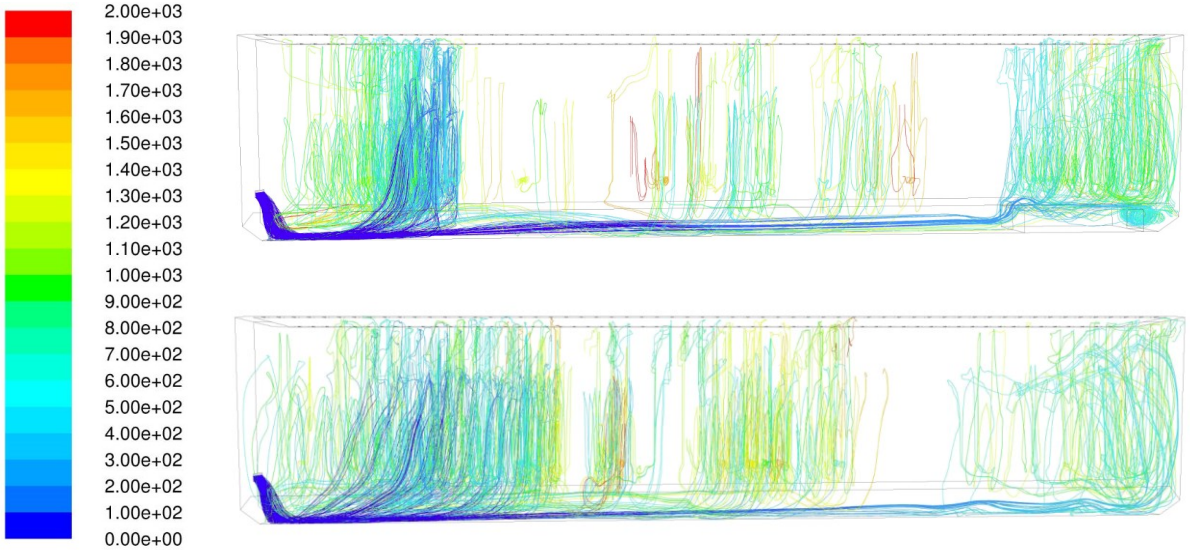

Figure 110: Pathlines for the obstacle flow simulation (top) compared to the standard case (bottom), top view

Figure 111 and Figure 112 show the minimum and average inhibitor activity in the electrode gaps. The obstacle causes a higher minimum and average activity in the last part of the tankhouse cell. The activity increases at gap 100 when the bottom layer is interrupted by the obstacle. In the first part of the tankhouse cell the activity is smaller than the standard case.

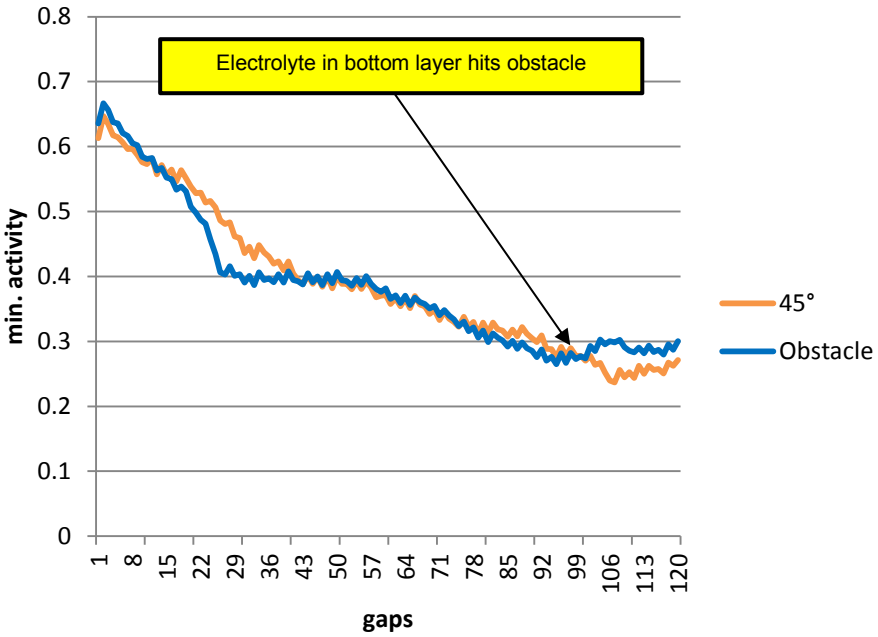

Figure 111: Minimum inhibitor activity for the obstacle flow

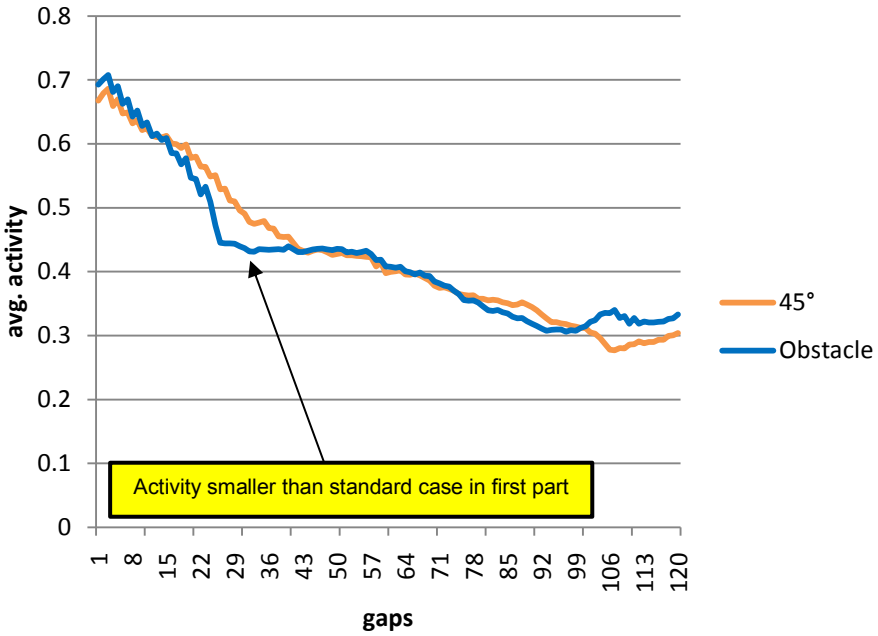

Figure 112: Average inhibitor activity for the obstacle flow

Figure 113 shows the minimum inhibitor activity and overall inhibitor distribution for the obstacle flow simulation compared to the standard case. The obstacle flow simulation shows two areas of low concentration before and after the obstacle. The electrode gaps directly above the obstacle have a higher activity.

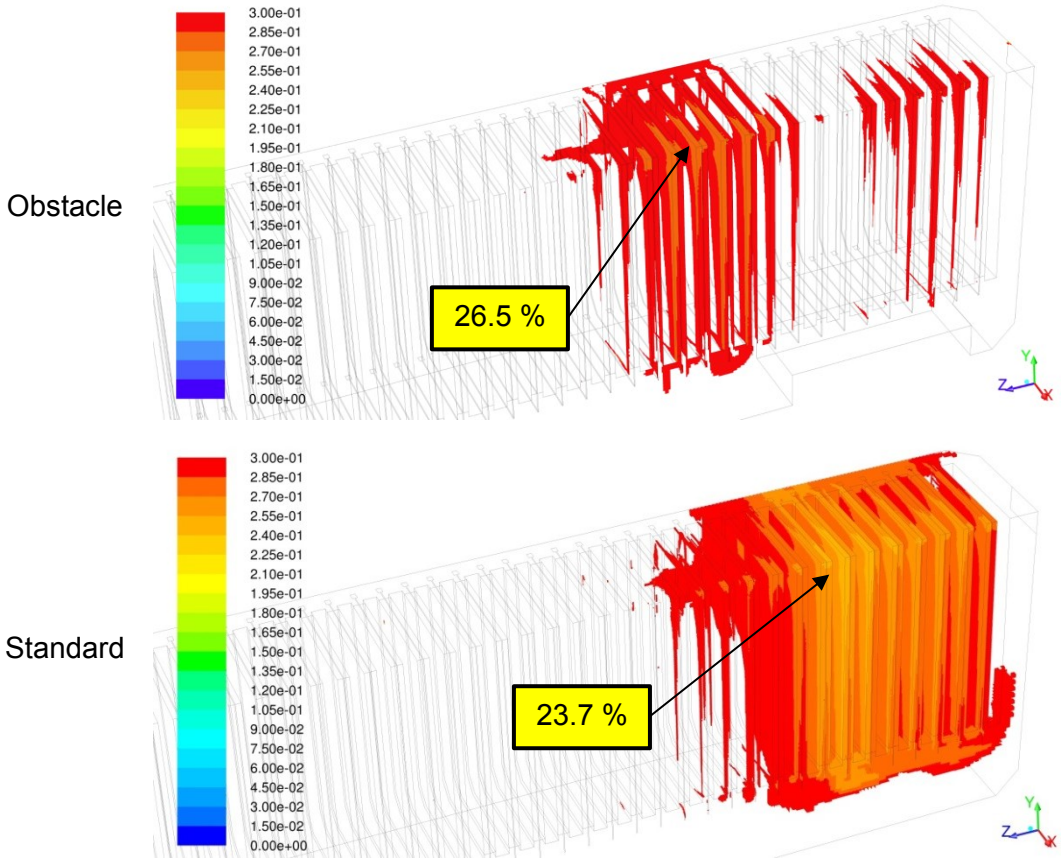

Figure 113: Minimum inhibitor activity and overall inhibitor distribution for the obstacle flow simulation (top) and the standard case (bottom)

The obstacle flow simulation performed very well compared to standard case. The absolute minimum in the tankhouse cell was found to be 26.5 % compared to the 23.7 % in the standard case. The volume below 30 % inhibitor activity for the obstacle flow is smaller than the in standard case, even though the total number of cathodes that has an inhibitor activity smaller than 30 % is 14 for the obstacle flow case and 13 for the standard case. The results are also shown in Table 27.

Table 27: Results of the obstacle flow simulation compared to the standard case

Case	# cathodes < 30 %	Lowest activity
Standard case	13	23.7 %
Obstacle	14	26.5 %

The modification of the bottom layer is a very promising approach to optimize the electrolyte flow in the whole tankhouse cell. By forcing the electrolyte to flow through the electrode gaps rather than just exit the tankhouse cell at the outlet the inhibitor can be much better utilized. It should me remarked that the geometry of the obstacle was not designed primarily to increase the inhibitor activity but to show the feasibility of the bottom layer modification. A quadratic block shape was chosen because of the easy meshing rather than its ability to channel the electrolyte flow. A more thorough design of the obstacle can surely further optimize the electrolyte flow and therefore the inhibitor activity distribution.

9 Summary

This work introduces a new way to simulate the electrolyte flow behavior and inhibitor activity in full industrial scale copper electrorefining cells. In the copper electrorefining process the anodic low quality copper is submerged alternatively with steel cathodes in a $CuSO_4$-H_2SO_4-H_2O electrolyte. When applying an electric current, the copper electrochemically dissolutes into the electrolyte in the form of Cu^{2+} cations. From there the copper is transported by diffusion and convection to the cathode, where it is electroplated onto the cathode surface. Impurities included in the anodic copper either do not dissolute in the electrolyte and form the anode slime or cannot be electroplated under the chemical conditions and remain in the electrolyte. The processes of dissolution and electroplating lead to a change in density in front of the electrodes. This density differences introduce an upward motion near the cathode and a downward motion near the anode, a behavior that is revered to as natural convection. Additionally an electrolyte motion is caused by the continuous addition of fresh electrolyte at the inlet and the equal removal of spend electrolyte at the outlet. This so called forced convection is necessary to reduce the pollution of the electrolyte with impurities and ensures a high quality cathodic copper.

The first part of this work was to find a suitable simulation method to simultaneously study the effects of natural and forced convection in an industrial scale copper electrorefining cell including 61 anodes and 60 cathodes. The mature problems of this task are the differences in size scales between the natural convection and the forced convection. The natural convection is based on density changes in boundary layer near the cathodes with a thickness of less than 1 mm. Comparing this to the forced convection based on electrolyte flow patterns in a tankhouse cell that measures 6 m in length reveals the difficulty of the simulation approach. With the given computer technology, a full simulation approach of the whole electrorefining tankhouse cell is unpractical, if not impossible. The numerical mesh on the one hand needs to be fine enough to achieve a good resolution of the electrode processes and on the other hand must be computable in a reasonable amount of time.

In order to take the whole tankhouse cell into account the simulation has to be split into a couple of separate steps. First the mass transport processes were simulated in a small, “local” part of the cell. The simulation domain included one anode and the two neighboring cathodes. In this reduced geometry the cell density was set very high with a mesh size of 500 µm at the electrodes. The Cu^{2+} concentration was simulated by including a scalar transport equation with the corresponding boundary conditions at the electrode surfaces. The density change of inhibitor was modelled by using a body force term dependent on the scalar

concentration. The scalar concentration and the density change model were simultaneously calculated in the simulation until a steady state result could be extracted. From this result the velocity vectors in every volume element were saved.

The second step in the simulation was to investigate the electrolyte flow conditions at the inlet of the tankhouse cell. The electrolyte is entering the tankhouse cell via a submerged entry nozzle. The inlet design has a high influence on the overall electrolyte flow pattern in the tankhouse cell and must be simulated separately in order to gain the correct values for the velocities and turbulence parameters. The simulation was performed on a simplified geometry, not including the electrode gaps. Like the local electrode simulation the steady state velocity vector and turbulence parameter results were saved in a point-type profile matrix to later be interpolated in the “global” simulation.

The last step in the simulation of the tankhouse cell was to include the velocity vectors and turbulence parameters from the local simulation and the inlet simulation into a separate “global” simulation domain including all 61 anodes and 60 cathodes. In this simulation domain the mesh size was drastically increased to allow the meshing of a full scale tankhouse cell. Onto this courser mesh the previously found velocity data was interpolated and a simulation was set up with the correct boundary conditions at the inlet. This way the interaction between natural and forced convection could be simulated in a full scale copper electrorefining cell.

Due to the limits in computer technology a compromise had to found between accuracy of simulation and computational effort. The largest mesh used in this work includes 29 million volume elements and was calculated on a SGI computer cluster using 24 CPUs in parallel. The computation time for a single simulation of this size was 20 days. Increasing the number of CPUs only marginally accelerates the simulation process as the bottleneck in these simulations is the allocated memory rather than CPU performance.

The second part of this work includes a parameter study on the effects of different inlet geometries and other parameters on the electrolyte flow and inhibitor activity distribution. The inhibitor activity was calculated on the previously simulated electrolyte flow pattern. The inhibitor activity is reduced inside tankhouse cell by two mechanisms: consumption at the cathodes and decomposition in the tankhouse cell due to high temperature and low pH-values. The effects of decomposition on inhibitors are studied in depth and for the given electrolyte composition the half-life is known. The mechanisms behind the consumption of inhibitors at the cathodes however are not completely known. Therefore a model was

introduced that bases on empirical knowledge provided by the industry partners. The interaction of both models allows the simulation of the inhibitor behavior in the tankhouse cell for different parameter studies. Since the inhibitor activity does not influence the electrolyte flow, the calculation can be performed using a frozen flux formulation (calculating a scalar transport equation on a steady state velocity field). Using this technique allows to calculate the steady state inhibitor activity in a matter of minutes.

The parameter study includes a variation of the inlet angle, the inlet shape, the vertical position of the inlet, a study on multi inlet designs, a variation of the inlet flow rate and the influence of different crops on the electrolyte flow patterns and inhibitor distribution. Especially the variation of inlet design and position are of interest, as they are easy to implement in a given electrorefining tankhouse cell. For the variation of the inlet design and position as well as for the variation of mass flow, a new set of inlet simulation and global simulation is required. Since the different crops studies include changed anode-cathode geometries, a new set local simulation in addition to the global simulation is necessary.

The parameter study shows a high influence of the inlet design and position on the electrolyte flow in the tankhouse cell. The best inhibitor distribution and highest glue activities can be found when using wide and thin inlet designs rather than narrow and high inlet designs. The inlet is best positioned 125 to 200 mm above the tankhouse cell bottom, as higher positioned inlets result in lower inhibitor activity and distribution. Steeper inlet angles (55°) show better results than shallow inlet angles (35°) as they influence the formation of the bottom electrolyte layer. By increasing the mass flow and therefore increasing the bath changes per hour a higher inhibitor distribution can be achieved, of course this can also increase the amount of dispersed anode slime floating in the electrode gaps and can decrease the cathode copper quality.

10 Conclusion and Foresight

The introduced simulation approach allows the modeling of the interaction between the small scale natural convection and the large scale forced convection. The resulting electrolyte flow pattern shows the mechanisms behind the electrolyte circulation in full scale copper electrorefining tankhouse cells. The electrolyte entering the tankhouse at the submerged inlet nozzle forms a bottom layer along the centerline of the cell. The flow inside this layer is directed towards the outlet. From this layer, some of the electrolyte is pushed outside towards the walls from where the flow direction is changed upwards into the space between the electrodes and the outer wall. From this position, the natural convection inside the electrode gaps causes a net flow inside the anode cathode spacing. Inside the electrode gaps the influence of forced convection disappears. Depending on whether the electrolyte is entering the electrode gaps near the anode or near the cathode, the flow is directed downwards or upwards, following the movement caused by the density change induced natural convection. The downward facing electrolyte flow leaves the anode cathode gap a can either be pushed towards the outer wall and be circulated into the next anode cathode gap or rejoin the bottom layer and finally exit the tankhouse cell at the outlet. The upward facing electrolyte flow follows the cathode to its top and is directed outwards toward the wall. There it gets recirculated into a neighboring electrode gap.

The importance of the bottom layer as a transport mechanism in the copper electrorefining tankhouse cell becomes obvious when simulating the inhibitor activity distribution. The strong electrolyte stream transports fresh inhibitor toward the electrode gaps close to the outlet in a matter of minutes. This causes a certain amount of inhibitor to exit the tankhouse cell without being consumed at the cathodes. The parameter studies in which the bottom layer was influenced, resulting in an increased residence time, altogether showed a lower inhibitor activity in the critical areas close to the outlet. In order to utilize the glue before it exits the tankhouse cell a simulation was set up to actively adapt the electrolyte flow shortly before the exit. By implementing an obstacle in the bottom layer the electrolyte is forced to flow around the object and is pulled into the electrode gaps. The shape and size of the obstacle should be further improved to increase its ability to channel the electrolyte flow into electrode gaps with a low glue activity.

11 Literature

[1] Davenport W.: Extractive Metallurgy of Copper. Pergamon, 2002.

[2] Pavlek F.: Metallhüttenkunde. Berlin; New York; de Gruyer, 1983.

[3] Filzwieser I.:The analysis and mathematical modelling of the parameters influencing cathodic deposits in copper refining electrolysis. Dissertation, University Leoben, Austria, 2005.

[4] Houlachi G.E., J.D. Edwards and T.G. Robinson: Proceeding of the sixth international Copper-Cobre conference; Volume 5 Copper Electrorefining and Electrowinning. (2007), 202-241.

[5] Chen T.T. and J.E. Dutrizac: Mineralogical characterization of anode slimes: Part 6 – pressure leached slimes from the CCR division of Noranda Minerals Inc. Canadian Metallurgical Quarterly, Vol. 29, No. 1 (1990), 39-42.

[6] Ullmann F.: Ullmanns Encyclopädie der technischen Chemie. Fourth edition, Volume 3, Verlag Chemie, Weinheim 1973.

[7] Ibl, N.: Die Rolle des elektrolytischen Stoff- und Ladungstransportes in der Elektrometallurgie, Erzmetall 22 (1969), 87-98.

[8] Newman J.S.: Electrochemical Systems, Prentice Hall, Englewood Cliffs, N.Y. 1973.

[9] Hamann C.H. and W. Vielstich: Elektrochemie. Wiley-VCH, Weinheim, 1998, 177-182.

[10] Rombach E., J. Krüger: Grundlagen der Elektrolysetechnik. GDMB Vol. 81: Elektrolyseverfahren in der Metallurgie, (1997), 9-28.

[11] Schab D. and K. Hein: Problems of anodic and cathodic mass transfer in copper refining electrolysis with increased current densities, Canadian Metallurgical Quartaly 31, (1992), 173-179.

[12] Ibl N. and R.H. Müller: Studies of natural convection at vertical electrodes, Journal of the Electrochem. Society, No. 105, (1958), 346-353.

[13] Awakura Y., Y.Takanaka and Y. Kondo: Studies on the velocity profile in natural convection during copper deposition at vertical cathodes. Electrochemica Acta 21 (1976), 789-797.

[14] Schab D.: Elektrolytischer Stoffübergang und Elektroktistallisation bei der Kupferraffinationselektrolyse mit erhöhten Stromdichten. Dissertation, TU BAF, 1981.

[15] Lange H.J., K. Hein, I. Bauer and D. Schab: Aspekte der Elektrodenkinetik bei Metallelektrolysen. GDMB Vol. 81: Elektroverfahren in der Metallurgie, (1997), 137-160.

[16] Hein K.: Theoretische Grundlagen elektrochemischer Prozesse der Metallgewinnung, Script, TU BAF, 1975.

[17] Winand R.: Electrocrystallizaion. Process metallurgy 3: Application of polarization measurements in the control of metal deposition, Elsevier Science Publishers B.V, Amsterdam, (1984), 47-83.

[18] Ettel V.A., A.S. Gendron and B.V. Tilak: Electrowinning Copper at high current densities. Metallurgical Transactions, Vol, 6B, (1975), 31-36.

[19] Putzschke M.: Ein Beitrag zur hydrometallurgischen Verarbeitung von Krätzekupfer in schwefelsauren Lösungen. Dissertation, TU BAF, 1989.

[20] Schab D., K. Hein: Einfluss von Elektrolyttemperatur und –zusammensetzung auf die Kathodenqualität bei einer Kupferraffinationselektrolyse mit erhöhten Stromdichten. METALL 43, (1989), 1066-1072.

[21] Krajewski W.: Grundbegriffe der elektrolytischen Metallabscheidung. GDMB No. 37: Elektrolyse der Nichteisenmetalle, (1982), 1-41.

[22] Schab D. and K. Hein: Wachstumsstrukturen und Oberflächenformen von Kupferkathoden – Einfluss von Leim und Thioharnstoffzusätzen bei erhöhten Stromdichten. METALL 42, (1998), 1086-1091.

[23] Forsen O, A. Kotzschmar and A.E. Antila: Die Bedeutung organischer Additive bei der Kupferelektrolyse. Galvanotechnik 86, (1995), 3580-3590.

[24] Frederich O.: Numerische Simulation und Analyse turbulenter Strömungen am Beispiel der Umströmung eines Zylinderstumpfes mit Endscheibe. Dissertation, TU Berlin, Germany, 2010.

[25] Ferziger J.H., M. Peric: Computational Methodes for Fluid Dynamics. Springer Verlag, 1999.

[26] Patankar S.V.: Numerical Heat Transfer and Fluid Flow. Hemisphere Publishing Corporation, 1980.

[27] Hussain A.K.M.F.: Coherent structures and turbulence. Journal of fluid mechanics 173, (1986), 303-356.

[28] Pope S.B.: Turbulent Flows, Cambridge University Press, 2000.

[29] Schade H.: Tensor Analysis. De Gruyter, 1980.

[30] Schade H. and E. Kunz: Strömungslehre. De Gruyter, 1980.

[31] Breuer M., M. Pourique and W. Rodi: Large eddy simulation of internal and external flows. Specoaö Issue of ZAMM, Issue 4: Applied Science - Especially Mechanics, Akademie Verlag, Berlin, (2002), 235-238.

[32] Schlichting H.: Grenzschichttheorie. Braun Verlag,Karlsruhe, 1968.

[33] Rung T., L. Xue, J. Yan, M. Schatz and F. Thiele: Numerische Methoden der Thermo- und FLuidmechanik. Script, TU Berlin, 2002.

[34] Yannakopolous T. and A, Brenner: Isolation of the Diffusion Layer at an Electrode and the Determination of Concentration Polarization. Jounral of the Electrochemical Society 105, (1958), 521-528.

[35] Ibl N., Y. Barranda and G. Tümpler: Zur Kenntniss der natürlichen Konvektion bei der Elektrolyse: Interferometrische Untersuchungen der Diffusionsschicht. Helvetica Chimica Acta 37, (1954), 583-597.

[36] Awakura Y. and Y. Kondo: Concentration Profile in the Cathodic Diffusion Layer. Journal of Electrochem. Society 13, (1976), 1183-1193.

[37] Starsinzky H., K. Hein and D. Schab: Strömungsbedingungen in Elektrolysezellen für die elektrolytische Kupferraffination. Neue Hütte 18, (1973), 346-352.

[38] Awakura Y., Y. Takanaka and Y. Kondo: Studies on the Velocity Profile in Natural Convection During Copper Depoition at Vertical Cathodes. Electrochemica Acta 21, (1976), 787-797.

[39] Alavyoon F.: Unsteady Natural Convection and Mass Transfer in Copper Electrolysis with a Supporting Electrolyte, Electrochemica Acta 37, (1992), 333-344.

[40] Eklund A., F. Alavyoon and R.I. Karlsson: Theoretical and Experimental Studies of Free Convection and Stratification of Electrolyte in a Copper Refining Cell II. Inlfuence of the Supporting Electrolyte. Electrochemica Acta 37, (1992), 695-704.

[41] Eklund A., F. Alavyoon and R.I. Karlsson: Theoretical and Experimental Studies of Free Convection and Stratification of Electrolyte in a Copper Refining Cell. Electrochemica Acta 36, (1991), 1345-1354.

[42] Simon R.: Untersuchung zur Konvektion in einer Plattenelektrolyse. Diploma thesis, TU BAF, Freiberg, 1995.

[43] Ziegler D. and J.W. Evans: Mathematical Modelling of Electrolyte Circulation in Cells with Planar Electrodes – Part I: Electrorefining cells. Journal of Electrochem. Soc. 133, (1986), 559-566.

[44] Ziegler D.: A Study of Electrorefining and Electrowinning Cell Hydrodynamics. Dissertation, University of California, Berkleley, 1984.

[45] Hein K., G. Hanko, A. Filzwieser and M. Stelter: Untersuchungen zur Hydrodynamik bei der Kupfergewinnungselektrolyse, BHM 144, (1999), Issue 1, 6-13.

[46] Lackner A.: Strömungssimulation in verschiedenen Reaktorenn der E-Metallurgie, Dissertation, Montanuniversität Leoben, Austria, 1996.

[47] Starzinksy H.: Strömungsbedingungen in Elektrolysezellen – ein Beitrag zu Raffinationslektrolyse des Kupfers. Dissertation TU BAF, Freiberg, 1972.

[48] Schab D., H.J. Lange and K. Hein: Neue Elektrolysebäder für die Gewinnungs- und Raffinationslektrolyse, Neue Hütte 20, (1975), 179-186.

[49] Andersen A.K. and V. Archipov: Verfahren und Vorrichtungen zur elektrolytischen Trennung eines Metalls aus einer verunreinigten Lösung. Patent DL-PS 66944.

[50] Schab D.: Elektrolytischer Stoffübergnag und Elektrokristallisation bei der Kupferraffinationseletrolyse mit erhöhten Stromdichten. Habilitation thesis, TU BAF, Freiberg, 1982.

[51] Jaskula M., J. Hotlos: Densities and Viscosities of CuSO4-H2SO4-H2O Solutions. Hydrometallurgy 21, (1988), 1-7.

[52] Davenport W.G. and D.C. Price: Densities, Electrical Conductivities and Viscosities of CuSO4/H2SO4 Solution in the Range of Modern Electrorefining and Electrowinning Electrolytes. Metall.Trans. 11B, (1980), 159-163.

[53] Lackner A., K. Pachler, P. Paschen and K. Hein: CFD-Simulation of Copper Electrolysis – a Way to a new Cell Design. Proc. of the Symp. on CFD and Heat/Mass Transfer Modelling in the Metallurgical Industry. Ed.: S. Argyropoulos and F. Mucciardi, Montreal Canada, (1996), 293-304.

[54] Gu Z.H., J. Chen and T.Z. Fahidy: A study of anodeic slime behaviour in the electrorefining of copper. Hydrometallurgy 37, (1995), 149-167.

[55] Chen T.T. and J.E. Dutrizac: Mineralogical overview of the behaviour of gold in conventional copper electrorefinery anode slime processing circuits. Minerals and Metallurgical Processing, Vol. 25, No. 3, (2008), 156-164.

[56] Ling X., Z.H. Gu and T.Z. Fahidy: Anode Slime Behaviour in a Laboratory-Scale Copper Electrorefining Process. The Canadian Journal of Chemical Engineering, Vol. 72, August, (1994), 683-694.

[57] Thuy M., H. Antrekowitsch and J. Pesl: Recovery of Valuable Metals from Anode Slime of the Secondary Copper Industry. BHM, 149, (2004); Issue 1, 9-15.

[58] Leahy M.J. and M.P. Schwarz: Modelling Natural Convection in Copper Elecrorefining: Describing Turbulence Behaviour for Industrial-Sized Systems. Metallurgical and Materials Transactions B, Volume 42B, August, (2011), 875-890.

[59] Leahy M.J. and M.P. Schwarz: Experimental Validation of a Computational Fluid Dynamics Model of Copper Electrowinning. Metallurgical and Materials Transactions B, Volume 41B, December, (2010), 1247-1260.

[60] Leahy M.J. and M.P. Schwarz: Computational Fluid Dynamics Modelling of a Natural Convection in Copper Electrorefining. 16th Australasian Fluid Mechanics Conference. December (2007), 112-116.

[61] Plawsky J.: Tansport Phenomena Fundamentals, Second Edition. Rensselaer Polytehnic Institute, CRC press, 2010.

[62] Faber T.E.: Fluid Dynamics for Physicists. Cambridge University Press, 1995.

[63] Lappa M.: Fluids, Materials & Microgravity: Numerical Techniques and Insights into the Physics. Elsevier Ltd, 2004.

[64] Doche O., F. Bauer and S. Tardu: Direct Numerical Simulation of an electrolyte deposition udner a turbulent flow – A first approach. Journal of Electrochemical Chemistry, Number 664, (2012), 1-6.

[65] Nelissen G., A. Van Theemsche, C Dan, B Van den Bossche and J. Deconinck: Multi-ion transport and reaction simulations in turbulent parallel plate flow. Journal of Electroanalytical Chemistry, Number 563, (2004), 213-220.

[66] Nelissen G., G. Weyns, P. Maciel, J. Deconinck, O.V. Vyver and H. Deconinck: Numerical study of the influence of the anode position and the electrolyte flow on the deposition of copper on a wire. Electrochemica acta, number 52, (2007), 6584-6591.

[67] Pohjoranta A., A. Mendelson and R. Tenno: A copper electrolysis cell model including effects of the ohmic potential loss in the cell. Electrochemica Acta, Number 55, (2010), 1001-1012.

[68] Pohjoranta A. and R. Tenno: A computational multi-reaction model of a Cu electrolysis cell. Electrochemica Acta, Number 54, (2009), 5949-5958.

[69] Kemminger A. and A. Ludwig: Modelling the Electrolyte Flow in a Copper Electrorefining Cell. Proceedings of European Metallurgical Conference 2013, volume 2, ed: S. Eicke and M. Hahn, GDMB, (2013), 795-805.

[70] Comission on Isotopic Abundances and Atomic Weigths, Standard atomic weights 2014. Online: http://www.ciaaw.org/atomic-weights.htm, 11.05.2012.

[71] Webelements, Copper: the essentials. Online: www.webelements.com/copper, 11.05.2012.

[72] National Bureau of Standards: Journal of Reserach, volume 9, (1932), 681.

[73] Gladysz O., P. Los and E. Krzyzak: Influence of concentrations of copper, leveling agents and temperature on the diffusion coefficient of cupric ions in industrial electro refining electrolytes. Journal of Applied Electrochemistry, 37, (2007), 1093-1097.

[74] Piret N.L.: Tools for Optimizing Cu Elecrodeposition: Modeling and Reagent Addition Monitoring. Journal of Metallurgy, April (2002), 17-18.

[75] Hu E.W., W.R. Roser and F.E. Rizzo: The role of proteins in electrocrystallization during commercial electrorefining. Internation Symposium on Hydrometallurgy, ed. D.J.I. Evans and R.S. Shoemaker, AIME, New York, (1973), 155-170.

[76] Seban M.B., J.D. Scott and R.M. Cassidy: Collagen proteins in electrorefining: rate constants for glue hydrolisis and effects of molar mass on glue activity. Metallurgical Transactions, 23B, Issue 4, (1992), 125-133.

[77] Knuutila K., O. Forsen and A. Pehkonen: The effect of the CollaMat system for measuring glue activity in copper electrolyte in the laboratory and in the production plant. EPS Congress, ed. G.W. Warren, TMS, Warrendale, (1995), 559-569.

[78] Wang C.T. and T.J. O'Keefe: The influence of additives and their interactions on copper electrorefining. Proceedings of the International Symposium on Electrochemistry in Mineral and Metal Processing, Volume 84-10, ed. P.E. Richardson, S. Srinivasan and R. Woods, The Electrochemical Society, Pennington, (1984), 655-670.

[79] S. Krzewska, L. Pajdowski, H. Podsiadly and J. Podsiadly: Electrochemical Determination of Thiourea and Glue in the Industrial Copper Electrolyte. Metallurgical Transaction B, Volume 15, Issue 3, (1984), 451-459.

[80] Stantke P.: Using CollaMat to Measure Glue in Copper Electrolyte. Journal of Metallurgy, April (2002), 19-22.

[81] Blechta V.K., Z.Z. Wang and D.W. Krueger: Glue Analysis and Behaviour in Copper Electrolyte. Metallurgical Transaction B, Volume 24, Issue 2, (1993), 277-287.

12 List of Figures

13 Table Directory

1 Appendix A

1.1 Local simulation

The following UDS specifies the boundary conditions at the electrodes, i.e. it defines the amount of Cu^{2+} flux at the anode and cathode surfaces due to the local current density. The UDS also defines the body force term causing the electrolyte to sink at the anodes and rise at the cathodes.

The Profile Term will specify the amount of Copper produced at the anode as a function of the current density j

```
#include "udf.h"
#define j_an 258                    /*Anode exchange current density in A/m2*/
#define j_ca 258                    /*Cathode exchange current density in A/m2*/
#define alpha_an 0.6                /*Anode transfer coefficient*/
#define alpha_ca 0.4                /*Cathode transfer coefficient*/
#define n_el 2                      /*Current number (2 e-)*/
#define F 96485.3365                /*Faraday constant in C/mol*/
#define R 8.31
#define T 336.17
#define nu_ca 0.08
#define nu_an 0.01
#define cCu2b 0.037295
#define Beta 0.0022
#define MCu 0.06355
DEFINE_PROFILE(CUGenerate_kathode,t,i)
{
face_t f;
real j;
F_UDSI(f,t,0);
j=j_an*exp((alpha_an*n_el*F*nu_an)/(R*T))-j_ca*(F_UDSI(f,t,0)/cCu2b)*exp((-
alpha_ca*n_el*F*nu_ca)/(R*T));
begin_f_loop(f,t)
{
F_PROFILE(f,t,i) = -j*MCu/(n_el*F);          /*Input für UDS in kg/m2/s*/
}
```

```
end_f_loop(f,t)
}
DEFINE_PROFILE(CUGenerate_anode,t,i)
{
face_t f;
real j;
F_UDSI(f,t,0);
j=j_an*exp((alpha_an*n_el*F*nu_an)/(R*T))-j_ca*(F_UDSI(f,t,0)/cCu2b)*exp((-
alpha_ca*n_el*F*nu_ca)/(R*T));
begin_f_loop(f,t)
{
F_PROFILE(f,t,i) = j*MCu/(n_el*F);                    /*Input für UDS in kg/m2/s*/
}
end_f_loop(f,t)
}
DEFINE_SOURCE(Body_Force,c,t,dS,eqn)
{
real B, source, gravity, konz;
C_UDSI(c,t,0);
gravity=9.81;
konz=C_UDSI(c,t,0)*C_R(c,t);
C_UDMI(c,t,0)=konz;
B=C_R(c,t)*gravity*Beta*(C_UDMI(c,t,0)-cCu2b*C_R(c,t));
source=-B;
dS[eqn]=0.0;
return source;
}
```

1.2 Define diffusivity

The following UDS specifies the turbulent diffusivity. The diffusion due to turbulent motion is much higher than the molecular diffusion alone. It must therefore be included into the transport equation.

```
UDF that computes turbulent diffusivity for turbulent scalar transport
#include "udf.h"
real C_lam = 1.12484e-6;
DEFINE_DIFFUSIVITY(turb_diff,c,t,i)
{
real DT;
DT= C_lam + C_MU_T(c,t) / 0.7;                    /*Schmidt Number = 0.7*/
return DT;
}
```

1.3 Glue_consumption

The following UDS specifies the reduction of glue activity due to consumption at the cathodes. The UDS must set as a flux boundary condition at the cathodes.

```
/*The Profile Term will specify the amount of Inhibitor consumed at the electrodes */
#include "udf.h"
#define consumptionkonstant -0.001216648                    Decay rate kg/m²s
DEFINE_PROFILE(Consumption_kathode,t,i)
{
face_t f;
begin_f_loop(f,t)
{
F_UDSI(f,t,0);
if (F_UDSI(f,t,0) < 0.05)
F_PROFILE(f,t,i) = consumptionkonstant * F_UDSI(f,t,0);     No negative concentrations
else
F_PROFILE(f,t,i) = consumptionkonstant;                     Input for sink term in kg/m2s
}
end_f_loop(f,t)
#endif
}
```

1.4 Glue_decay

The following UDS specifies the reduction of glue activity due to decomposition in the whole tankhouse cell. The UDS must set as a cell zone condition in all fluid zones.

```
/*The Profile Term will specify the amount of inhibitor decayed in the electrolyte*/
#include "udf.h"
#define k 0.15659992                          k'*Rho
DEFINE_SOURCE(Inhib_decay,c,t,dS,eqn)
{
real source;
C_UDSI(c,t,0);
source=-k*C_UDSI(c,t,0);                      kg/m³s
dS[eqn]=-k;                                   Explicit source term
return source;
}
```

1.5 Define_velocity

The following UDS overwrites the cell values for velocities with the previously calculated mean velocities. It must be set as cell zone condition for the electrode gap cell zones.

UDF to overwrite the velocity in a domain with the average velocity vectors calculated from time-sampled data. Must be implemented in the cell zone conditions panel => fixed values X,Y,Z vel.

```
#include "udf.h"
#include "mem.h"
DEFINE_PROFILE(X_Vel,t,i)
{
cell_t c;
begin_c_loop(c,t)
{
C_PROFILE(c,t,i) = C_STORAGE_R(c,t, SV_U_MEAN)/delta_time_sampled
}
end_c_loop(c,t)
}
DEFINE_PROFILE(Y_Vel,t,i)
{
cell_t c;
begin_c_loop(c,t)
{
C_PROFILE(c,t,i) =C_STORAGE_R(c,t, SV_V_MEAN)/delta_time_sampled;
}
end_c_loop(c,t)
}
DEFINE_PROFILE(Z_Vel,t,i)
{
cell_t c;
begin_c_loop(c,t)
{
C_PROFILE(c,t,i) = C_STORAGE_R(c,t, SV_W_MEAN)/delta_time_sampled;
}
end_c_loop(c,t)
}
```

2 Appendix B

2.1 Standard case 45° inlet angle velocity field

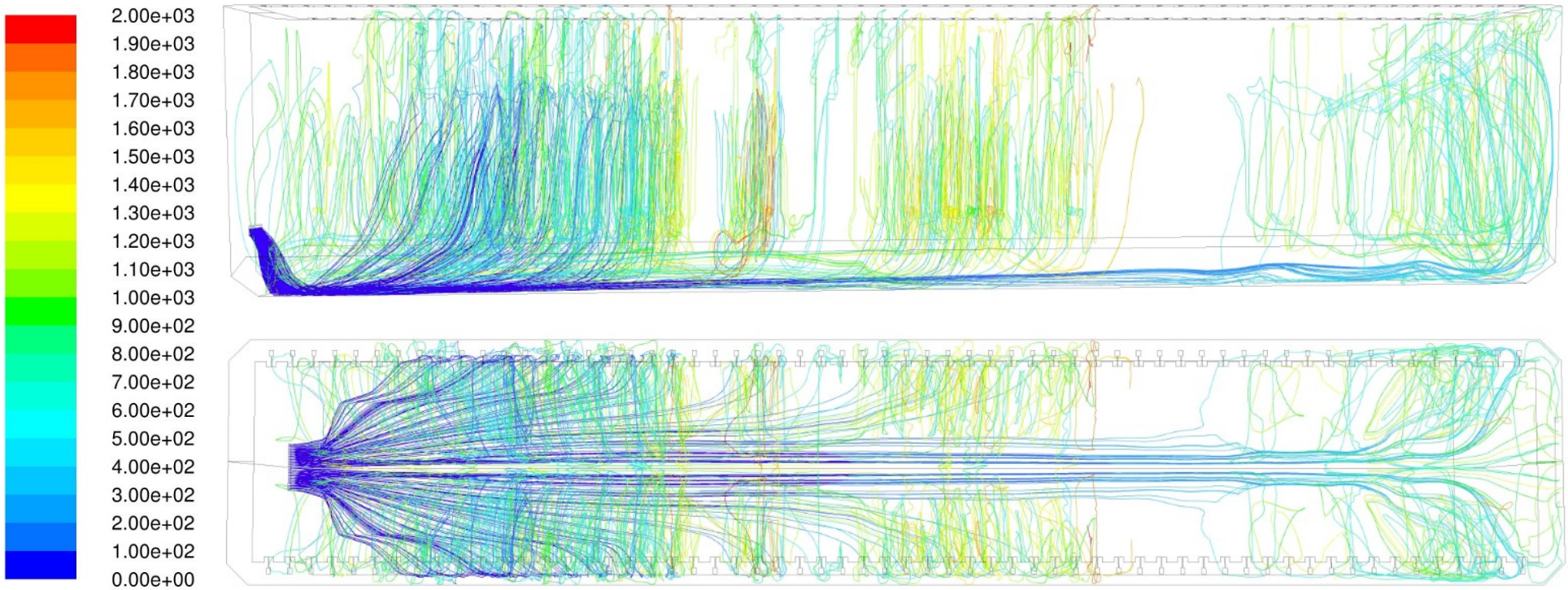

Figure 114: Pathlines colored by time [s]; standard case

2.2 Variation of the inlet angle

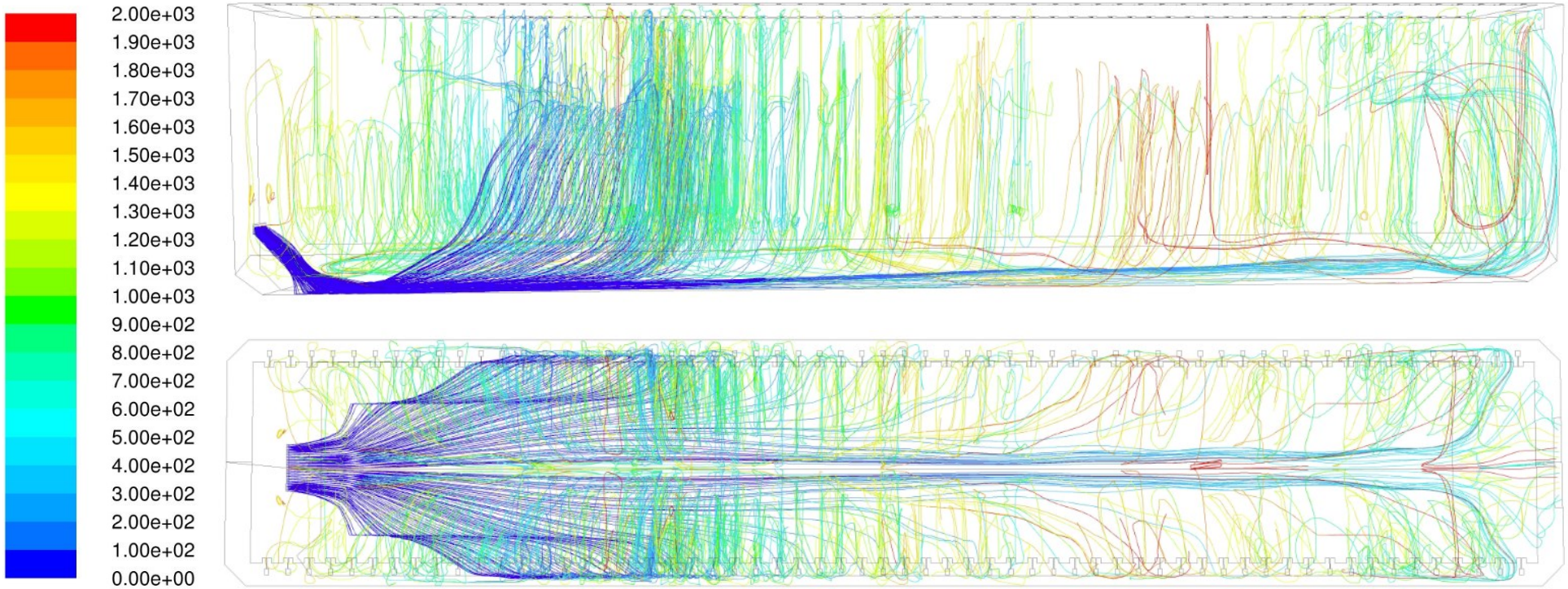

Figure 115: Pathlines colored by time [s]; 35° inlet angle

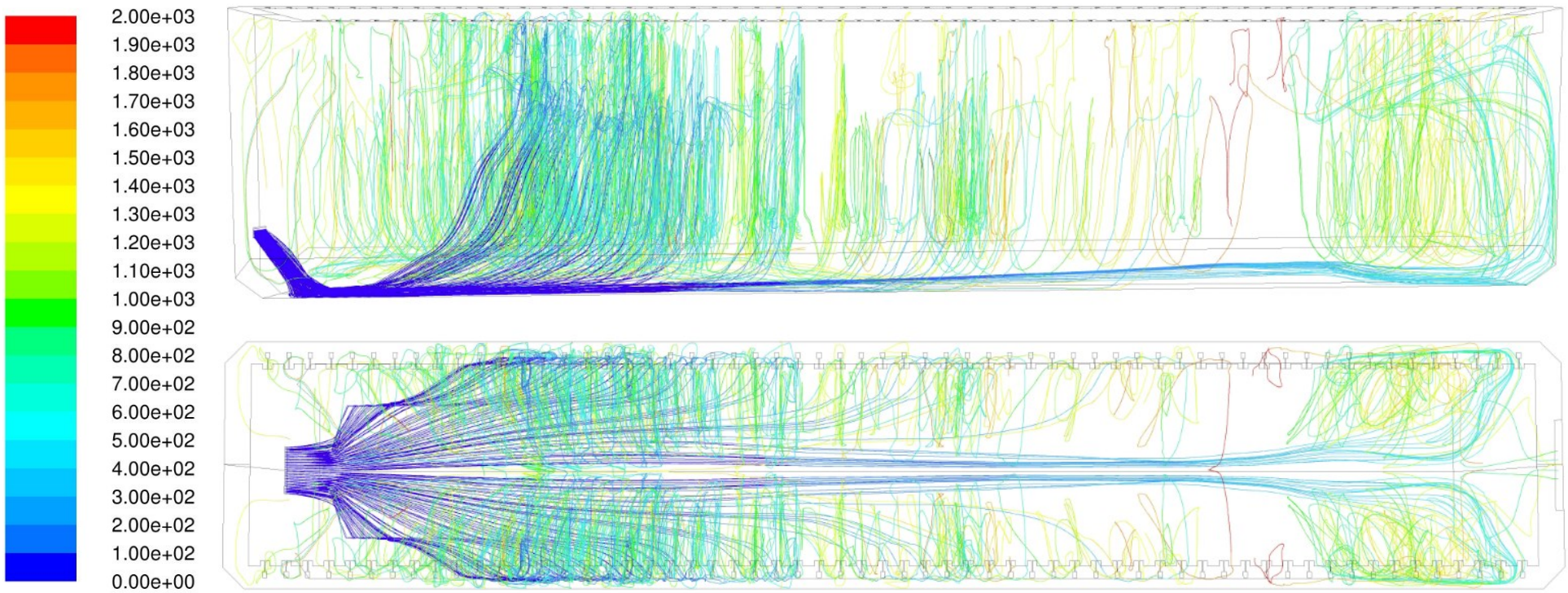

Figure 116: Pathlines colored by time [s]; 40° inlet angle

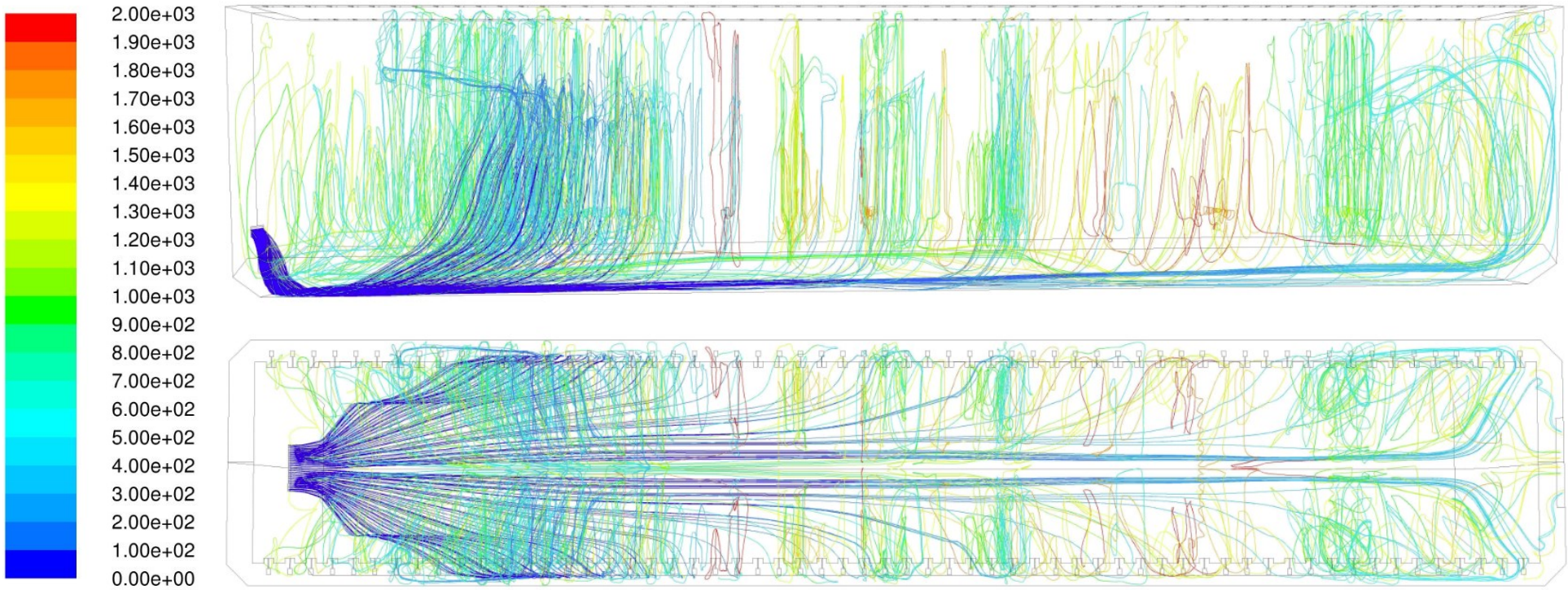

Figure 117: Pathlines colored by time [s]; 50° inlet angle

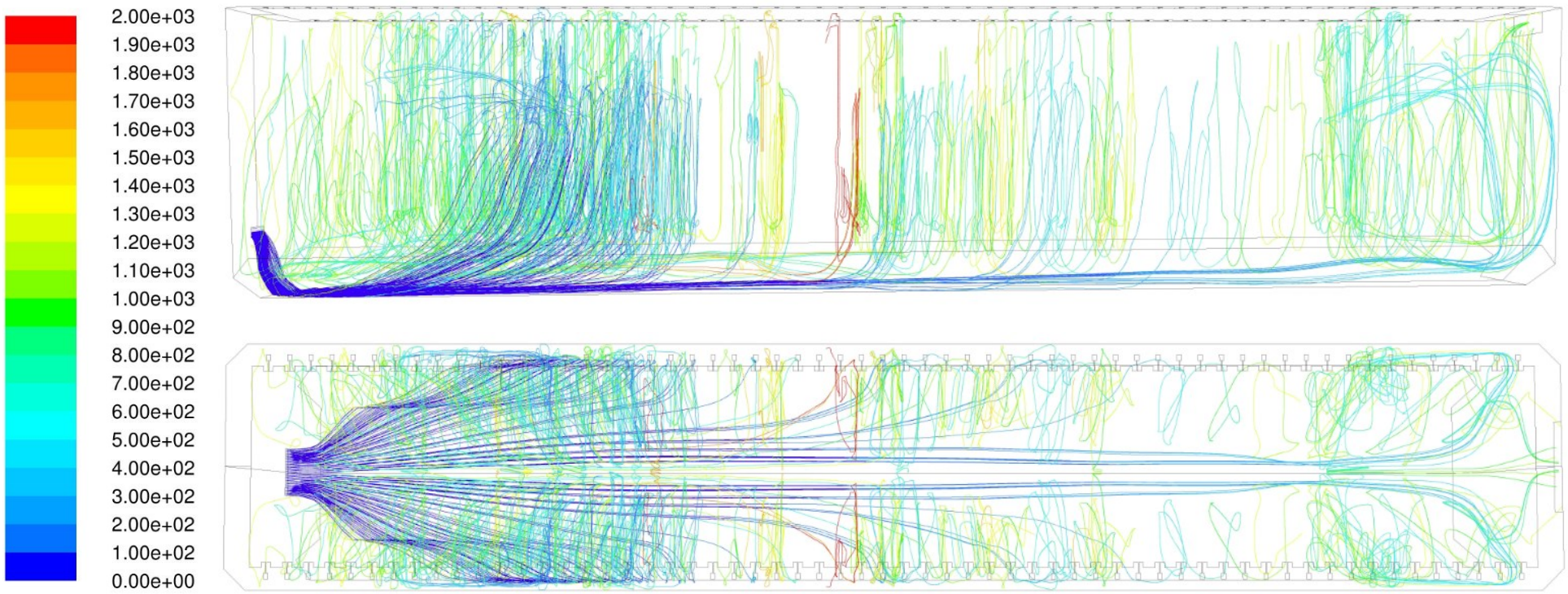

Figure 118: Pathlines colored by time [s]; 55° inlet angle

2.3 Variation of the inlet elevation

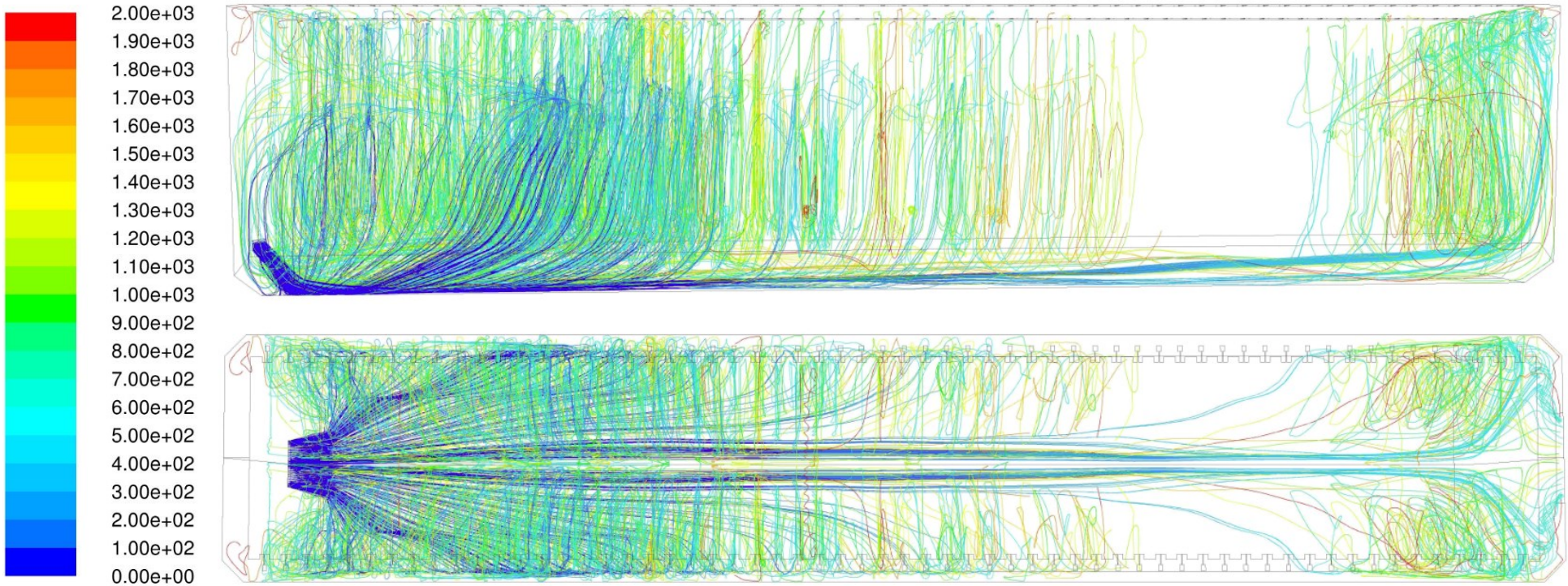

Figure 119: Pathlines colored by time [s]; low elevation 1

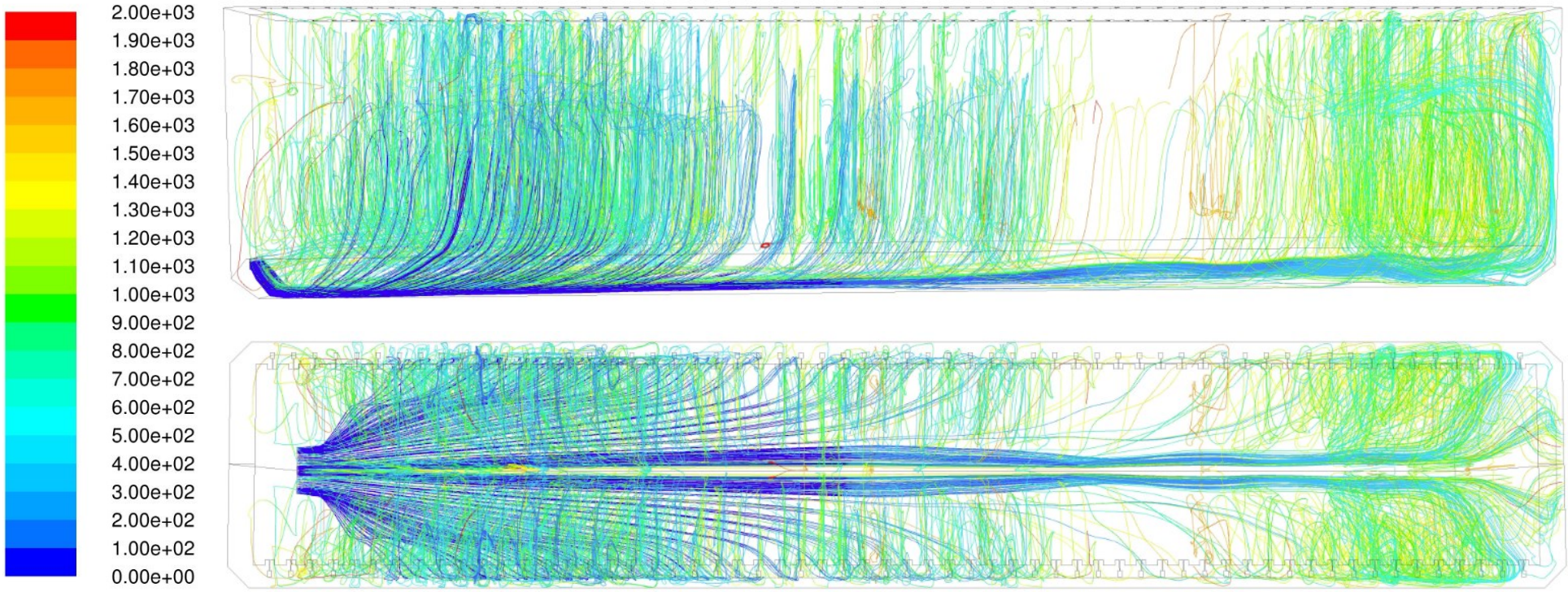

Figure 120: Pathlines colored by time [s]; low elevation 2

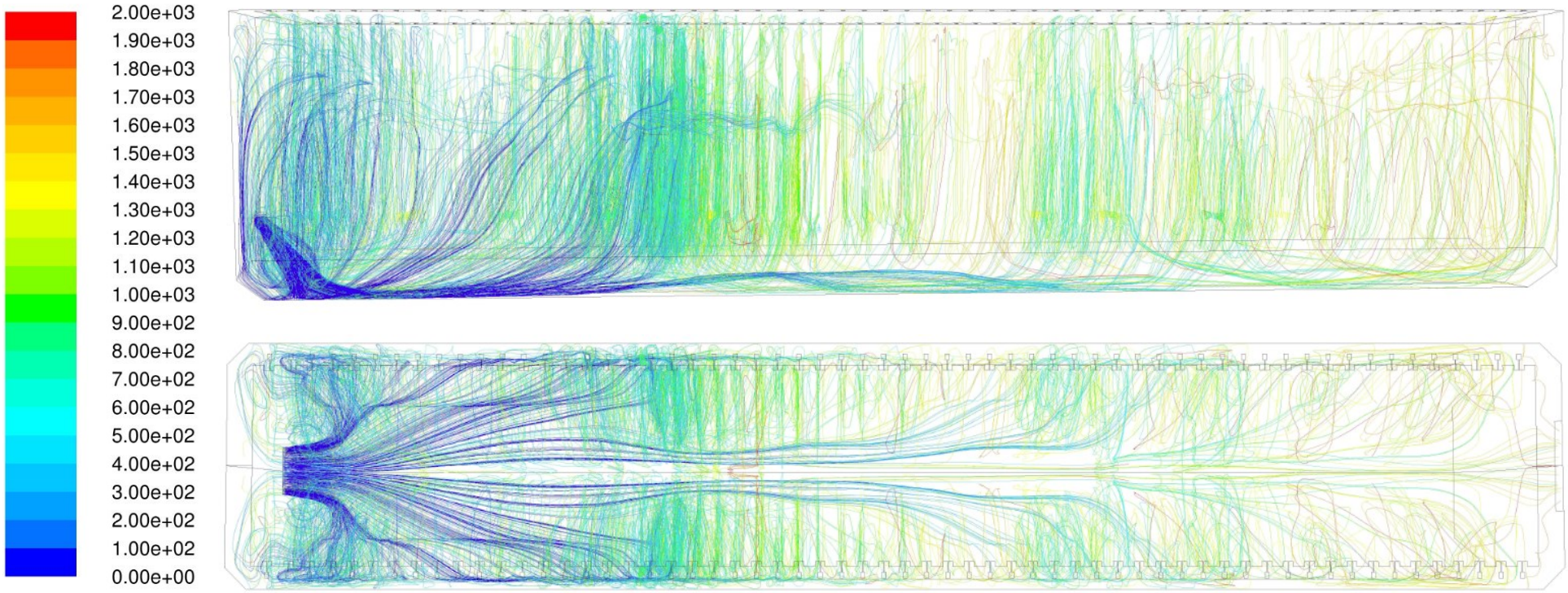

Figure 121: Pathlines colored by time [s]; high elevation 1

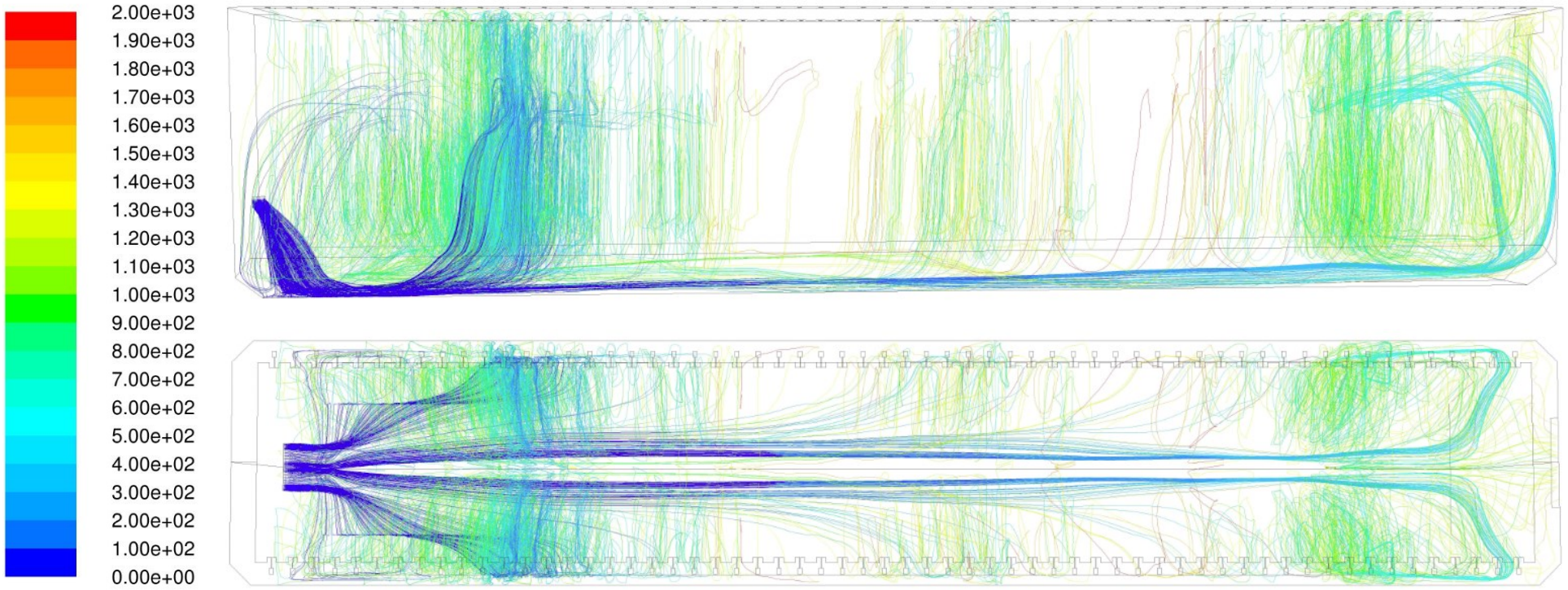

Figure 122: Pathlines colored by time [s]; high elevation 2

2.4 Variation of the inlet shape

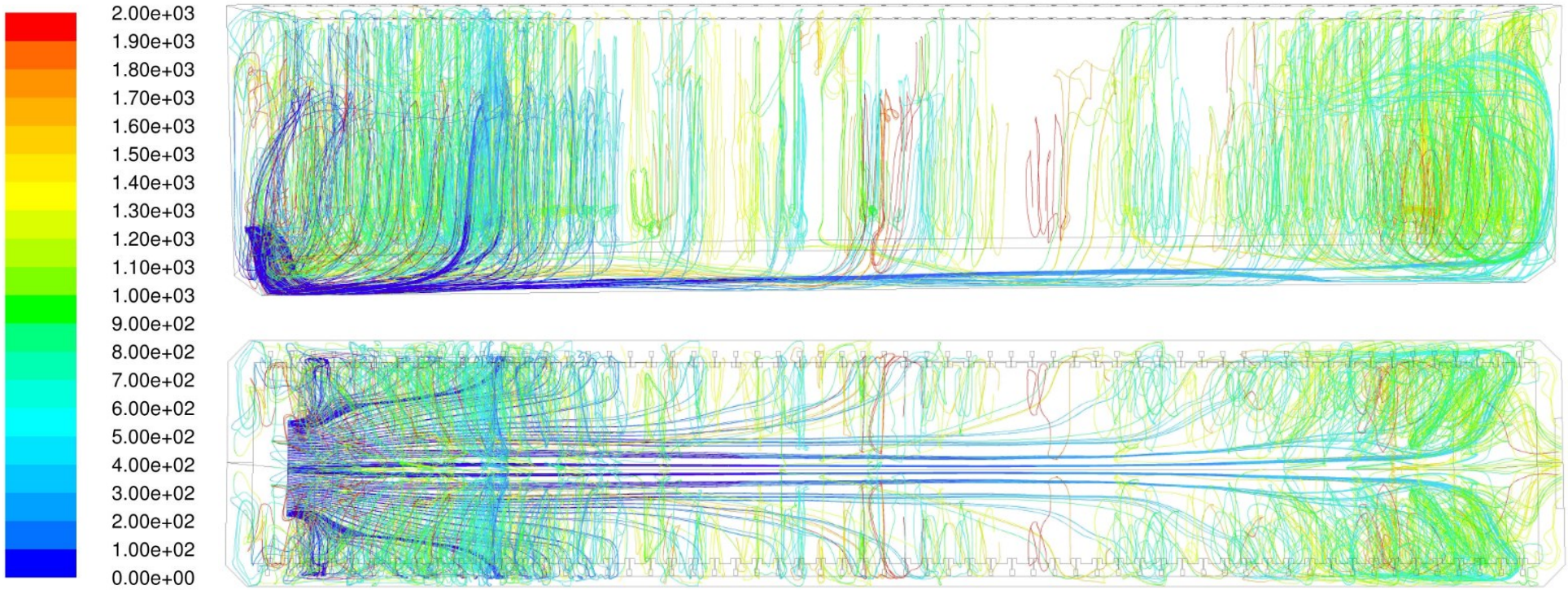

Figure 123: Pathlines colored by time [s]; inlet shape 1

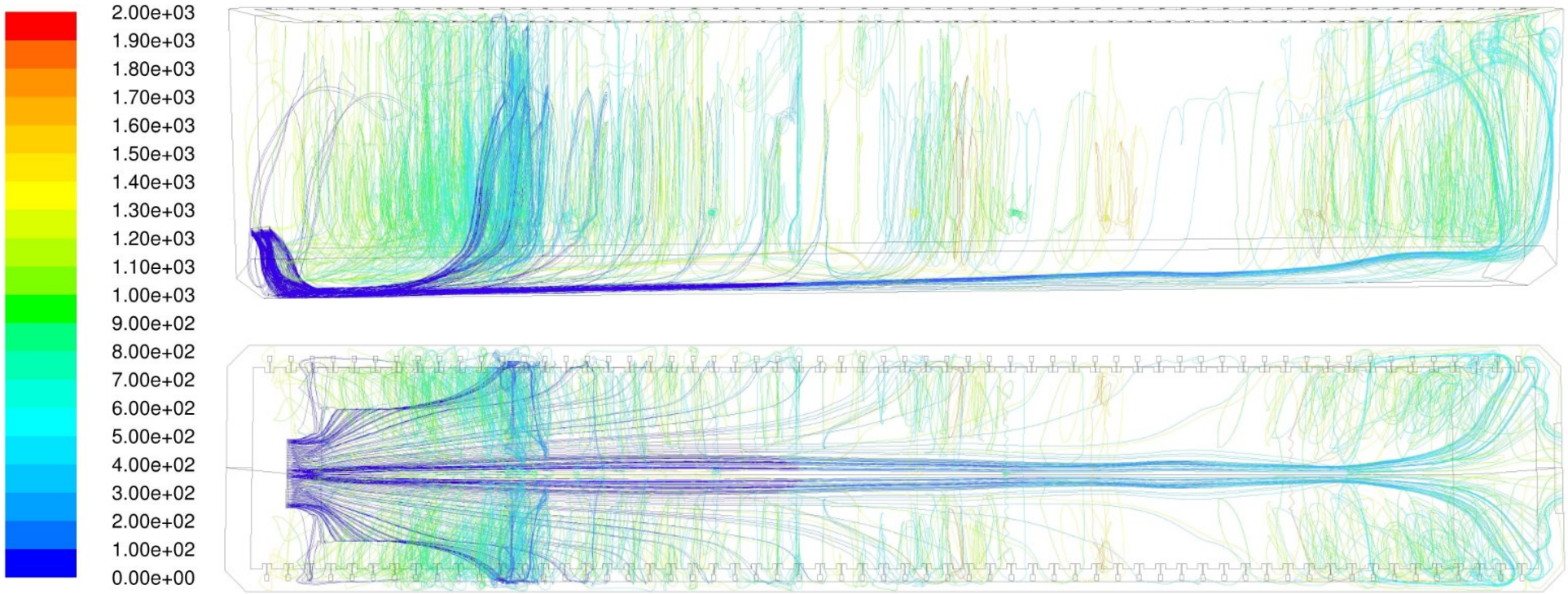

Figure 124: Pathlines colored by time [s]; inlet shape 2

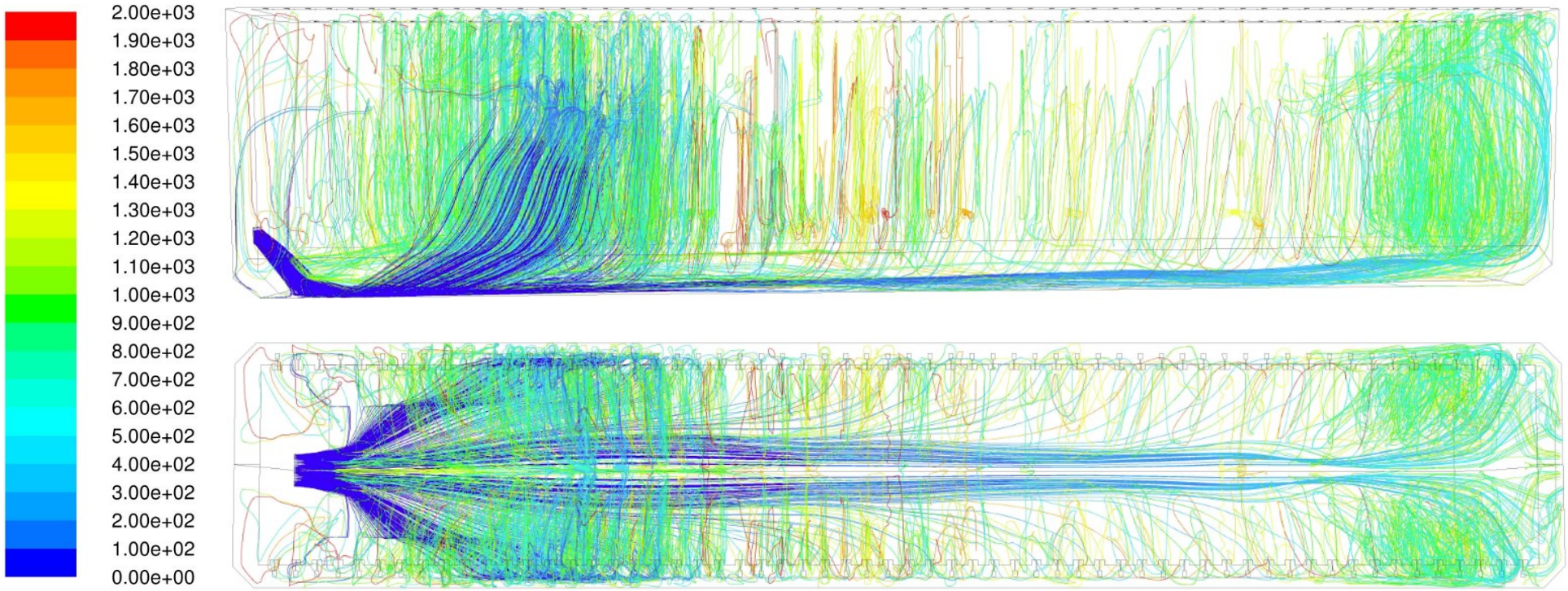

Figure 125: Pathlines colored by time [s]; inlet shape 3

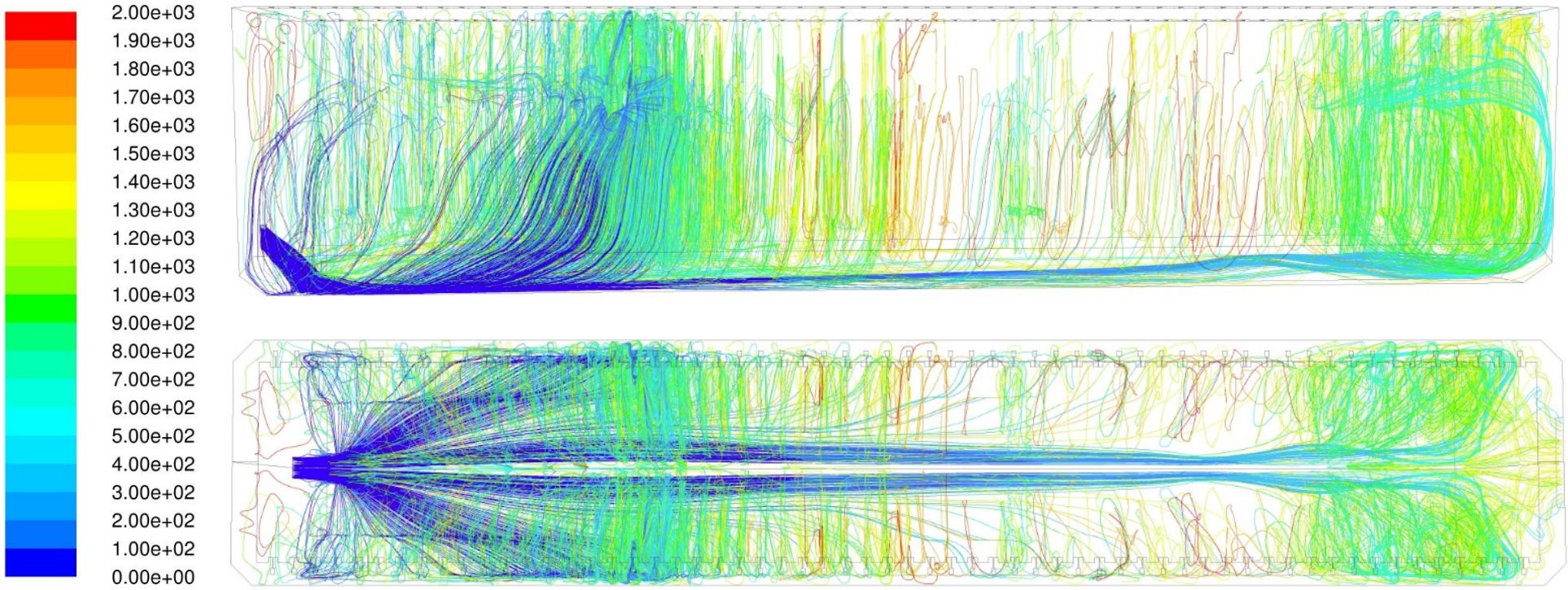

Figure 126: Pathlines colored by time [s]; inlet shape 4

2.5 Multi inlet designs

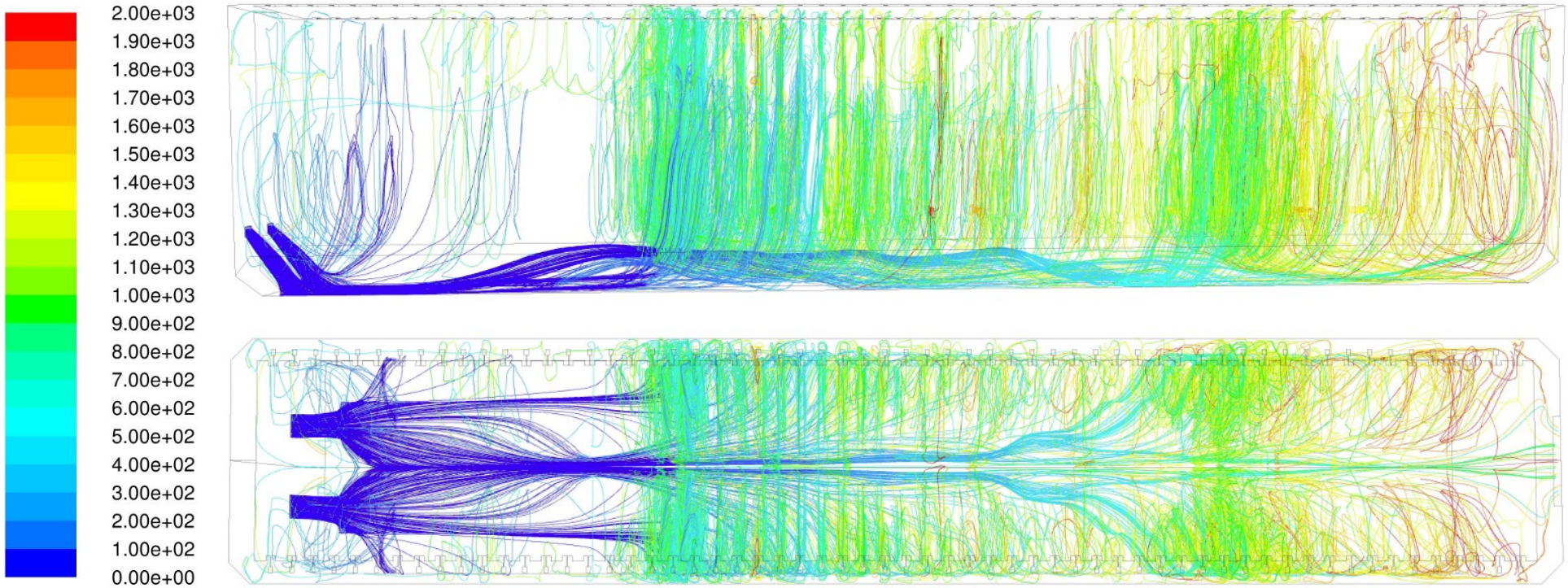

Figure 127: Pathlines colored by time [s]; multi inlet design 1

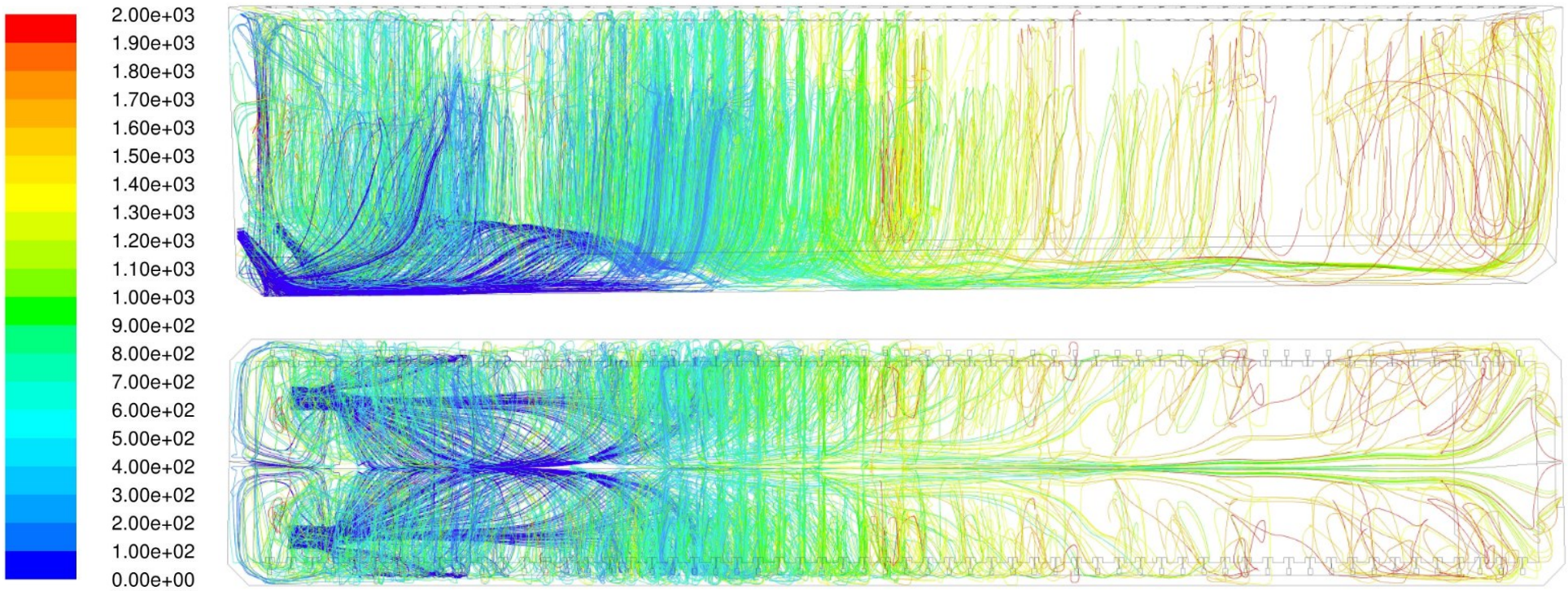

Figure 128: Pathlines colored by time [s]; multi inlet design 2

2.6 Different crops

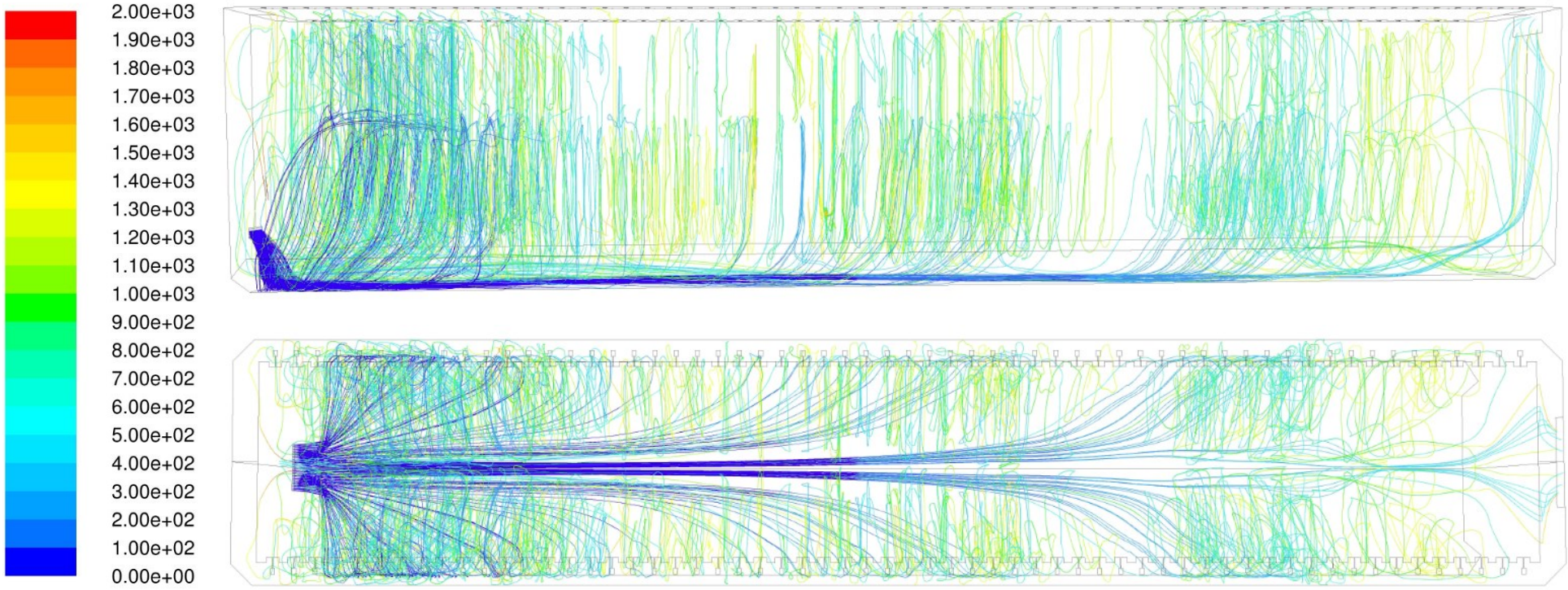

Figure 129: Pathlines colored by time [s]; crops 2

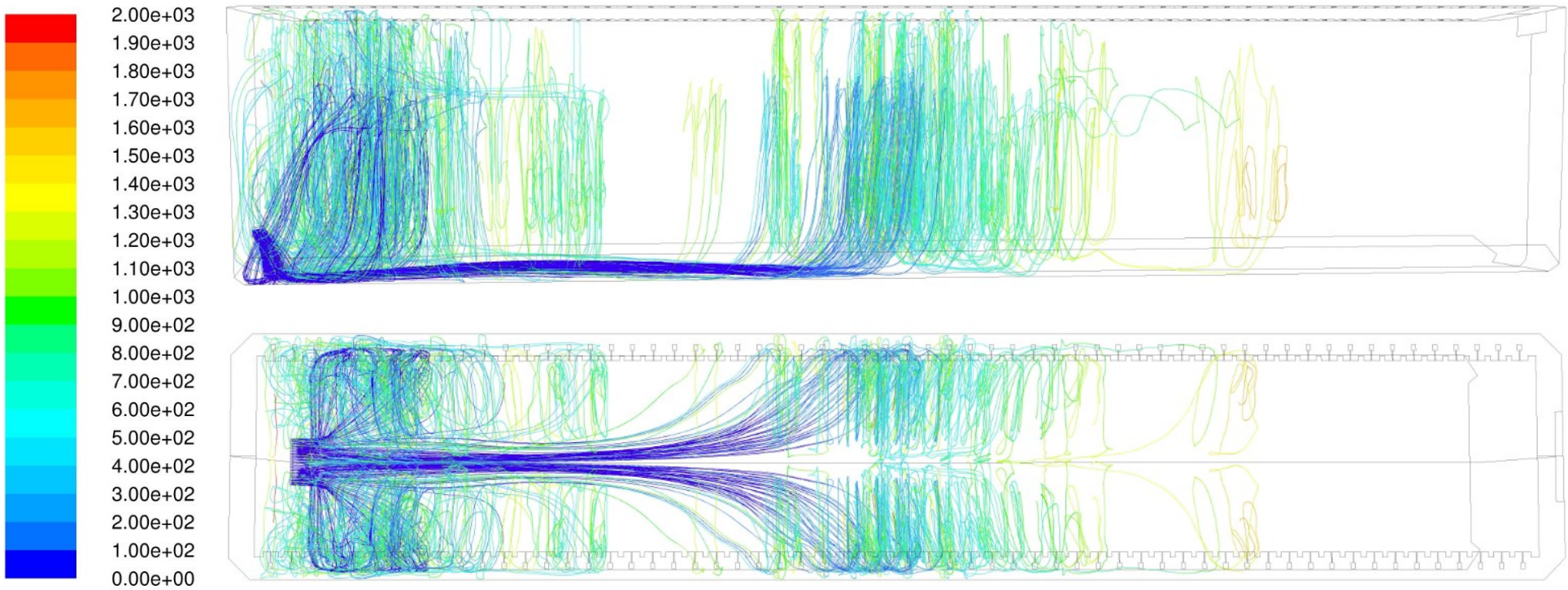

Figure 130: Pathlines colored by time [s]; crops 3 start

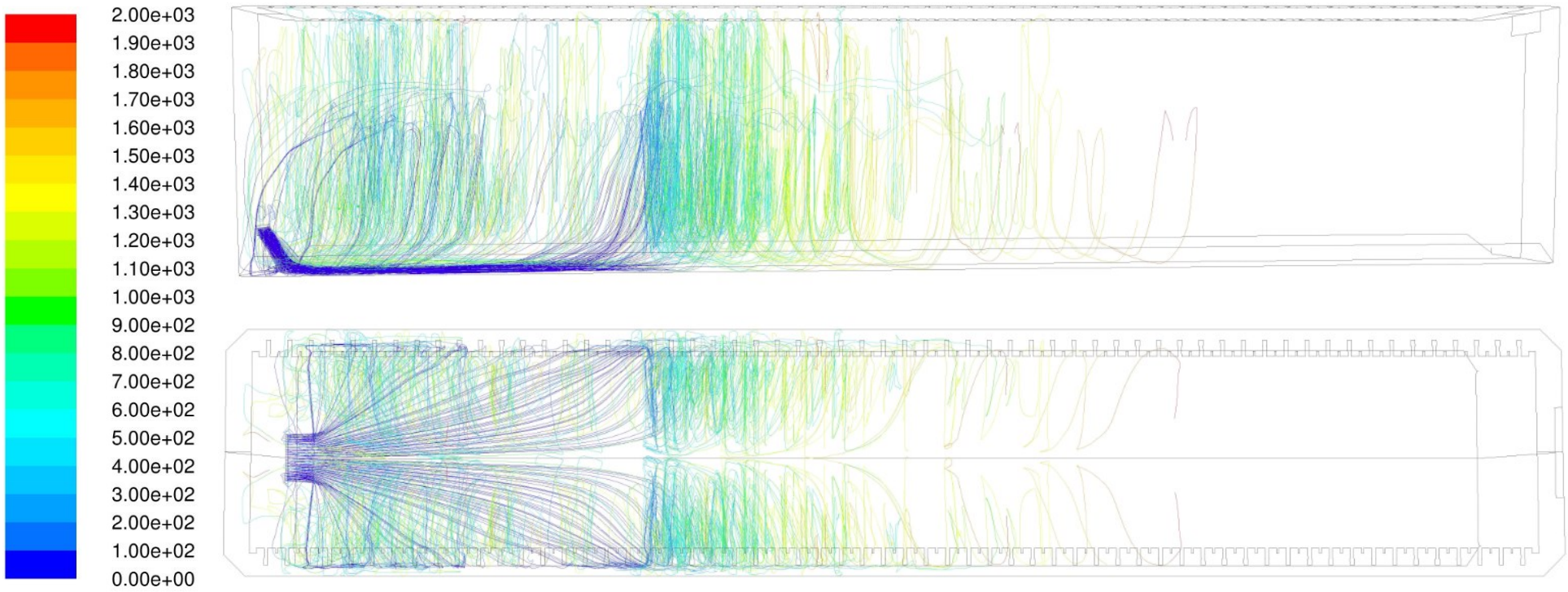

Figure 131: Pathlines colored by time [s]; crops 3 end

2.7 Variation of the flow rate

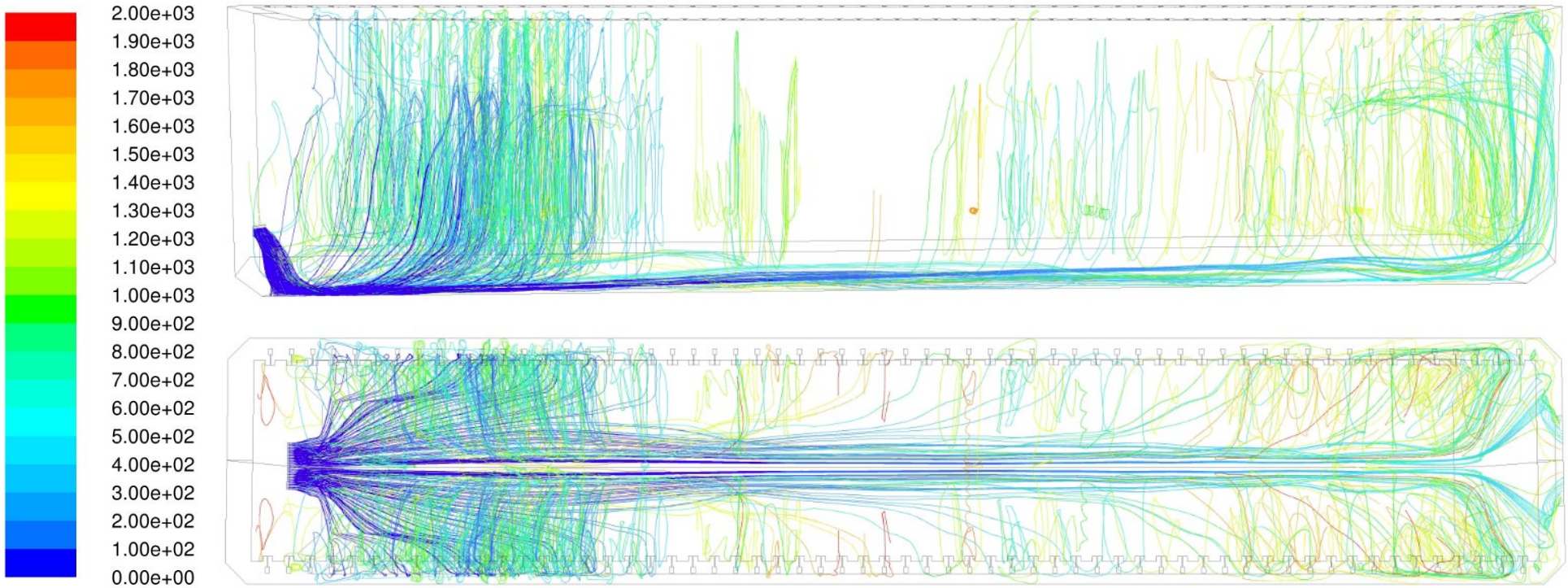

Figure 132: Pathlines colored by time [s]; flow rate 1 (-20%)

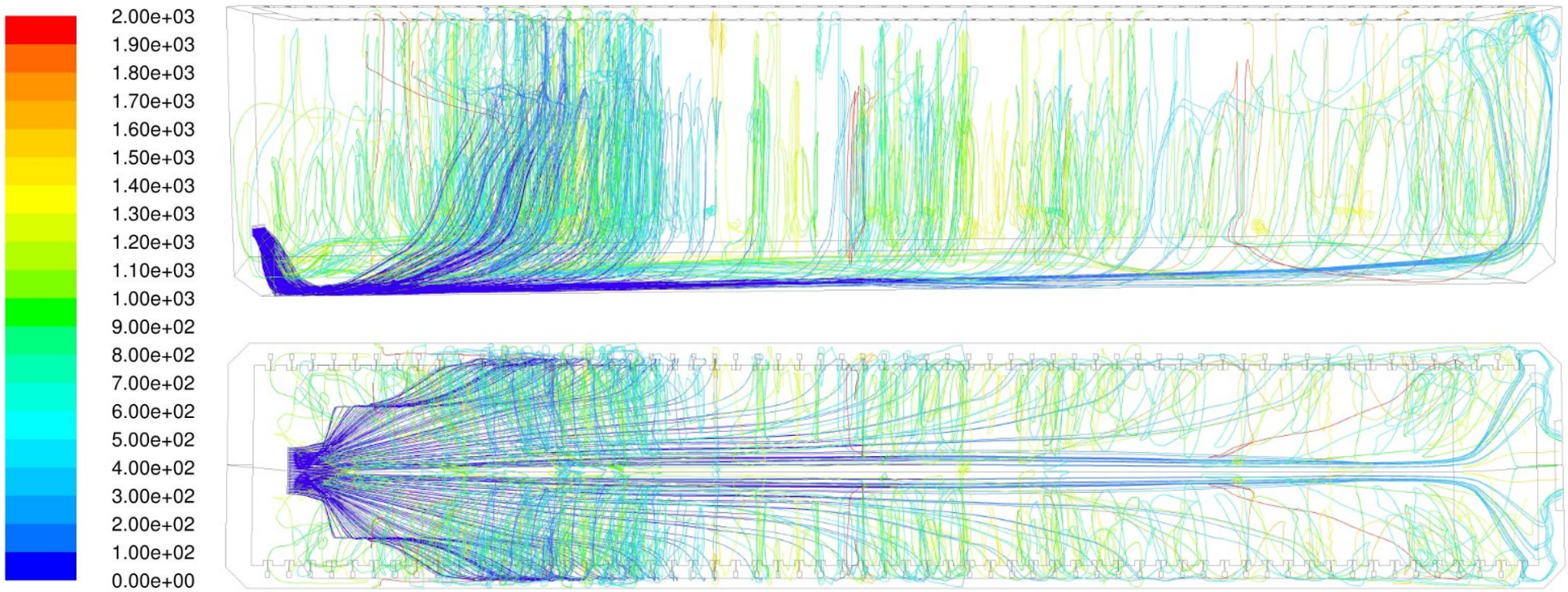

Figure 133: Pathlines colored by time [s]; flow rate 2 (+20%)

2.8 Obstacle flow

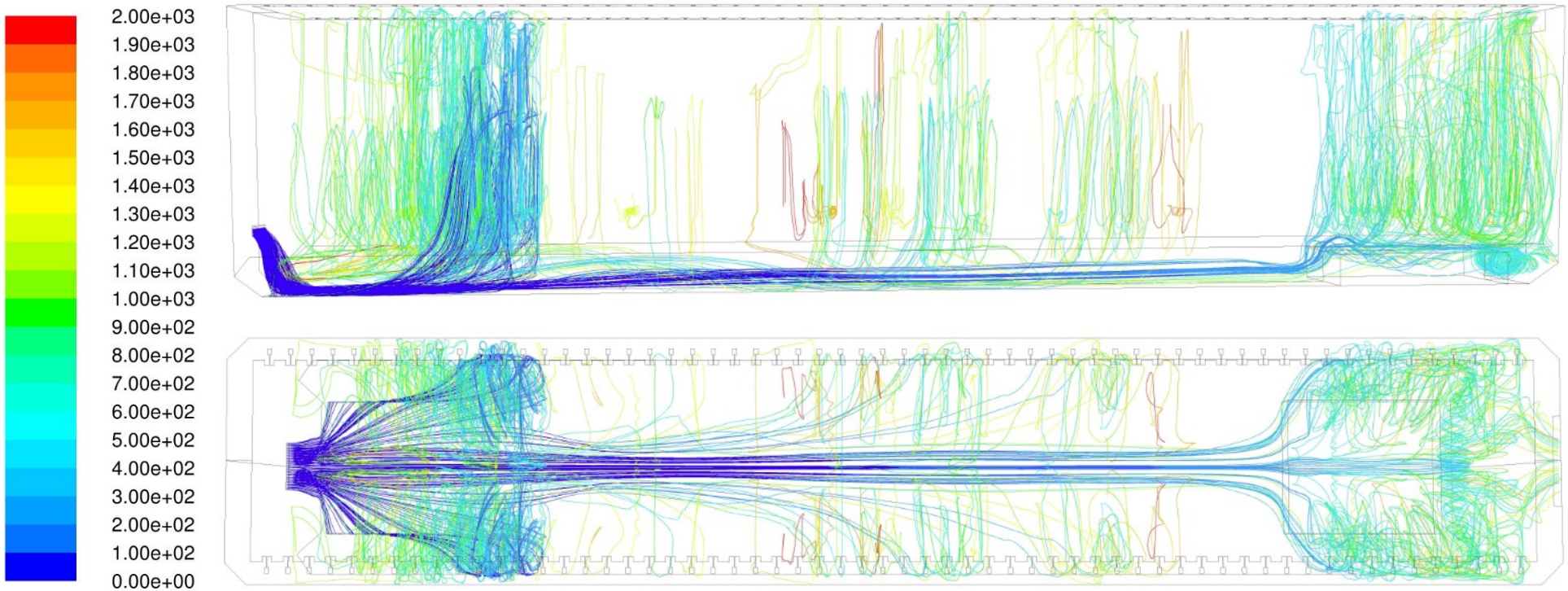

Figure 134: Pathlines colored by time [s]; obstacle flow